

Advanced Characterisation of Deposits in Diesel Fuel Filters

Submitted March 2021, in fulfillment of
the conditions for the award of the
Engineering Doctorate.

Matteo Spanu
4289993

Supervised by Prof. Colin E. Snape, Dr. David J. Scurr

School of Chemical Engineering
University of Nottingham

I hereby declare that this dissertation is all my own work, except as indicated in the text:

Signature _____

Date _____ / _____ / _____

Abstract

The fuel filtration system is an integral part of the internal combustion engine. With the ever more stringent emission limits and desire for performance from vehicles, resultant changes to the FIE have meant that they are less tolerant of contaminant particulates and deposit build up. The fuel filter is situated between the fuel tank and the FIE and is used to remove as much of the contaminant as possible to minimise damage to the FIE. As with FIE, blocking of the fuel filters can lead to reduction in performance, increase in emissions, increase in fuel contamination seen by the FIE, and in extreme cases, engine malfunction. In order to mitigate deposit build up, additives such as DCA are commonly employed, but first an understanding of the deposit is necessary in order to design effective additives.

SEM-EDX, XPS and SIMS have played a vital part in identifying a variety of different deposits that can be present on fuel filters from laboratory and engine test rigs as well as fuel filters from the field. Tandem MSMS has also been employed to unambiguously identify some of the chemical species. Depth profiling of the deposit is now commonly used to describe the deposit on FIE, and in this thesis we will employ similar techniques to describe the layering of deposits in diesel fuel filters for the first time.

As the data from SIMS can be large, a purpose-built script "compound_finder" was design to be able to assign possible formula to large amounts of SIMS peaks. The user can change a variety of settings including elements and isotopes to consider, deviation and intensity limits to customise their search.

As the fuel saturated filters were all analysed in-situ, this thesis characterised common SIMS peaks that are present in dual phase melt blown fibres to enable the differentiation between deposit and filtration media. The compound_finder script was used to assign a series of PAH ions which saturated the reference filter spectra.

A custom multi-pass filtration rig was designed to test the effects of different combinations of FAME, HVO and petroleum diesel on filters. The initial flow rates of the seven combination of fuels ranged from 55 to 110 L/h. Whilst all fuel combinations reduced in flowrate after 40 hours of running, after 27 hours a B100 fuel blend blocked the filter. Using 3D OrbiSIMS, it was possible to unambiguously assign the presence of sterol glucoside in the deposit to less than 0.1 ppm deviation.

Eight filters from different DW10 engine tests using combinations of DCA, corrosion

inhibitor and detergents alongside different sodium sources were analysed. SEM-EDX revealed that the morphology of the deposits varied between filters from particle like features trapped in the filter pores to film like layers covering the fibres. 3D OrbiSIMS data showed the presence of dodecyl succinic sodium salts in filters that had a film like layer. Depth profiles of the deposit were explored for the first time and showed the presence of multiple layers in the film like deposit. The first layer which generally appeared to reduce in intensity within 100 s of sputtering contained sodium chloride, organonitrogen and sodium carbonate species, although the latter was seen in the bulk deposit in other filters. The second layer, the bulk of the deposit contained sodium salts and carbonates, as well as other acid species. In some of the engine test filters that did not have a layer like film, alkylbenzene sulfonate (ABS) ions were present on the surface of the filters.

Three field filters from different geographical locations were analysed. The deposit morphology and chemistry varied between them with the presence of inorganic film like deposit inbetween the fibres as well as complex organic structures and iron oxide particles. As with the engine test filters, depth profiling of the deposit on these field filters was applied for the first time to show multiple layers. A large contingent of the SIMS data of a European and North American filters can be attributed to the presence of calcium associated ions found in the bulk of the deposit. The North American filter also showed a presence of sodium associated salts and carbonates on the surface and in the bulk of the deposit. In both the European and North American filters, the surface and initial part of the bulk deposit had a presence of ABS. In a filter from the Asian region, iron oxide particles were seen alongside the presence of a polyisobutylene succinimide fragmentation ion series.

Publications

Edney, M. K., Lamb, J. S., Spanu, M., Smith, E. F., Steer, E., Wilmot, E., Reid, J., Barker, J., Alexander, M. R., Snape, C. E. and Scurr, D. J. (2020), 'Spatially resolved molecular compositions of insoluble multilayer deposits responsible for increased pollution from internal combustion engines', ACS Applied Materials Interfaces **12**, 51026—51035.

Spanu, M., Reid, J., Barker, J., Scurr, D. and Snape, C. E. (2018), 'Detailed characterisation of diesel fuel filter deposits by ToFSIMS and other analytical methods', *in* '12th International Colloquium Fuels Conventional and Future Energy for Automobiles'.

Acknowledgements

I firstly wish to express my appreciation to Innospec and the EPSRC for the financial support and opportunity given to me throughout undertaking this EngD.

My sincere gratitude goes to my academic supervisors Professor Colin Snape and Dr. David Scurr. They have been incredibly patient and given thoughtful supervision throughout this process of researching and writing this thesis.

I would like to thank in particular my industrial supervisors Dr. Jim Barker and Ms. Jacqueline Reid for their support and encouragement.

I also wish to thank Mr. Dave Pinch, Dr. Edward Wilmot, Dr. Will Meredith, Dr. Elizabeth Steer, Dr. Craig Stoppiello, Dr. Nichola Starr, and Ms. Stefanie Kern for training and guidance with their respective expertise.

I would also like to thank my colleagues at the University of Nottingham. Lastly, I would like to thank my friends and family for their unconditional support.

Contents

Abstract **i**

Publications **iii**

Acknowledgements **v**

Abbreviations **xxi**

1 Introduction **1**

1.1 The Diesel Engine 1

1.2 Diesel and Biofuels 2

1.3 Global Light-Duty Vehicle Market 4

1.4 Emission Standards 7

1.5 Fuel Standards 8

1.6 Diesel Engine Advancements 9

1.7 Fuel Filter Advancements 10

1.8 Additives 11

1.9 Aims and Objectives 13

2 Literature Review **14**

2.1 Deposit Formation 14

2.2 Engine and Laboratory Testing 16

2.3 Scanning Electron Microscopy – Energy Dispersive X-Ray Spectroscopy . . 17

2.4 X-Ray Photoelectron Spectroscopy 18

2.5 Secondary Ion Mass Spectrometry 21

2.5.1 Time-of-Flight Secondary Ion Mass Spectrometry (ToF-SIMS) . . . 23
2.5.2 Orbitrap-Secondary Ion Mass Spectrometry . . . 24
2.6 Multivariant Analysis . . . 25
2.6.1 Principal component analysis . . . 25
2.6.2 Non-Negative Matrix Factorisation . . . 26
2.7 Gaps in the literature . . . 27

3 Methods 28
3.1 Samples . . . 28
3.1.1 Control Samples . . . 28
3.1.2 Engine Test Samples . . . 28
3.1.3 Laboratory Test Samples . . . 29
3.1.4 Field Samples . . . 29
3.1.5 Vacuum Drying . . . 30
3.2 In-House Rig Methodology . . . 30
3.3 Analysis Techniques . . . 32
3.3.1 Scanning Electron Microscope and Energy-Dispersive X-ray Spectroscopy . . . 32
3.3.2 X-Ray Photoelectron Spectroscopy . . . 33
3.3.3 Static Secondary Ion Mass Spectrometry . . . 34
3.3.4 Dynamic Secondary Ion Mass Spectrometry . . . 37
3.4 SIMS Data Analysis . . . 37
3.4.1 Data Pre-Processing . . . 37
3.4.2 Principal Component Analysis . . . 38
3.4.3 Non-Negative Matrix Factorisation . . . 39
3.4.4 Homologous Series Finder . . . 39

4 Control Test Samples 41
4.1 Introduction . . . 41
4.2 Scanning Electron Microscope . . . 41

4.3 X-Ray Photoelectron Spectroscopy 43
4.4 Static Secondary Ion Mass Spectrometry 47
4.5 Discussion 53
4.6 Conclusion 54

5 Laboratory Test Samples **55**
5.1 Introduction 55
5.2 Filtration Rig 56
5.3 Scanning Electron Microscopy 59
5.4 X-Ray Photoelectric Spectroscopy 62
5.5 Dynamic Secondary Ion Mass Spectrometry 65
5.6 Discussion 70
5.7 Conclusions 70

6 Engine Test Samples **72**
6.1 Introduction 72
6.2 Scanning Electron Microscope 73
6.3 X-Ray Photoelectron Spectroscopy 79
6.4 Static Secondary Ion Mass Spectrometry 82
6.5 GCIB Orbi-SIMS Analysis 90
6.5.1 Static Secondary Ion Mass Spectrometry 90
6.5.2 Dynamic Secondary Ion Mass Spectrometry 96
6.6 Discussion 102
6.7 Conclusions 104

7 Field Samples **105**
7.1 Introduction 105
7.2 Scanning Electron Microscope 106
7.3 X-Ray Photoelectron Spectroscopy 111
7.4 Dynamic Secondary Ion Mass Spectrometry 114
7.4.1 North American Filter (FSF 001) 114

7.4.2 Asian Filter (FSF 002) 118
7.4.3 European Filter (FSF 003) 123
7.5 Discussion 126
7.6 Conclusion 127

8 Final Conclusions **129**

9 Future Work **132**

Bibliography **133**

Appendices **149**

A SEM-EDX Work **149**

B Compound_finder **155**

C Identified Molecular Ions **165**

List of Tables

1.1 Properties of various biodiesels compared to ULSD meeting ASTM D975 standard, from EIA (2018) 4

1.2 Progression of euro emission standards from Euro 1-6. *From Euro 5, PM was also defined by number of particles, shown in (brackets). Data combined from Euro 1 (EEC, 1993*c*), Euro 2 (EC, 1994), Euro 3-4 (EC, 1998*a*), Euro 5-6 (EC, 2007) 7

1.3 Progression of US emission standards from Tier 1 and 2. *Known as non-methane hydrocarbons (NMHC) in 1997. Values in Tier 2 are from bin 8, adapted from (EPA, 2016) 8

3.1 Information of the physical nature of the reference filters. 28

3.2 Engine Test Filter (ETF) sample references with the additives and contaminants used in the CEC F-98-08 DW10B engine test. 29

3.3 Location and fuel information of three filters from the field. 30

3.4 Flowrates through the filtration rig with no filter installed and density of the fuel mixtures at $25°C$ 31

3.5 Fuel composition standards for each in-house multi-pass filtration test using a 2^3 factorial experimental design 32

3.6 Binding energy ranges for each scan type 34

3.7 ToF calibration peaks 35

3.8 Orbitrap^{TM} calibration peaks 36

4.1 Binding energy ranges for the C1s components of the control filters. 44

4.2 Proposed formula for the oxygen containing positive ions labeled in Figure 4.5c (c) and their respective DBE and deviations 50
4.3 Proposed formula for the oxygen containing negative ions labeled in Figure 4.8 and their respective DBE and deviations 52

5.1 Experiment ID and fuel combinations used in the form Yxxx, where Y is the fuel type and xxx is the % v/v. 56
5.2 Flowrates through the filtration rig with no filter installed and density of the fuel mixtures at $25°C$. 56
5.3 Calculated time taken for flowrate to reach 50% of initial flowrate for each experiment based on the gradient of the line of best fit, calculated from Equation 1.1, and the R^2 number for the data. 58
5.4 Binding energy ranges for the C1s components of LTFs and reference filter CF 003 (Chapter 4.3). 62
5.5 Proposed formulas and their respective deviations of the peaks identified in LTF 002 (Figure 5.8). 66
5.6 Proposed formulas and their respective deviations of the peaks identified in LTF 002 (Figure 5.9). 68

6.1 Additive and contaminations added to fuel used in DW10 engine test. . . . 73
6.2 Binding energy ranges for the C1s components of ETFs and reference filter CF 002 (Chapter 4.3). 79
6.3 Proposed formulas and their respective deviations of the peaks identified in the PC loadings of the ToF-SIMS data (Figure 6.9). 83
6.4 Proposed formulas and their respective deviations of the peaks identified in the PC loadings of the ToF-SIMS data (Figure 6.14). 92
6.5 Proposed formula for peaks identified in Figure 6.20 97

7.1 Summary of fuel used and geographical origin of field sample filters. 105
7.2 Binding energy ranges for the C1s components of ETFs and reference filter CF 002 (Chapter 4.3). 111

7.3 Proposed formulas and their respective deviations of the peaks identified in Figure 7.7. 115
7.4 Proposed formulas and their respective deviations of the peaks identified in Figure 7.10. 119
7.5 Proposed formulas and their respective deviations of the peaks identified in Figure 7.11. 120
7.6 Proposed formulas and their respective deviations of the peaks identified in Figure 7.15. 123

C.1 Proposed formulas of ions identified in this thesis, their respective deviations and information on their origin. 165

List of Figures

1.1 Pressure-volume diagram of a diesel cycle, adapted from Nazridoust (2004) 2

1.2 Transesterification process of vegetable oil to form biodiesel, adapted from Diesel (2001) 3

1.3 Percentage share of diesel cars in Europe, Japan and the US between 1990 and 2015, adapted from Transport and Environment (2017) 5

1.4 CO_2 emissions from European diesel and petrol cars compared to Japanese cars between 1990 and 2015, adapted from Cames and Helmers (2013) . . . 6

1.5 Simplified diesel engine fuel injection system schematic, from Richards (2014) 10

1.6 Additive chemistry examples, adapted from ATC (2013) 12

2.1 Schematic of Sitogluside (steryl glucoside). 15

2.2 Collated C1s envelope chemical state ranges of graphite, carbon black, graphene, carbon nanotubes, carbides, and polymers adapted from (Chen et al., 2020). 20

2.3 Schematic of the SIMS process. Adapted from Vickerman (2009). 21

3.1 Laboratory Filtration Rig Diagram 31

3.2 Post processing schematic for static SIMS data 36

3.3 Voxel representation of a Secondary Ion Mass Spectrometry image 38

4.1 From SEM analysis a a) secondary electron image of CF 002. EDX analysis showed the b) carbon, c) oxygen, and d) silicon distribution on the filter. . 42

4.2 From SEM analysis a a) secondary electron image of CF 002. EDX analysis showed the b) carbon, c) oxygen, and d) silicon distribution on the filter. . 43
4.3 a) Survey spectra of CF 003 including elemental regions and b) elemental compositions of reference filters from XPS survey spectra. 45
4.4 Line fitting analysis of (a) high-resolution C1s spectra of CF 003, alongside (b) percentage composition of deconvoluted C1s components of reference filters 46
4.5 Positive 3D Orbi-SIMS a) full ion spectra of CF 002, b) isolated CxHy ion peaks characterised with the compound_finder, and c) total ion spectra from a) after removal of the $C_xH_yz^+$ ions using the compound_finder script. The proposed formula of the ion peaks assigned are shown in Table 4.2 . . 48
4.6 Level of unsaturation vs number of carbon atoms for proposed compositions of $C_xH_y^+$ ions in CF 002. 49
4.7 Positive ion MSMS spectra of a) 226.0778 m/z, b) 348.0933, and c) 577.1347 m/z from control sample CF 002. 50
4.8 Orbi-SIMS negative $C_xH_yO_z$ ion peaks of CF 002 51
4.9 Negative ion MSMS spectra of a) 475.1041 m/z and b) 549.1048 m/z from control sample CF 002. 52

5.1 a) % Flowrate over time of LTF 003 (B100) which blocked after 28 hours and b) image of the reservoir side of the filter post experiment. 57
5.2 a) % Flowrate over time of experiment B10H10 fuel mix (blue). Line of best fit (orange) is calculated using the least squares method (Equation 5.1) and b) image of the reservoir side of the filter after 35 hours. 58
5.3 From SEM analysis a a) secondary electron image of unblocked LTF 003 (B100). EDX analysis showed the b) carbon and c) oxygen distribution on the filter. 60
5.4 From SEM analysis a a) secondary electron image of blocked LTF 003 (B100). EDX analysis showed the b) carbon and c) oxygen distribution on the filter. 61

5.5 a) Survey spectra of LTF 003 (B100) including elemental regions and b) elemental compositions of reference filter CF 001 (Chapter 4.3) and lab test filters (LTF) from XPS survey spectra. 63

5.6 High-resolution XPS spectra of the C1s region of LTF 002 (D100). 64

5.7 Averaged compositions of the C1s envelopes for each of the LTFs and reference filter CF 003 (Chapter 4.3). 65

5.8 LTF 002 (D100) positive ion 3D Orbi-SIMS spectra with C_xH_y removed. Proposed formula of identified peaks are shown in Table 5.5. 66

5.9 LTF 003 (B100), blocked filter, positive ion 3D Orbi-SIMS spectra with C_xH_y removed. Proposed formula of identified peaks are shown in Table 5.6. 67

5.10 Positive ion depth profile of selected ions in blocked LTF 003, point-to-point normalised with total ion. 69

5.11 Negative ion depth profile of selected ions in blocked LTF 003, point-to-point normalised with total ion. 69

6.1 From SEM analysis a a) secondary electron image of ETF 025. EDX analysis showed the b) carbon and c) oxygen distribution on the filter. 74

6.2 From SEM analysis a a) secondary electron image of ETF 023. EDX analysis showed the b) carbon, c) oxygen, d) sodium, e) chlorine, f) silicon, and g) sulphur distribution on the filter. A particulate deposit is highlighted. . 75

6.3 From SEM analysis a a) secondary electron image of ETF 022. EDX analysis showed the b) carbon, c) oxygen, and d) sodium distribution on the filter. 76

6.4 From SEM analysis a a) secondary electron image of ETF 027. EDX analysis showed the b) carbon, c) oxygen, and d) sodium distribution on the filter. 77

6.5 From SEM analysis a a) secondary electron image of ETF 026. EDX analysis showed the b) carbon, c) oxygen, and d) sodium distribution on the filter. Area of low sodium density highlighted. 78

6.6 a) Survey spectra of CF 003 including elemental regions and b) elemental compositions of reference filters from XPS survey spectra. 80

6.7 High-resolution XPS spectra of the C1s region of ETF 027. 81

6.8 Averaged compositions of the C1s envelopes for each of the ETFs and reference filter CF 002 (Chapter 4.3). 82

6.9 PCA analysis on the ToF-SIMS data of the ETFs and a reference filter, CF 002, showing the a) scores plot of PC 1 and 2. b) Loading for PC 1 and c) PC 2. Peaks identified are shown in Table 6.3 84

6.10 Positive ToF-SIMS images of ETF 022 a) total ion and normalised b) Na^+, c) $C_3H_7^+$, d) $C_4H_9^+$, e) Na_2OH^+, and f) $CO_3Na_3^+$ ions using delayed extraction mode. 85

6.11 Positive ToF-SIMS images of ETF 023 a) total ion and normalised b) $SiC_3H_9^+$, and c) $Si_2C_5H_{15}O^+$ ions using delayed extraction mode. 86

6.12 Positive ToF-SIMS images of ETF 026 a) total ion and normalised b) Na^+, c) Na_2OH^+, and d) $CO_3Na_3^+$ ions using delayed extraction mode. 87

6.13 Positive ToF-SIMS images of ETF 027 a) total ion and normalised b) Na^+, c) $C_3H_7^+$, d) $C_4H_9^+$, e) Na_2OH^+, and f) $CO_3Na_3^+$ ions using delayed extraction mode. 89

6.14 PCA analysis on the ToF-SIMS data of the ETFs and a reference filter, CF 002, showing the a) scores plot of PC 1 and 2. b) Loading for PC 1 and c) PC 2. Peaks identified are shown in Table 6.4. 91

6.15 a) Schematic of possible DDS salt and b) tandem MSMS spectrum of the $C_4H_4O_4Na_3^+$ ion in ETF 022. 93

6.16 Concentrations of sodium associated ions in ETFs and reference filter CF 002. 93

6.17 Tandem MSMS spectrum of $Si_3C_4H_{15}O_5^+$ ion in ETF 023. 94

6.18 Concentrations of di-acid ions in ETFs and reference filter CF 002. 95

6.19 Concentrations of ABS ions in ETFs and reference filter CF 002. 96

6.20 a) NNMF plot of two endmembers that describe the different layers seen in ETF 026, b) the m/z coefficients that define endmember 1, and c) the m/z coefficients that define endmember 2. Proposed formula of the identified peaks are shown in Table 6.5. 98

6.21 Depth profile of selected positive ion peaks in ETF 022 using 3D Orbi-SIMS. 99

6.22 Depth profile of selected positive ion peaks in ETF 026 using 3D Orbi-SIMS.100

6.23 Depth profile of selected positive ion peaks in ETF 027 using 3D Orbi-SIMS.100

6.24 Depth profile of selected positive ion peaks in ETF 023 using 3D Orbi-SIMS.101

6.25 Depth profile of selected negative ion peaks in ETF 025 using 3D Orbi-SIMS.102

7.1 From SEM analysis a a) secondary electron image of FSF 001. EDX analysis showed the b) carbon, c) oxygen, d) sodium, and e) silicon distribution on the filter. Highlighting strand like deposit present in the silicon EDX chemical map. 107

7.2 From SEM analysis a a) secondary electron image of FSF 002. EDX analysis showed the b) carbon, c) oxygen, d) silicon, and e) iron distribution on the filter. Highlighting particle deposit present in the EDX chemical maps. 109

7.3 From SEM analysis a a) secondary electron image of FSF 003. EDX analysis showed the b) calcium, and c) sulfur distribution on the filter. 110

7.4 a) Survey spectra of FSF 001 (US) including elemental regions, and b) elemental compositions of reference filter CF 002 and field sample filters (FSF) from XPS survey spectra. 112

7.5 High-resolution XPS spectra of the C1s region of FSF 001. 113

7.6 Averaged compositions of the C1s envelopes for each of the FSF and reference filter CF 002 (Chapter 4.3). 113

7.7 FSF 001 (US) positive ion 3D Orbi-SIMS spectra. Proposed formula of identified peaks are shown in Table 7.3. 115

7.8 Positive ion depth profile of selected peaks from FSF 001 (US). 117

7.9 Negative ion depth profile of selected peaks from FSF 001 (US). 118

7.10 FSF 002 (Asia) positive ion 3D Orbi-SIMS spectra. Proposed formula of identified peaks are shown in Table 7.4. 119
7.11 Positive ion spectra (580 - 680 m/z) of FSF 002 (Asia) highlighting similar peaks. Proposed formula of the identified peaks are shown in Table 7.5. . . 120
7.12 Schematic of PIBSI and its possible fragmentation patterns labelled in red in Figure 7.11. 121
7.13 Positive ion depth profile of selected peaks from FSF 002 (Asia). 122
7.14 Negative ion depth profile of selected peaks from FSF 002 (Asia). 123
7.15 FSF 003 (EU) positive ion 3D Orbi-SIMS spectra with CxHy ions removed. Proposed formula of identified peaks are shown in Table 7.6. 124
7.16 Positive ion depth profile of selected peaks from FSF 003 (EU). 125
7.17 Negative ion depth profile of selected peaks from FSF 003 (EU). 125

A.1 From SEM analysis a secondary electron image of LTF 002 (D100). 150
A.2 From SEM analysis a secondary electron image of LTF 004 (B20. 150
A.3 From SEM analysis a secondary electron image of LTF 005 (H100). 151
A.4 From SEM analysis a secondary electron image of LTF 006 (H20). 151
A.5 From SEM analysis a secondary electron image of LTF 007 (B50H50). . . 152
A.6 From SEM analysis a secondary electron image of LTF 008 (B10H10). . . 152
A.7 From SEM analysis a secondary electron image of ETF 020. 153
A.8 From SEM analysis a secondary electron image of ETF 021. 153
A.9 From SEM analysis a secondary electron image of ETF 024. 154

Abbreviations

ABS	Alkylbenzene Sulfonate
CF	Control filter
CO	Carbon Monoxide
DBE	Double Bond Equivalent
DCA	Deposit Control Additive
DDS	Dodecenylsuccinic
DoT	Department of Transport
EDX	Energy Dispersive X-Ray Spectroscopy
ETF	Engine Test Filter
FAME	Fatty Acid Methyl Esters
FIB	Focused Ion Beam
FIE	Fuel Injector Equipment
FSF	Field Sample Filter
FT-IR	Fourier Transform Infrared Spectroscopy
IDI	Internal Diesel Injector
GDI	Gasoline Direct Injection
HC	Hydrocarbon
HVO	Hydrogenated Vegetable Oil
LTF	Laboratory Test Filter
MALDI	Matrix-Assisted Laser Desorption/Ionization
NNMF	Non-Negative Matrix Factorisation
OEM	Original Equipment Manufacturers
PAA	Poly(acrylic acid)
PAH	Poly Aromatic Hydrocarbon
PBT	Poly(butylene terephthalate)
PC	Principal Component
PCA	Principal Component Analysis
PET	Poly(ethylene terephthalate)
PIBSI	Polyisobutenyl Succinicimide
PM	Particulate Matter
SEM	Scanning Electron Microscopy
SG	steryl glucosides
SIMS	Secondary Ion Mass Spectrometry
SVD	Singular Value Decomposition
ToF	Time of Flight
XPS	X-Ray Photoelectric Spectroscopy

Chapter 1

Introduction

1.1 The Diesel Engine

In 1892 Rudolf Diesel received patents for his work titled "Method of and Apparatus for Converting Heat into Work" (Diesel, 1892). His belief was that the combustion of any fuel would be able to be converted into motive power. In coalition with Maschinenfabrik-Augsburg (later known as MAN), Diesel's patent led to the creation of the first of three protypes of the diesel engine.

The diesel engine works on the diesel cycle shown in Figure 1.1. The ignition of fuel is caused by the elevated temperature of the air in the cylinder through adiabatic compression. This means that unlike the petrol engine the diesel engine does not require a spark to initiate ignition. First the air in the cylinder is compressed so that the temperature is greater than what is required for combustion to take place, steps 1-2. The atomised fuel is then gradually introduced, steps 2-3, resulting in spontaneous combustion. The expansion of the cylinder, steps 3-4, is regulated to counterbalance the rise in temperature and therefore most of the energy is converted into motive energy (Diesel, 1892). Because there is less of a temperature increase in a diesel engine compared to the petrol engine the former is more thermally efficient. Diesel fuel also boasts a higher energy density compared to gasoline (IOR Energy, 2010).

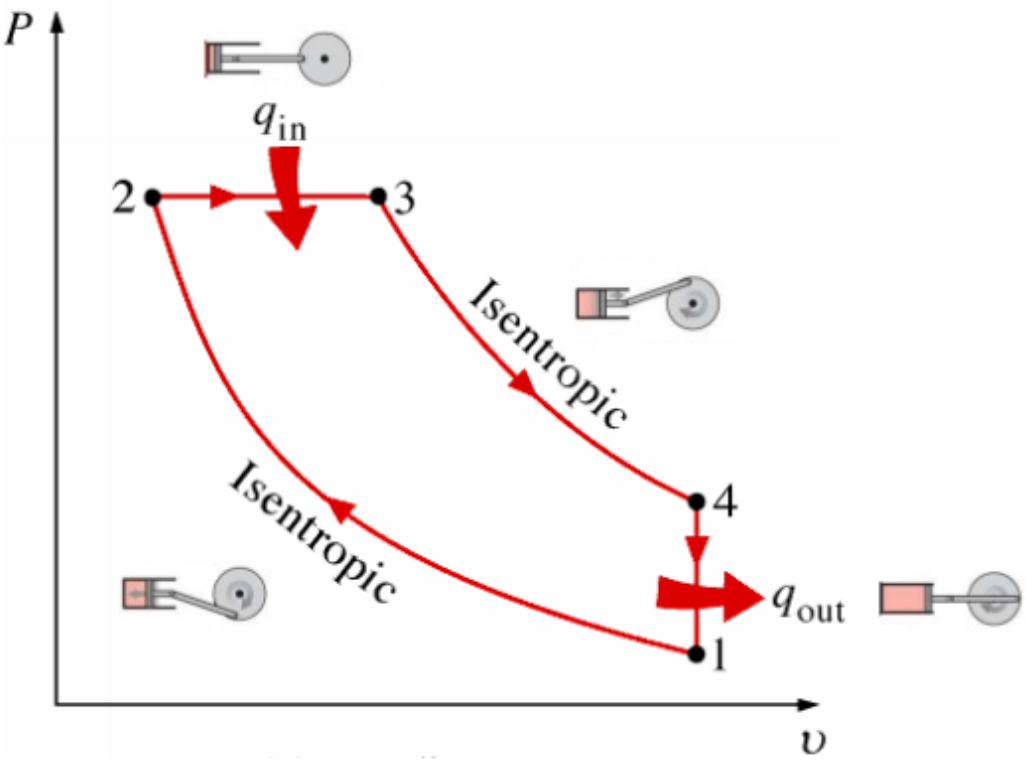


Figure 1.1: *Pressure-volume diagram of a diesel cycle, adapted from Nazridoust (2004)*

1.2 Diesel and Biofuels

Diesel fuel contains hydrocarbons of between 12-20 carbons, which are mainly composed of linear and branched alkanes, cycloalkanes and aromatics (Gad, 2005) (Speight, 2018). Crude oil, the feedstock of petroleum, typically contains between 0.04 – 14 %w/w of sulfur and 0.3-2 %w/w of nitrogen (Speight, 2018). The negative economic effects on the refineries, as well as on emissions from burning of petroleum (discussed later), make it essential for refineries to remove as much of the nitrogen and sulphur compounds as possible (Speight, 2018). The current process for removal is through hydrodesulfurization (HDS) a catalytic chemical process to remove sulphur from fuel. It is discussed by Srivastava (2012) and Alkhalili et al. (2017), that this method is costly and does not remove heterocyclic sulfur compounds. They suggest the use of lower cost operations such as bio-desulfurization (BDS) among others. The HDS process is also cited to remove other polar compounds containing nitrogen and oxygen (Richards, 2014).

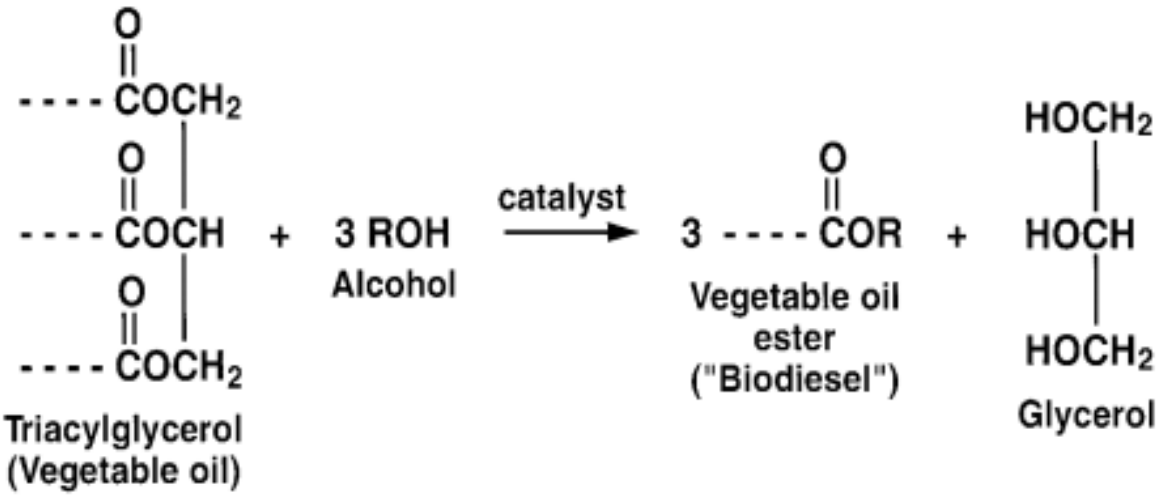


Figure 1.2: *Transesterification process of vegetable oil to form biodiesel, adapted from Diesel (2001)*

The main diesel fuel properties that effect the performance of diesel engines are the cetane number, low-temperature flow characteristics, lubricity, and stability, these are discussed in detail by Richards (2014). The cetane number is used to determine the quality of fuel which indicates the combustion speed and compression needed for ignition.

In the 1990's biodiesel, as used in diesel engines, began to gain traction in Europe because of high petroleum prices. In the US, it was not until the 9/11/2001 terrorist attack, where a change in awareness of energy security, resulted in an uptake of biofuel Pacific Biodiesel (2019). Although the process of transesterification of vegetable oils (Duffy, 1853) was conducted prior to Rudolf Diesel receiving patents for his work on diesel engines, it was not until 1937, where a Belgian inventor, G. Chavanne, filed a patent (Chavanne, 1937) for what is today known as the process for making biodiesel (Figure 1.2). The benefit of biodiesel was that it was able to be used on its own or blended with diesel.

The alcohol used in the transesterification process is typically methanol, however, the feedstock can vary from vegetable, animal to used cooking oils. In table 1.1, various properties of a select few feedstock compared to ULSD in the US are presented. Biodiesel is a renewable source of energy and is favoured by environmentalists as it has shown to reduce the amount of carbon dioxide (CO_2) emissions by 74% compared to petroleum diesel (Ingram, 2015). A review by Dimitriadis et al. (2018) also lists several other benefits

Table 1.1: *Properties of various biodiesels compared to ULSD meeting ASTM D975 standard, from EIA (2018)*

	Cloud point (°C)	Cetane number	Oxidative stability (mg/100 mL)
Soybean oil	0.9	47	16
Canola oil	-3.3	55	44.9
Choice white grease	7	64	72
Inedible tallow	16	62	41
Yellow grease	6	58	6.2
ULSD	-45 to -7	47	2.3

of the use of fatty acid methyl esters (FAME) over petroleum diesel including low sulphur content, good lubricity as well as general reduction in emissions. However, an increase in nitrogen oxides (NO_x) emissions from steady state and transient operating conditions was observed with the use of FAME by several others as well as increased fuel consumption due to the lower energy content. Another problem of FAME is its high-water solubility.
To overcome these limitations another type of biofuel was developed, hydrogenated vegetable oil (HVO). HVO are straight chain paraffins which are free of sulphur and aromatic compounds (Dimitriadis et al., 2018). Due to their nature, they offer good fuel stability, low water solubility and a high cetane number. However, due to the absence of sulfur and oxygen compounds their lubricity is very low (NESTE Oil, 2012). It is commented by Dimitriadis et al. (2018) that although HVO is meant to substitute directly into conventional diesel engines or as blends, it is largely unproven.

1.3 Global Light-Duty Vehicle Market

In 2015 there were nearly one billion passenger vehicles on the road. The largest passenger car markets were in Europe, USA, China, and Japan (OCIA, 2015).
As a result of the robustness and reliability of the diesel engine as well as the efficiency and energy density it has been favoured in heavy-duty applications such as lorries, buses, trains, and ships (Transport and Environment, 2017). For light duty vehicles, the petrol engine was historically widely chosen as it was regarded as more driveable due to its higher engine speeds and responsiveness. Advancements in the technology of the diesel engine

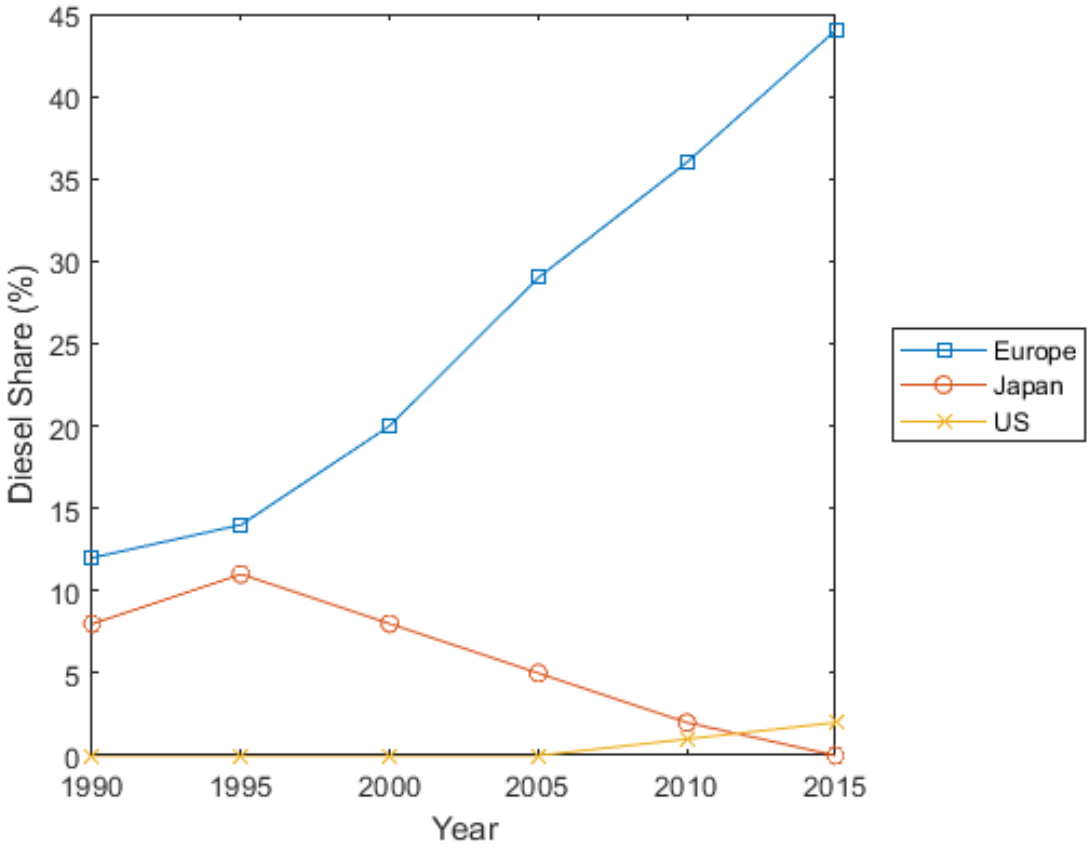


Figure 1.3: *Percentage share of diesel cars in Europe, Japan and the US between 1990 and 2015, adapted from Transport and Environment (2017)*

brought forth the introduction of the turbo-charger and the common rail fuel management systems (Transport and Environment, 2017), aiding the driveability of diesel engines.

The European boom in uptake of light duty diesel vehicles (Figure 1.3) during the 1990's is largely attributed to the lower taxation on diesel fuel (Cames and Helmers, 2013). Some countries, such as France and Spain, even offered reduced vehicle tax on new diesel cars(Transport and Environment, 2017). These tax alleviations came because of the European strategy on emission standards following the Kyoto protocol (UNFCCC, 2008), adopted in 1997, which in the transport sector, appeared to be largely tackling the CO2 emissions. The Japanese strategy to reduce CO2 emissions, however, was to increase the hybrid car market share, which reported in Cames and Helmers (2013), resulted in a faster decrease in CO2 emissions, from new cars, than both European petrol and diesel cars (Figure 1.4). In other global markets such as the United States (US) and China, the shift to diesel was not replicated as it was not favoured by low taxation and weaker

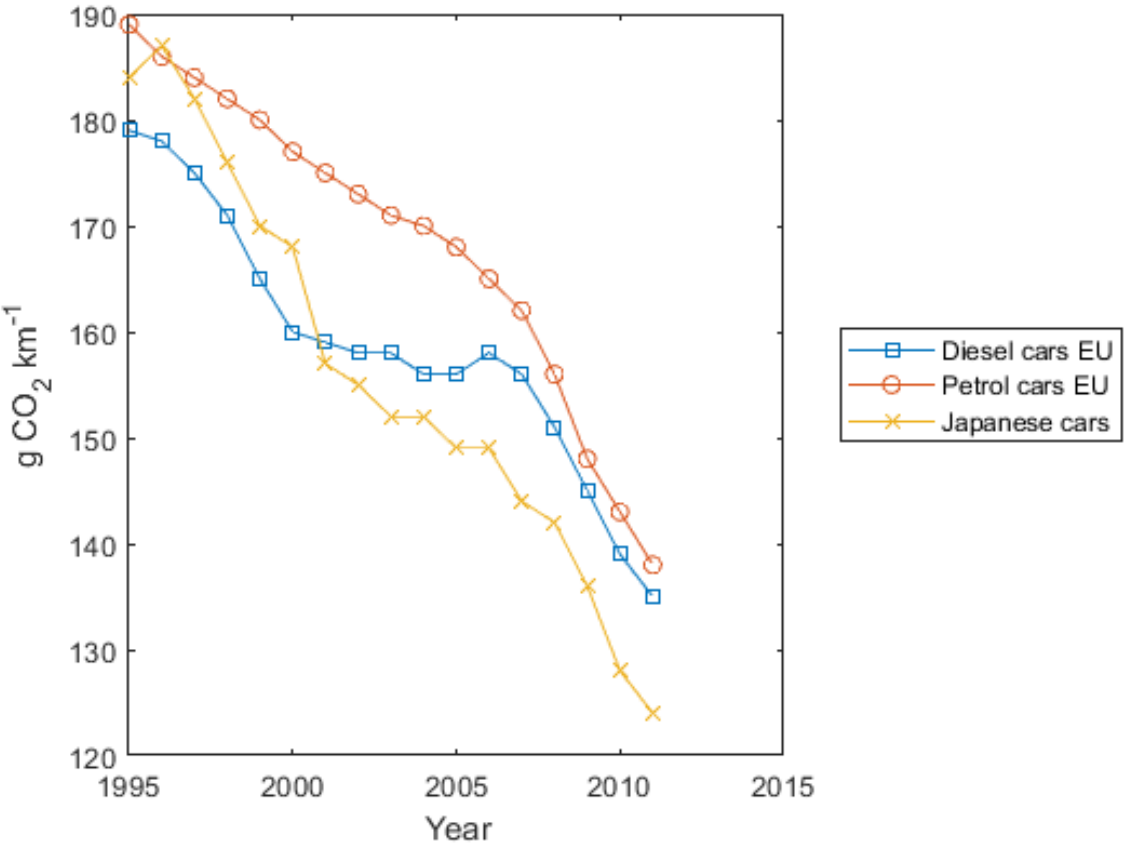


Figure 1.4: *CO_2 emissions from European diesel and petrol cars compared to Japanese cars between 1990 and 2015, adapted from Cames and Helmers (2013)*

environmental standards (Transport and Environment, 2017).

In 2013 a study conducted by the International Council on Clean Transportation (ICCT) found that some diesel engines from the Volkswagen Group were emitting 5 to 35 times the NO_2 emissions than the emissions standard (ICCT, 2015). This was to be known as the "Dieselgate scandal". Following the scandal, European government's attitude towards diesel fuel policies shifted. Cities such as London (Auto Express, 2018), Düsseldorf and Stuttgart (Autovista Group, 2018) started to introduce bans on the use of diesel in certain areas if the vehicles do not meet a certain standard. A report by the EEA (2016) correlated 70,000 premature deaths to NO2 exposure. In 2017, the UK government announced that the sale of new petrol and diesel vehicles will be prohibited by 2040 BBC (2017). Diesel's share of new passenger vehicles in Europe dropped 20% from 2016 to 2019 ACEA (2020). A report by the DoT (2018) estimated the number of vehicles in the UK would increase between 30-60% from the 2018 numbers. In the report, under their most environmentally

friendly scenario, in which there is a fast uptake in zero emission vehicles such as electric cars, the number of diesel vehicles forecasted in the UK was around 1.5%. In 2030, Bloomberg New Energy Finance estimates the total number of vehicles to grow to 1.4 billion(BloombergNEF, 2020).

1.4 Emission Standards

In the 1960's the first emission standards were introduced in the USA under the Clean Air Act of 1963 (EPA, 2007). Led by the Environmental Protection Agency (EPA), this bill was aimed at reducing carbon monoxide (CO), unburnt hydrocarbons (HC) and NO_x emissions in response of numerous cases of smog that covered cities and towns in California (Gardner, 2014) and Pennsylvania (EPA, 2007).

1992 marked the beginning of amendments of restrictions, imposed by the European Union, on the original directive of emission limits introduced in 1970 (EEC, 1993*a*). These tackled emissions including NO_x, particulate matter (PM), CO and HC (EEC, 1993*c*). The standardisation body, CEN, implemented the superseding directives: Euro 1 through to 6 in 2014 (EC, 2016).

From Euro 3 the NO_x limit was separated from HC and NO_x content (table 1.2). Addressing the effects of very fine PM emissions, particle numbers were limited alongside of mass from Euro 5 onwards to ensure that the best available technology, particulate filters at the time, were used (Diesel Net, 2007).

Table 1.2: *Progression of euro emission standards from Euro 1-6. *From Euro 5, PM was also defined by number of particles, shown in (brackets). Data combined from Euro 1 (EEC, 1993c), Euro 2 (EC, 1994), Euro 3-4 (EC, 1998a), Euro 5-6 (EC, 2007)*

Emission (g/km)	Euro 1 (1992)	Euro 2 (1996)	Euro 3 (2000)	Euro 4 (2005)	Euro 5 (2011)	Euro 6 (2015)
CO	2.72	1	0.64	0.5	0.5	0.5
HC + NO_2	0.97	0.7	0.56	0.3	0.23	0.17
NO_2	-	-	0.5	0.25	0.18	0.08
PM *	0.14	0.08	0.05	0.025	0.005 ($6x10^{11}$/km)	0.005 ($6x10^{11}$/km)

Table 1.3: *Progression of US emission standards from Tier 1 and 2. *Known as non-methane hydrocarbons (NMHC) in 1997. Values in Tier 2 are from bin 8, adapted from (EPA, 2016)*

Emission (g/km)	Tier 1 (1997)	Tier 2 (2009)
CO	2.625	2.625
NO_x	0.781	0.125
PM	0.063	0.013
NMOG	0.194*	0.078
HCHO	-	0.011

In 1990, the transport sector accounted for 14% of the total carbon dioxide (CO_2) emissions in the European Union (EEA, 2018). By 2012, the EU committed to reducing its total CO_2 output by 8% under the Kyoto Protocol of 1997. The US also initially committed to a target of reducing CO_2 emissions by 7%, although in 2001 pulled out of the agreement (BBC, 2001).

In the US, the 1963 Clean Air Act was amended in 1990 (EPA, 1990). This was the basis for which the tier system (1-2) dictated the emissions standards of vehicles (Table 1.3). From tier 2 the EPA introduced a bin number 1-8 (permanent) to which manufacturers could dictate which bin their fleet belonged to. Each bin becomes increasingly "dirty" as the number increases, bin 8 is shown in table 1.3. Due to the vehicle emission problems in Los Angeles (CARB, 2021), a separate emission standard was created in California defined by the California Air Resource Board (CARB). These two standards aligned when the 3rd iteration of each, Tier 3 (EPA) and LEVIII (CARB), were phased in from 2017 to 2025 (Diesel Net, 2016).

1.5 Fuel Standards

Alongside the emissions standards introduced by European Committee for Standardization (CEN), directives to reduce sulfur content of fuel were also being introduced in Europe under the directive 93/12/EEC (EEC, 1993*b*). The maximum sulfur limit in diesel fuel for highway vehicles of 0.2 %wt was further reduced to 350 ppm in 2000 (EC, 1998*b*), 50 ppm in 2005 (EC, 2003) and finally to 10 ppm in 2011 with a minimum cetane number of

51 (EC, 2009). The introduction of these sulphur limits was met by some criticism where the secretary general of Europia, the oil refining industry association, believed that to meet the demand for low sulfur fuels could increase CO_2 emissions by 50% (EURACTIV, 2008). Alongside these directives, limits on the aromatic content and cetane numbers were also set. In the US, the EPA, oversaw the transition from low sulfur diesel (500 ppm) in 1993 (GPO, 1990) to ultra-low sulphur diesel (ULSD) (15 ppm) from 2006 for highway diesel fuel (GPO, 2001).

The development of standards for biodiesel started in the 1990's as they started to get more traction. The American Society for Testing and Materials (ASTM) which dictated the standards for fuels in the US modified its specification for diesel oil, ASTM D975 (ASTM, 2020*b*), to allow up to 5% biodiesel to be blended into diesel fuel. While ASTM D7467 (ASTM, 2020*a*) is the specification for blends from B6 to B20, where Bxxx refers to the volume/volume ratio of diesel to biodiesel. In Europe, EN590 (CEN, 2009), which like the US is the diesel fuel specification, covers up to 7% FAME content.

1.6 Diesel Engine Advancements

Rudolf Diesel's concept of the diesel engine relied on gravity to pull pulverised coal into the combustion chamber (Diesel, 1892). Around the same time, a British inventor, Akroyd Stuart, had proposed another type of compression ignition engine (Richards, 2014). These were to be known as the initial designs of the direct (DI) and indirect injection engines (IDI), respectively. As time went on the pulverised coal fuel used in the DI engine was replaced by liquid fuel.

A disadvantage that the diesel engine had compared to a gasoline engine was the specific power output. In 1905 a Swiss inventor, Büchi, patented the first derivation of what is today known as the turbocharger (Hartman, 2007). The device used the hot exhaust air to spin a turbine which forced compressed air into the combustion chamber and as a result improved the power output of the engine. The first commercial car to adopt the turbocharger was the Mercedes-Benz 300 series in 1954 (Daimler, 2009).

Various inventors proposed ideas for the injection of liquid fuel into the combustion cham-

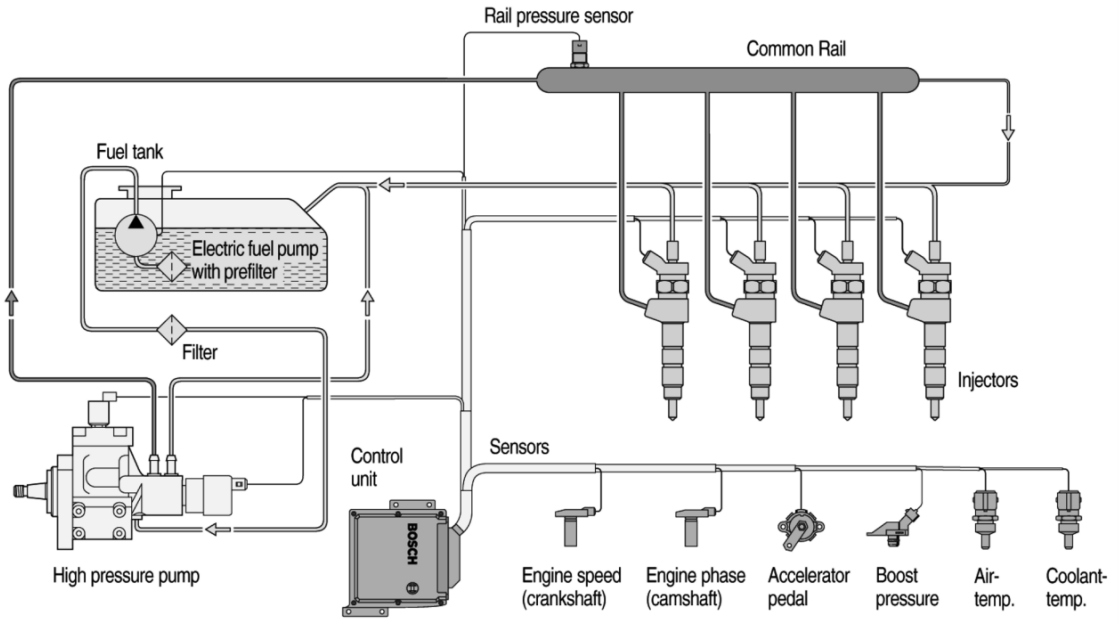


Figure 1.5: *Simplified diesel engine fuel injection system schematic, from Richards (2014)*

ber, summarised in Richards (2014). As fuel injection technology moved forward to keep up with the ever more stringent emission standards and desire for higher performant vehicles, it became apparent that there was a need to increase the injection pressure of the fuel. This brought forth the modern implementation of the high-pressure common rail system (Figure 1.5) which is credited to Fiat Auto (Buratti et al., 2004). Buratti et al. also commented on the improvement in the injector nozzle hole characteristics which include the reduction in size of the orifice, as a result the filtration of fuel will become increasingly important.

1.7 Fuel Filter Advancements

Diesel fuel filters are commonly located between the fuel tank and the injectors (Figure 1.5). It is well known that the fuel filter is of serious importance to the engine (Roosa and Hodgkins, 1972). The filter removes foreign contamination that may be present in the fuel before it gets to the fuel injection equipment (FIE) which may cause permanent damage. The increase in required pressure of FIE to meet ever stringent emissions standards resulted in the tightening of orifices in the FIE. The fuel quality and better filtration sys-

tems is therefore of paramount importance. Filter media commonly made from cellulose can retain particles larger than 5 µm (Richards, 2014). As the filters remove particles from the fuel they can start to block. To avoid large pressure drops because of clogging, the use of depth filters is common. This filter technology increases the surface area of the filter allowing more fuel to pass through before the pressure drop increases.

As the use of biodiesel, a highly water-soluble fuel, became more popular, filtration media needed to change as water in the FIE can cause severe wear (Lambert, 2004). The implementation of dual-phase media which consists of a layer with hydrophobic properties and cellulose layer, which boasted good dirt holding capacity and water separation (Krasinski and Gradon, 2016) became more common.

1.8 Additives

Historically the purpose of fuel additives has been to help improve various problematic properties of diesel fuels. Common diesel fuel additives include stability, lubricity, cold-flow and cetane number improvers as well as deposit control additives (DCA), anti-foam additives and corrosion inhibitors (Figure 1.6).

Antioxidant additives (stability improvers) are usually added to fuel deemed to be prone to oxidation (ATC, 2013). If left untreated this can lead to the formation of sediment and insoluble gums which can block the filtration systems (Richards, 2014). Cold flow additives usually target two main properties of fuel; the cloud and pour point. The prior is the temperature at which wax crystals start to form and are visible and the latter is the point at which the amount of wax is no longer in solution and prevents the fuel from pouring (Bennet, 2014). The composition of cold flow additives is usually proprietary. Silicon containing additives are effective anti-foams which can help complete filling of fuel tanks. The use of DCA has become more important with the advancement of FIE. DCA has been employed to minimise the build-up of deposit in and around the injectors (ATC, 2013; Richards, 2014). As mentioned, the process of HDS also removes polar compounds from diesel fuel. Studies have shown that the removal of these polar compounds have resulted in lubricity problems. To rectify this, lubricity improvers contain

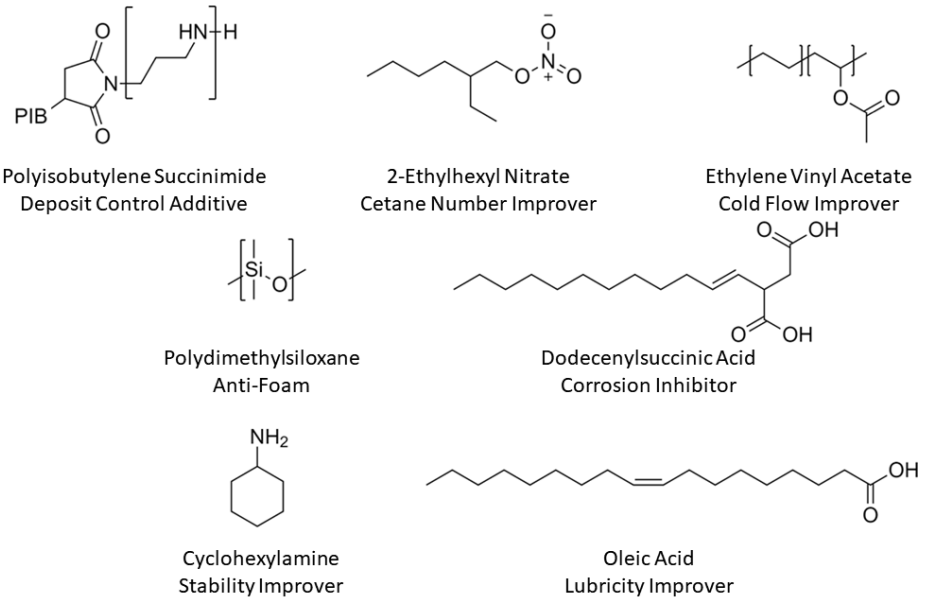


Figure 1.6: *Additive chemistry examples, adapted from ATC (2013)*

polar compounds such as carboxylic acids and esters (Bennet, 2014; Richards, 2014).

1.9 Aims and Objectives

The ever advancing of analytical techniques means that there is a plethora of new methods for identification of chemical species. This thesis looks to revitalise the topic surrounding the identification of species that can lead to fuel filter deposits. We will use SEM-EDX, XPS and SIMS to identify new and confirm deposit species seen in literature from filter deposits. In the area of FIE deposit analysis it has been shown that deposits can be layered, this area has not been shown in filter deposits and will be addressed.

As the data produced when doing SIMS work can be large it is beneficial to find a way to assign multiple peaks efficiently. A script has been generated with the aim of assigning possible formula to positive and negative ion data with user selected conditions such as: elements and isotopes to consider, deviation and intensity limits.

Bench/laboratory test rigs and engine tests are instrumental to the identification of deposit sources as they remove the effect of external contaminations that may add to the complexity of the deposits. A multi-pass filtration rig will be designed to test the effect that different combinations of fuels have on filters. A general way to test the performance of the filter is to periodically check the flow rate. Unless the flow rate of the experiment significantly lowers before, each run will last around 40 hours excluding downtime.

Whilst testing combinations of fuels is expected to show some filter blocking, filters in the field are also subjected to fuel with contamination and additives. Filters from a DW10 engine test will be analysed using the techniques discussed to understand the effect that combinations of some of the additives and contamination that filters may be exposed to in the field.

Lastly the limitation of these tests on their own are that they do not fully represent the environment that occurs in the field, it is therefore imperative that the analysis of filters from the field is also done. In this thesis three filters of different geographical location will be analysed to see the effects and if there is any correlation between different environments and fuel specifications and the deposits seen in diesel fuel filters.

Chapter 2

Literature Review

2.1 Deposit Formation

With the evolution of fuel injection equipment (FIE) to reach the more stringent emission legislation described in Chapter 1, fuel injection systems are more susceptible to blocking. This problem largely arises as a result of the smaller clearances and resultant lower tolerance of the FIE on the presence of contaminants, water and build-up of deposit (Lambert (2004); Tang et al. (2016)). There is a wide range of causes of deposits on FIE summarised in Barker et al. (2013) as including low-cost lubricating oils, poorly processed vegetable oils, dirt, rust as well as microbial growth and fuel degradation products. Perhaps one of the most widely researched cause of engine deposit is the result of formation from sodium products (Barker et al. (2012, 2013, 2020); Cardenas Almena et al. (2012); Lacey et al. (2012)). It has been reported that sodium may enter the fuel from upstream of the fuel filling stations as well as from fuel additives (Barker et al. (2013); Ullman et al. (2008)). A study by Lambert (Lambert, 2004) found that the number of particles in fuel increased in areas where there was high amount of dust at filling stations.

To combat some of the problems related to the presence of abrasive particulates in fuel, there has been a push by original equipment manufacturers (OEM) for technology advancements in fuel filtration systems to remove as much of the contaminants from the fuel prior to entering the FIE Verdegan et al. (2015). To meet the dimensional constraints of a fuel filter (for retro fitting) and maximise the capacity, a variety of different type of

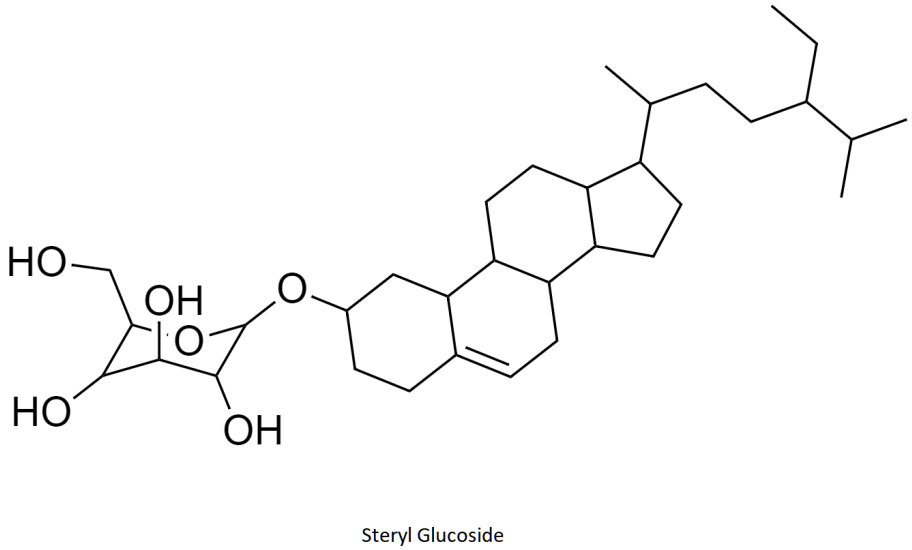


Figure 2.1: *Schematic of Sitogluside (steryl glucoside).*

pleats are used dependant on manufacturer, summarised in Lambert (2004). The design of fuel filtration media must consider the water-fuel separation. This is out of the scope of the thesis but detailed work can be found in Lambert (2004) which studied water - diesel interaction with fuel filters and in Tang et al. (2016) which used water - biodiesel blends.

The introduction of FAME based biofuels as an alternate to or blended with petroleum diesel have led to numerous cases of filter blocking (Jolly et al. (2010); Lee et al. (2007); Pfalzgraf et al. (2007); Tang et al. (2008)). The work by Jolly et al. (2010) reviewed that there is strong evidence that steryl glucosides (SG) (Figure 2.1) are a key factor in the formation of above cloud point precipitates. As SGs do not readily redissolve into the biofuel once formed it is implicated that these can be a cause of filter blocking. Another problem of biodiesel is the formation of acids through degradation (Omori et al. (2011); Sugiyama et al. (2007)), although they have also been shown to be oxidation products in petroleum diesel (Lewis et al., 2010). It is possible that these acids are precursors to the inorganic sodium products discussed prior. Another biofuel that has gained recent popularity is hydrogenated vegetable oils (HVO), although their interaction with filters has not been reported.

Perhaps the most commonly used technique to characterise the deposits that are found on diesel fuel filters is Fourier transform infrared spectroscopy (FT-IR). Barker, Richards, Snape and Meredith (2009); Cardenas Almena et al. (2012); Tanakaa et al. (2013) all used FT-IR to show the presence of carboxylates in FIE deposits. Work by Schwab et al. (2010) commented on the relative sizes of the hydrocarbon peaks compared to the carbonyl peak to propose that deposit on the injector was a result of short hydrocarbon chain acids or di-acid hydrocarbons. The latter was confirmed through tandem MSMS discussed later. Later, engine test work by Barker et al. (2013), also found that the use of di-acid additives showed the build-up of deposits in injectors, however, no deposit was found on the fuel filter. The work by Cardenas Almena et al. (2012) also inferred that the presence of succinic acid in mono-acid lubricity additives resulted in injector sticking.

More recently, other analytical techniques have been employed in a bid to further characterise and confirm the finding presented. These will be discussed alongside some basic background information on the technique later.

2.2 Engine and Laboratory Testing

Engine tests have been used in industry in a bid to mimic the conditions of that are seen in vehicles on the road (Hawthorne et al., 2008). The most recent engine test to be developed is the DW10 engine test, which consists of multiple working and shutdown cycles of a Peugeot DW10 engine (Barker et al. (2011, 2013); Hawthorne et al. (2008)) discussed further in Chapter 3.1.2. Although primarily used to test the effects of contaminants and additives on FIE (Cardenas Almena et al. (2012); Schwab et al. (2010)), Barker et al. (2013) published findings on filters deposits as well as the FIE which showed that whilst the addition of di-acid and dimer-acid hydrocarbons to the fuel did not result in filter plugging, the use of a mono-acid lubricity additive did. The work done by Barker et al. used energy dispersive X-ray spectroscopy to characterise the deposits on the blocked filters from the engine test and are discussed later.

Another method used to simulate engine conditions is the use of laboratory bench testing. Custom rigs are designed with selected components that are found in engines (Gopalan

et al. (2019); Spanu et al. (2018); Tang et al. (2016)). The benefit of running a custom bench rig over a full engine test is not only the reduced cost but also the practicality, although it is noted that on-road vehicle testing would be the most realistic (Hawthorne et al., 2008). Barker, Richards, Snape and Meredith (2009) also wrote that the problem with testing filters from the field is the uncertainty on uncontrolled variables including origin, fuel and filter type, the load cycle and general house-keeping. All though there are several filtration performance testing methods, the most commonly used are the ISO 13353 and ISO 19438 , the latter of which is used to measure the capacity and cumulated efficiency (Lambert, 2004).

A fuel degradation rig described in Gopalan et al. (2019) contradicted findings by standard oxidation tests and showed that no deposition on filters occurred when using FAME blended diesel fuels. Pre-prepared solutions of carboxylate salts were shown by Lacey et al. (2012) to only deposit on filters if the micelles were of sufficient size. The latter of these bench test studies used FT-IR to characterise the deposit but neither used techniques which can characterise the structures of deposits such as secondary ion mass spectrometry and X-ray photoelectron spectroscopy.

2.3 Scanning Electron Microscopy – Energy Dispersive X-Ray Spectroscopy

Scanning electron microscopy (SEM) is probably the most widely used technique of these present in this thesis. The technique is used to map out the topography of a sample which can offer resolutions of 1 – 20 nm. Secondary, back scattered electrons and X-rays are emitted from the surface of a sample as a result of the interaction with the atoms and the primary electron that is used to irradiate it. These emissions are collected by a suitably positioned detector and an image is created (Hafner, 2007). Traditionally SEM is completed in high vacuum conditions to ensure that the primary and secondary electrons are not scattered by the atmosphere between the source, sample, and detectors. The environmental SEM works on much of the same principals as traditional SEM except for

the ability to tolerate vapour in the sample chamber (Sano et al., 2008).

Energy dispersive X-ray spectroscopy (EDX) is commonly employed in tandem with SEM to provide elemental composition mapping. As discussed, when a primary electron irradiates the surface of a sample X-rays can be emitted because of the interaction between the electron and surface atoms. The X-rays emitted will have characteristic energies dependant on the element which are measured by an energy dispersive spectrometer.

Work by Barker et al. (2013) used EDX analysis to show the presence of sodium and calcium on the engine test filters which in conjunction with FT-IR analysis it was suggested to be a result of the mixture of metals and organic acids. A study by Quingley et al. (2010) also noted the presence of calcium on another filter using EDX, but no sodium was seen. Spanu et al. (2018) presented SEM images in conjunction with EDX analysis to describe the appearance and chemistry of diesel filter deposits. In the work it is shown that deposits from the field can differ in morphology from particulate matter to layer like sodium containing structures. Some of the morphologies, including organic films and granular particulate deposits, are also seen in SEM work shown by Barker, Richards, Goodwin and Wooler (2009).

2.4 X-Ray Photoelectron Spectroscopy

X-Ray photoelectron spectroscopy (XPS) is a quantitative spectroscopic technique that identifies elements based on their photoelectric properties. When an X-ray irradiates the surface of a material the photon can either pass through the atoms with no interaction, scattered by an atomic orbital electron (Compton scattering) or interact and transfer the total photon energy to an orbital electron (Ratner and Castner, 2009). The latter of which describes the basis of XPS analysis.

An XPS plot consists of the number of electrons detected at specific binding energy. The binding energy is calculated using Einstein's photoelectric effect theorem (Equation 2.1), where the binding energy (BE) of an electron is related to the energy of an X-ray source (hv) and the kinetic energy (KE) measured by the XPS detector.

When an element is bombarded with high energy-particles an electron can be ejected

from the inner shell of an atom. When an electron is ejected from the innermost K shell, a vacancy is created, which when an electron from the L shell fills this vacancy a $K\alpha$ emission line is emitted. Al and Mg X-rays are the recommended radiation of choice for XPS dues to their narrow $K\alpha$ emission lines (Wagner, 1978), with an energy and line width of 1486.6 eV, 0.85 eV and 1253.6 eV, 0.7 eV respectively. Because the energy of an X-ray of a defined wavelength is know it is possible to calculate the binding energy.

$$BE = hv - KE \tag{2.1}$$

Because the binding energy varies based on the nuclear charge of the atom (Ratner and Castner, 2009), characteristic peaks arise when certain elements are present in the sample. Analysis of the binding energy can be described in more detail using Koopmans' theorem (Koopmans, 1934), which describes the binding energy of a photoelectron is the difference between the final and initial state energy.

While shifts in binding energies can be used to describe the chemical state information which can be adequately interpreted on initial state effects, Ratner and Castner (2009) wrote that "... caution must be made against solely using initial state effects for interpreting chemical shifts". The binding energy that is observed for the C1s, which is in line with the initial state effect, increases as the number of oxygen atoms bonded to carbon increases. As the oxygen atom is more electronegative than carbon, the electrons are drawn away from the carbon nucleus, increasing the positive charge of the carbon and as a result increases the binding energy of C1s (Figure 2.2).

Chen et al. (2020) published a review on C1s envelope analysis of various carbon structures in which the binding energies of the chemical state information agrees with popular XPS databases such as Beamson and Briggs (1992); Moulder et al. (1992).

XPS has been used to understand the various deposit formations that occur in diesel FIE using both low-resolution survey spectra and high-resolution spectra analysis. Galante-Fox and Bennet (2012) linked the presence of nitrogen, carbon and oxygen from a survey spectrum to PIBSI type DCAs which was also seen by Herbstman and Virk (1991) but described to be the DCA working as intended. Work by Smith et al. (2002) studied how

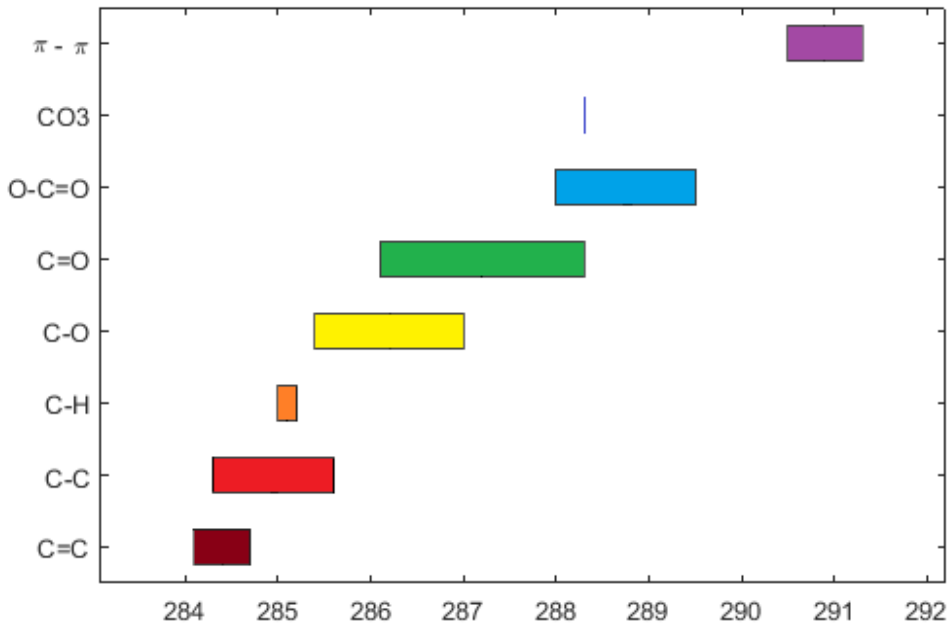


Figure 2.2: *Collated C1s envelope chemical state ranges of graphite, carbon black, graphene, carbon nanotubes, carbides, and polymers adapted from (Chen et al., 2020).*

deposits on an in situ heavy-duty diesel engine piston were affected with depth. The presences of calcium in the bulk of the deposit rather than at the deposit – substrate interface was suggested to be indicative of the formation during operating periods rather than when turning the engine on. More recently Lamb et al. (2021) used XPS to compliment secondary ion mass spectrometry depth profiles to quantify different organic and inorganic layers present on injectors in light-duty vehicle of different geographical origin. Although XPS has been used to confirm the important filter properties in particular the hydrophobic capabilities (Park et al. (2011); Zanini et al. (2008)), it has scarcely been used for the analysis of deposits on diesel fuel filters. A study by Edney et al. (2020a) outlined similarities and differences between GDI, IDI and diesel fuel filter deposits from different geographical origins using survey XPS data highlighting the presence of sodium, nitrogen as well as calcium sources in diesel fuel filters.

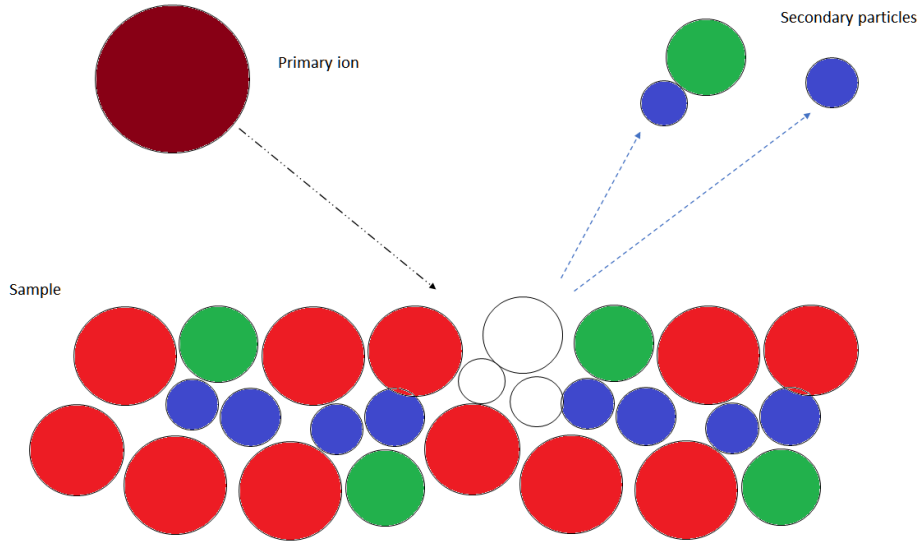


Figure 2.3: *Schematic of the SIMS process. Adapted from Vickerman (2009).*

2.5 Secondary Ion Mass Spectrometry

In secondary ion mass spectrometry (SIMS), the surface of a sample is bombarded by either electrons, neutral species, clusters of or atomic ions (Vickerman, 2009), the latter two will be discussed in this work. The source of bombardment is known as the primary ion beam. The collision of the primary ion beam and the surface of the sample results in the emission of secondary particles which can consist of neutral atoms or molecules as well as atomic and cluster ions, known as secondary ions (SI) (Figure 2.3) of which the neutral component accounts for the majority (95%) (Vickerman, 2009). Only the ionised yield can be guided towards the mass analyser, which has been shown to be largely influenced by the surrounding chemical environment (Benninghoven (1994); Johansson (2006)). This is known as matrix effect is often considered a negative and limiting factor for SIMS applications in elemental characterisation and essentially why SIMS is often classed as a semi-quantitative technique.

SIMS emerged as a technique of importance for surface analysis in the late 1960's as a result of work by Benninghoven (1970) which showed that analysis of the secondary ion was possible with the use of low current densities of the primary ion. At the turn of the 21st century interest in the use of polyatomic cluster primary ions increased. A review by

Wucher (2006) projected that the use of these clusters as a primary ion source delivered greater yields of high mass species.

SIMS analysis can be separated into two areas, static and dynamic-SIMS. The later refers to the bulk analysis of a sample as a function of sputter time (depth), whereas static SIMS is the analysis of the surface monolayer of the sample. In static-SIMS the primary ion dose is of lower energy as compared to the energy of the primary ion beam in dynamic-SIMS (Edney et al., 2020b).

In static SIMS there is an emphasis on the information received from a specific unit of sputtered surface (image resolution). In contrast, Dynamic-SIMS, requires high sensitivity to the specific elemental ions (mass resolution). There are currently four widely used mass analysers; the magnetic sector, the Quadrapole, time-of-flight (ToF) mass analyser (Vickerman, 2009) and more recently the Orbitap^{TM} (Zubarev and Markov, 2013).

The primary ion source of the SIMS instruments discussed in this thesis were delivered in pulses, the duty cycle can be used to define the percentage of the time that a primary ion beam irradiates the sample's surface. In an OrbiTrap^{TM} analyser the ion trap, which is used to collect the SI, is limited by its size which requires the duty cycle to be kept low, as compared with a Quadrupole analyser (Loboda and Chernushevich, 2009). Likewise in ToF-SIMS, due to the periodic nature of the primary ion beam, the duty cycle is low as the subsequent pulse of secondary ions cannot be analysed prior to the current pulse of secondary ions reaching the mass analyser.

To obtain a high spatial resolution a small spot size is required. This is achieved by placing a smaller aperture on the primary ion's beam path. As a consequence there is a reduction in primary ion beam current of which the secondary ion yield has a linear dependence on (Jenčič et al., 2019). For this application, typically a monatomic or small-cluster ion beam such as Bi_3^+ are used as a primary ion source as they feature high currents and small spot sizes.

The use of liquid metal technology for bulk analysis is constrained by their static limit, which if surpassed can result in damage to the sample (Touboul et al. (2005); Fletcher et al. (2008)). Another primary ion source that is used for SIMS applications is the gas

cluster ion beam. Research has showed that increasing the cluster size of the gas ion leads to an increase in the secondary ion yield (Rabbani et al., 2015). Studies have also found that large cluster gas ion beams reduced the subsurface damage on organic samples induced by ion irradiation (Ninomiya et al. (2009); Niehuis et al. (2013)) which make this type of beam suitable for depth profiling.

2.5.1 Time-of-Flight Secondary Ion Mass Spectrometry (ToF-SIMS)

The ToF analyser works on the principal of accelerating the secondary ions at a given potential so that the ions roughly have the same kinetic energy Vickerman (2009). These ions travel through the flight tube until they hit the analyser. The time taken (t) increases with mass shown by Equation 2.2, where L is the length of the flight path, V is the potential by which the ions are accelerated, and m/z is the mass-to-charge ratio of the ion.

$$t = L\sqrt{\frac{m}{2sV}} \tag{2.2}$$

The sensitivity advantages possessed by the ToF analyser discussed by Vickerman (Vickerman, 2009) and Zubarev and Markov (Zubarev and Markov, 2013) compared to the other analysers suggest that ToF-SIMS is perhaps the most suited to the chemical mapping of a sample. However, the limiting parameter of the spatial resolution is the secondary ion yield which, as discussed, is considerably less than the neutral particle yield.

The mass resolution of the ToF spectrometer is limited by the spread in flight time of ions with the same m/z ratio (Carlsohn and Nilsson, 2007). Delayed extraction, a technique that is has been used in MALDI for many years is now gaining popularity in the ToF-SIMS users, boasts the ability to be an efficient solution to this problem. Delayed extraction works on the principal of delaying the application of the accelerating voltage, which is applied as a potential gradient (Carlsohn and Nilsson, 2007) in order to focus the flight time distributions. Work by Vanbellingen et al. (2015) has showed that applying

delayed extraction to ToF-SIMS offers mass resolutions of 10,000 (at 385.4 m/z) whilst maintaining a spatial resolution of 400 nm.

ToF-SIMS is now a popular analytical tool for the study of GDI and IDI deposits. Work by Feld and Oberender (2016) used ToF-SIMS to show that deposit on injectors from the field had a wide variety of organic and inorganic chemistry from different fuel types which was also reported by Barker et al. (2012, 2014, 2020); Dallanegra and Caprotti (2014). The work by Barker et al. (Barker et al., 2012) also brought forward the idea that deposits on IDIs were layered which was also seen by Dallanegra and Caprotti (2014) in different injectors from the field. Tandem MSMS was employed by Schwab et al. (2010), alongside the FT-IR work discussed, to characterise and confirm the presence of di-acids and inorganic salts that were present on diesel injectors from the field and engine tests.

In contrast, the use of ToF-SIMS for the characterisation of diesel deposits on filters is seldom used, with FT-IR and SEM being the methods of choice. Work by Feld and Oberender (2016) used ToF-SIMS analysis to link the plugging of fuel filters, which were exposed to biodiesel fuel, to the presence of sterol glucosides. The work also commented on the presence of ions representing oleic and linoleic acids as well as a high intensity of the sodium ion in the positive ion spectra.

2.5.2 Orbitrap-Secondary Ion Mass Spectrometry

Based on the concept of electrostatically trapping ions in an orbit around a spindle developed by Kingdon in the 1920's, a first proof-of-principal published by Markov (2000) showed the potential mass resolution of the Orbitrap^{TM} analyser. Due to the properties of the Quadro-logarithmic potential, described in the paper by Markov, when the ions are trapped, their axial motion is only dependent on its angular frequency. The angular frequency (ω) is defined by Equation 2.3, where k is the force constant and m/z is the mass-to-charge ratio.

$$\omega = \sqrt{\frac{k}{(m/z)}} \tag{2.3}$$

In context, work published by Passarelli et al. (2017) showed that the 3D OrbiSIMS, a

hybridized TOF.SIMS 5 and Q Exactive™ HF Orbitrap ™MS showed a resolving power of 480,000 (at 200 m/z) which far surpasses even the theoretical resolving power of ToF instruments (20,000) (Vickerman, 2009).

As the use of the Orbitrap™ mass analyser is a relatively new technique the application of it in the field is in its infancy, especially in the fuel deposit field. A recent study by the University of Nottingham group (Edney et al., 2020a), previously discussed, employed the use of a hybrid 3D OrbiSMS for the first time for the analysis of diesel and gasoline deposits to confirm the layer like structure of deposits in IDIs proposed by Barker et al. (2012). Edney's study also evidenced the presence of high mass organic and inorganic structures including PAH, alkylbenzene sulfonates and sodium salts at low deviations in the injector and filter deposits, previously only speculated. The work also used tandem MSMS, the fragmentation of selected ions, to verify the assignment of succinimides, inorganic salts and ABS. The latter of which agreed with the assignments made by Lamb et al. (2021) who used tandem MSMS on a diesel injector of different geographical location.

2.6 Multivariant Analysis

2.6.1 Principal component analysis

The use of principal component analysis (PCA) is popular in fields with high-dimensional data, such as SIMS. PCA is a statistical method commonly used to reduce the dimensionality of large datasets (Trindade, 2018). These fewer dimensions contain a summary of the original data called principal components (PC). PCs describe the relatedness to the original data. The first PC aims to minimise the distance between the proposed PC and the original data whilst projecting the largest variance, the subsequent PCs maximise the variance and minimise the difference under the constraint that they are directional orthogonal to its previous PC.

The benefit of reducing the dimensionality of large data sets is the ease of comparison between variables. Work by Barker et al. (2017) used PCA on different jet fuel thermal oxidation tester (JFTOT) samples to show that carboxylates were present in larger quan-

tities on injector needles that had been exposed to biofuels compared to ULSD. Initial work by Spanu et al. (2018) used PCA to deconvolute data from a variety of different filters from the field, engine tests and lab rig tests. The statistical technique confirmed initial thoughts that sodium salts were contributing factors to the formation of layered deposits on filters. This thesis will build on this work with the aim of using new analytical methods and statistical methods.

2.6.2 Non-Negative Matrix Factorisation

NNMF as the name suggests is the factorisation of a matrix, M, into two non-negative matrices, W and H. Although this multivariant analysis is an approximation, in image analysis or depth profiling where the data is inherently positive, NNMF is commonly used to present data as it is easier to interpret.

$$M \approx WH \tag{2.4}$$

Using the Statistics and Machine Learning toolbox in MATLAB, this study computed NNMF using the multiplicative update (MU) algorithm, although other algorithms described in Berry et al. (2007) are available. The MU algorithm in conjunction with "Poisson scaling" has found to distinguish between different components in ToF-SIMS data more accurately than the alternating least-squares algorithm (Trindade, 2018), although the latter converges faster (Berry et al. (2007); Gillis and Glineur (2012)).

Because of uncertainty due to noise, when collecting data from ToF-SIMS, a scaling method is commonly used to pre-process the data. The low counting rates in the ToF-SIMS data result in large uncertainty, this means that standard scaling approaches such as using the inverse of variances cannot be used (Keenan and Kotula (2004); Trindade (2018)). Instead, Poisson scaling, detailed in Keenan and Kotula (2004) as weighting the data, was employed to scale the data (Equation 2.5). Where G is the diagonal matrix of the row-wise mean of M and H is the diagonal matrix of the column-wise mean of M.

$$M_{scaled} = G^{-1/2} * M * H^{-1/2} \tag{2.5}$$

It appears that NNMF has not been used to deconvolute depth profiles of deposits in IDI or diesel fuel filter deposits. As the datasets produced by ToF-SIMS and OrbiSIMS are very large, both PCA and NNMF will be powerful tools to aid the deconvolution of data.

2.7 Gaps in the literature

Although the general characterisation, through analytical and implicative techniques, of fuel filter deposits have been made, advancement in analytical methods have been made over the last ten years. The idea that deposits in the FIE are layered have been proposed and more recently studied. With regards to deposits on diesel fuel filters this area has not been studied to date

Chapter 3

Methods

3.1 Samples

3.1.1 Control Samples

To gain a reference point for the analysis of contaminated fuel filters, two different types of unused filters were studied. Although it is not possible to get the exact compositions of the filters as they are proprietary, it is possible to deduce the physical nature of the filter (Table 3.1). In Chapter 4 there is an in-depth discussion of the types of filters that are common to fuel filtration. It is assumed that the CF 002 and 003 are possible dual phase cellulose-polyester fibre. CF 003 was later used as the filtration media for the lab test samples.

Table 3.1: *Information of the physical nature of the reference filters.*

Sample Reference	Membrane Type
CF 002	Dual phase
CF 003	Dual phase

3.1.2 Engine Test Samples

The set of filters in this section were provided by Innospec Inc. from a DW10B engine test. The DW10B is a 2.0 L, common rail, turbo-charged engine mounted to a test-bed in line with the CEC F-98-08 specification CEC (1998). The tests were carried out using

Table 3.2: *Engine Test Filter (ETF) sample references with the additives and contaminants used in the CEC F-98-08 DW10B engine test.*

Sample Ref	Fuel	Additive	Contaminant
ETF 020	RF-06	Detergent, Corrosion Inhibitor	0.5 ppm Sodium
ETF 021	RF-06	LMWT PIBSI	-
ETF 022	RF-06	Corrosion Inhibitor	3 ppm Sodium Napthenate
ETF 023	RF-06	Detergent	-
ETF 024	RF-06	Detergent, Corrosion Inhibitor	0.5 ppm Sodium
ETF 025	RF-06	LMWT PIBSI	-
ETF 026	RF-06	Detergent, Corrosion Inhibitor	1 ppm Sodium
ETF 027	RF-06	Corrosion Inhibitor	1 ppm Sodium

reference diesel fuel RF-06-03 with a combination of additives and contaminants detailed in table 3.2. Although the test procedure suggests the addition of 1ppm Zinc, none was added.

The DW10B test is designed to demonstrate injector fouling in modern engines when using certain fuels as well as the ability of detergent fuel additives to control these deposits. A test cycle consists of 12-stages and lasts 1 hour. First, new injectors are bedded-in for 16 cycles with reference fuel (RF-06). The test fuel is then flushed through the engine and is run for 8 cycles, a 4-hour soak period follows before this is repeated 3 times or until the engine failed to start. The filters were then removed for analysis.

3.1.3 Laboratory Test Samples

An in-house test rig, described in more detail in section 3.2, was used to subject filters to various combinations of fuels. The fuels used were petroleum diesel, soybean bioidiesel and HVO.

3.1.4 Field Samples

Three filters from the field were analysed, provided by Innospec Inc. The geographical location of the filters are detailed in Table 3.3. The fuels used are also listed, however the fuel type used in the filter from the Asian region was unknown.

Table 3.3: *Location and fuel information of three filters from the field.*

Filter ID	Location	Possible fuel standard
FSF 001	USA	ASTM D975
FSF 002	Europe	EN590
FSF 003	Asia	Unknown

3.1.5 Vacuum Drying

Many of the analytical techniques used require the samples to be characterised in a high vacuum, such as SEM, XPS, Orbi and ToF-SIMS. Initial work in Spanu et al. (Spanu et al., 2018) showed that drying the filters in a vacuum oven at 140 °C and $1x10^{-4}$ bar pressure for 8 hours removed 95% of the hydrocarbons in the diesel fuel whilst leaving the heavy deposit. This method was followed for all the samples presented in this thesis.

3.2 In-House Rig Methodology

An in-house filtration rig was designed (Figure 3.1) to replicate the multi-pass filtration standard ISO 19438 ISO (2003). Fuel is displaced by a lift pump through a filter and either recirculated during the experimental run or passed through to a collection beaker when measuring the flowrate. The temperature of the fuel in the reservoir and the ambient temperature were recorded using a thermocouple at 30 second intervals. Fuel temperature of each run was kept between 15 and 40°C in-line with typical operating temperatures for fuel tanks in Europe Grigoratos et al. (2019). The ambient temperature ranged between 20 and 30°C. Each standard was run between 35-40 hours, unless stated, using 1 L of fuel per five 8-hour blocks. Only a 1 L reservoir was used as it was found that a 2 L reservoir resulted in a higher flowrate through the system. The flowrate of the fuel through the filter was measured by shutting the re-circulation valve and opening the valve to the collection vessel. Fuel was collected for about 15 seconds, when the reservoir was between 23-24°C, weighed and the flowrate calculated using the density of the fuel. Prior to each run the fuel was passed through the system with no filter installed in the filter housing to determine the maximum flowrate (Table 3.4).

To understand how different fuels and their combinations affected the deposit on filters, a

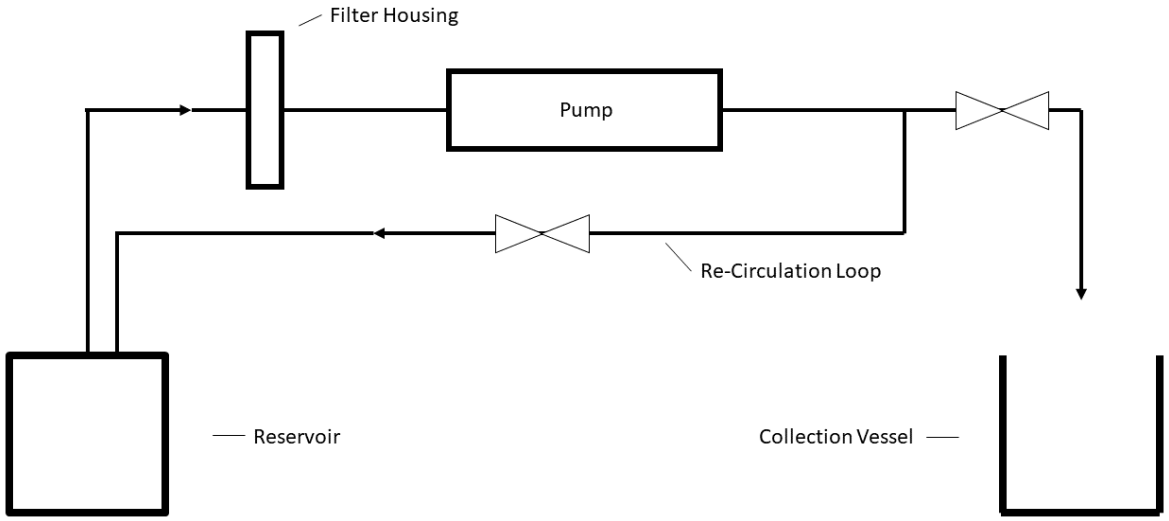


Figure 3.1: *Laboratory Filtration Rig Diagram*

Table 3.4: *Flowrates through the filtration rig with no filter installed and density of the fuel mixtures at* $25°C$

Test	Flowrate with no filter installed L/min	Fuel Temperature $°C$	Density at $25°C$ kg/m^3
LTF 002	0.92	23.7	832
LTF 003	0.96	23.8	880
LTF 004	1.43	23.8	842
LTF 005	1.89	23.8	780
LTF 006	1.03	23.8	822
LTF 007	1.53	23.7	830
LTF 008	1.21	23.9	832

Table 3.5: *Fuel composition standards for each in-house multi-pass filtration test using a 2^3 factorial experimental design*

Test	Diesel (RF-06) %	Biodiesel (SBMEs) %	HVO (C10-20 Alkane) %
LTF 001	0	0	0
LTF 002	100	0	0
LTF 003	0	100	0
LTF 004	80	20	0
LTF 005	0	0	100
LTF 006	80	0	20
LTF 007	0	50	50
LTF 008	80	10	10

two-level (2^k) factorial experimental design approach was employed. The discrete variable, levels, were the inclusion/exclusion of a type of fuel. Three types of fuel dictated that the design would be a three-factorial experiment, k = 3, leading to 8 different vol/vol ratios before repeats (Table 3.5).

Fuels

Three types of fuel were used in this study: biodiesel, HVO and petroleum diesel. The biodiesel used was a soybean product, soybean oil methyl esters (SBMEs or methyl soyate), the HVO contained branched and linear C_{10}-C_{20} alkane chains and the diesel used was No. 2 diesel fuel. For the tests, the fuels were either pure or a combination of the three and no additives were used

3.3 Analysis Techniques

3.3.1 Scanning Electron Microscope and Energy-Dispersive X-ray Spectroscopy

Due to the nature of the samples the electron microscope used was the FEI Quanta 650 ESEM, an environmental scanning electron microscope (ESEM). The advantage of using an ESEM is the ability to examine samples that cannot be kept at a high vacuum conditions due to the volatiles present, which is inherent of the saturated filter samples even

after the drying process described. Although it is also possible to analyse backscattered electrons with the ESEM, in this thesis only the secondary electrons and X-Rays are considered.

Each sample was mounted onto a Carbon adhesive disc to aid with the charge dissipation and to allow the sample not to require a sputter coating. The chamber pressure was kept between 60 -100 Pa depending on the degree of charging on each sample in the low vacuum mode. An X-Ray cone was fitted to the detector to reduce the beam gas path length and resultant electron scattering described in Chapter 2.3. The spot size of 4 nm was used with an acceleration voltage of 10 kV. The working distance was kept around 10 mm, the optimum distance for energy-dispersive X-ray spectroscopy. For chemical analysis, an Oxford Instruments X-Max-150 EDX detector was used, controlled through the AZtecLive software.

3.3.2 X-Ray Photoelectron Spectroscopy

For the XPS analysis, a Kratos AXIS ULTRA DLD was used with a mono-chromated Al $k\alpha$ X-ray source (1486.69 eV). For each sample, three areas were measured. A wide scan of low resolution (pass energy 80 eV, step size 0.5eV, sweep time 20 minutes) as well as a high-resolution scan (20 eV pass energy, step size 0.1 eV, sweep time 10 minutes) were taken, the binding energy range for each scan are shown in table 3.6. Spectra were acquired using the Kratos VISION II software.

Post-processing and analysis of the spectra were completed in CasaXPS Version 2.3.23PR1.0. For each area of analysis, the spectra were charge corrected using the corresponding high-resolution C 1s peak set to 285 eV. The wide-scan spectra were used to estimate the total atomic percentage of the detected elements, whilst the high-resolution spectra were used to model potential chemical compositions. To improve the signal-to-noise ratio the three wide scan spectra for each area analysed were summed.

It is possible to smooth the data in the CasaXPS software using a variety of different methods. In this work, when reported, high-resolution data will be smoothed using the Savitzky-Golay quadratic smoothing method Savitzky and Golay (1964). The method

Table 3.6: *Binding energy ranges for each scan type*

Scan Type	Binding Energy eV
Low-Resolution	
Wide Scan	1400 - -5
High-Resolution	
C 1s	302 - 279
N 1s	412 - 392
O 1s	542 - 522
Na 1s	1084 - 1064
Si 2p	112 - 97
S 2p	174 - 160
Ca 2p	357 - 343
Zn 2p	1059 - 1019

takes two inputs; degree of the polynomial and the number of data channels to consider when computing the convolution kernel.

To deconvolute the high-resolution spectra to obtain specific species and transition information, it is common practice to create a background curve that the photoelectric peak sits on. To account for the effect of inelastic scattering of electrons in this work the Shirley background Shirley (1972) type was used, although others are available.

For the C 1s high-resolution scan a peak model was created which takes the following constraints: line shape, area, FWHM and position. Various line shapes can be used, however for this work a 30% Gaussian to 70% Lorentzian (GL(30)) character is used.

3.3.3 Static Secondary Ion Mass Spectrometry

The 3D Orbi-SIMS can perform static SIMS in two modes: 1. liquid metal ion gun (LMIG) with the time-of-flight column for the analysis of the sputtered ions 2. gas cluster ion beam (GCIB) analysed by the Orbitrap. In LMIG mode, a Bi3+ ion source was used to fragment the surface of the sample, whilst the in the GCIB mode, an Ar3000 gas cluster was used. The ToF column allows for enhanced lateral resolution but the Orbitrap can collect higher mass ions due to the less aggressive fragmentation caused by the GCIB. Spectral and image data were captured in Surface Lab 7.1c, unless stated.

Table 3.7: *ToF calibration peaks*

Positive		Negative	
Ion	m/z	Ion	m/z
CH_3	15.022927	C	12.000549
C_2H_5	29.038577	C_2	24.000549
C_3H_7	43.045227	C_3	36.000549
C_4H_9	57.069877	C_4	48.000549
		C_5	60.000549

Liquid Metal Ion Gun

Samples that had been vacuum dried were analysed in the 3D Orbi-SIMS. Two 500 x 500 µm2 LMIG ion images, per polarity were captured from different areas of the filter. Each image had a 256 x 256 pixel2 resolution, 20 scans were taken as the scan time is relatively fast. A delayed extraction (analyser) method with a delay of 0.085 µs, fast imaging mode (LMIG source) and flood gun (300 V anode, 2 µs delay, 21 V energy, 2.3 A filament) settings were used, with a cycle time of 100 µs.

All the spectra from the LMIG analysis were calibrated using common ions present and are detailed in table 3.7 with the deviations below ± 50 ppm unless stated.

As the area of the images are considered large, each ion image was then split into four 250 x 250 µm2 regions of interest (ROI) (Figure 3.2). These sub-sections have large enough areas to be classed as repeat measurements and allowed the creation of confidence intervals around repeat samples. These pseudo-repeats are individually processed prior to the principal component analysis (PCA) and then grouped based on parent sample.

Gas Cluster Ion Beam

As with the LMIG mode, the same sample preparation is completed prior to analysis with the GCIB. An Ar_{3000}+ GCIB source was used with a total energy of 20KeV and a pressure of 26 bar in imaging mode. The spot size was 5µm with an injection time of 500 ms. The analyser was set to imaging mode (2 KV) with a cycle time of 200 µs and a maximum mass resolution of 240,000 (at 200 m/z). The flood gun setting (300 V anode, 2 µs delay, 21 eV energy, 2.3 A filament) was used to aid with charge compensation. RF transfer mode was enabled at 2KV energy for organic molecules. As each sample charged

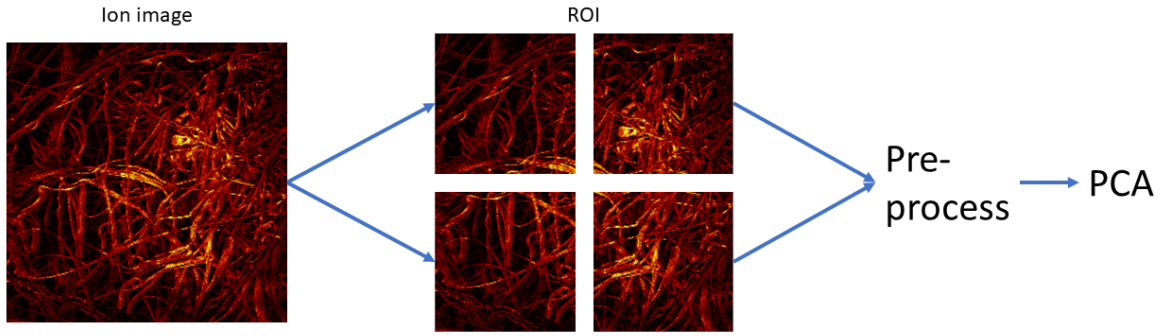


Figure 3.2: *Post processing schematic for static SIMS data*

at different levels the target potential to reduce this effect is indicated per sample. The duty cycle dose for the images was set to 4.4%. The Orbitrap was calibrated following the method described in Passarelli et al. (2017) using the Ag ion cluster ions detailed in Table 3.8, with the overall deviation kept below ± 3 ppm.

The time taken to capture an ion image using the Orbitrap is much longer than the LMIG mode, only one ion image of 400 x 400 µm2 size per polarity with one scan was captured at an image resolution of 80 x 80 pixels^2. To aid with sample charging, the

Table 3.8: *Orbitrap^{TM} calibration peaks*

Positive		Negative	
Ion	m/z	Ion	m/z
^{107}Ag	106.90454	^{107}Ag	106.90464
^{109}Ag	108.90421	^{109}Ag	108.9053
$^{107}Ag^{109}Ag$	215.8093	$^{107}Ag^{109}Ag$	215.8104
$^{107}Ag_2{}^{109}Ag$	322.71439	$^{107}Ag_2{}^{109}Ag$	322.71549
$^{107}Ag_3{}^{109}Ag_2$	538.52424	$^{107}Ag_3{}^{109}Ag_2$	538.52534
$^{107}Ag_4{}^{109}Ag_3$	754.33409	$^{107}Ag_4{}^{109}Ag_3$	754.33519
$^{107}Ag_5{}^{109}Ag_4$	970.14394	$^{107}Ag_5{}^{109}Ag_4$	970.14504
$^{107}Ag_6{}^{109}Ag_5$	1185.95379	$^{107}Ag_6{}^{109}Ag_5$	1185.95489
$^{107}Ag_7{}^{109}Ag_6$	1401.76364	$^{107}Ag_7{}^{109}Ag_6$	1401.76474
$^{107}Ag_8{}^{109}Ag_7$	1617.57349	$^{107}Ag_8{}^{109}Ag_7$	1617.57458

pressure regulation setting was activated, using Argon gas, bringing the chamber pressure to 9x10^{-7} mbar. Although this did occasionally drop to 6 x10-7 mbar where indicated. The images were then sectioned into four 200 x 200 µm quadrants (Figure 3.2). Each region was then individually processed and PCA was then conducted.

3.3.4 Dynamic Secondary Ion Mass Spectrometry

For the depth profile analysis, an Ar3000+ GCIB source was used with a total energy of 20KeV and a pressure of 26 bar in analysis mode. The spot size was 20 µm with a maximum injection time of 500 ms. The analyser was set to analysis mode 2 KV and the same flood gun settings, RF transfer mode and cycle time as with the static sims GCIB were used. The duty cycle dose was set to 38.5 of the total beam energy resulting in a primary current of 218 pA. The area analysed was 300 x 300 µm^2 with an interlaced border to reduce boundary effects. Chamber pressure regulation was turned on using the same settings as with the static SIMS GCIB analysis.

Dynamic SIMS data should be imagined in a three-dimensional Cartesian coordinate form: x, y, and z. Where x is the m/z of the ions, y is the intensity of each ion and z is the scan number or depth. Using the SL7 software, a spectrum of all the scans is created. Selected ions are now chosen and their varying intensity per scan can be viewed. For initial analysis, all ions with a total ion count of above a specified amount were selected for data-processing.

3.4 SIMS Data Analysis

3.4.1 Data Pre-Processing

To produce coherent reports when analysing data, it is common practice to pre-process the raw data. The first very first transformation used is the normalisation of each of the SIMS spectra by its total ion count. Scaling the variables (ion intensity) between 0 and 1 allows the direct comparison of spectra. If there were no normalisation, comparison between spectra would be largely offset by the difference in total ions collected between

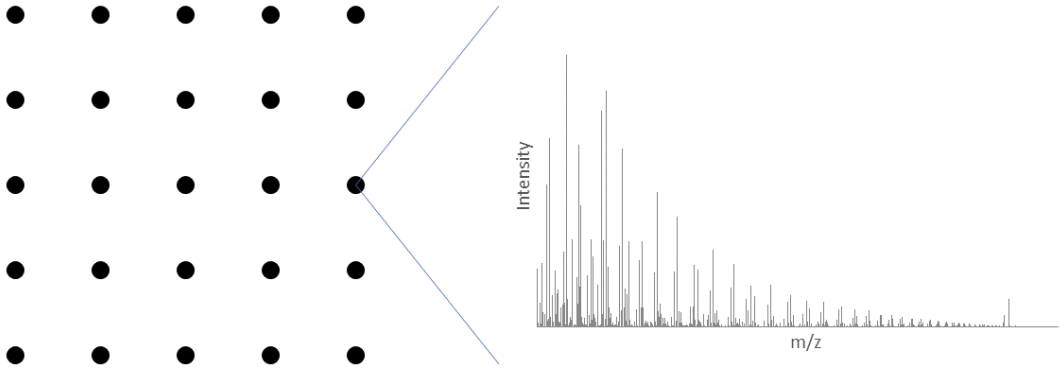


Figure 3.3: *Voxel representation of a Secondary Ion Mass Spectrometry image*

samples.

Ion images created from static SIMS (LMIG and GCIB) can be normalised on a voxel by voxel basis in a similar way. Each data point (voxel) has its own spectra (Figure 3.3), the total ion count of that spectra is represented by the intensity of the voxel. Normalising each voxel can reduce the topographical effects on the intensity, where areas that are in better focus result in more ions being collected. This affect is prominent in samples which have large features such as filter fibres.

If depth profiles are thought of as a collection of a series of data points over time, the depth profiles presented in this thesis were all normalised point-to-point against the total ion count at each collection time.

3.4.2 Principal Component Analysis

PCA was computed with the Statistics and Machine Learning toolbox in MATLAB, using the singular value decomposition (SVD) algorithm to obtain the scores and loadings of each PCs. The data must be mean centred, otherwise the first PC can point in the direction of the mean of the data (Gallagher et al. (2020); Jolliffe and Cadima (2016); Trindade (2018)). No variable weighting is applied when computing PCA. In this work

the principal components were considered until the sum explained at least 80% of the data. It is indicated if further standardisation, such as square root and Poisson scaling, is included prior to PCA analysis.

3.4.3 Non-Negative Matrix Factorisation

NNMF is computed with the Statistics and Machine Learning toolbox in MATLAB, using a multiplicative update algorithm with one repetition and a maximum of 100 iterations. When NNMF is used for static SIMS ion image analysis, Poisson scaling was applied to the normalised data. For depth profile analysis from the dynamic SIMS data, square root standardisation was applied to the data prior to computing NNMF.

3.4.4 Homologous Series Finder

Due to the heterogeneous nature of the samples, a technique to isolate possible homologous series is required to make the identification of possible ions is easier. One way to check for a series is to use the "peak difference" tool provided in Surface Lab 7 or the "label relative to selected mass" in XCallibur. These allow the user to find the mass difference between two peaks and identify the possible chemistry of the difference. These tools are particularly powerful in aiding the discovery of organic compounds due to their fragmentation patterns. The use of these two techniques to characterise the different ions present are limited by the presence of multiple other mass peaks which may not be part of the same series. To manage this, an algorithm "compound_finder" (Appendix B) designed in MATLAB aimed to isolate mass peaks that are related to a set criterion.

The basis of compound_finder is to cycle through different combinations of elements to match masses within specified parameters of acceptance: deviation from the true mass, minimum intensity of the mass peak and the double-bond equivalents (DBE), otherwise known as the degree of unsaturation. The calculated mass-to-charge ratio is defined by equation 3.1, the elemental masses were taken from Coursey et al. database Coursey et al. (2015). If the spectrum being processed is positive, the mass-to-charge of the electron is

subtracted from the total or it is added for a negative spectrum.

$$Mass\text{-}to\text{-}Charge\ (m/z) = \sum (Element_{quantity} * Element_{m/z}) \pm electron_{m/z} \tag{3.1}$$

The deviation in ppm is then calculated by equation 3.2. The deviation of the measured mass (mass_inten_matrix(i,1)) from the calculated Mass-to-Charge ratio (calc_mass) must be less than that specified for the user for the formula to pass this acceptance.

$$Deviation\ (ppm) = \frac{m/z_{measured} - m/z_{calculated}}{m/z_{calculated}} \tag{3.2}$$

The third parameter of acceptance, DBE, is calculated using

$$DBE = C + \frac{N - H - X}{2} + 1 \tag{3.3}$$

where C, N, H and X are the number of carbon, nitrogen, hydrogen and halogen atoms in the ion, respectively. This determines the total number of double bonds and rings in a molecule. For a proposed molecule to be accepted by compound_finder, DBE ≥ 0 unless it contains no carbon atoms. This is to mitigate formula being proposed that is not chemically possible due to the there being too many hydrogens.

Although the mass resolution of the Orbi-SIMS data is high, the limitation of this algorithm is with the assignment of multiple different ion possibilities for one mass peak. The user should use chemical intuition on whether certain formulas are possible. The presence of homologous peak series can help identify fragments and use the isotope pattern analysis functions in SL7 and Xcallibur.

Chapter 4

Control Test Samples

4.1 Introduction

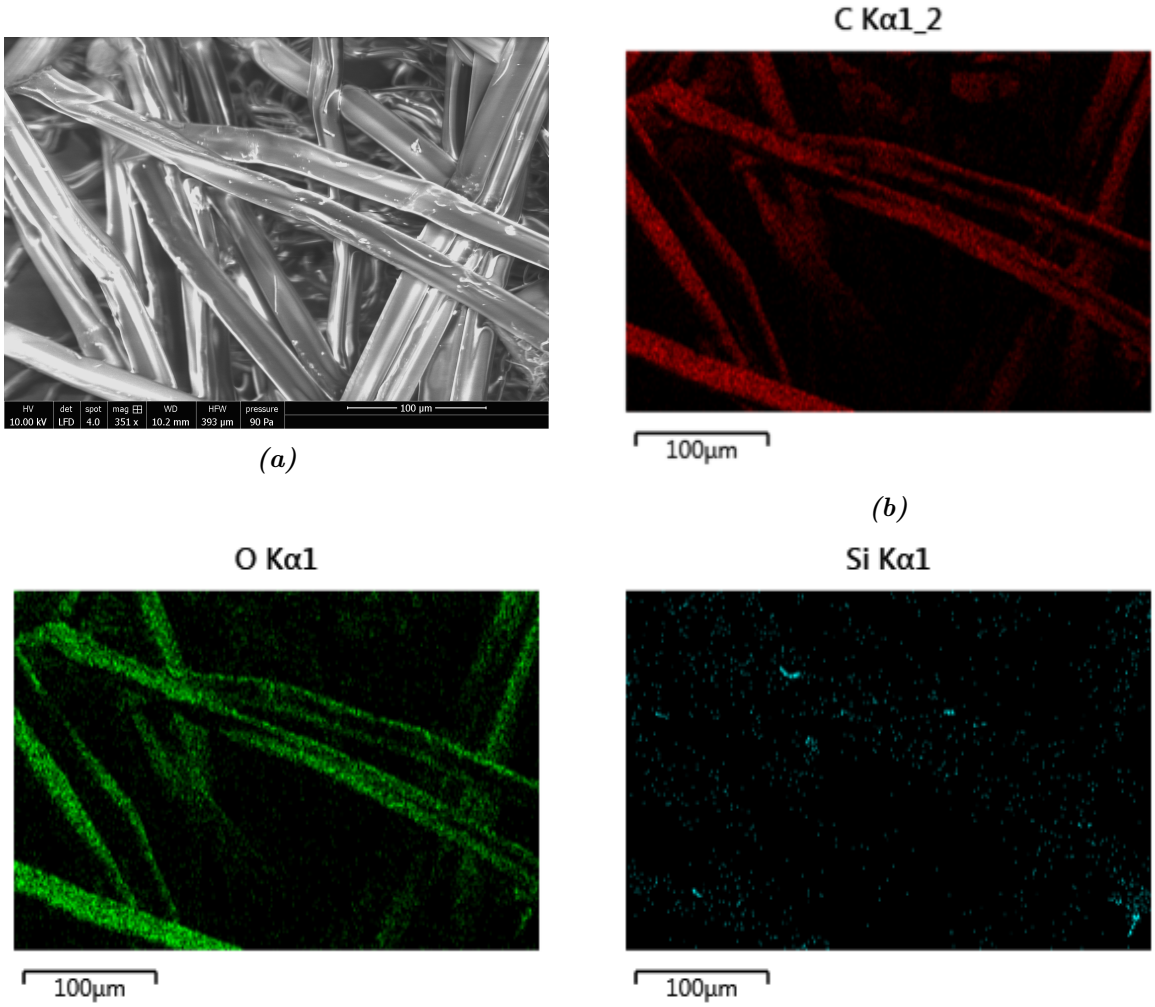
In this chapter analysis of the filtration media using scanning electron microscopy, energy-dispersive X-Ray spectroscopy (EDX), X-Ray photoelectron spectroscopy (XPS) and Orbitrap – secondary ion mass spectrometry (Orbi-SIMS) is described. In order to characterise the deposits on the filtration media it is of paramount importance to distinguish the composition of the filtration media first. This reference can then be considered and excluded from the data in order to isolate the chemical composition of the deposit.

Two dual-phase reference filters were analysed and these will the basis of the subsequent chapters. For consistency, as with the lab test (LTF), engine test (ETF) and field sample filters (FSF), the control filters (CF) were vacuum oven dried for 8 hours at 140 °C and 1 x10^{-4} bar prior to analysis.

4.2 Scanning Electron Microscope

Scanning electron microscopy is a useful technique that allows the identification of the morphology of the sample. Coupled with EDX it is possible to understand the bulk composition and spatial chemistry of the sample surface.

A secondary electron scan of the control filter CF 002 revealed that the fibres of the filters were non-woven by nature and around 25 µm in diameter Figure 4.1. EDX analysis



(a) *(b)* *(c)* *(d)*

Figure 4.1: *From SEM analysis a a) secondary electron image of CF 002. EDX analysis showed the b) carbon, c) oxygen, and d) silicon distribution on the filter.*

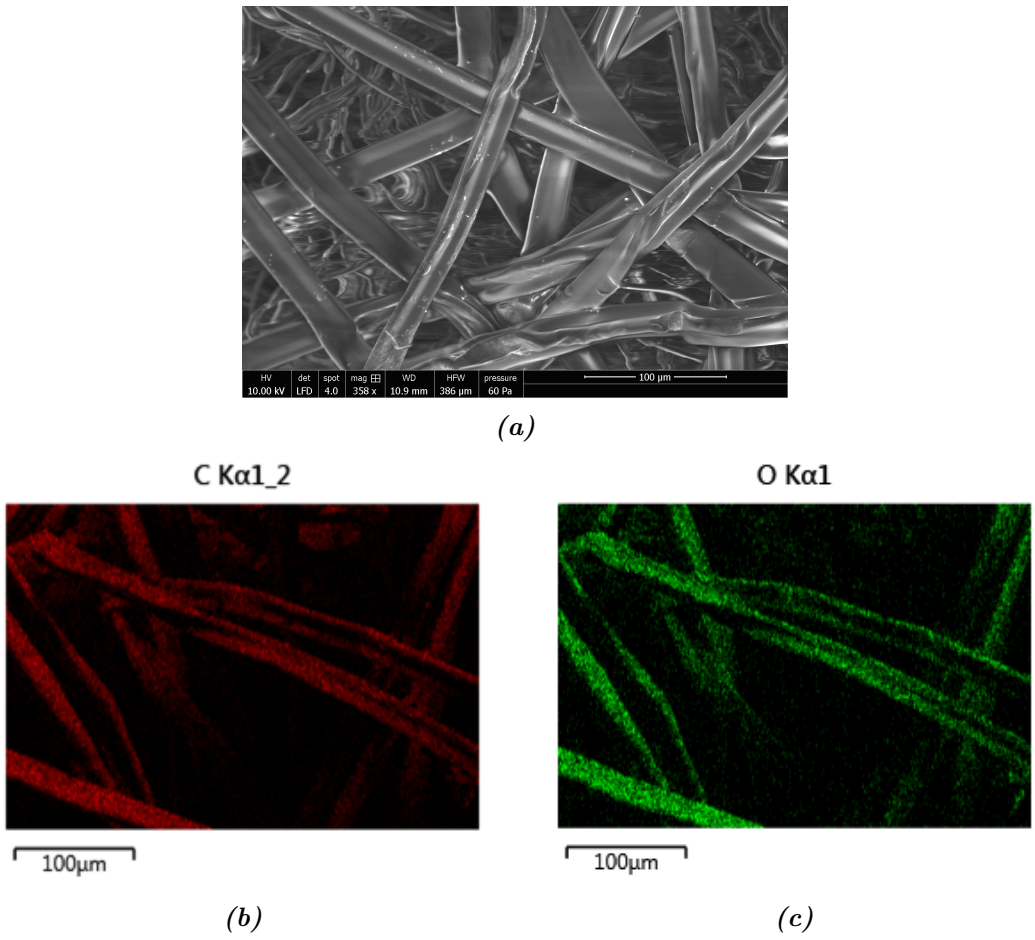


Figure 4.2: *From SEM analysis a a) secondary electron image of CF 002. EDX analysis showed the b) carbon, c) oxygen, and d) silicon distribution on the filter.*

revealed that as expected the bulk composition of the sample was organic however there were some blemishes of silicon present in localised areas on the fibres.

Similarly, the media of CF 003 (Figure 4.2) was an organic non-woven material, but no silicon was present on the surface.

4.3 X-Ray Photoelectron Spectroscopy

XPS is a useful tool to quantify the elemental composition of the sample surface. As this technique is quantitative it can be used in tandem with Orbi-SIMS data, which can be skewed by the easy of ionisation, to give context to the compositions of the sample.

Using a XPS survey spectrum one can obtain atomic signatures from the sample. For each sample three points were analysed from the surface, the points were then summed to get an average composition as well as increasing the signal to noise ratio as described

Table 4.1: *Binding energy ranges for the C1s components of the control filters.*

	C=C	C-C	C-O	C=O	O-C=O	$\pi - \pi*$
B.E range (eV)	284	284.9 - 285	286 - 286.6	287 - 287.7	288.9 - 289.3	290.5 - 291.3

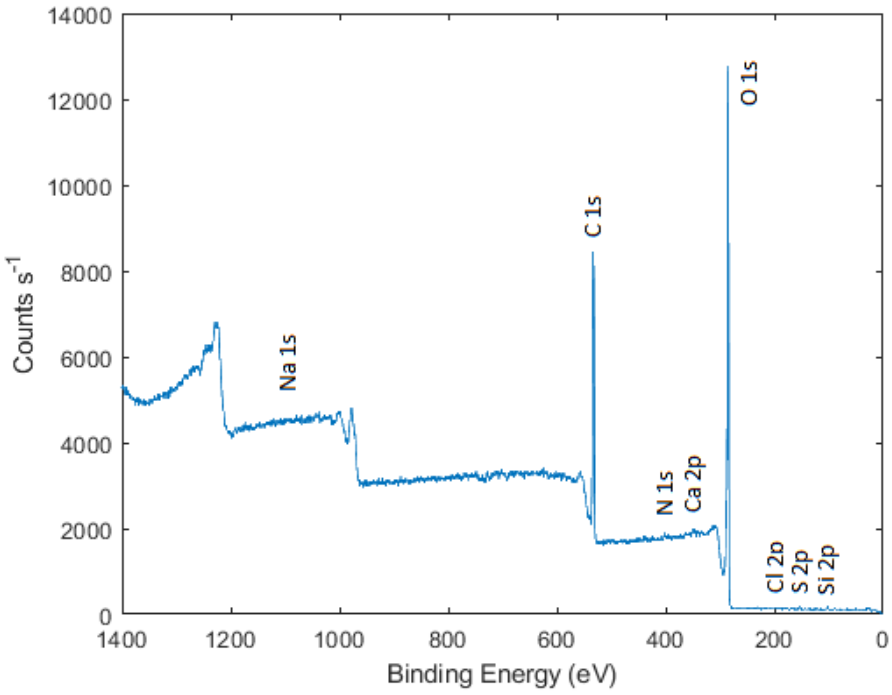
in Chapter 3.3.2.

In conformity with the EDX analysis the surface of both control filters were largely organic (Figure 4.3b). The atomic C:O ratio of CF 002 (4.0) was slightly lower than CF 003 (4.9) which seems to agree with the EDX data, where the oxygen map of CF 002 (Figure 4.1) appears to have a greater pixel density in comparison to CF 003 (Figure 4.2). Small percentages of nitrogen(CF 002: 0.3%At, CF 003: 0.5%At) and silicon (CF 002: 0.2%At, CF 003: 0.4%At) were seen in the summed survey spectra of both filters (Figure 4.3b, these are thought to be surface contamination. Contamination peaks are commonly seen in XPS analysis due to the high surface sensitivity of the technique.

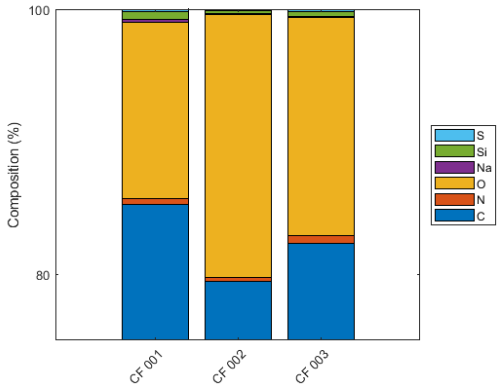
Alongside the quantification of elements through XPS survey spectra, it is also possible to analyse the C1s envelopes. This approach shows the possible bonding characteristics present on the samples. The line fittings were made with the characteristics described in Table 4.1.

The analysis of the C1s envelopes is shown in Figure 4.4. The majority of the C1s envelope of CF 003 was attributed to the sp3 bonded carbon, whereas the carbon atoms in CF 002 were mostly joined to oxygen atoms, although C-C was still most prominent individual bonding type. The presence of a shake-up peak at around 291 eV binding energy (4 %At) in CF 002 suggests that there was a presence of aromatic structures in the filtration media, whereas in CF 003 the shake-up peak was small and accounted for 1 %At. A weak peak of sp2 carbon was also seen in CF 002 although its contribution to the C1s envelope was minimal.

Quantification of the C-C, C-O and O-C=O bonding in the C1s envelope of the CF 003 (72 : 19 : 9 %At) filtration media somewhat follow the reference spectra of several common polyesters. Poly(ethylene terephthalate) (PET), (61 : 19 : 20 %At), described by Louette et al. (2005*b*) poly(butylene terephthalate) (PBT), (67 : 18 : 15 %At), in Burrell and Chera (1999) and poly(acrylic acid) (PAA), (68 : 16 : 16 %At), in Louette et al. (2005*a*).

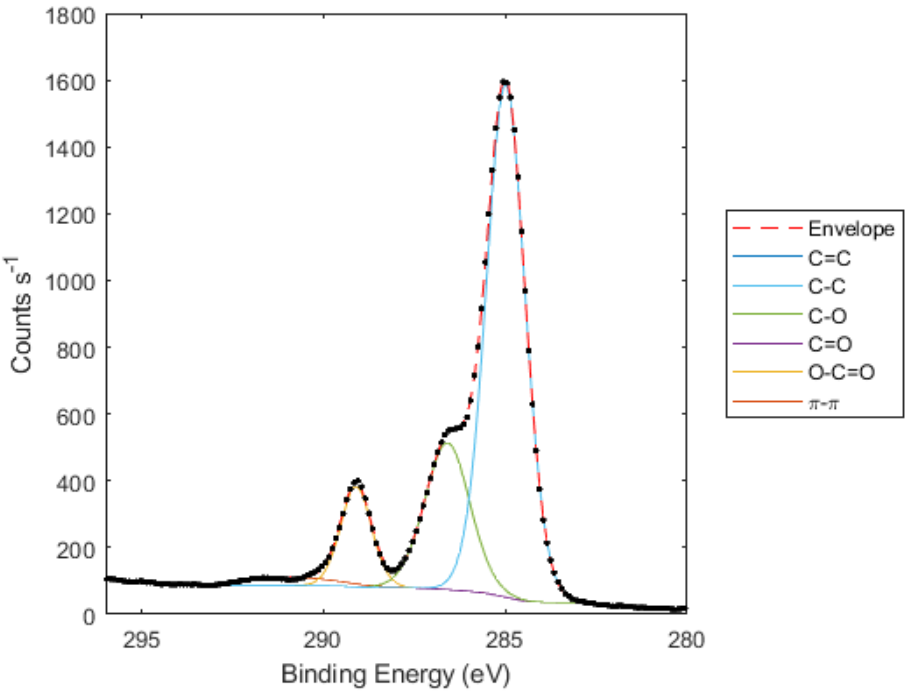


(a)

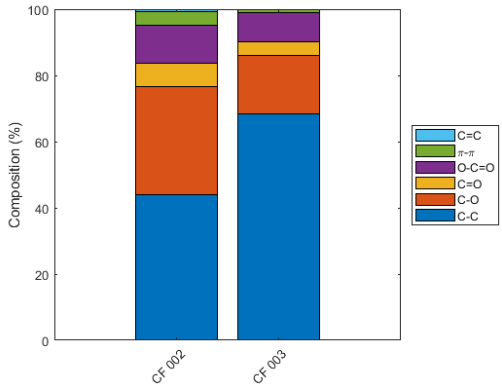


(b)

Figure 4.3: *a) Survey spectra of CF 003 including elemental regions and b) elemental compositions of reference filters from XPS survey spectra.*



(a)



(b)

Figure 4.4: *Line fitting analysis of (a) high-resolution C1s spectra of CF 003, alongside (b) percentage composition of deconvoluted C1s components of reference filters*

It is not possible to deduce which polyester it represents from the C1s envelope due to uncertainties in surface contamination, although, the presence of a shake-up peak in CF 002 rules out PAA. It is thought that polyesters are also used to make the filtration media of CF 002 although the surface appears to be contaminated so it is not possible to deduce the possible chemistry.

4.4 Static Secondary Ion Mass Spectrometry

Using the Orbitrap$^{(TM)}$ as the analyser in the 3D Orbi-SIMS allows for much greater mass resolution as compared to the ToF-SIMS. It is therefore possible to assign ions with much more certainty. The softer fragmentation when using an $Ar_{3000}{}^{+}$ gas cluster as the primary ion beam to sputter the sample results in the increased presence of high mass ions. This technique will be pivotal in analysing the parent ions of the deposit present but first it is important to analyse the ions that may be present in the filters in order to exclude them from the data.

The positive polarity spectra of both filters were dominated by the presence of aromatic carbonaceous carbons, a representation of the total positive ion spectra of CF 002 is shown in Figure 4.5a. Using the compound_finder script discussed in Chapter 3.4.4 and constraining the settings to search for carbon and hydrogen containing ions with deviations $< \pm$ 5 ppm for $<$ 95 m/z and $< \pm$ 2.5 ppm for $>$ 95 m/z it was possible to isolate all the possible carbonaceous ions from the spectra shown in Figure 4.5b. In order to reveal the underlying chemistry of the non-solely-carbonaceous peaks the carbonaceous peaks in shown in Figure 4.5b were removed to reveal peaks shown in Figure 4.5c. These will be discussed in more detail later.

The degree of unsaturation or double bond equivalents (DBE) is a method to quantify how many rings, double-bonds and triple-bonds are present in an organic structure. In this thesis we will assume that ring structures carry a weight of 1 DBE, plus 1 for any subsequent double bonds in the ring. The DBE of the identified carbonaceous peaks increased linearly (gradient $\sim$1.1) with the increase in carbon number ($R^2 = 0.98$) (Figure 4.6). Due to the fragmentation that occurs in SIMS several values of DBE for each carbon

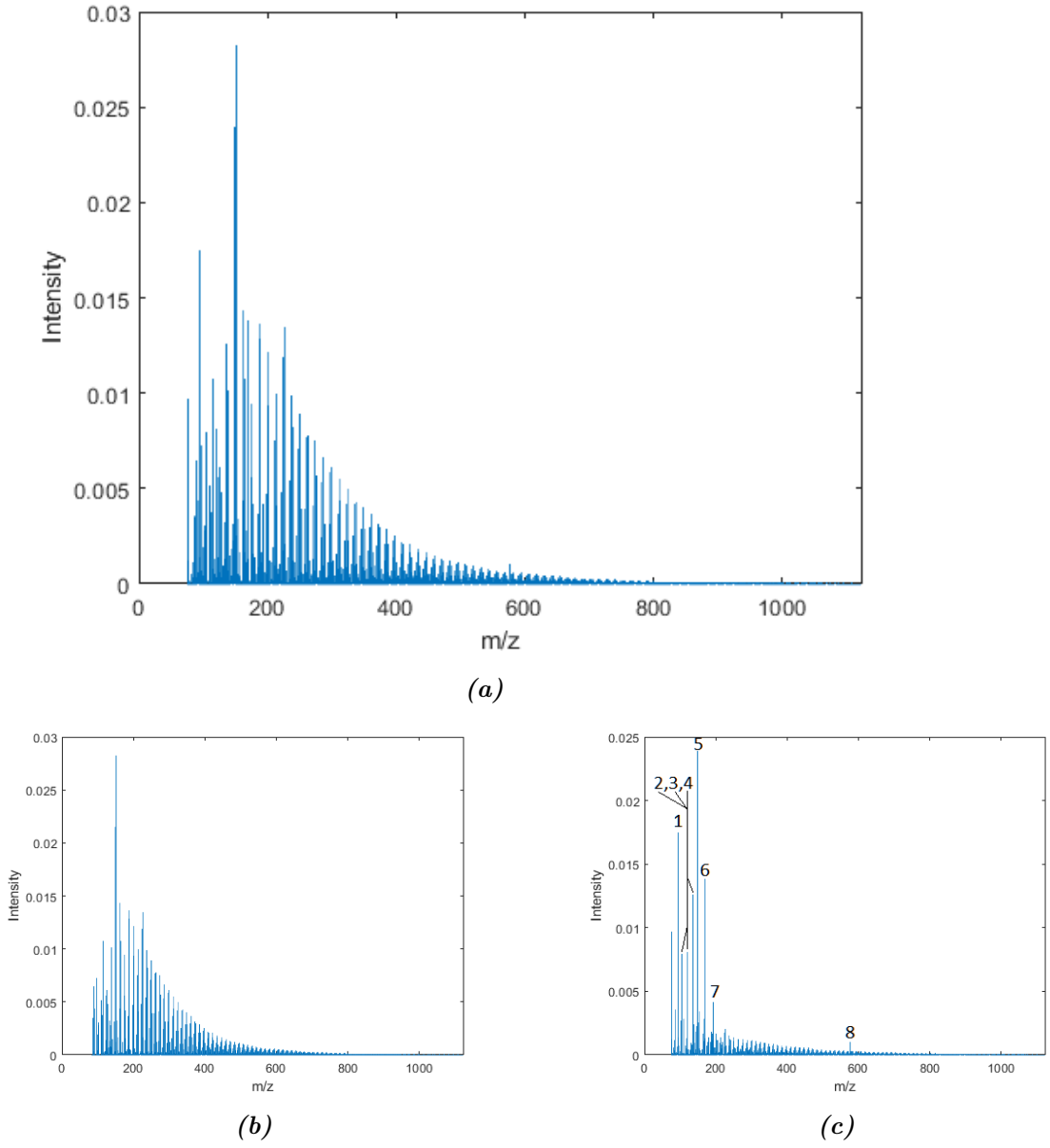


Figure 4.5: *Positive 3D Orbi-SIMS a) full ion spectra of CF 002, b) isolated CxHy ion peaks characterised with the compound_finder, and c) total ion spectra from a) after removal of the $C_xH_yz^+$ ions using the compound_finder script. The proposed formula of the ion peaks assigned are shown in Table 4.2*

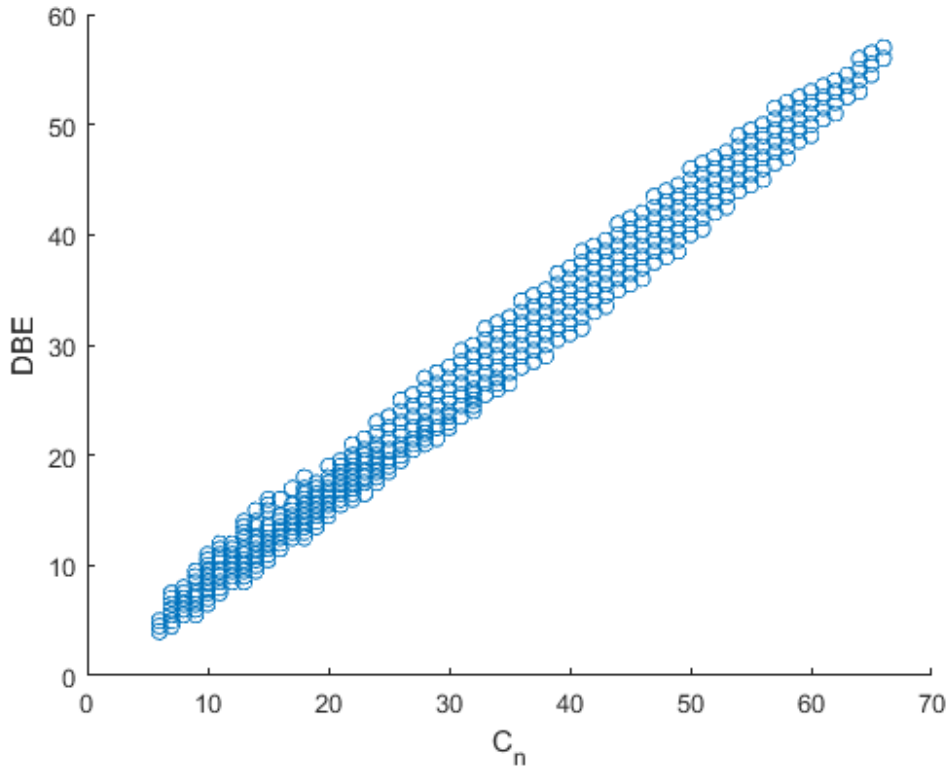


Figure 4.6: *Level of unsaturation vs number of carbon atoms for proposed compositions of $C_xH_y^+$ ions in CF 002.*

number (C_n) were found. The lowest DBE for C_6 was 4 ($C_6H_6^+$) and for C_{66} was 56 ($C_{66}H_{22}^+$). It is also noted that the parity of x and y in the general formula $C_xH_y^+$ is always the same.

The suggested chemical formula of these ions suggests the presence of PAH ions. In filters from the field these PAH ions were seen, and it was initially thought that these arose from the recirculation of combustion products in the fuel (Edney et al., 2020a). However, as these are clean filters, it is possible that the origin of the ions, specific to diesel fuel filters, is a result of degradation of organic material while sputtering as PAHs are not expected to be present in the filtration media.

Tandem MSMS is an extremely powerful technique for the identification and confirmation of mass peaks. Selected ions from the first MS are split and MS is completed on these smaller ion fragments which may give more information on the species. MSMS was completed on two Proposed PAH ions, $C_{18}H_{10}^+$ (226.0778 m/z) and $C_{28}H_{12}^+$ (348.0933 m/z) and are shown in Figure 4.7a and 4.7b confirming the PAH assignment.

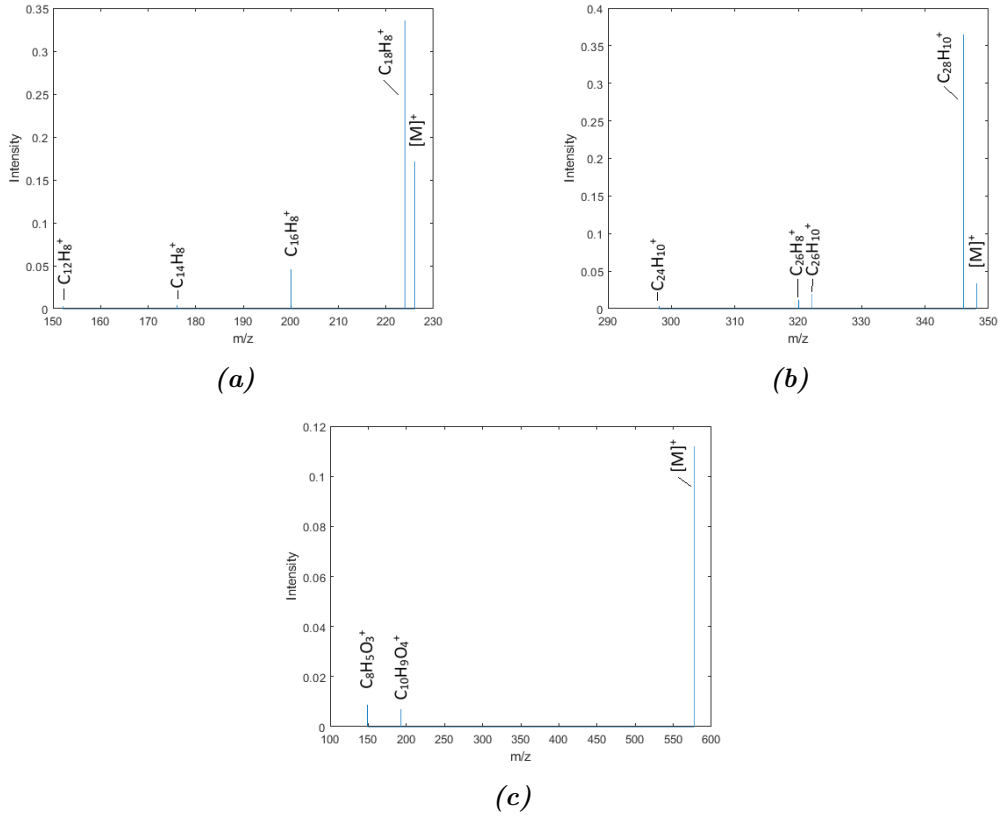


Figure 4.7: *Positive ion MSMS spectra of a) 226.0778 m/z, b) 348.0933, and c) 577.1347 m/z from control sample CF 002.*

Removing the carbonaceous peaks from the positive ion spectra (Figure 4.5) reveals the presence of lower intensity oxygen containing organic ion peaks tabulated in Table 4.2. These oxygen containing ion peaks will also need to be removed from the data of blocked filters as they are postulated to be molecular and fragmentation ions from the filtration media. The peak at 577 m/z has been characterised in Briggs (1986) to be a result of a cyclic trimer formed when (PET) is heated to above 130 °C.

MSMS was completed on the positive ion peak at 577 m/z which fragmented into two

Table 4.2: *Proposed formula for the oxygen containing positive ions labeled in Figure 4.5c (c) and their respective DBE and deviations*

ID	Proposed formula	Deviation (ppm)	DBE	ID	Proposed formula	Deviation (ppm)	DBE
1	$C_6H_7O^+$	2.1	3.5	5	$C_8H_5O_3{}^+$	−0.5	6.5
2	$C_7H_5O^+$	0.9	5.5	6	$C_{12}H_9O^+$	−0.9	8.5
3	$C_7H_5O_2{}^+$	−0.1	5.5	7	$C_{10}H_9O_4{}^+$	−0.5	6.5
4	$C_7H_4O_3{}^+$	−0.7	6	8	$C_{30}H_{25}O_{12}{}^+$	1.0	18.5

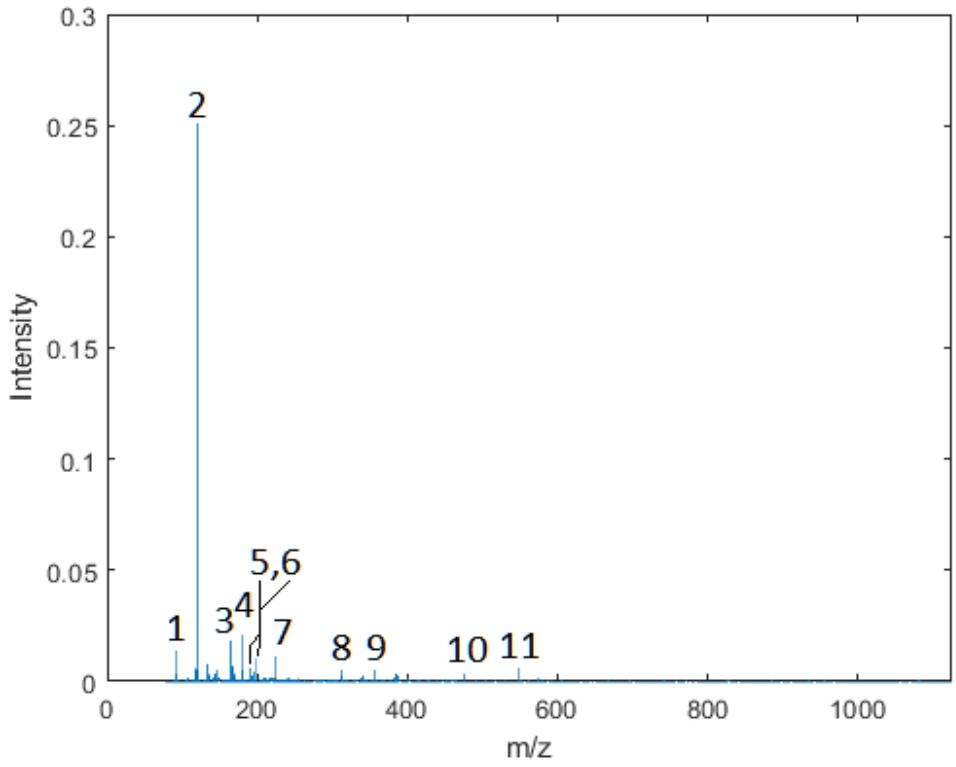


Figure 4.8: *Orbi-SIMS negative $C_xH_yO_z$ ion peaks of CF 002*

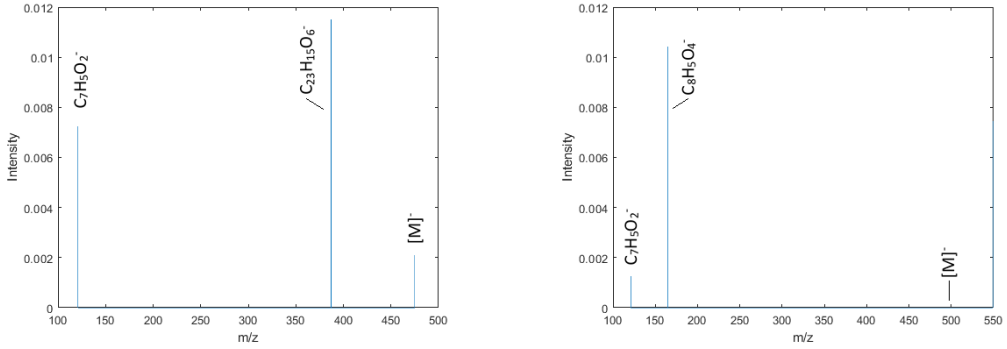
of the oxygen containing ions shown in Table 4.2, $C_8H_5O_3^+$ and $C_{10}H_9O_4^+$ (Figure 4.5c) suggesting that the peaks 5, 7 and 8 are likely related. $C_{10}H_9O_4^+$, is suggested to be the parent $[M+H]^+$ ion which is a monomer of PET. The oxygen containing ions proposed for CF 002 (Table 4.2) were also seen in CF 003 which suggests that the surface of CF 002 must have been subject to a significant layer of contamination when conducting XPS.

The negative ion spectra (Figure 4.8) was largely populated by oxygen containing organic ions tabulated in Table 4.3. These ions were common to both control filters and as with the positive ions these will need to be removed when analysing the negative polarity spectra of the diesel fuel filters.

MSMS was completed on the two highest mass negative ions in Table 4.3, shown in Figure 4.9. MSMS confirmed that these two assignments were correct, the latter likely a $[3M\text{-}C_2H_5\text{-}H]^-$, where M is a PET monomer, and that the lower mass ions in Table 4.3 are likely fragments of the polymers.

Table 4.3: *Proposed formula for the oxygen containing negative ions labeled in Figure 4.8 and their respective DBE and deviations*

ID	Proposed formula	Deviation (ppm)	DBE	ID	Proposed formula	Deviation (ppm)	DBE
1	$C_6H_5O^-$	0.1	4.5	7	$C_{14}H_9O_3^-$	2.1	10.5
2	$C_7H_5O_2^-$	1.6	5.5	8	$C_{17}H_{13}O_6^-$	2	11.5
3	$C_8H_5O_4^-$	1.6	6.5	9	$C_{18}H_{13}O_{8^-}$	1.7	12.5
4	$C_{13}H_9O^-$	1.7	9.5	10	$C_{26}H_{19}O_9^-$	1.3	17.5
5	$C_{10}H_7O_4^-$	2.2	7.5	11	$C_{28}H_{21}O_{12}^-$	1.7	18.5
6	$C_{13}H_9O_2^-$	2	9.5				



(a) ***(b)***

Figure 4.9: *Negative ion MSMS spectra of a) 475.1041 m/z and b) 549.1048 m/z from control sample CF 002.*

4.5 Discussion

SEM-EDX showed that the bulk surface composition of both control filters were of non-woven organic material. Analysis of the survey spectra and C1s envelope confirmed that CF 003 was likely a polyester, but it was not possible to distinguish between PBT, PAA and PET. Work with the 3D Orbi-SIMS confirmed the presence of the latter in both control filters.

It is thought that the fibrous material at the top of the filtration media on both control filters is the same, however, the C1s envelope was dominated by oxygen bonded carbon. XPS is a very surface sensitive technique so it is possible that this is a result of contamination on the surface of CF 002. The presence of silicon in the EDX analysis of CF 002 suggests that the surface was contaminated.

The positive spectra of both control filters were dominated by the presence of PAH $[M]^+$ ions ranging from C_6 (DBE: 4) through to C_{66} (DBE: 56) alongside other fragmentations of the parent ion. In XPS, the aromatic component, however, was shown to be a minor constituent in the control filters. This is an example of the limitations of using SIMS as an analytical technique, where the data is influenced by matrix effect discussed in Chapter 2.5. Using the compound_finder script it was possible to assign all of these carbonaceous peaks within ± 2.5 ppm above 95 m/z. Removal of the carbonaceous peaks revealed the presence of various oxygen containing ions.

A cyclic trimer PET ion $[3M]^+$ was seen in the positive 3D Orbi-SIMS data which is discussed in literature (Briggs, 1986) to be a result of heating the polyester above 130 °C. Tandem MSMS was also used to confirm the assignments. Alongside this, multiple oxygen containing peaks in both polarities have been identified, including the parent PET ion, which can be considered when analysing the 3D Orbi-SIMS data in the subsequent chapters.

4.6 Conclusion

In this study we used a combination of techniques to establish the chemistry and morphology of the control samples used in the rest of this thesis. Using an in-house designed algorithm we are able to identify a plethora of ions that are collected in the SIMS analysis within ± 2.5 ppm deviation. A series of PAH ions ranging from C_6 through to C_{66} dominated the positive ion spectra collected by the 3D Orbi-SIMS. Removing this series of peaks from the data and re-running the algorithm revealed the presence of PET monomers and other oxygenated ions.

It is important to note that the removal of the carbonaceous series is an important step for the identification of underlying ionic compounds which aren't as readily ionised. This is highlighted through XPS, known to be a strong quantification method, and EDX analysis which showed that while the filter was largely carbonaceous, 15-20% of the composition was oxygen.

Chapter 5

Laboratory Test Samples

5.1 Introduction

In literature, summarised in Chapter 2, it is proposed that the source of deposit in diesel engine fuel filters can originate from a variety of sources. In this chapter a filtration rig was designed to mimic some of the conditions that a fuel filter may experience in a vehicle. The design is based on a multi-pass filtration test standard, ISO 19438 (ISO, 2003), which covers the continuous injection of contaminant into fuel that is circulating through a fuel filter. The aim of ISO 19438 is to test various performance parameters of a fuel filter including: contaminant capacity, particulate removal, and differential pressure. For this work no contaminants were added to the fuels as the aim is to see the effects that straight and blended diesel and biofuels have on filtration media. The addition of contaminants to fuel will be discussed in Chapter 6.

The filter used for the lab test filters was the same as CF 003, which is characterised in Chapter 4. The filters were exposed to a variety of fuel compositions as described in Chapter 3.1.3, for 8-hour cycles and then rested overnight. The 1 L reservoir was replaced at the start of each 8-hour cycle. The filters were then vacuum oven dried for 8 hours at $140°C$ and $1x10^{-4}$ bar prior to being analysed by scanning electron microscopy (SEM), energy-dispersive X-Ray spectroscopy (EDX), X-Ray photoelectron spectroscopy (XPS) and Orbitrap^{TM} secondary ion mass spectrometry (Orbi-SIMS).

Table 5.1: *Experiment ID and fuel combinations used in the form Yxxx, where Y is the fuel type and xxx is the % v/v.*

ID	Fuel Used
LTF 001 (CF 001)	None
LTF 002	D100
LTF 003	B100
LTF 004	B20
LTF 005	H100
LTF 006	H20
LTF 007	B50H50
LTF 008	B10H10

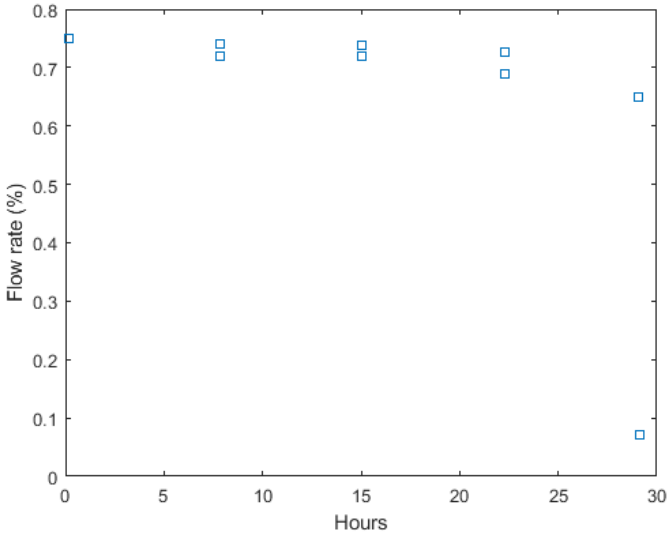
Table 5.2: *Flowrates through the filtration rig with no filter installed and density of the fuel mixtures at* $25°C$.

Filter ID	Flowrate with no filter installed (L/min)	Fuel Temperature $(°C)$	Density at $25°C$ (kg/m^3)
LTF 002	0.92	23.7	832
LTF 003	0.96	23.8	880
LTF 004	1.43	23.8	842
LTF 005	1.89	23.8	780
LTF 006	1.03	23.8	822
LTF 007	1.53	23.7	830
LTF 008	1.21	23.9	832

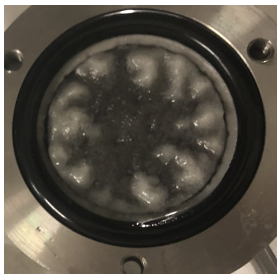
5.2 Filtration Rig

A lab filtration rig was built based on the design of the multi-pass filtration rig standard ISO 19438 (ISO, 2003). The premise of the rig is to recirculate fuel from a reservoir through a filter to recreate the conditions that a fuel filter might face in a vehicle. A schematic of the rig can be found in Chapter 3.1.3. ISO 19438 includes specification for adding contaminants to the fuel however, only reference fuel was used for this experiment. 1 L of fuel was recirculated for 8 hours after which the fuel was replaced.

As described in Chapter 3.1.3, eight different combinations of fuels were tested summarised in Table 5.1. Prior to each run, the fuel was passed through the system with no filter installed in the filter housing and the flowrate was measured (Table 5.2). Flow rates in the subsequent figures will be shown as a percentage of the flow rate with no filter installed. As expected, the flow rate reduced with time in all experiments, although only one experiment's flowrate (LTF 003) reduced to below 20 % of the initial flow rate (Figure 5.1a). It



(a)



(b)

Figure 5.1: *a) % Flowrate over time of LTF 003 (B100) which blocked after 28 hours and b) image of the reservoir side of the filter post experiment.*

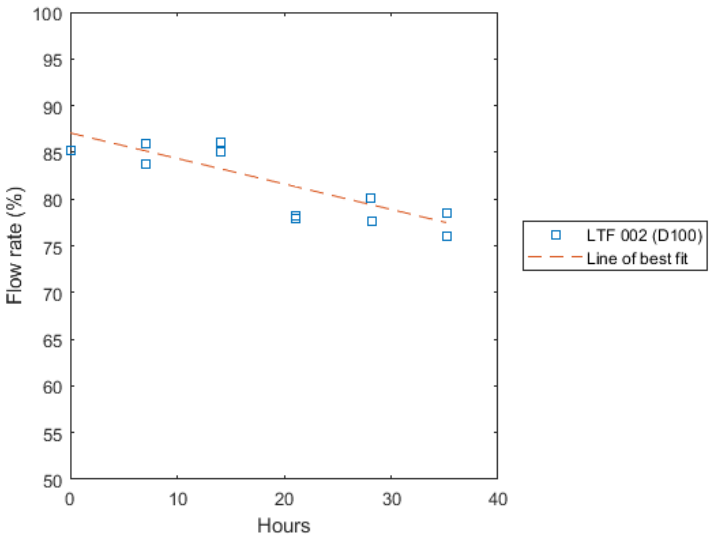
is important to note that the blocking occurred overnight, where the filter was allowed to rest before the next 8-hour cycle was conducted. A white sludge formed on the surface of the filter (Figure 5.1b) which was not seen when using other combinations of fuels. This was not present after the drying process.

Using the least squares method, the gradient of the line of best fit was calculated (Equation 1.1) where gradient, m, is calculated using the mean, $\bar{X}$, of the time (x) and mean, $\bar{Y}$, of the % of the flow rate without a filter installed (y). The gradient of each run is tabulated in Table 5.3. For this work it is assumed that when the flow rate of the fuel is below 50 % of the initial flow rate it is considered blocked.

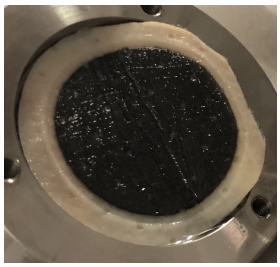
$$m = \frac{\sum_{i=1}^{n}(x_i - \bar{X})(y_i - \bar{Y})}{\sum_{i=1}^{n}(x_i - \bar{X})^2} \tag{5.1}$$

The R^2 value, a statistical measure that shows the variance of a dependent variable (flow rate) that is explained by an independent variable (time) was calculated for each experiment and tabulated in Table 5.3.

With exception of LTF 003 and 005 the R2 value was above 0.7, suggesting that the line of best fit will be a good indicator of a trend. The low R^2 value of LTF 003 was skewed due to the last flow rate taken (10 %) when the filter was assumed to be blocked (Figure



(a)



(b)

Figure 5.2: *a) % Flowrate over time of experiment B10H10 fuel mix (blue). Line of best fit (orange) is calculated using the least squares method (Equation 5.1) and b) image of the reservoir side of the filter after 35 hours.*

5.1a).

Using the gradient of each LTF experiment, blended fuels; B20, H20, B50H50 and B10H10 would take longer to reach 50 % of the initial flowrate compared to the straight fuels (B100 and H100). The gradient of LTF 003 suggests that it would take 50 hours to reach 50 % of the initial flow rate, however, it only took 27 hours. This could show that blocking of the filter occurred at an exponential rate rather than linear. Taking flow rate readings more often would confirm this. LTF 002, 100

Table 5.3: *Calculated time taken for flowrate to reach 50% of initial flowrate for each experiment based on the gradient of the line of best fit, calculated from Equation 1.1, and the R^2 number for the data.*

Experiment	Fuel Mix	Gradient m (% of total flowrate/hour)	Hours until 50% flow rate	R^2
LTF 002	D100	-0.0000202	337	0.71
LTF 003	B100	-0.000157	49.7	0.33
LTF 004	B20	-0.0000233	308.2	0.87
LTF 005	H100	-0.0000534	138.7	0.51
LTF 006	H20	-0.0000307	223.1	0.7
LTF 007	B50H50	-0.0000306	219.6	0.76
LTF 008	B10H10	-0.0000455	162.9	0.72

5.3 Scanning Electron Microscopy

Secondary electron scans revealed that, excluding the blocked LTF 003, the morphology between LTFs remained similar to the reference filter CF 003 (Chapter 4.2) with the fibrous nature of the filter having no deposit present (Appendix A). An unblocked filter that used 100 % FAME is shown in Figure 5.3a where there was no apparent build-up of deposit as with LTF 002,004-008 (Appendix A). EDX on this sample revealed that the bulk composition was organic, and no other contaminant was seen.

In contrast to the unblocked LTF 003, the morphology of a blocked LTF 003, showed a build up of organic deposit between the fibres with bulges on the fibres (Figure 5.4a). EDX analysis showed that the deposit was composed of carbon and oxygen.

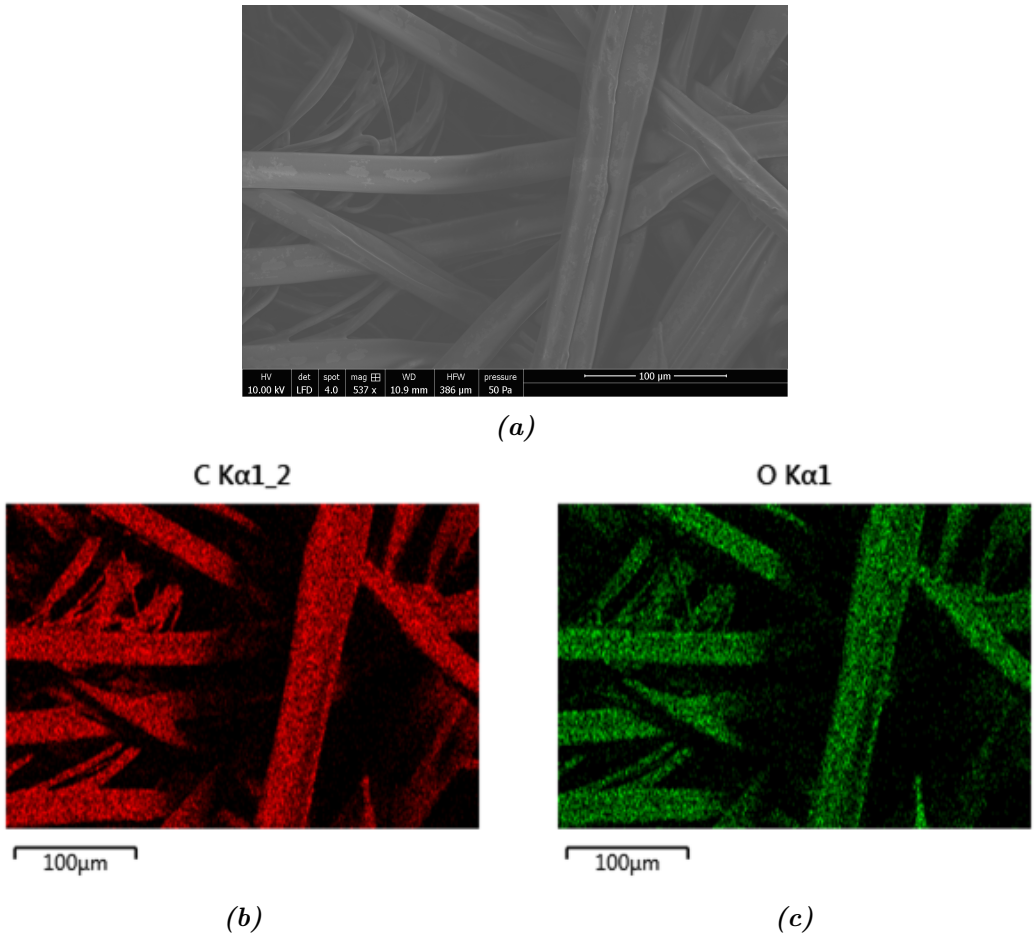


Figure 5.3: *From SEM analysis a a) secondary electron image of unblocked LTF 003 (B100). EDX analysis showed the b) carbon and c) oxygen distribution on the filter.*

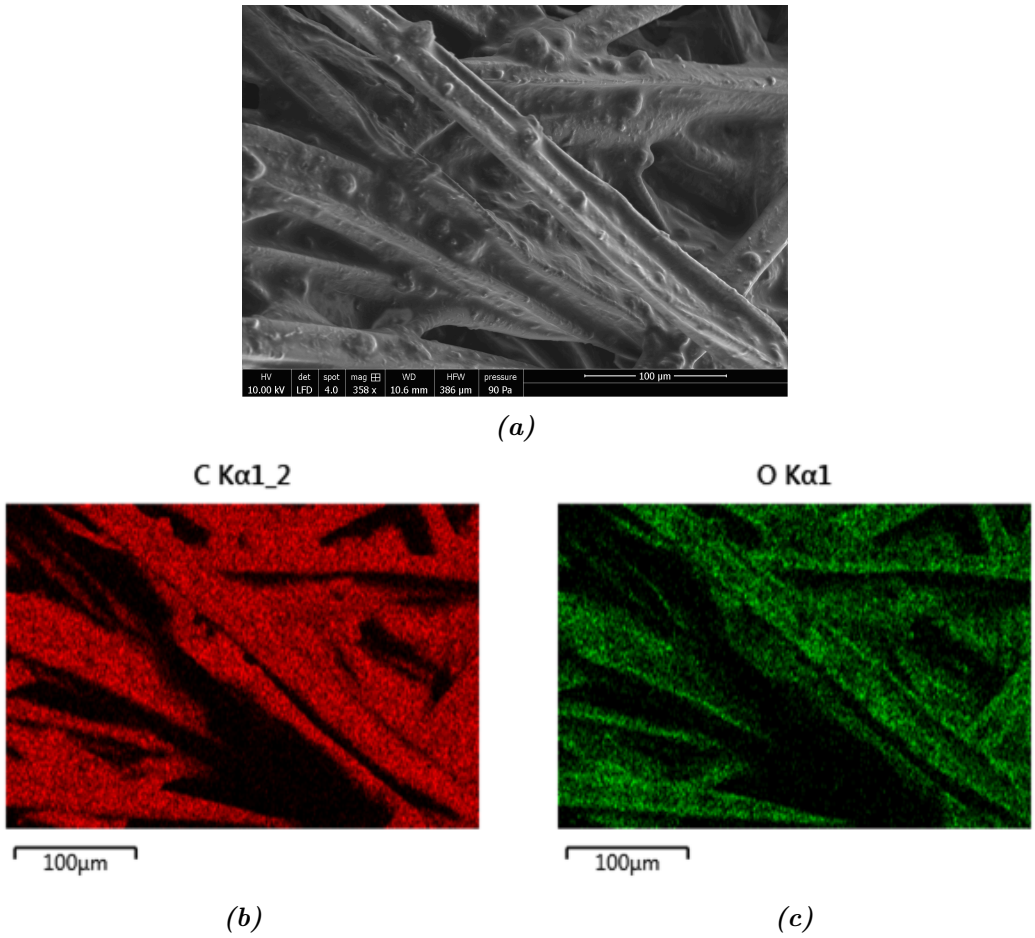


Figure 5.4: *From SEM analysis a a) secondary electron image of blocked LTF 003 (B100). EDX analysis showed the b) carbon and c) oxygen distribution on the filter.*

5.4 X-Ray Photoelectric Spectroscopy

Using a XPS survey spectrum one can obtain atomic signatures from the sample. For each sample three points were analysed from the surface, the points were then summed to get an average composition as well as increasing the signal to noise ratio as described in Chapter 3.3.2. The average compositions of each sample are shown in Figure 5.5b alongside an example survey spectrum of unblocked ETF 003 (B100).

As expected, the atomic concentrations of the ETFs were dominated by carbon and oxygen. ETF 002 had the largest concentration of nitrogen which is present in small quantities in diesel fuel suggesting that nitrogen containing components of diesel fuel are selectively retained by the surface of the filtration media. Some silicon is present on the surface of LTF 003 – 005 and 007 which is likely contamination as no additive was added to the fuel.

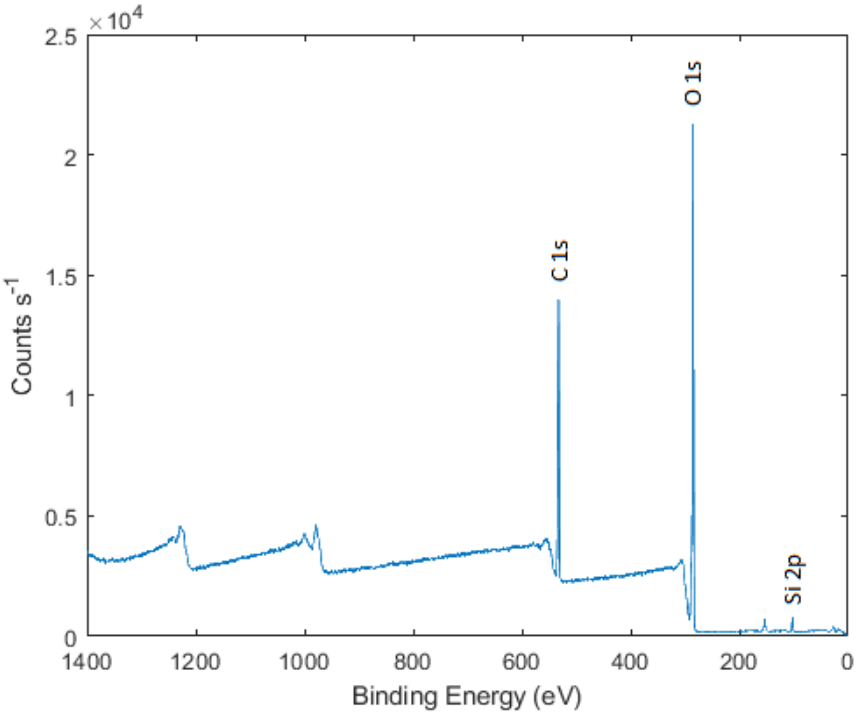
LTF 002, 004, 006 and 008 all had elevated atomic C:O ratios (8.1, 6.3, 8.9 and 8.0 respectively) compared to that of the reference filter CF 001 (4.9). These LTF all had blends of fuel that contained some diesel, suggesting that diesel could cause some carbonaceous deposit formation on the surface of filters.

Alongside the quantification of elements through XPS survey spectra, it is also possible to analyse the C1s envelopes. This approach shows the possible bonding characteristics present on the samples. The refence C1s envelope of CF 001 can be found in Chapter 4.3. The line fittings were made with the characteristics described in the Table 5.4.

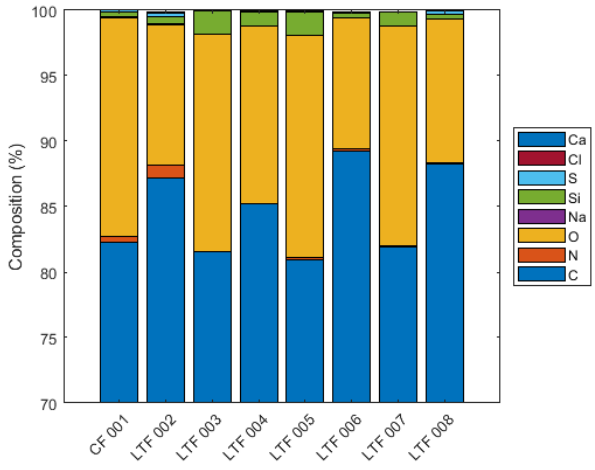
From the averaged compositions of the C1s envelopes, LTF 002 and 003 had similar concentrations of each peak to the reference filter, with LTF 003 having a smaller concentration of C=C peak (Figure 5.7). LTF 004 – 008 had lower concentrations of the C-C peak compared to the reference. LTF 005 the filters that were exposed to a H100 fuel

Table 5.4: *Binding energy ranges for the C1s components of LTFs and reference filter CF 003 (Chapter 4.3).*

	C=C	C-C	C-O	C=O	O-C=O	$\pi - \pi*$
B.E range (eV)	284 - 284.4	284.8 - 285	286 - 286.4	287 - 287.4	288.6 - 289.2	290.5 - 291



(a)



(b)

Figure 5.5: *a) Survey spectra of LTF 003 (B100) including elemental regions and b) elemental compositions of reference filter CF 001 (Chapter 4.3) and lab test filters (LTF) from XPS survey spectra.*

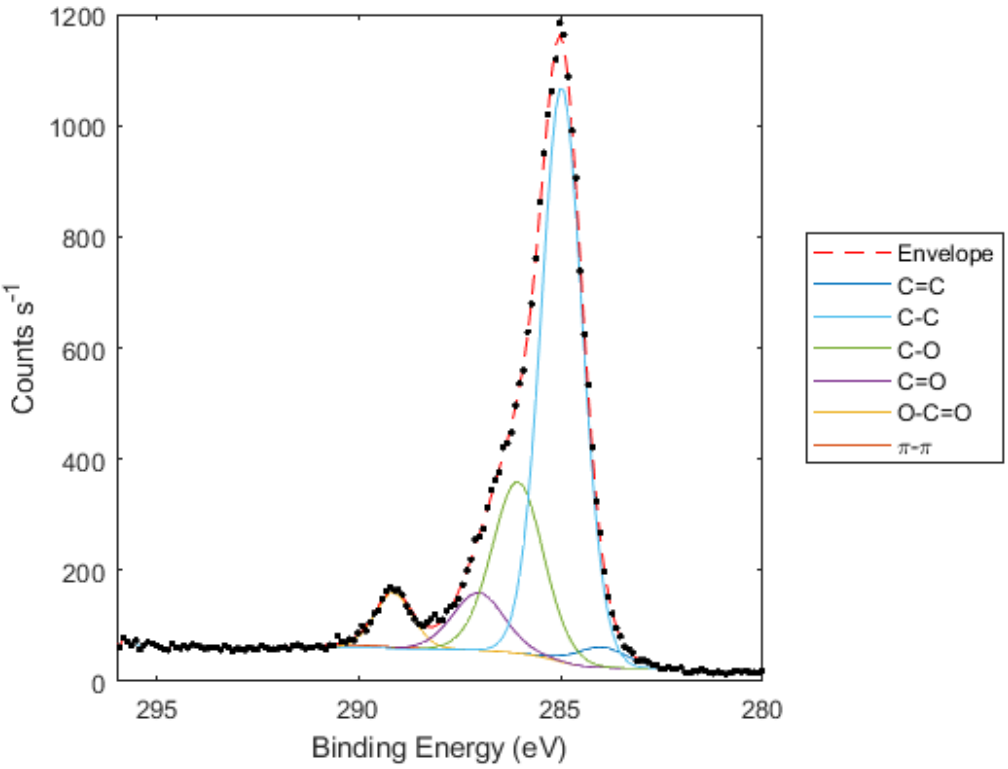


Figure 5.6: *High-resolution XPS spectra of the C1s region of LTF 002 (D100).*

blend had the largest concentration of a sp2 carbon although this was not expected as the HVO fuel used was composed mainly of straight and branched alkanes. All the filters that were exposed to straight or blended HVO fuel (LTF 004 – 008) all had a presence of a "shake-up" peak suggesting the presence of an aromatic ring.

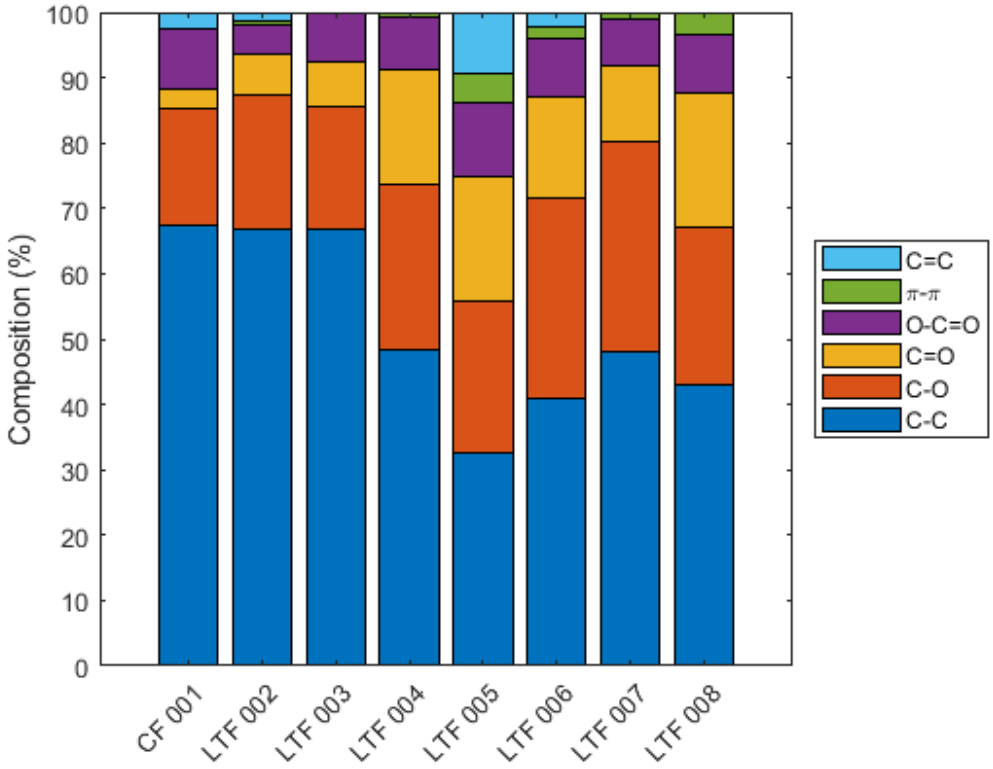


Figure 5.7: *Averaged compositions of the C1s envelopes for each of the LTFs and reference filter CF 003 (Chapter 4.3).*

5.5 Dynamic Secondary Ion Mass Spectrometry

Using the Orbitrap^{TM} as the analyser in the 3D Orbi-SIMS allows for much greater mass resolution as compared to the ToF-SIMS. It is therefore possible to assign ions with much more certainty. Softer fragmentation using an $Ar3000^{+}$ gas cluster as the primary ion beam to sputter the sample results in the increased presence of high mass ions.

As discussed in Chapter 3.3.4 a total ion spectrum can be generated from the dynamic SIMS which shows the composition of the whole depth profile. Excluding the blocked ETF 003 (B100), all the spectra were dominated by carbonaceous peaks similar to that seen in the reference filter CF 001 (Figure 4.5). Removing these peaks revealed the presence of oxygen containing peaks, 1-7 and 9 (Table 5.5), all of which were seen in the reference filters.

The peak at 326 m/z (ID: 8, Figure 5.8) has been attributed to didecyldimethylammonium chloride (DDAC) which is used as an antiseptic agent for biocidal applications (Wegh et al., 2017). This peak was only seen in LTF 002 and the blocked LTF 003 and not in

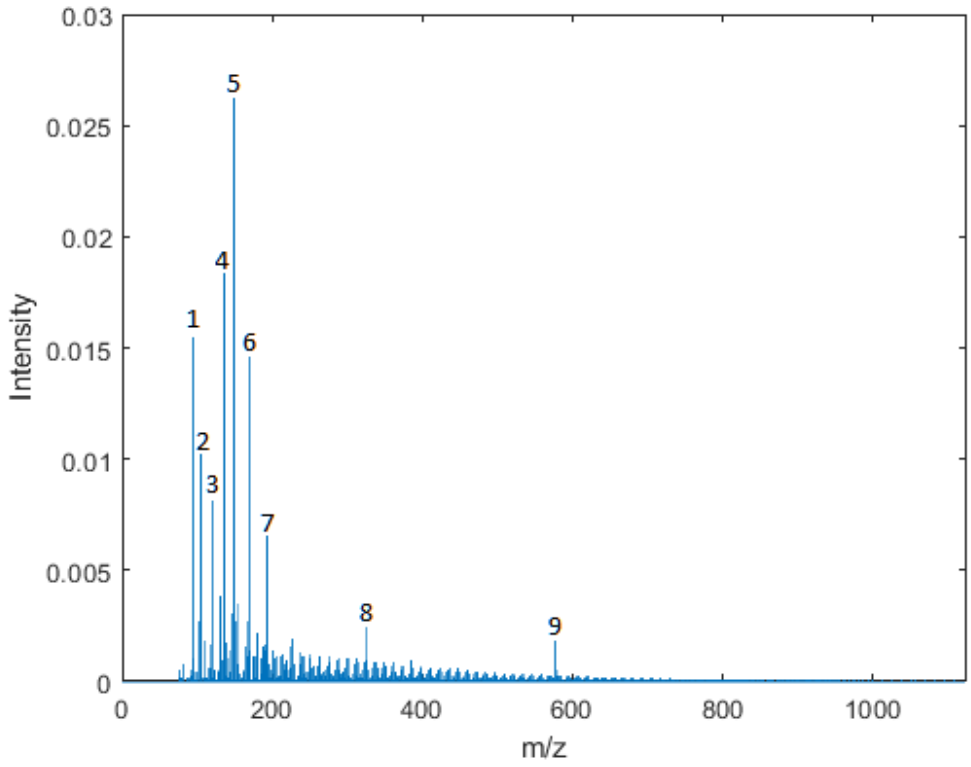


Figure 5.8: *LTF 002 (D100) positive ion 3D Orbi-SIMS spectra with C_xH_y removed. Proposed formula of identified peaks are shown in Table 5.5.*

the reference samples. No other peaks were prominent among the LTFs excluding the blocked LTF 003 confirming the SEM data which suggested that no deposit was found on the other LTFs.

In contrast, the blocked LTF 003 only showed a presence of low mass ($<$ 200 m/z) carbonaceous peaks in the positive ion spectra which have been removed from Figure 5.9 for clarity. Ion peaks 7 and 8 suggest the presence of a sitogluside. The same pair of ions was seen in ToF work by Feld and Oberender (2016) on the deposit of biodiesel residues in filter, however, the use of the 3D Orbi-SIMS allows the characterisation of these deposits

Table 5.5: *Proposed formulas and their respective deviations of the peaks identified in LTF 002 (Figure 5.8).*

ID	Proposed Formula	Deviation	ID	Proposed Formula	Deviation
1	$C_6H_7O_6^+$	2.1	6	$C_{12}H_9O^+$	-0.9
2	$C_7H_5O^+$	0.9	7	$C_{10}H_9O_4^+$	-0.5
3	$C_7H_5O_2^+$	-0.1	8	$C_{22}H_{48}N^+$	-0.1
4	$C_7H_4O_3^+$	-0.7	9	$C_{30}H_{25}O_{12}^+$	1
5	$C_8H_5O_3^+$	-0.5			

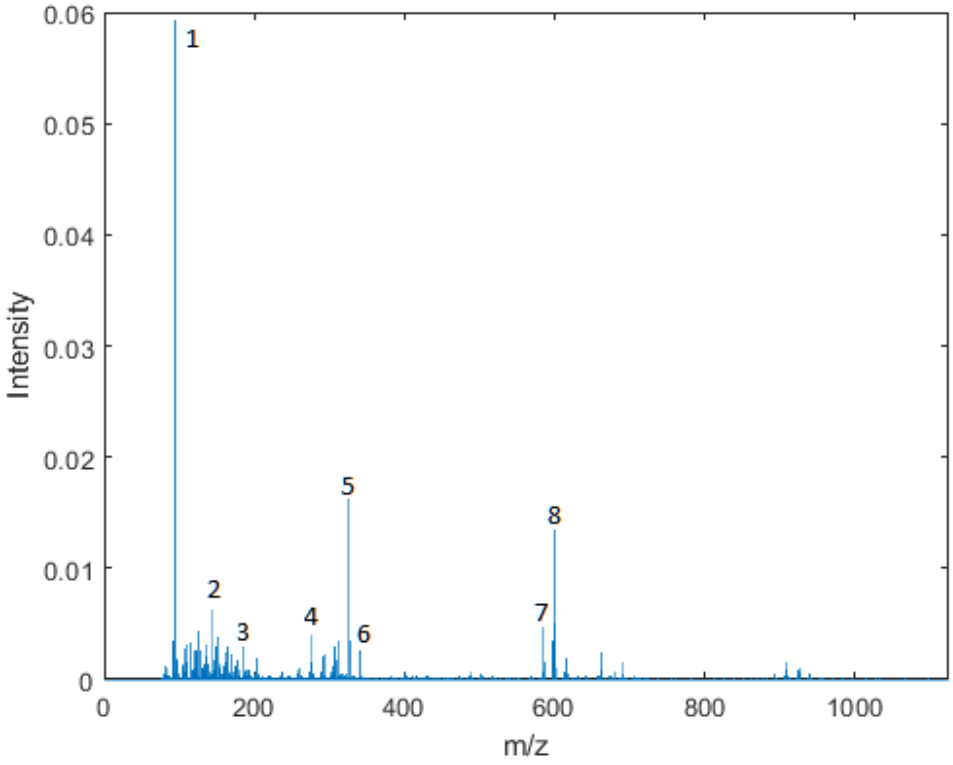


Figure 5.9: *LTF 003 (B100), blocked filter, positive ion 3D Orbi-SIMS spectra with C_xH_y removed. Proposed formula of identified peaks are shown in Table 5.6.*

with much greater certainty than before. The molecular ion is thought to have sodium as its adduct $[M+Na]^+$. The level of unsaturation of the total ion (6) fits well with the presence of five rings and one double bond present in the glucocides.

$C_6H_7O^+$ ion peak was present in the refence filters and other LTFs although the high concentration and the absence of other filter fibre peaks in large concentrations suggests that this $[M+H]^+$ ion is likely from another source. It is possible that this ion is a degradation fragmented ion of the sterol glucoside from the deposit alongside the ions identified as 2 in Table 5.6.

The ion representing DDAC seen in LTF 002 (D100) was also seen in the blocked LTF 003 (B100) filter alongside an another of its ion fragment which has been characterised in Wegh et al. (2017).

One of the benefits of using the 3D Orbi-SIMS is the ability to retrospectively analyse selected ions. From the total ion data discussed, positive and negative ion peaks intensities were tracked as a function of sputter time. Details on the settings used are summarised

Table 5.6: *Proposed formulas and their respective deviations of the peaks identified in LTF 002 (Figure 5.9).*

ID	Proposed Formula	Deviation	ID	Proposed Formula	Deviation
1	$C_6H_7O^+$	1.7	5	$C_{22}H_{48}N^+$	-0.1
2	$C_{10}H_9O^+$	-1.3	6	$C_{18}H_{29}O_2{}^+$	-0.1
3	$C_{12}H_{28}N^+$	-1	7	$C_{34}H_{58}O_6Na^+$	0
4	$C_{10}H_{19}O_4{}^+$	-0.1	8	$C_{35}H_{60}O_6Na^+$	0.1

in 3.3.4.

From the analysis of the positive ion depth profile (Figure 5.10) it is clear that the DDAC ion and its fragmentation described in Table 5.6 (ID: 3 and 5) are present throughout the filter. Although their relative intensity drops rapidly at the start of the sputter. It reaches a minimum concentrations at around 400 seconds of spluttering, then slowly increasing in intensity with sputter time. This shows the importance of combining static and dynamic SIMS analysis to put into context the concentrations of ions throughout a sample. If only the initial layer was taken, the user may think that the sample is heavily laden with DDAC, which it's presence is shown to be largely skewed by its concentration at the surface of the deposit. The sterol glucoside appeared to reduce in intensity with sputter time suggesting that this is deposited on at the surface of the deposit. The ion representing FAME (ID: 6, Table 5.6), remained constant throughout the filter.

An ion pair of the FAME ($C_{16}H_{31}O_2{}^-$ and $C_{18}H_{35}O_2{}^-$), which are unique to the blocked LTF 003, both have an unsaturation level of 1, attributed to the double bonded oxygen. These ions initially decreased in intensity a high rate however the rate decreased over time (Figure 5.11).

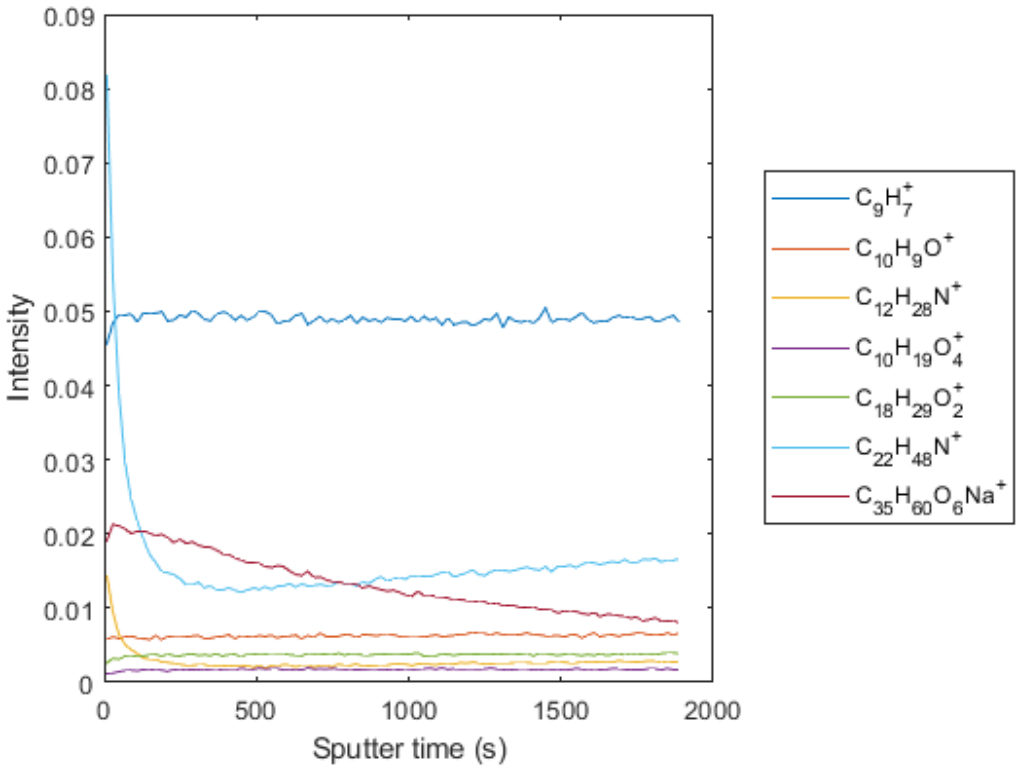


Figure 5.10: *Positive ion depth profile of selected ions in blocked LTF 003, point-to-point normalised with total ion.*

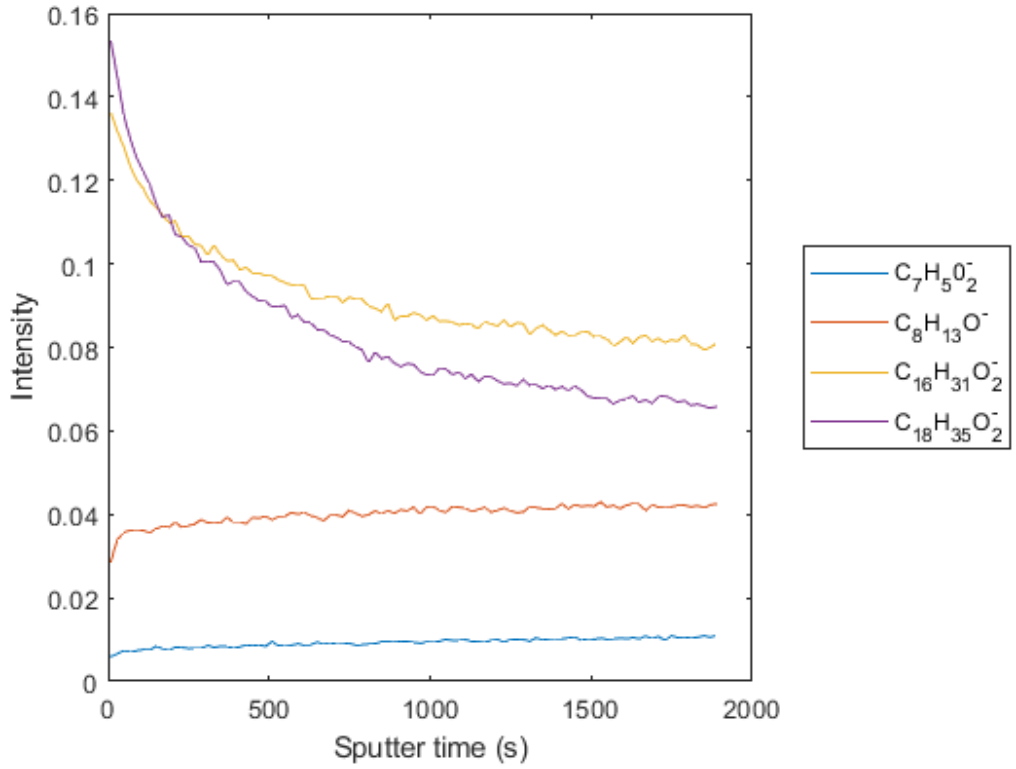


Figure 5.11: *Negative ion depth profile of selected ions in blocked LTF 003, point-to-point normalised with total ion.*

5.6 Discussion

Excluding one of the LTF 003 (B100 fuel) experiments, none of the experiment's flow rates were below 70% of the initial flow rate after 40 hours of running (5 x 1 L) fuel through them. However, they all showed a decreasing trend of flow rate over time. The exception blocked after 28 hours, however it was not a gradual blocking, but a steady decrease followed by a sudden blocking overnight when the fuel filter was left to rest.

SEM revealed that none of the unblocked filters had any deposit present on the filtration fibres. In the blocked LTF 003 (D100), there appeared to be an organic film forming on and between the polyester fibres which also covered particle like features. It is not understood whether these features were the precursor to the deposit.

Using data from positive polarity SIMS depth profile it was shown that the deposit changed in composition with depth which has previously not been shown. An initial decrease in intensity of an ion representing DDAC was followed with a steady increase deeper into the bulk deposit. Sitogluside was entrained throughout the deposit but its intensity decreased as a function of depth. While the intensity of an ion representing the unsaturated FAME was constant throughout the filter deposit in the positive ion spectra, in the negative ion SIMS depth profile, the saturated FAME ions decreased as a function of sputter time.

The study in this chapter only presented the results of filters subjected to clean fuel. Doping of the fuels prior to running the in-house fuel filtration rig with known and proposed contaminants such as the work shown by (Csontos et al., 2020), could provide an insight into the formation of deposits on filters on different fuel mixtures.

5.7 Conclusions

This study discussed the use of a purpose built in-house fuel filtration system to mimic the fuel re-circulation systems found in diesel fuel vehicles. Using bench top equipment is far cheaper than running engine tests and can be used for initial investigations on fuel filter deposits.

Various mixes of petroleum diesel, biodiesel and HVO were tested but only the use of B100 blocked the fuel filter within a 40 hour run. A build up of organic deposit on the fuel filter was shown using SEM-EDX. Using 3D Orbi-SIMS analysis a large amount of data was collected for the deposit, the algorithm discussed in previous chapters aided in the removal of a series hydrocarbon ions attributed to the filter membrane, discussed in Chapter 4, which revealed a pair of ions assigned to a Sitogluside.

Chapter 6

Engine Test Samples

6.1 Introduction

Engine tests are commonly used in industry to test the effects of adulterated fuel mixtures on FIE and the effectiveness of additives on deposit formation (Barbour et al. (2014); Barker et al. (2013); Barker and Reid (2014)). As part of the set-up of the engine, similar to that shown in Figure 1.5, fuel is passed through a filter prior to injection into the combustion chamber. The test used a CEC F-98-08 DW10B engine CEC (1998) and the fuel used was RF-06-03 (European certification test fuel).

In this chapter, eight filters that had been exposed to different mixtures of additives and contaminants added to the fuel, described in Chapter 3.1.2, summarised in Table 6.1, will be analysed. Generally, the additives were composed of detergent and corrosion inhibitor packages with various sodium sources added as contaminants. Although the specification of these engine tests is for the FIE, filters are exposed to similar conditions that are experienced in the field. The benefit of engine tests is the ability to control deposit inducing components and reduced exposures to external factors.

Four techniques have been employed for the analysis of these engine test filters (ETF) with the comparison to a reference, unused, filter CF 002 (Chapter 4). SEM-EDX allows for the topographical analysis of the filters with EDX employed for basic elemental analysis. As SIMS data can be skewed by the ease of ionisation, XPS is used to quantify the elemental composition of the deposits and filtration media. ToF-SIMS and 3D Orbi-SIMS have

Table 6.1: *Additive and contaminations added to fuel used in DW10 engine test.*

Sample Ref	Fuel	Additive	Contaminant
ETF 020	RF-06	Detergent, Corrosion Inhibitor	0.5 ppm Sodium
ETF 021	RF-06	LMWT PIBSI	-
ETF 022	RF-06	Corrosion Inhibitor	3 ppm Sodium Napthenate
ETF 023	RF-06	Detergent	-
ETF 024	RF-06	Detergent, Corrosion Inhibitor	0.5 ppm Sodium
ETF 025	RF-06	LMWT PIBSI	-
ETF 026	RF-06	Detergent, Corrosion Inhibitor	1 ppm Sodium
ETF 027	RF-06	Corrosion Inhibitor	1 ppm Sodium

gained increasing popularity in the study of diesel deposits on FIE (Barker et al. (2014); Edney et al. (2020a); Feld and Oberender (2016); Lamb et al. (2021)). This chapter will employ similar techniques to analyse deposits on diesel fuel filter.

As the amount of data from analytical technique increases, it becomes more important to use statistical analysis to aid in the deconvolution of the data. Multivariant analysis (MVA) encompasses many of these statistical techniques, of which principal component analysis (PCA) and non-negative matrix factorisation (NNMF) have been used in this chapter described in more detail in Chapter 2.6. The former has been used an initial search method for static secondary ion mass spectroscopy (SIMS) to identify key differences in the variance between samples. In data where there are no negative values, for example dynamic SIMS, the use of NNMF is more applicable as this MVA produces data which is described only using positive values.

6.2 Scanning Electron Microscope

Secondary electron scans on engine test filters (ETF) revealed a difference in morphology between samples. The filtration media for all the ETF presented here are a dual polyester-cellulose media.

The images for ETF 020, 21, 24 and 25 indicate the fibrous nature of the filters with no apparent deposit formation. This was confirmed with an EDX area scan of the image areas where only carbon and oxygen were present. A representative example of ETF025 is shown in Figure 6.1. SEM-EDX scans of ETF 020, 021, and 024 can be found in appendix

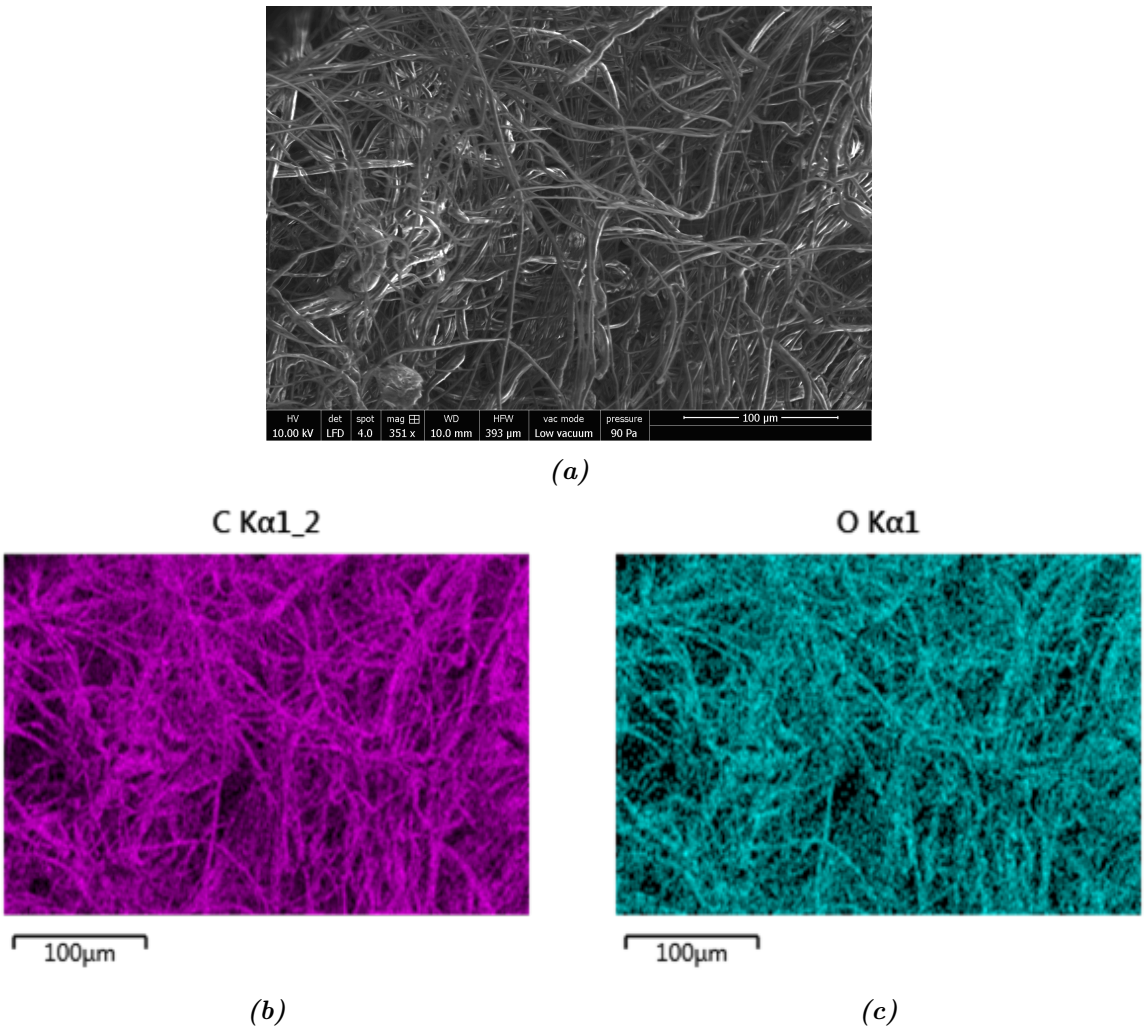


Figure 6.1: *From SEM analysis a a) secondary electron image of ETF 025. EDX analysis showed the b) carbon and c) oxygen distribution on the filter.*

A.

Although ETF023 was largely clear, there was an area of localised deposit, in the upper right corner, indicated in Figure 6.2. An EDX scan on this area revealed that this deposit consisted of two regions. sodium and Cl were present on the perimeter, whilst the inner region, contained sulfur, silicon and oxygen. The density of carbon appeared to be low in comparison in this structure.

The EDX map scans of ETF 022, 26 and 27 were dominated by sodium, carbon and oxygen. ETF 022 was completely covered by a layer of organic species associated with sodium with a trail of protruding fibres visible (Figure 6.3.

Although ETF027 showed areas of complete sodium coverage, there were also regions where the covering sodium layer stopped and fibres with particulates of sodium were

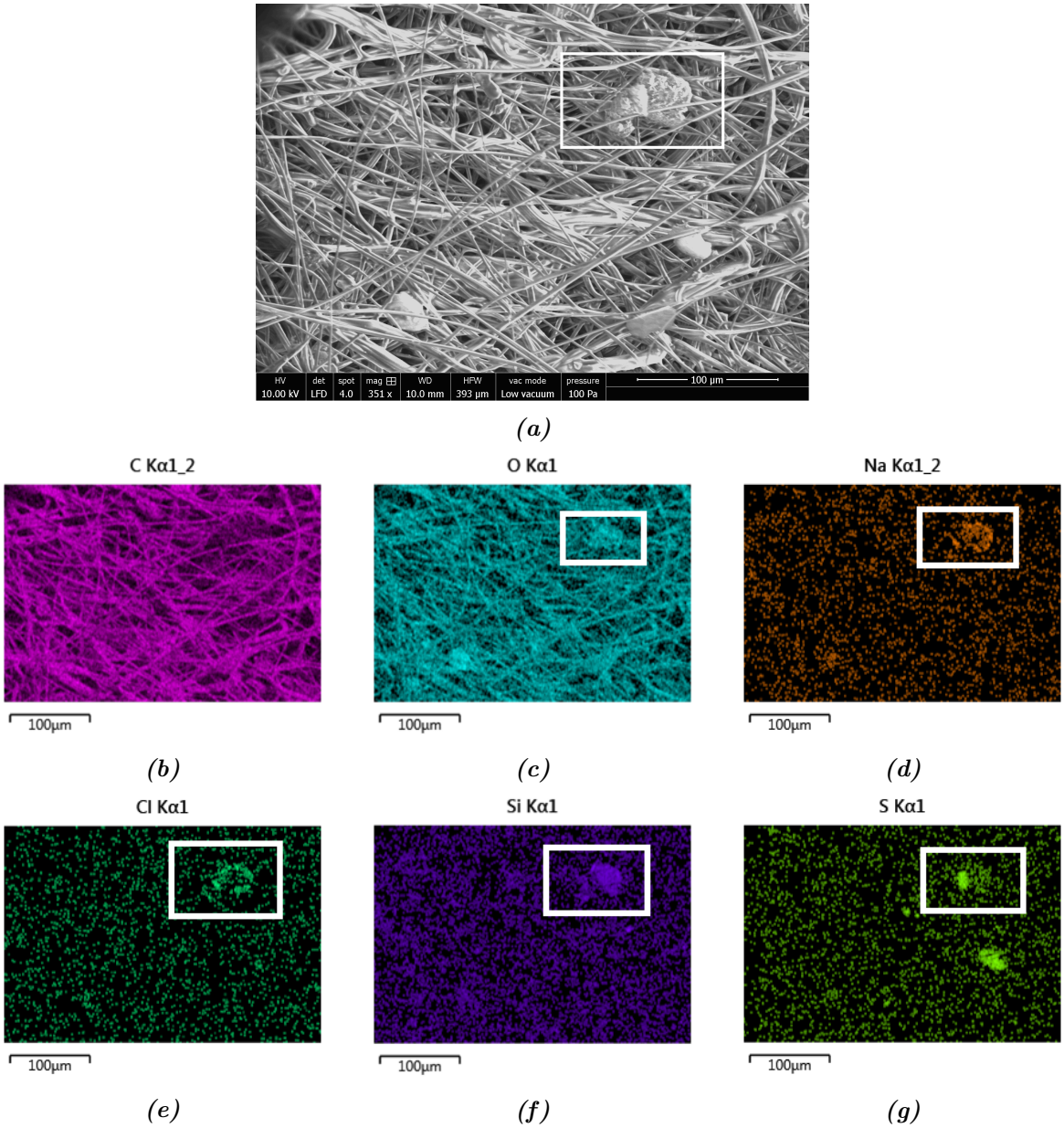


Figure 6.2: *From SEM analysis a a) secondary electron image of ETF 023. EDX analysis showed the b) carbon, c) oxygen, d) sodium, e) chlorine, f) silicon, and g) sulphur distribution on the filter. A particulate deposit is highlighted.*

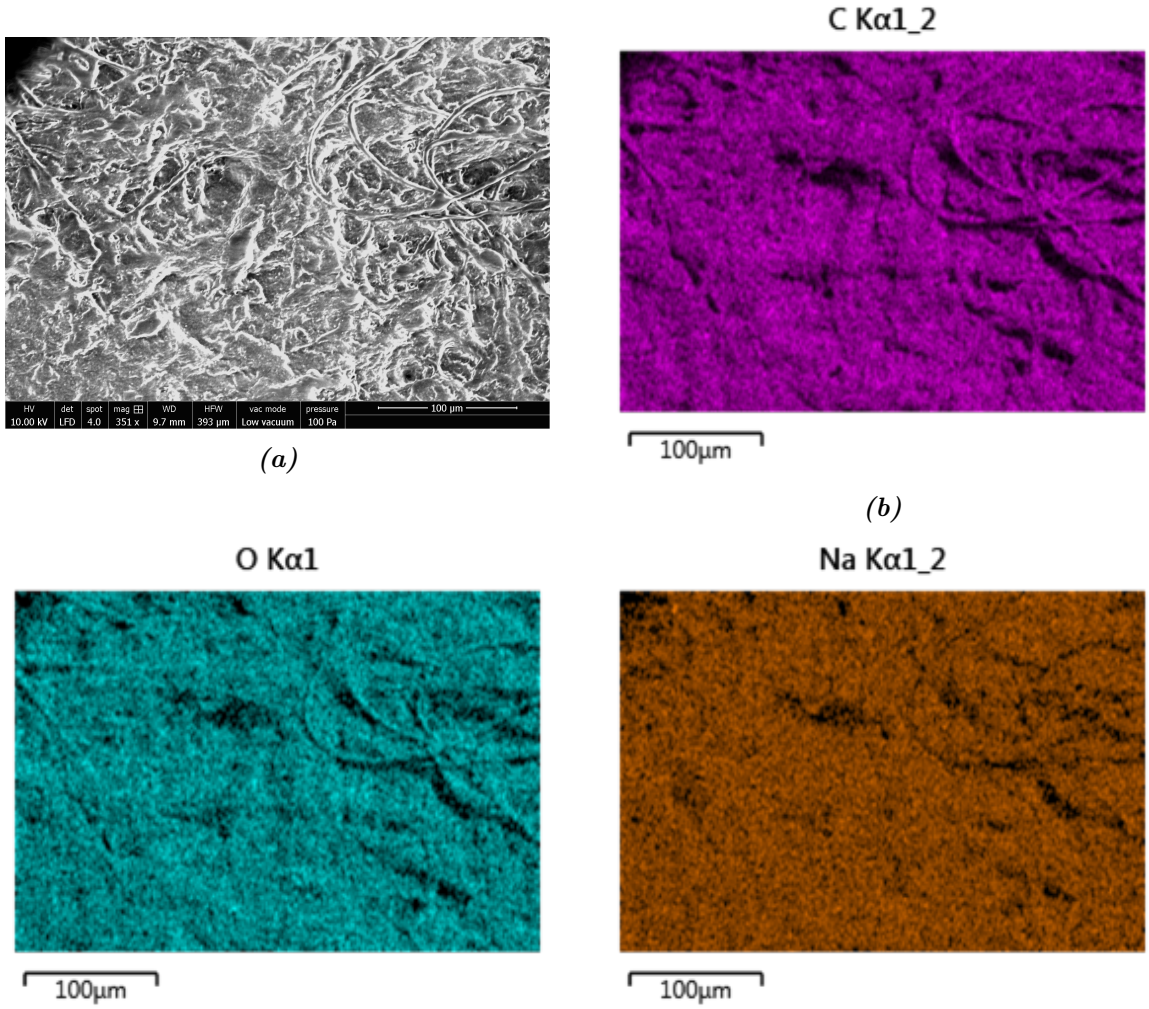


Figure 6.3: *From SEM analysis a a) secondary electron image of ETF 022. EDX analysis showed the b) carbon, c) oxygen, and d) sodium distribution on the filter.*

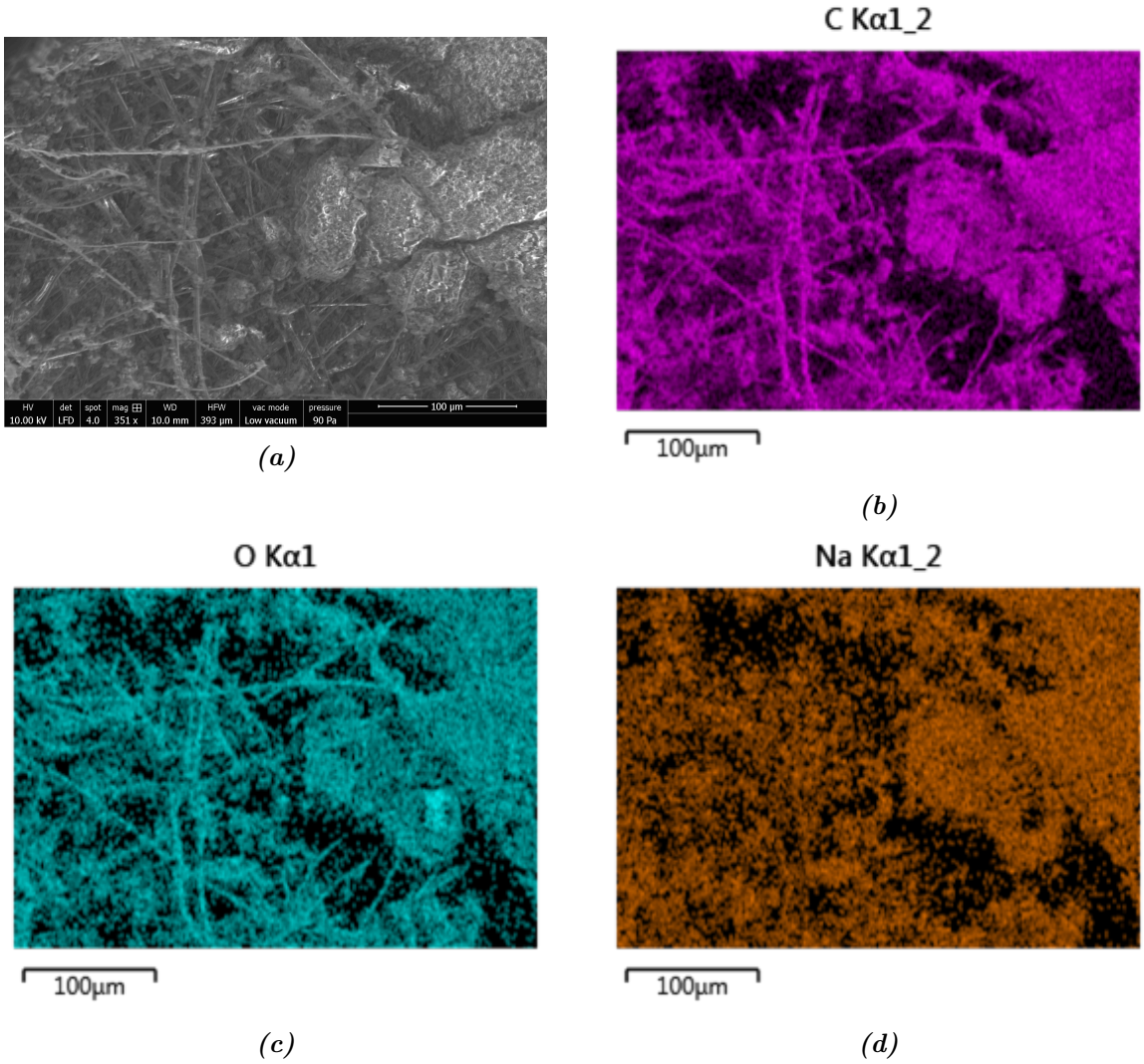
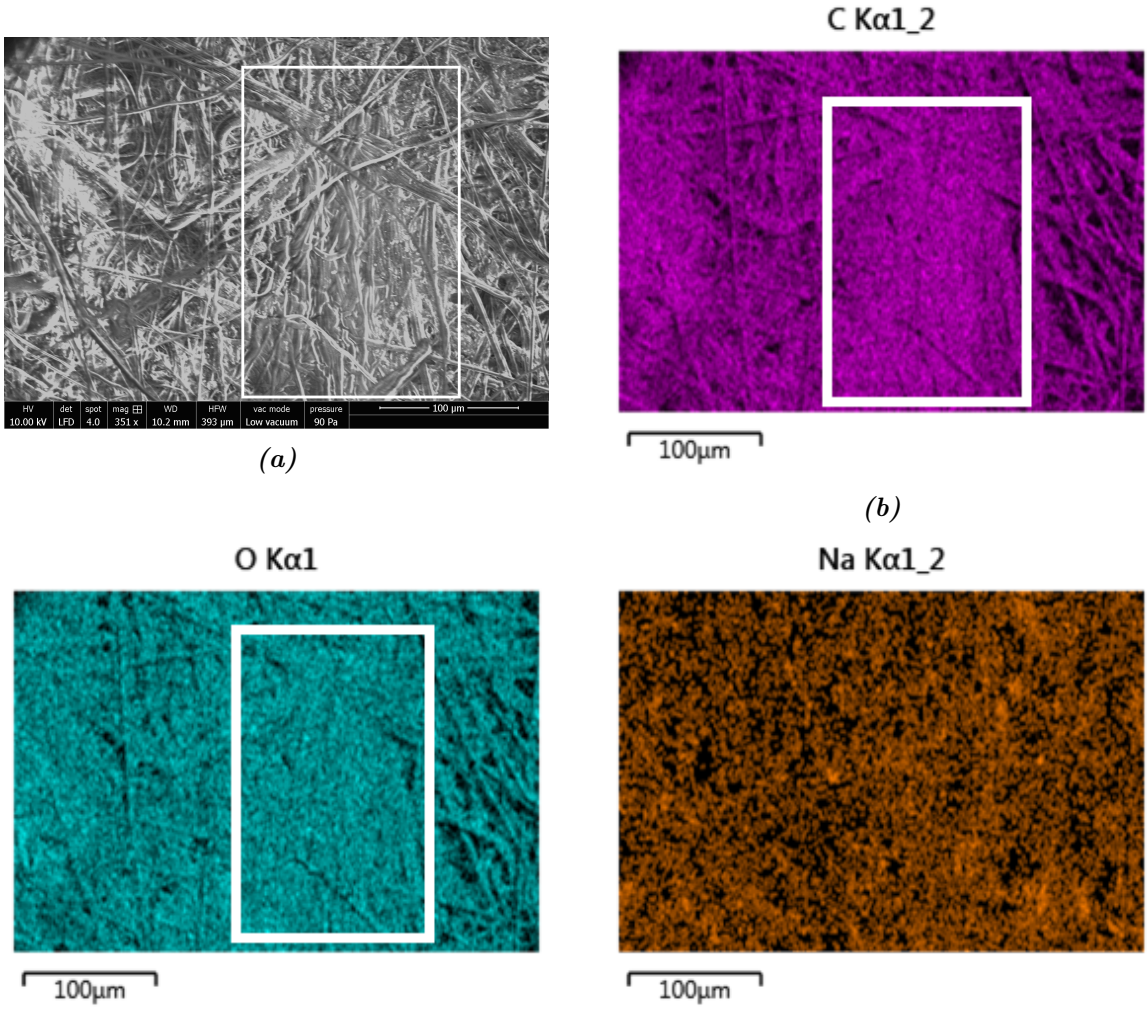


Figure 6.4: *From SEM analysis a a) secondary electron image of ETF 027. EDX analysis showed the b) carbon, c) oxygen, and d) sodium distribution on the filter.*

visible (Figure 6.4).

ETF 026 had some general distribution of sodium, however, there was no layer like coverage seen in ETF 022 and 027. A band of largely organic film is also seen localised in areas of less sodium density (Figure 6.5).



(a) *(b)* *(c)* *(d)*

Figure 6.5: *From SEM analysis a a) secondary electron image of ETF 026. EDX analysis showed the b) carbon, c) oxygen, and d) sodium distribution on the filter. Area of low sodium density highlighted.*

6.3 X-Ray Photoelectron Spectroscopy

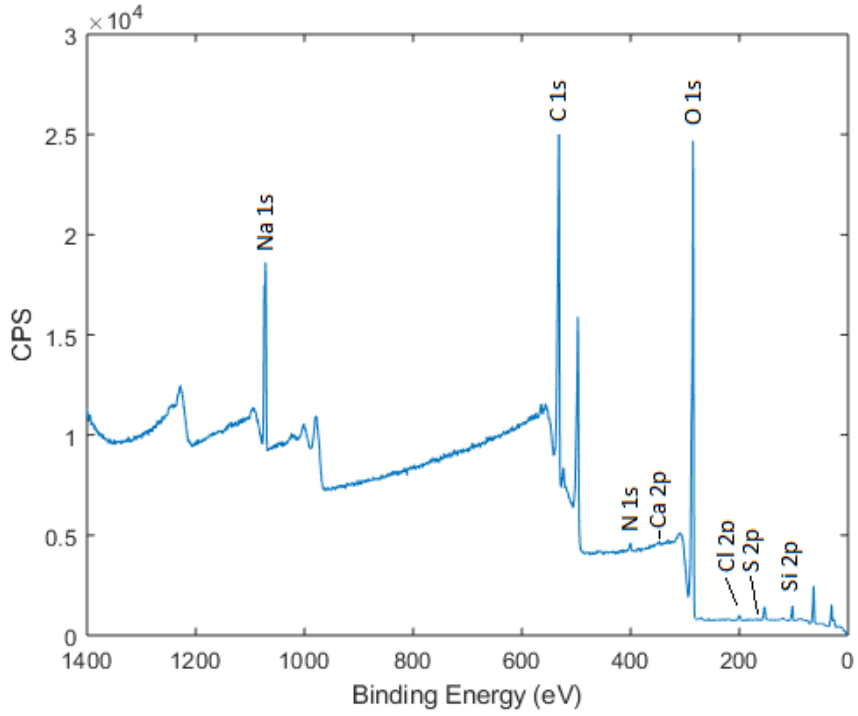
Using XPS survey spectra one can quantify atomic signatures from the sample. For each sample three points were analysed from the surface, the points were then summed to obtain average compositions as well as increasing the signal to noise ratio as described in Chapter 3.3.2. The average compositions of each sample and an example summed spectrum of ETF 026 is shown in Figure 6.6.

ETF 022, 26 and 027 had sodium atomic concentrations above 3.5 %At. Other samples, with the exception of ETF 020 (0.8 %At), were lower than 0.2 %At. The C:O ratio of the engine test filters, excluding ETF 023 and 026 (3.6 and 3.5), were greater (5.7-7.1) than the control filter CF 002, 4. In ETF 023 this is likely due to the increased concentration of silicon (8 %At). In ETF 026, however, the concentration of silicon was lower in comparison, around the same as ETF 024 and 025 (1-2 %At), so it is likely that the decrease in C:O is because of the sodium presence. In the high sodium containing filters the C:O ratios were 5.9, 3.5 and 5.7 (ETF 022, 026 and 027 respectively) suggesting that organic sodium structures on ETF 026 could be different to that on ETF 022 and ETF 027. N %At was greatest in the filters that were dosed with LMWT PIBSI, 2.9 and 1.6 %At for ETF 021 and 025 respectively. It is important to note that filters that had a detergent added, which commonly contain nitrogen species, also had an elevated N %At compared to CF 002, ETF 022 and 027 in which no detergent was used.

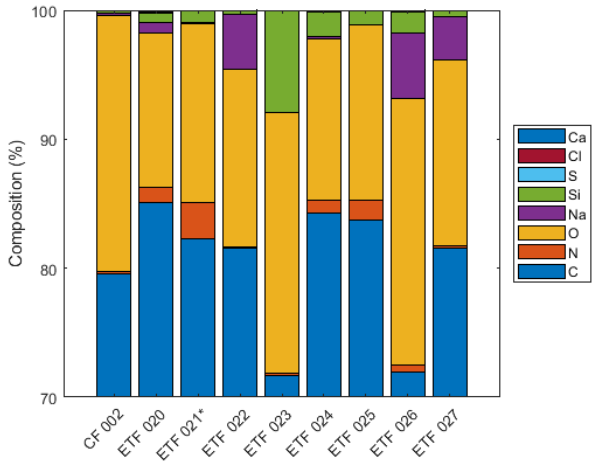
Alongside the quantification of elements through XPS survey spectra, it is also possible to analyse the C1s envelopes. This approach shows the possible bonding characteristics present on the samples. The refence C1s envelope of CF 002 can be found in Chapter 4.3. The line fittings were made with the characteristics described in the Methods (Chapter 3.3.2).

Table 6.2: *Binding energy ranges for the C1s components of ETFs and reference filter CF 002 (Chapter 4.3).*

	C-C	C-O	C=O	O-C=O	$\pi - \pi*$
B.E range (eV)	284.7 - 285.0	286.1 - 286.7	287.7 - 288.3	288 - 289.2	290.5 - 291.1



(a)



(b)

Figure 6.6: *a) Survey spectra of CF 003 including elemental regions and b) elemental compositions of reference filters from XPS survey spectra.*

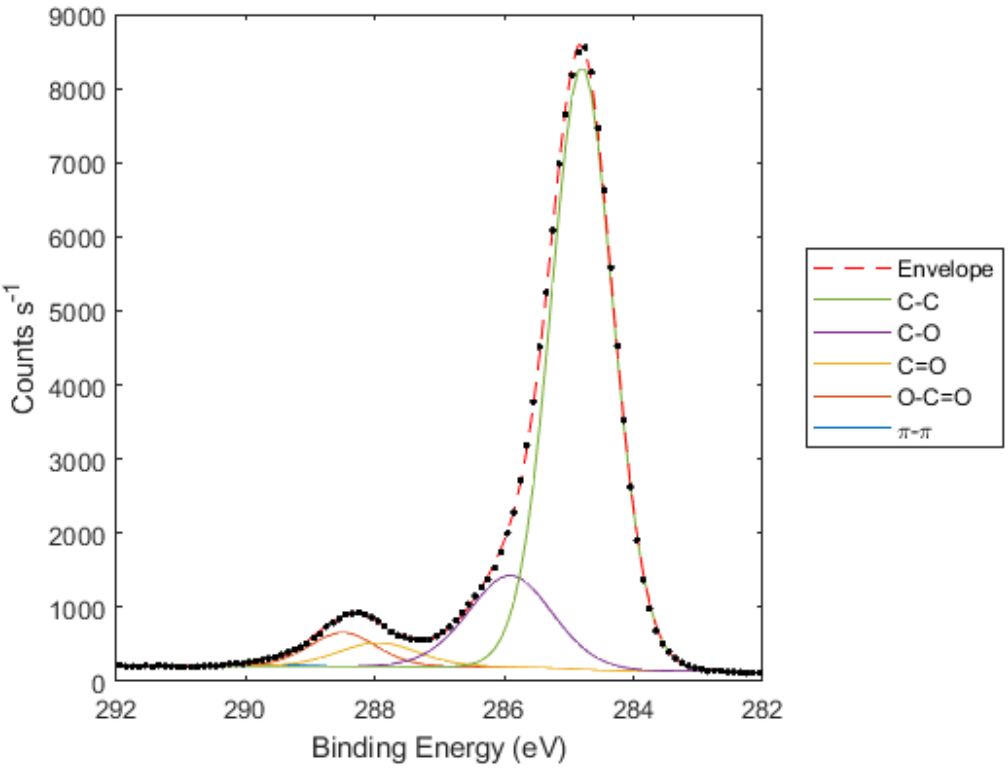


Figure 6.7: *High-resolution XPS spectra of the C1s region of ETF 027.*

In ETF 026 a "shake-up" peak at ∼290.50 eV (Figure 6.8) suggests the presence of an aromatic ring. No shake-up peaks were seen in any of the other ETFs. A peak at ∼287.70 eV is a result of a double bonded oxygen from a carbonyl group and was more prominent in ETF 026 In comparison to the other ETFs.

ETF 023 was the only sample which did not have a double bonded O peak from an acid at ∼289 eV (Figure 6.8). However, the C-O component of the C1s envelop was larger than other ETFs. The alcohol group bond generally represents a larger percentage area of the carbon to oxygen bonds in the C1s envelope compared to the other carbon to oxygen bonds. The exception to this is in ETF 022 and 027 the ratio of alcohol: acid is closer to 1:1.

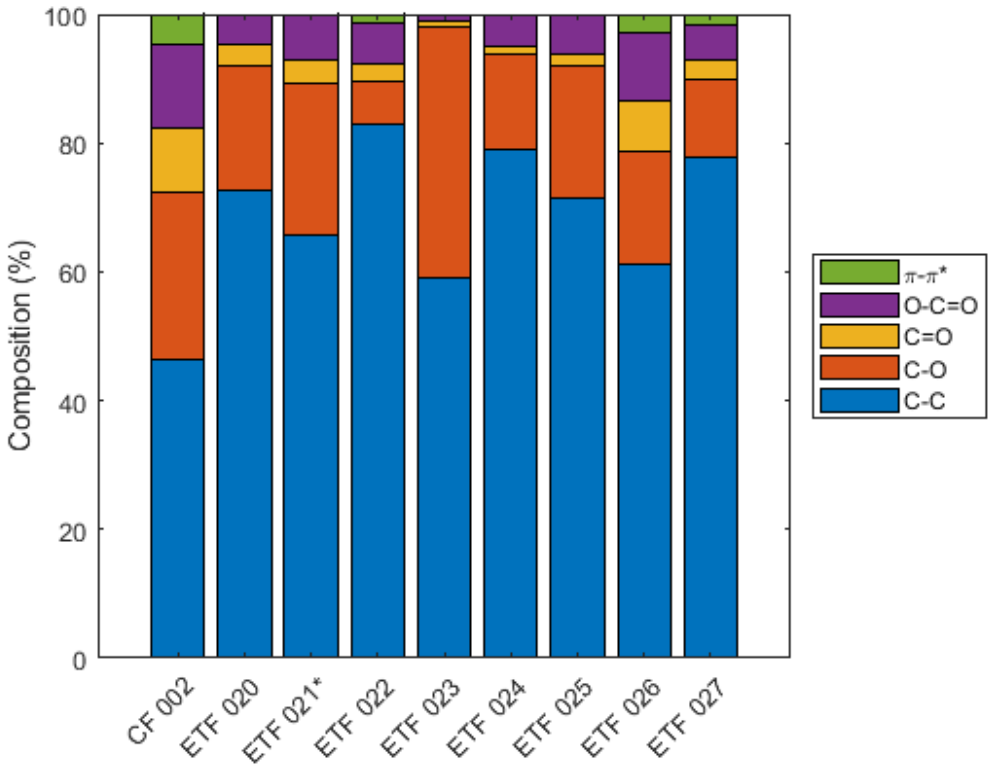


Figure 6.8: *Averaged compositions of the C1s envelopes for each of the ETFs and reference filter CF 002 (Chapter 4.3).*

6.4 Static Secondary Ion Mass Spectrometry

PCA is a commonly used for SIMS data analysis. The use of this statistical technique is to reduce the dimensionality of large datasets. Principal components (PC) are described by how much each mass effects it and the position on the scores plot is related to how the sample is described by the PC. As discussed in Chapter 3.4.1, two different areas (500 x 500 µm) of each filter surface were analysed using ToF-SIMS with a Bi_3^+ ion beam (LMIG). Using SL7 (IonToF GMBH) a list of around 200 peaks were collated using the peak search function for each ETF and CF 002, totalling 8 lists per polarity. Unique peaks from the lists were then combined to make a master list. The ion images were sectioned into 4 equal regions (ROI) to give a total of 8 unique areas (observations) per sample. The ion counts for each mass were normalised in respect to the total ion count for each ROI. The observations and peaks from the master list (variables) were then processed using PCA with the settings described in Chapter 3.4.2.

Figure 6.9 shows a scores plot generated from PCA alongside the loadings for PC1 and

Table 6.3: *Proposed formulas and their respective deviations of the peaks identified in the PC loadings of the ToF-SIMS data (Figure 6.9).*

ID	Suggested Formula	Deviation (ppm)	ID	Suggested Formula	Deviation (ppm)
1	Na	-28	6	$SiC_3H_9^+$	200
2	Na_2OH^+	-500	7	$Si_2C_5H_{15}O^+$	240
3	$CO_3Na_3^+$	207	8	$C_5H_{12}^+$	240
4	$C_3H_7^+$	-65	9	$C_2H_5O^+$	70
5	$C_3H_7O^+$	103			

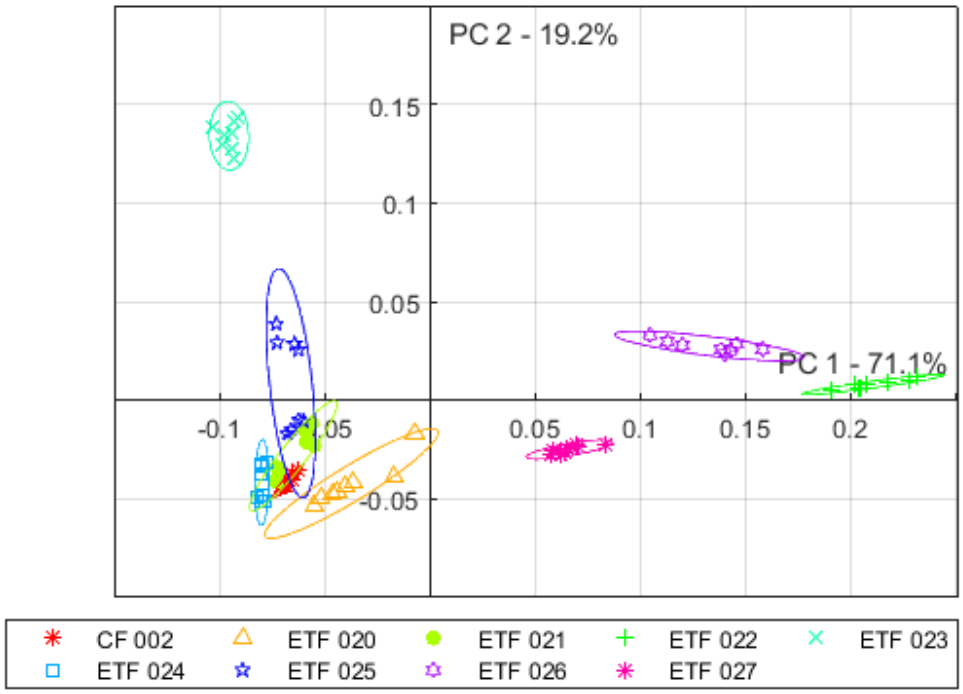
2. PC1 which accounted for 71 % of the total variance was largely dominated by sodium containing species (Table 6.3) in the positive direction. ETF 022, 026 and 027 were positively displaced for PC1. The presence of sodium containing species using ToF SIMS analysis has already been discussed in Spanu et al. (2018) for these specific filters. A combination of common polydimethylsiloxane (PDMS) peaks (Kala et al., 1997) alongside other organic ions were prominent in the negative PC1 direction.

Using PC2, which describes around 19 % of the variance, it is possible to deduce that ETF 023, which is positively displaced, has a high concentration of these PDMS peaks.

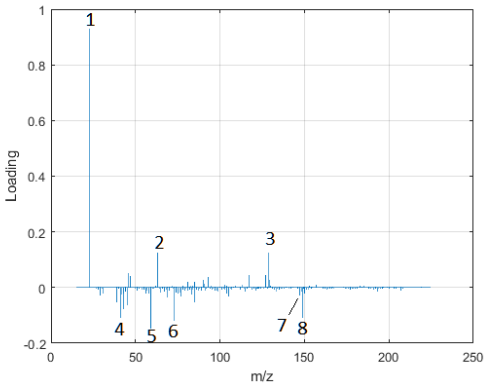
Normalising the specific ion images from delayed extraction mode with the ToF-SIMS data with respect to the total ion image, shows the distribution throughout the sample. In ETF 022 (Figure 6.10) the Na^+ ion was the dominant ion in the whole film like layer on the filter. Na_2OH^+ and $CO_3Na_3^+$ ions were also present in this film. Some of the intensity in this film was assigned to carbonaceous peaks $C_3H_7^+$ and $C_4H_9^+$ which is likely associated with the sodium species.

Analysis of the normalized ion images of $SiC_3H_9^+$ and $Si_2C_5H_{15}O^+$ (Figure 6.11) shows that the PDMS distribution covers all the filter fibres and there was no localised deposit. This is somewhat concurrent with the SEM-EDX analysis (Figure 6.2) although no localised concentration was seen in the ToF-SIMS ion image.

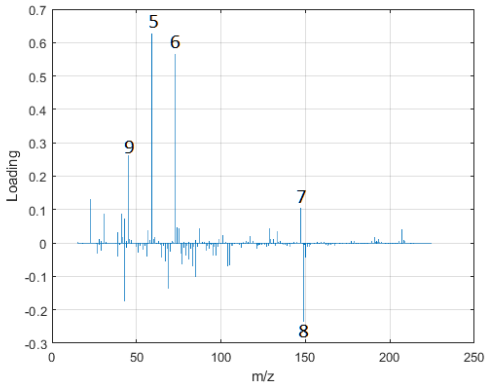
Although there was no film like layer on ETF 026, the normalised ion images of Na_+, Na_2OH^+ and $CO_3Na_3^+$ (Figure 16.12) showed a general distribution on and between the fibres which explains why ETF 026 was positively displaced in the PC1 direction (Figure 6.9), which was described by the aforementioned sodium associated ions.



(a)



(b)



(c)

Figure 6.9: *PCA analysis on the ToF-SIMS data of the ETFs and a reference filter, CF 002, showing the a) scores plot of PC 1 and 2. b) Loading for PC 1 and c) PC 2. Peaks identified are shown in Table 6.3*

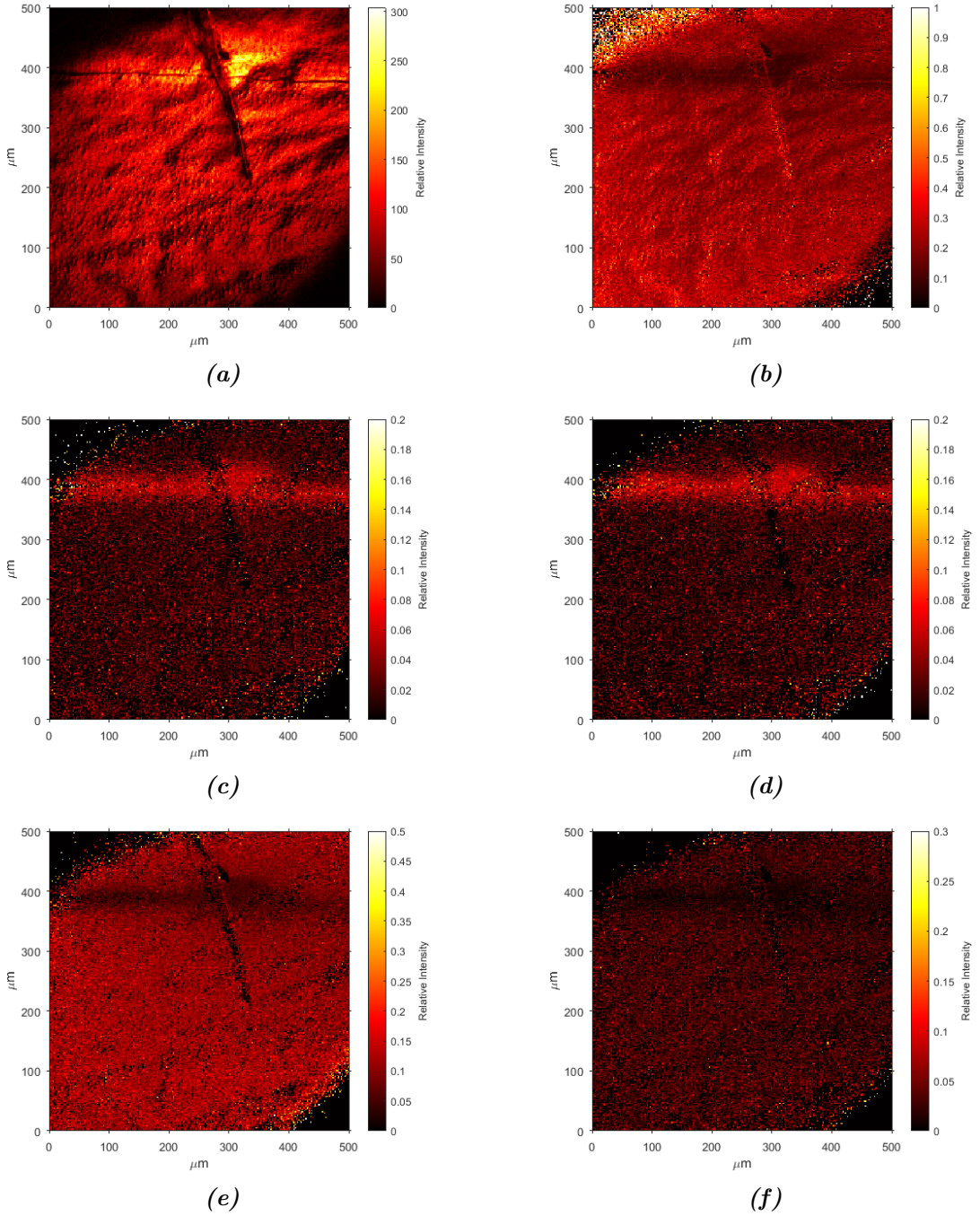


Figure 6.10: *Positive ToF-SIMS images of ETF 022 a) total ion and normalised b) Na^+, c) $C_3H_7^+$, d) $C_4H_9^+$, e) Na_2OH^+, and f) $CO_3Na_3^+$ ions using delayed extraction mode.*

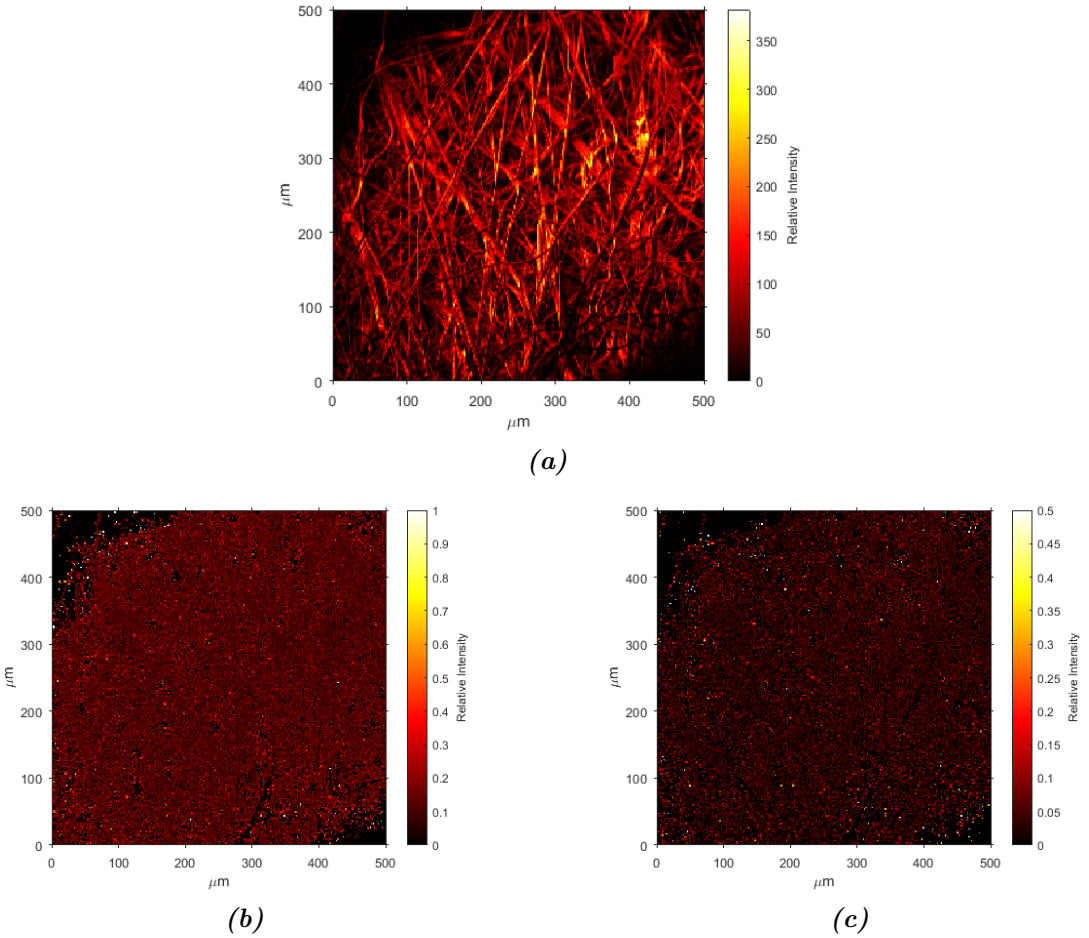


Figure 6.11: *Positive ToF-SIMS images of ETF 023 a) total ion and normalised b) $SiC_3H_9^+$, and c) $Si_2C_5H_{15}O^+$ ions using delayed extraction mode.*

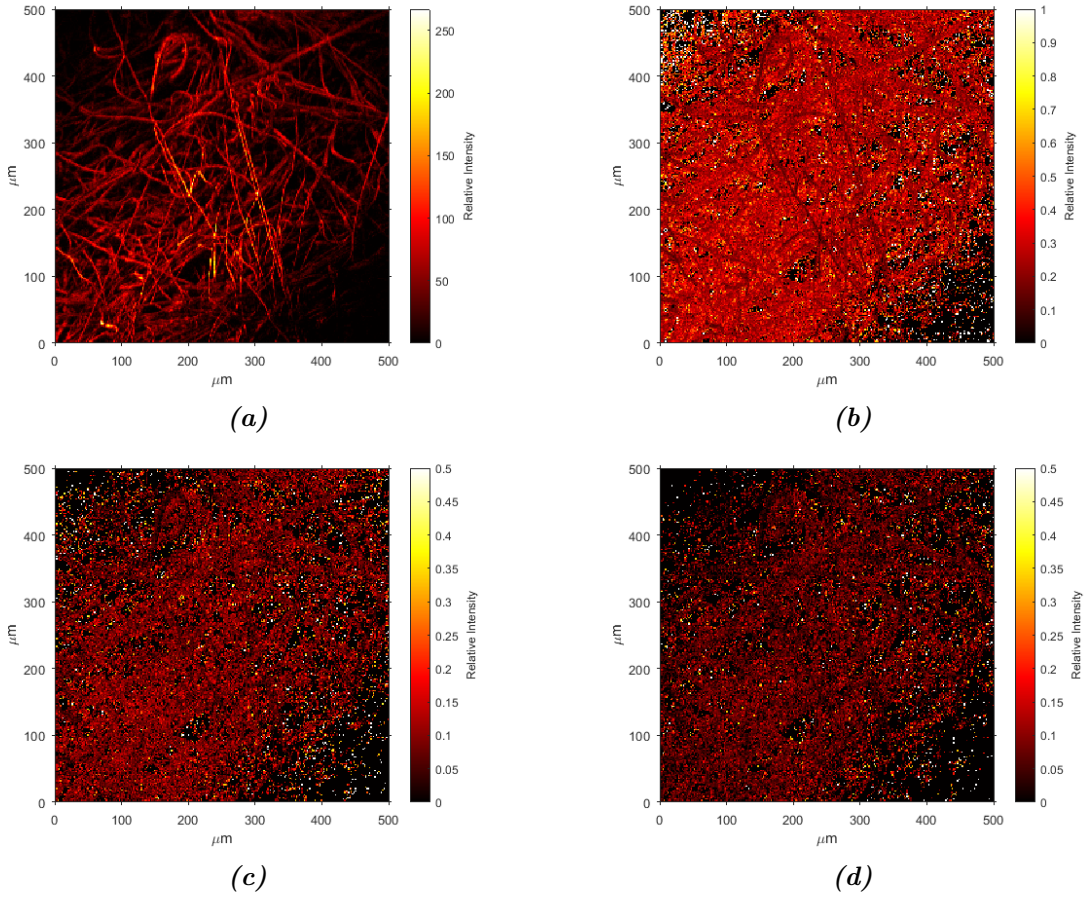


Figure 6.12: *Positive ToF-SIMS images of ETF 026 a) total ion and normalised b) Na^+, c) Na_2OH^+, and d) $CO_3Na_3^+$ ions using delayed extraction mode.*

As discussed, ETF 027 had a film like layer on covering the filter media. The sodium associated ions, Na+, Na2Oh+ and CO3Na3+ did not contribute to the intensity as much in ETF 027 (Figure 6.13) as in ETF 022 (Figure 6.10). This was due to more contribution from the carbonaceous $C_3H_7^+$ and $C_4H_9^+$ peaks, suggesting the presence of other carbonaceous species, longer carbonaceous chains in a sodium associated carbonaceous molecule, or both.

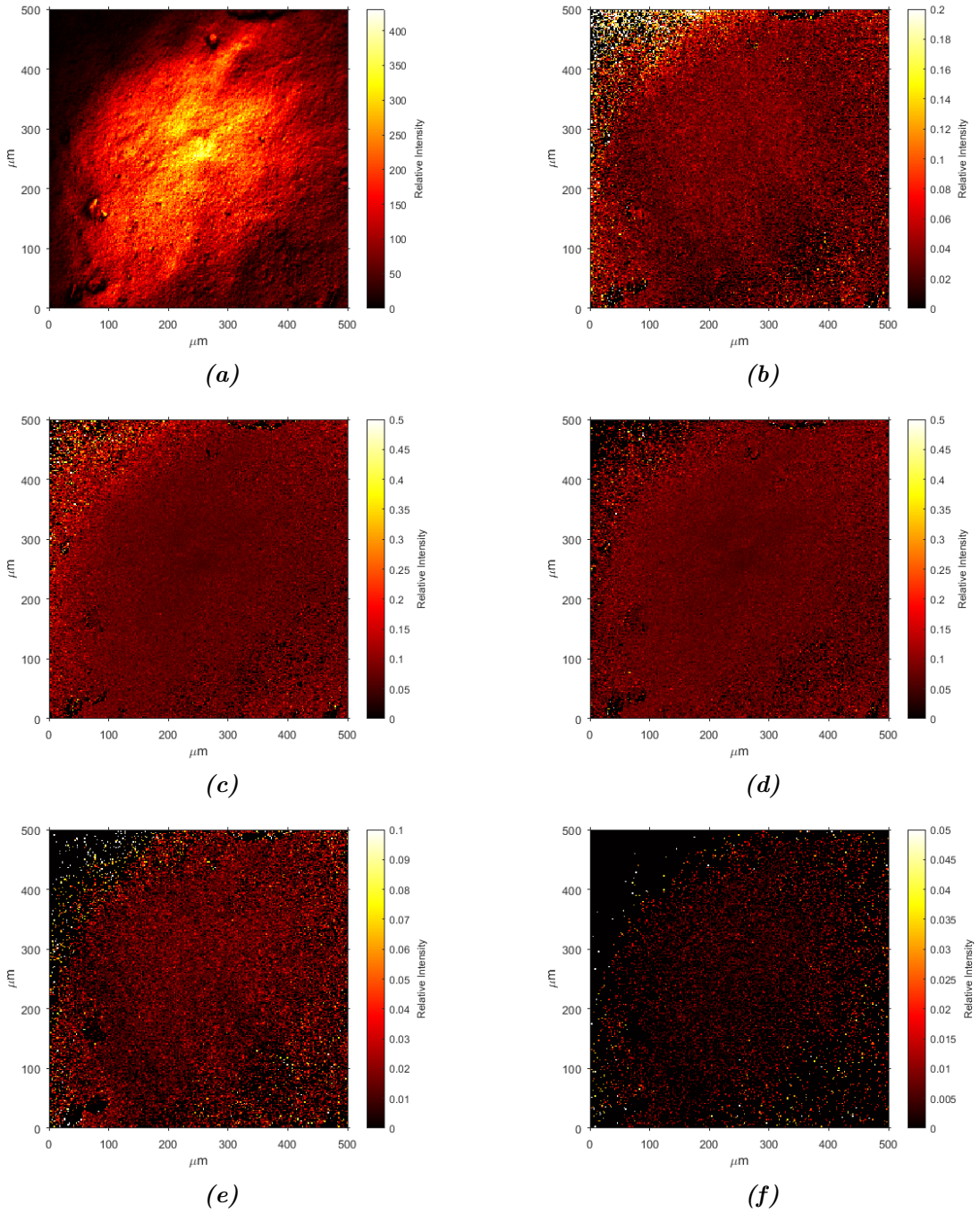


Figure 6.13: *Positive ToF-SIMS images of ETF 027 a) total ion and normalised b) Na^+, c) $C_3H_7^+$, d) $C_4H_9^+$, e) Na_2OH^+, and f) $CO_3Na_3^+$ ions using delayed extraction mode.*

6.5 GCIB Orbi-SIMS Analysis

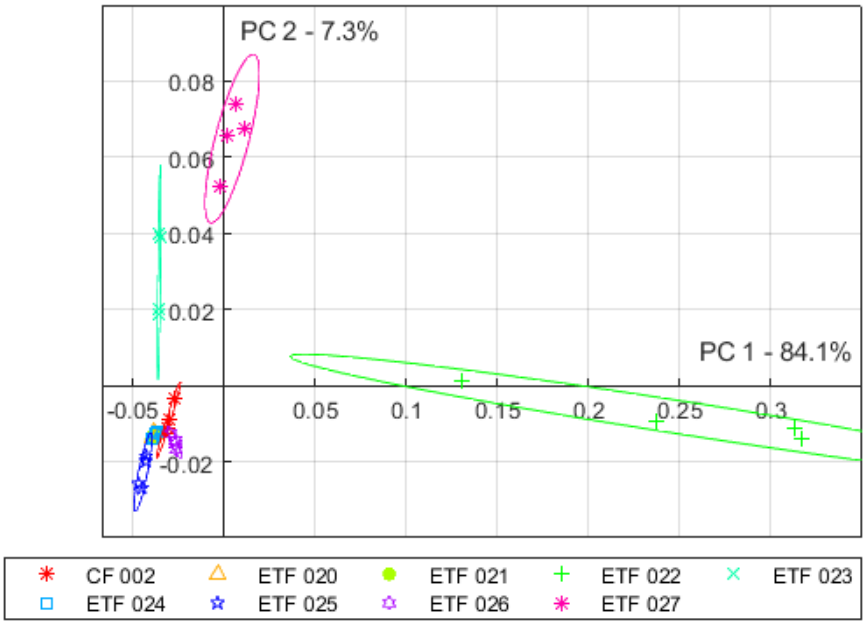
6.5.1 Static Secondary Ion Mass Spectrometry

As discussed, the use of the Orbitrap^{TM} analyser allows for much greater mass resolution as compared to the ToF-SIMS. As a result, it is possible to assign ions with more certainty than ever before. Due to the length of time it takes to complete one scan, only one area (400 x 400 µm) for both polarities was acquired. As discussed in the methods the positive polarity scan was over the same area as the first set of areas from the ToF-SIMS analysis and the negative polarity on the second set. The data pre-processing for PCA was mostly the same as with ToF-SIMS, however, the master peak list contained around 1000 peaks. The scores and loadings are shown in Figure 6.14. The large number of variables (mass peaks) which resulted in the loadings of PCA being more complicated to deconvolute.

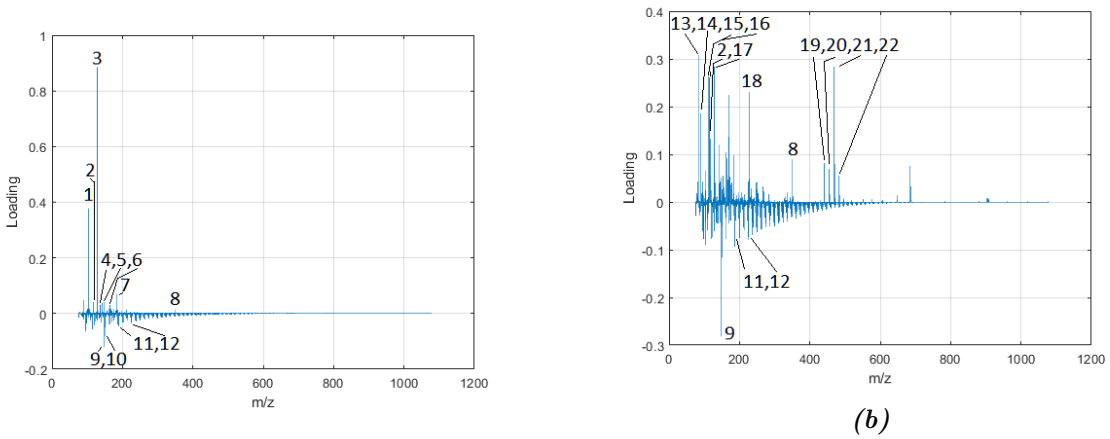
PC1, which explained 84 % of the variance, was dominated by organic and inorganic sodium ions.The Co3Na3+ ion was also present in the ToF-SIMS analysis. ETF 022 and 027 were positively displaced in the PC1 direction which is concurrent with the findings in the XPS surface compositions, where a contribution of above 3.5 %At. ETF 026, who's sodium concentration from the XPS analysis was also above 3.5 %At, was negatively displaced in the PC1 direction. This suggests that the sodium associated ions could be different.

Among the sodium ions in PC1 were two di-acid functionalities (7 and 8, Table 6.4). The suggested formula $[M+Na]^+$, is indicative of a di-sodium succinate and its parent ion fragment dodecenylsuccinic salt (DDS + 2Na) is shown in Figure 6.15. Due to their hydroscopic properties succinic compounds are commonly used to prevent corrosion in both gasoline and diesel engines (ATC, 2013).

The presence of DDS salt has been shown to be present in injector sticking (Barker et al. (2013); Schwab et al. (2010)). In the negative polarity ion analysis a $[M-H]^-$ ion of a single Sodium DDS salt ($C_{16}H_{26}O_4Na^-$) was present in high quantities in ETF 022 and 027 with trace amounts apparent in ETF 020 and 026. Using the 3D Orbi-SIMS, tandem MSMS (Passarelli et al., 2017) was completed on the head group ion (184.9795 m/z) confirming



(a)



(b)

Figure 6.14: *PCA analysis on the ToF-SIMS data of the ETFs and a reference filter, CF 002, showing the a) scores plot of PC 1 and 2. b) Loading for PC 1 and c) PC 2. Peaks identified are shown in Table 6.4.*

Table 6.4: *Proposed formulas and their respective deviations of the peaks identified in the PC loadings of the ToF-SIMS data (Figure 6.14).*

ID	Suggested Formula	Deviation (ppm)	ID	Suggested Formula	Deviation (ppm)
1	$Na_3H_2O_2^+$	1.6	13	$C_4H_7N_2^+$	3.9
2	$C_3H_3O_2Na_2^+$	0.1	14	$C_7H_7^+$	1.7
3	$CO_3Na_3^+$	-0.8	15	$C_6H_{11}N_2^+$	-0.7
5	$Na_3SO_3^+$	-0.5	16	$C_9H_7^+$	-0.2
6	$Na_3SO_4^+$	-0.5	17	$C_{10}H_8^+$	-1.2
7	$C_4H_4O_4Na_3^+$	-0.1	18	$Si_3C_4H_{15}O_5^+$	0.5
8	$C_{16}H_{26}O_4Na_3^+$	0.1	19	$C_{26}H_{42}O_4Na^+$	-0.8
9	$C_8H_5O^+$	-1.4	20	$C_{27}H_{44}O_4Na^+$	-1.8
10	$C_{12}H_8^+$	-1.6	21	$C_{28}H_{46}O_4Na^+$	0.6
11	$C_{15}H_9^+$	-1.5	22	$C_{29}H_{48}O_4Na^+$	0.5
12	$C_{18}H_{10}^+$	-0.4			

the assignment of $C_4H_4O_4Na_3^+$ through the presence of the peak at 62.9821 m/z, assigned as Na_2OH^+ (5.9 ppm) (Figure 6.15).

Di-sodium succinate ions were largely present in ETF 022 and 027 (Figure 6.16). They were also seen ETF 020 and ETF 026, however, as with CO_3Na^+, their normalised counts were 3 orders of magnitude smaller than in ETF 022 and 027. A detergent was added to ETF 020 and 026 (Table 6.1) indicating the effectiveness of removing/mitigating the build-up of the DDS salt.

The majority of the negative loadings for PC1 were organic compounds ($C_8H_5O^+$, $C_{12}H_8^+$, etc) that were present in also present in the reference filters. The presence of the sodium associated ions discussed in ETF 027 is high (Figure 6.16), but it is likely that the position on the scores plot in the PC1 direction is offset by the greater amount of some non-Na containing organic ions compared to ETF 022.

A variety of ions affected PC2, which explains 7% of the variance, in the positive direction. On trend with ToF-SIMS analysis, an organosilicon compound was in ETF 023, which was positively displaced in the PC2 direction. Although it does not follow the fragmentation pattern described by Kala et al. (1997), the Peak at 227.0223 m/z was given the assignment of $Si_3C_4H_{15}O_5^+$. It is possible that the different fragmentation pattern is a result of using a large gas cluster ion beam rather than a smaller cluster ion.

Tandem MSMS fragmented the ion into other Silicon containing ions, confirming the

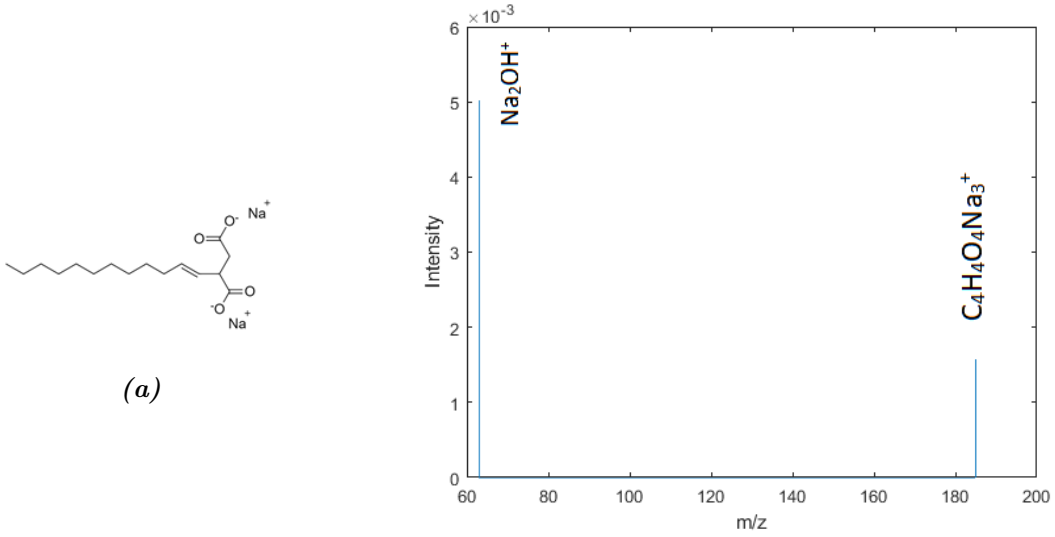


Figure 6.15: *a) Schematic of possible DDS salt and b) tandem MSMS spectrum of the $C_4H_4O_4Na_3^+$ ion in ETF 022.*

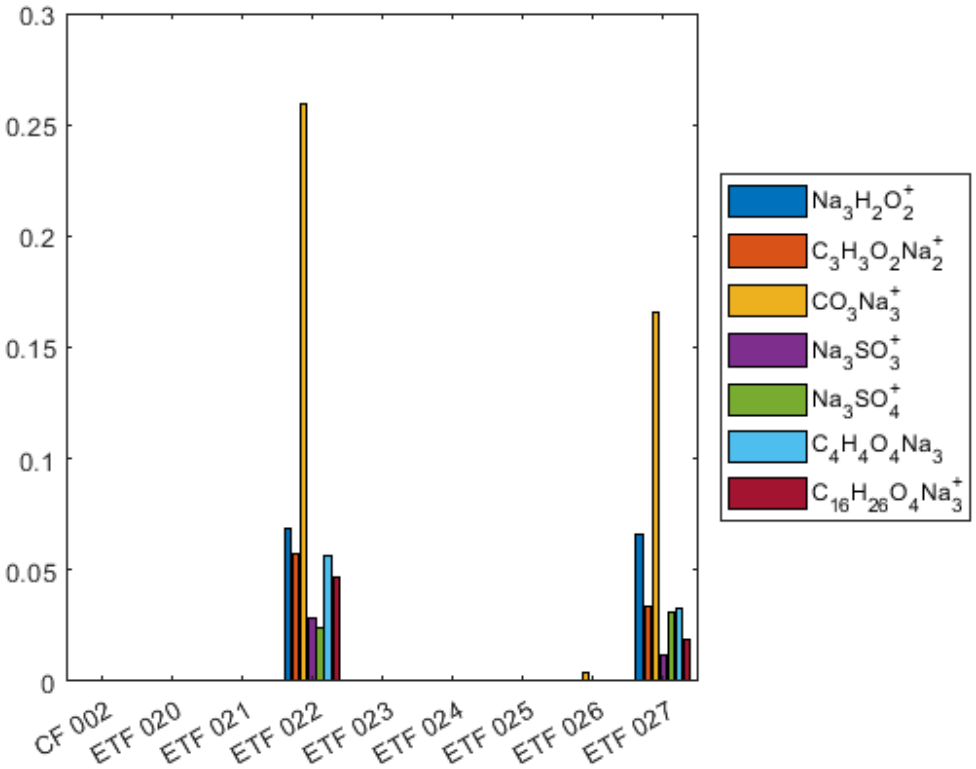


Figure 6.16: *Concentrations of sodium associated ions in ETFs and reference filter CF 002.*

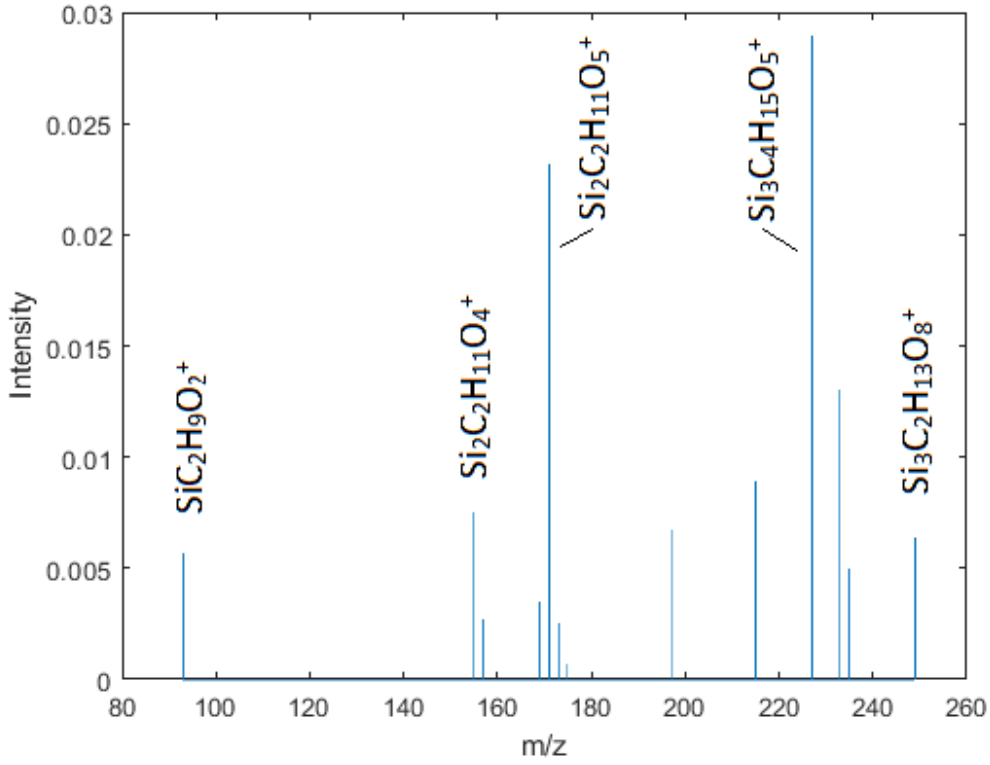


Figure 6.17: *Tandem MSMS spectrum of $Si_3C_4H_{15}O_5^+$ ion in ETF 023.*

assignment (Figure 6.171.17). It is important to note that the mass range that is chosen to analyse the ion also encapsulates $C_{18}H_{11}^+$, which was also present in ETF 023, as they have a similar mass (+ 0.063 m/z). The fragmentation peaks of the $C_{18}H_{11}^+$ are easy to distinguish and have been removed for clarity.

At higher mass of the PC2 loading a group of high mass organic molecules denoted 19-22 in Table 6.4. The putative formulas, $(C_nH_{2n-8}(COOH)_2Na)^+$, imply the presence of an aromatic dimer acid, which is thought to be added as a lubricity additive to ETF 027. It is likely that the sodium is an adduct to the ion as there is only one sodium attached with two acid groups available. This series of acids were largely present in ETF 027 and a small amount was seen in ETF 020 (Figure 6.18). It is possible that the presence of these ions could explain the higher intensity of carbonaceous ions ($C_3H_7^+$ and $C_4H_9^+$) seen in the ToF-SIMS ion image analysis of ETF 027 (Figure 6.13) compared to ETF 022.

Alkylbenzene sulphonates (ABS), a lubricant additive, has been shown to deposit on FIE and filters by the University of Nottingham group (Edney et al., 2020a) in diesel and gasoline engines. It was postulated that the presence of the negative ABS ion in the filter

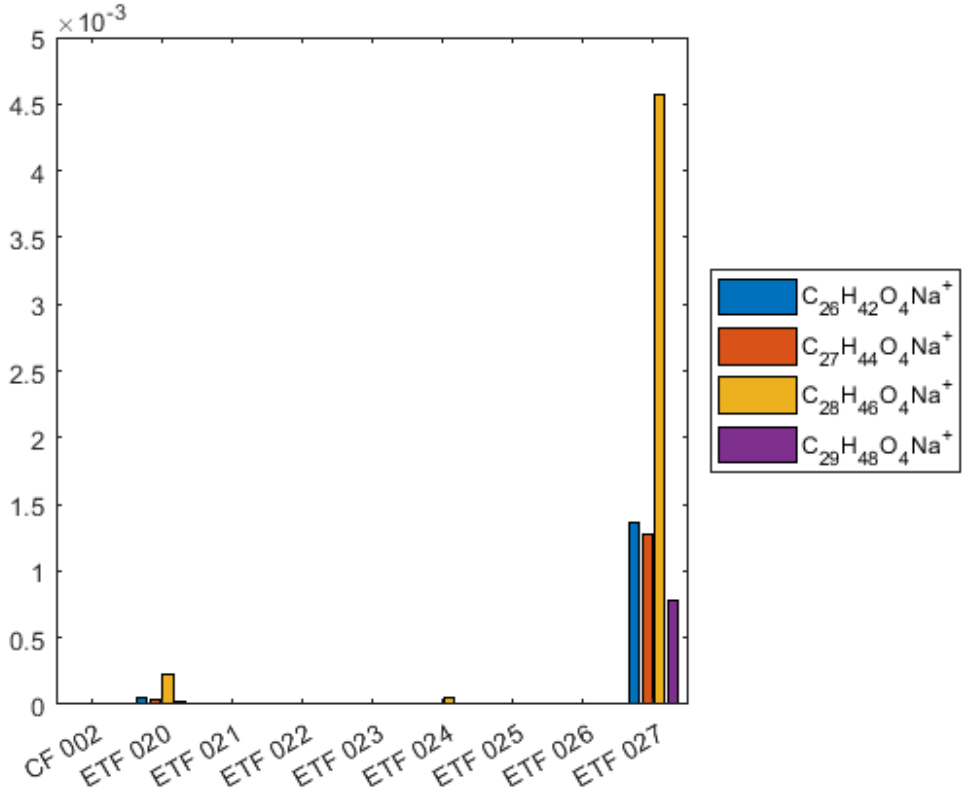


Figure 6.18: *Concentrations of di-acid ions in ETFs and reference filter CF 002.*

deposit is a result of recirculation of contaminated fuel from the injectors.

A list of around 7000 peak positions was created for each sample and polarity. The compound_finder script was used to find other related ion fragments containing the sulfonate, with number of sulfur and oxygen were constrained to 1 and 3 respectively. For each mass in the list, possible combinations of ions also containing carbon and hydrogen with a deviation of less than 2.5 ppm were calculated. 5 interesting fragmentation peaks containing a sulfonate were outputted and are shown in Figure 6.19.

Work by the University of Nottingham group (Lamb et al., 2021) used the tandem MSMS functionality of the 3D Orbi-SIMS to confirmed the composition assignment of the $C_8H_7SO_3^-$ (183.0123 m/z, 0.9 ppm deviation) ion which fragments into $C_8H_7O^-$ and SO_3^- ions. A series of sulfonated aromatic structures were present (C17-C19) at higher masses alongside the high mass ABS (C18) assigned in Edney et al. (2020a) with deviations of under 2 ppm. This ABS series was present in large amounts in ETF 023, 024 and 025 (Figure 6.19). Small amounts of the lowest mass ion fragment ($C_8H_7SO_3^-$) was also seen across all samples and in CF 002, suggesting that small amounts could also be

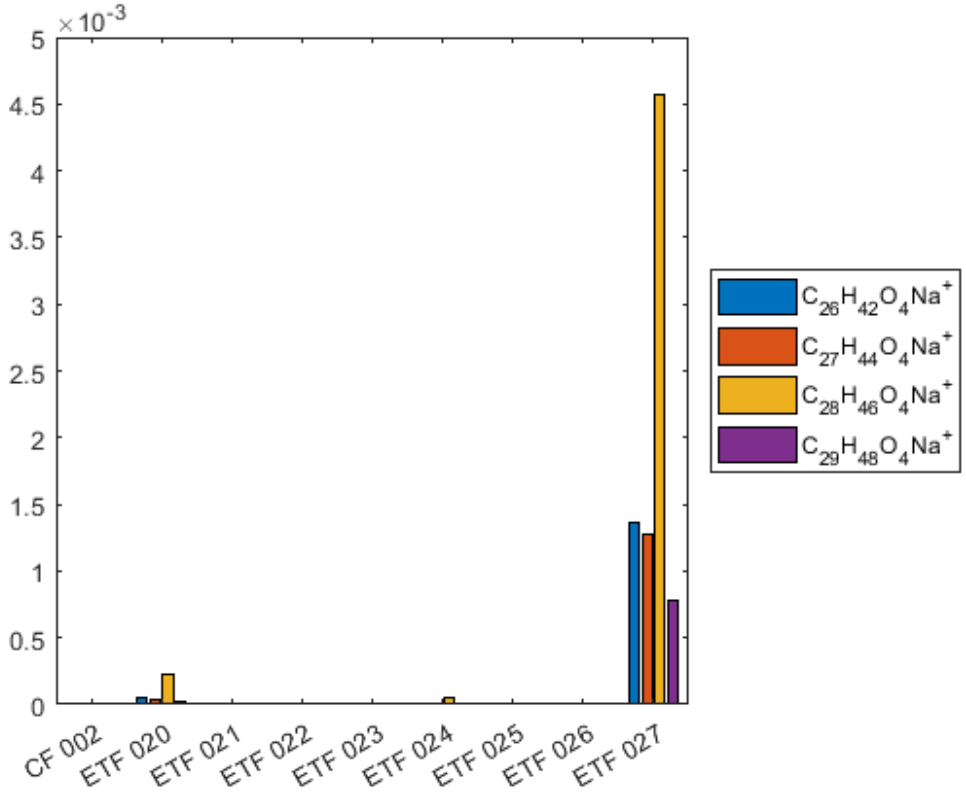


Figure 6.19: *Concentrations of ABS ions in ETFs and reference filter CF 002.*

a result of contamination. ABS is commonly used in lubricant oils as a detergent due to its head group's affinity to metal surface and hydrocarbon tail which allows for fuel solubility (ATC, 2013). Calcium is commonly used as the counter ion for ABS. Calcium hydroxide ions were found in ETF 024 and ETF 027, however, only trace amounts were found in ETF 023 and ETF 025 which had high amounts of ABS.

6.5.2 Dynamic Secondary Ion Mass Spectrometry

Dynamic SIMS or depth profiling is another technique that offers great insight into the structure of deposits. The first statistical method employed was to use NNMF, a common MVA technique used to analyse depth profiles. Selected "interesting" peaks from the static SIMS analysis and NNMF were then chosen to see how their intensity changed as the GCIB beam sputtered the sample's surface. The intensities were point-to-point normalised against the total ion as described in methods 3.4.1. NNMF produces two matrices, W and H which when multiplied are roughly equal to the original matrix. H is

Table 6.5: *Proposed formula for peaks identified in Figure 6.20*

ID	Suggested Formula	Deviation
		(ppm)
1	Na_2Cl^+	0.8
2	$Na_2{}^{37}Cl^+$	1
3	$CO_3Na_3{}^+$	-0.8

used to describe the profile and W is a column vector of the contribution of intensities of each mass.

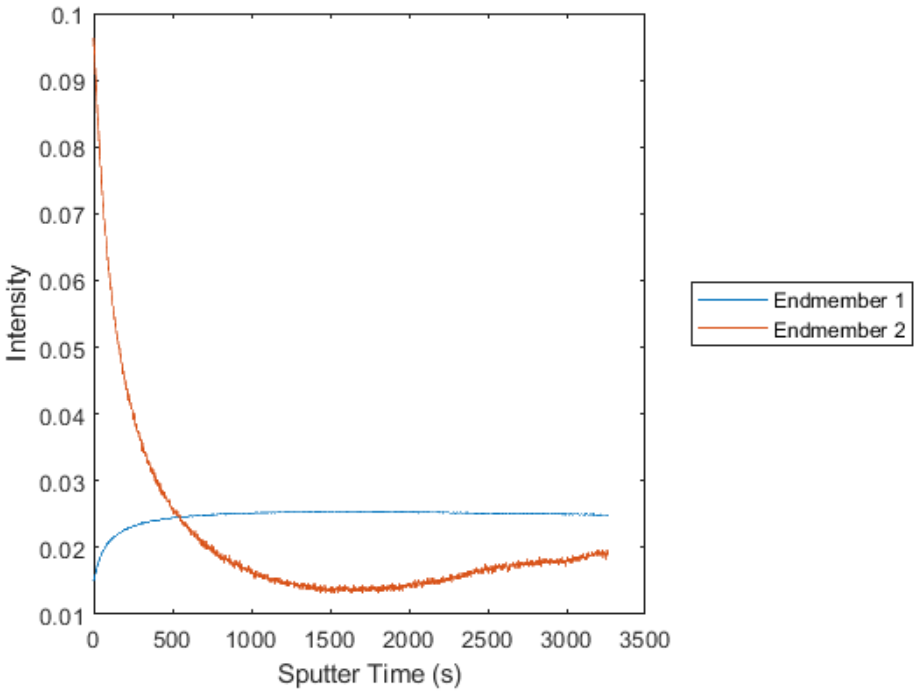
Apart from ETF 022 and ETF 027, NNMF showed that there were two general profiles seen in the samples. A representative of these profiles are shown by the two endmember plots in Figure 6.20 curated from NNMF of the positive ion depth profile on ETF 026. The NNMF plot shows the general trend of each endmember and the endmember loadings plot show how much each ion contributes to the NNMF scores plot.

The concentration of sodium organic ion film in ETF 022 dominated the spectra throughout. Endmember 1 represents the $C_xH_y{}^+$ and $C_xH_yO_z{}^+$ markers of the filter media that increases in intensity as the sputter time increases while Endmember 2 represents sodium chloride and $CO_3Na_3{}^+$ ions whose concentration decreased with depth.

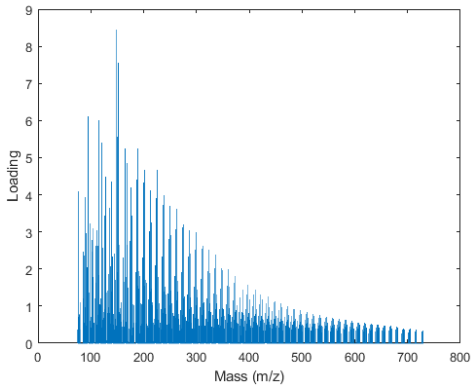
Figure 6.21 shows the positive ion depth profile of ETF 022. Trend analysis on $CO_3Na_3{}^+$, $C_3H_3O_2Na^+$and $C_4H_4O_4Na^+$ ions would suggest that the $CO_3Na_3{}^+$ may not be a suitable marker for the latter two ions. Whilst there was an initial increase in the $CO_3Na_3{}^+$ ion within the first minute of sputtering followed by a steady decrease which led to a plateau, the other two ions initially decreased and remained constant earlier on in the experiment. Pattern analysis can confirm that the $C_{16}H_{26}O_4Na_3{}^+$ ion is a parent ion to $C_3H_3O_2Na^+$and $C_4H_4O_4Na^+$ ions as they followed the same relative intensities throughout. A similar relationship between the ions was seen in ETF 027 (Figure 6.23).

Depth profiling also shows that the sodium containing layer that covered ETF 022 seen with the SEM-EDX analysis (Figure 6.3), is relatively thick and covers the filter fibres as there is no increase in the intensity of the $C_{12}H_9O^+$ ion, a prominent marker for the cellulose (Chapter 4.4).

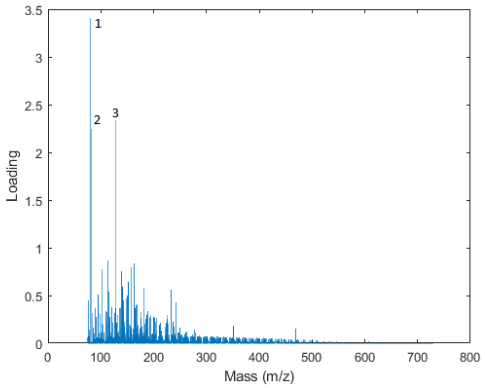
In Figure 6.21 three distinct composition profiles can be seen, an initial contamination



(a)



(b)



(c)

Figure 6.20: *a) NNMF plot of two endmembers that describe the different layers seen in ETF 026, b) the m/z coefficients that define endmember 1, and c) the m/z coefficients that define endmember 2. Proposed formula of the identified peaks are shown in Table 6.5.*

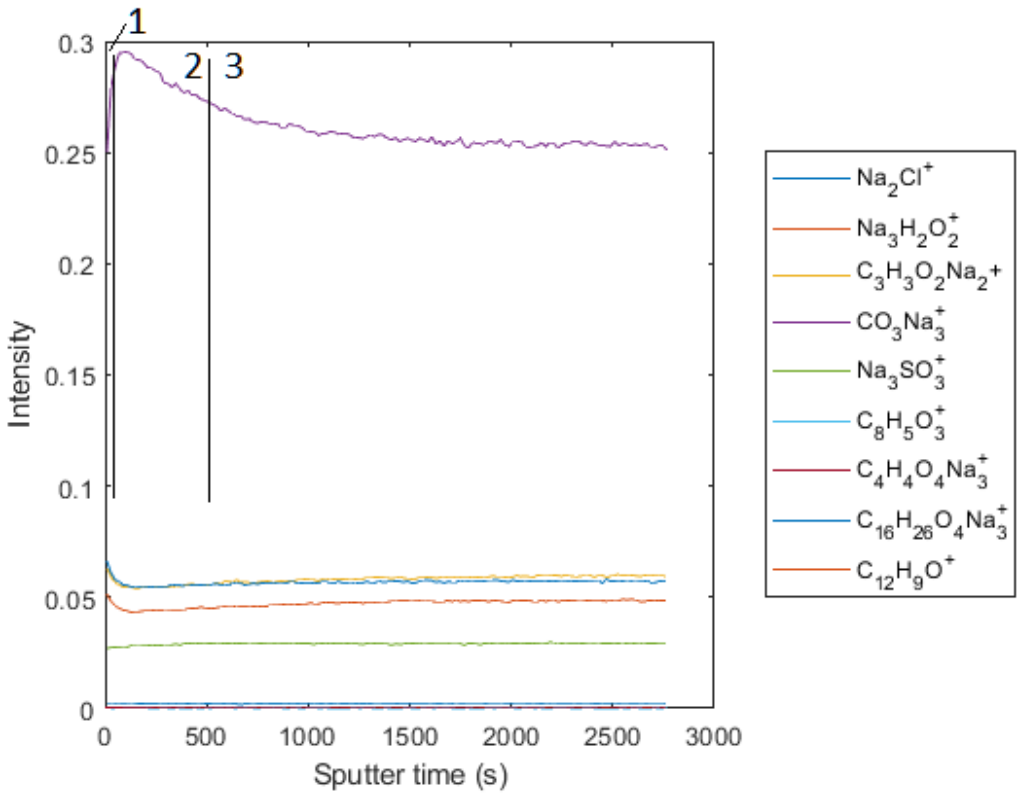


Figure 6.21: *Depth profile of selected positive ion peaks in ETF 022 using 3D Orbi-SIMS.*

layer consisting of DDS salt ions and fragmentations ($C_{16}H_{26}O_4Na_3^+$, $C_3H_3O_2Na_2^+$ and $C_4H_4O_4Na_3^+$ respectively). In the second section the sodium carbonate which initially increased in intensity started decreased and eventually plateaued to mark a third concentration profile.

In ETF 026 (Figure 6.22), some sodium chloride and its isotope were seen at the start of the depth profile, but decreased at a similar rate to the $CO_3Na_3^+$ ion. Meanwhile the cellulose marker increased and plateaued early in the run.

In ETF 027, NNMF showed that there were three major concentration change profiles as a function of depth. An initial contamination which contained cyclical nitrogen compounds and the dimer acid ion series (discussed earlier in this chapter) which decreased at an inverse exponential rate. The next profile showed that after an initial increase, sodium chloride and its isotope ions decreased in concentration as a function of sputter time (6.23). The third profile followed the $CO_3Na_3^+$ ion, which increased at a greater rate than the the di-acid markers. Again, suggesting that $CO_3Na_3^+$ may not be a suitable marker for DDS salt.

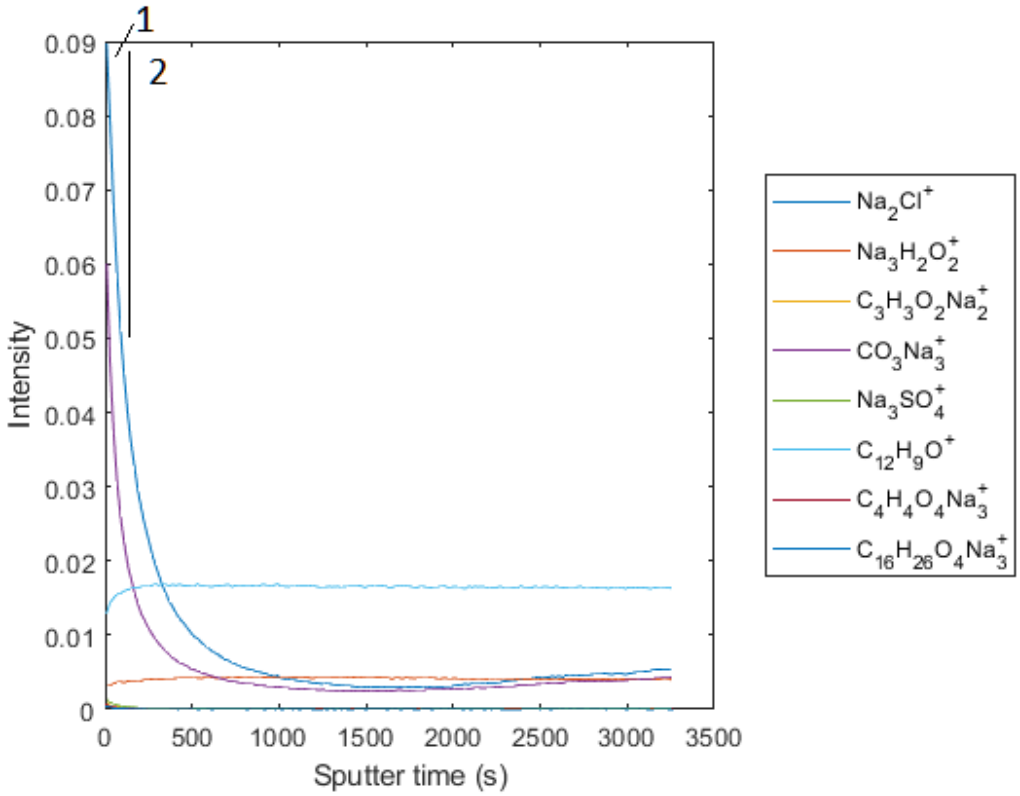


Figure 6.22: *Depth profile of selected positive ion peaks in ETF 026 using 3D Orbi-SIMS.*

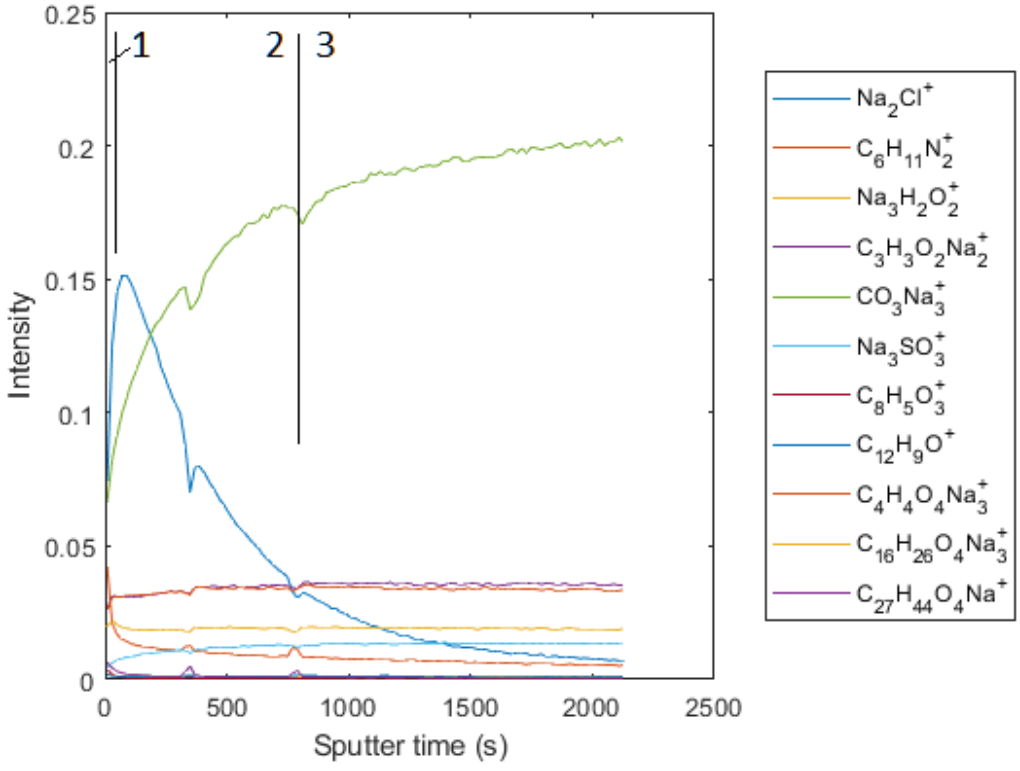


Figure 6.23: *Depth profile of selected positive ion peaks in ETF 027 using 3D Orbi-SIMS.*

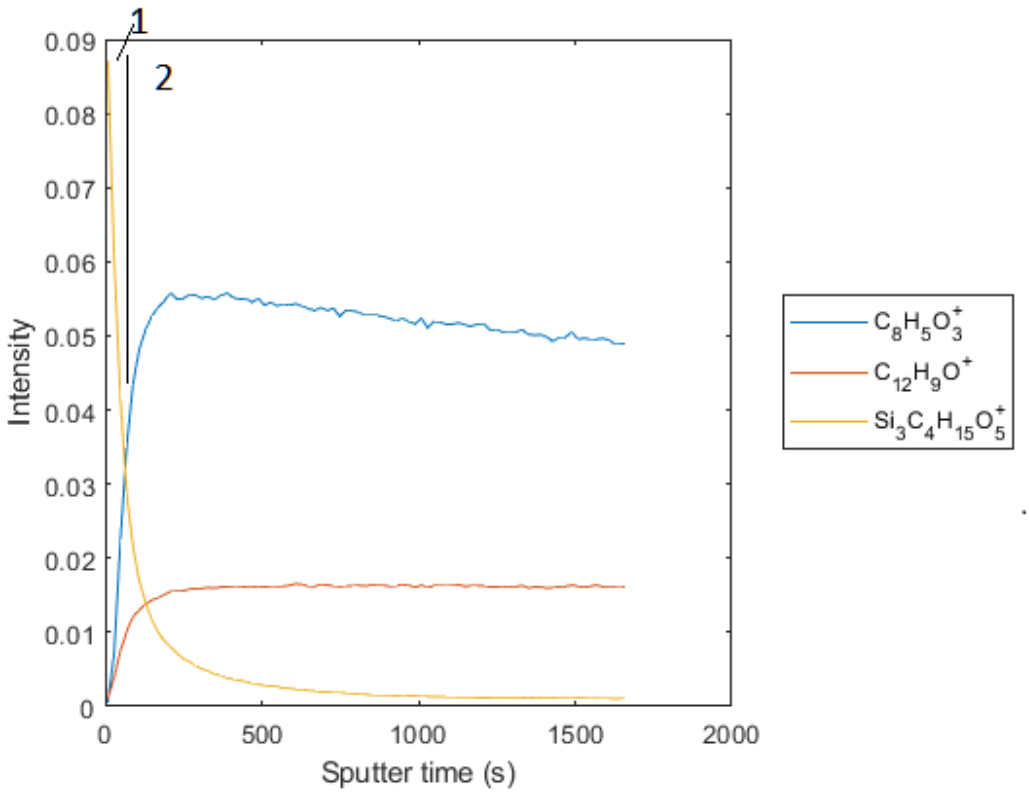


Figure 6.24: *Depth profile of selected positive ion peaks in ETF 023 using 3D Orbi-SIMS.*

The organosilicon component that was seen in the positive ion static SIMS analysis of ETF 023 decreased with sputter time (Figure 6.24). The increase in cellulose marker intensity over the same period suggests that the silicone is only present at the surface of the filter.

In the negative ion depth profiles of ETF 023, 024 and 025 the series of ABS ions all followed the same trend as shown in ETF 025 (Figure 6.25). They had a strong intensity at the surface but decreased rapidly whilst markers for the cellulose ($C_8H_5O_4^-$) remained steady throughout.

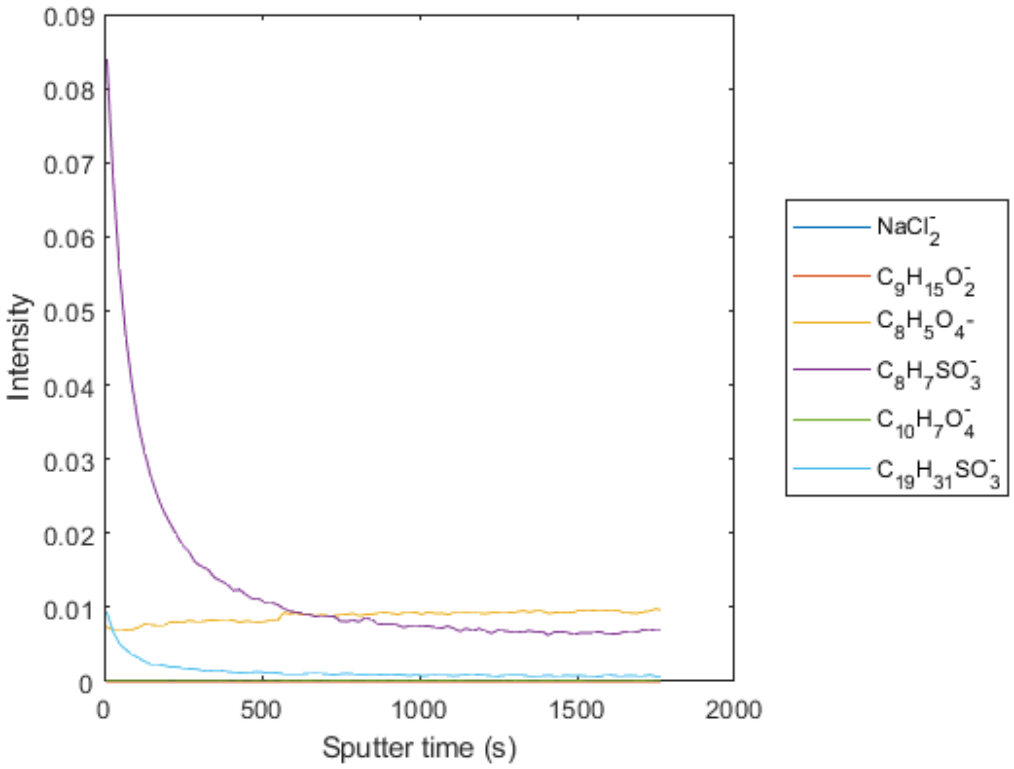


Figure 6.25: *Depth profile of selected negative ion peaks in ETF 025 using 3D Orbi-SIMS.*

6.6 Discussion

The morphology of the sodium species that was present on the surface of ETF 026 is visibly different to the layer like film that was present in ETF 022 and 027. Due to the high fragmentation of ToF-SIMS, it was not possible to distinguish the difference between these three filters. 3D Orbi-SIMS, however, showed that much of the higher mass sodium containing ions, such as $C_{16}H_{26}O_4Na_3^+$, were not present in ETF 026. SEM analysis also showed that there were some structures of localised deposit that were found in filter ETF 023. EDX analysis indicated that this was a heterogeneous structure, made up of silicone and oxygen contained by sulfur, sodium and chlorine elements.

In ETF 023 it was shown using delayed extraction and high spatial resolution ion imaging that the PDMS ions covered the filter fibres and no particle like deposit, seen in the SEM-EDX, was present. Sodium covered filters ETF 022 and 027 with a film like layer but in ETF 026 the sodium was only present on the filter fibres suggesting either a different composition or a precursor to the sodium film.

PCA analysis was initially used to identify key variances in the filter samples where the first two PCs represented ∼91 % of the variance. PC1 was largely dominated by sodium containing ions, but the inclusion of higher mass sodium containing ions meant that ETF 026 was no longer positively displaced in the PC1 direction compared to the PCA analysis of the ToF-SIMS data. The assignments of the higher mass sodium containing ions were DDS salt and its fragmentation ions. DDSA is added diesel fuel to mitigate corrosion. In this work we have shown that the formation of a layer like sodium containing film is likely a result of the interaction between the DDSA and a sodium source that was added as a contaminant in the engine test. The inclusion of a detergent has shown to largely decrease the presence of these salts, but, in the case of ETF 026, it does not remove all traces of organic sodium ions.

In ETF 027, a series of aromatic dimer acid ions containing sodium were identified. Comparison to other sodium containing ions ($CO_3Na_3^+$, $C_3H_3O_2Na^+$and $C_4H_4O_4Na^+$) suggested the adduct pattern followed $[M+Na]^+$. It is assumed that the ion was not a salt but rather an aromatic dimer acid ion with a sodium adduct. Through depth profile analysis the dimer acid ions were shown to be present at the surface and in the bulk of the filter deposit. Sodium chloride and cyclical nitrogen structures, seen in the static SIMS, were shown to be surface contamination. ABS ions were shown characterised for the first time in filters and shown to be largely present at the surface of the deposit but also entrained throughout the filter.

As expected, the samples with a film like layer had the highest sodium concentration. The presence of carbon and oxygen also indicated that the layer was organic associated with sodium. It also confirmed that although the detergent mitigated the build-up of an organic film, there was still a large amount of sodium left on the filter fibres. The 1:1 ratio of the C-O to O-C=O peak areas in ETF 022 and 027 in the analysis of the C1s envelope, showed that the organic film likely only contained carboxylate groups. The presence of these salts has largely been hypothesised in literature (Barker et al. (2020); Lacey et al. (2012); Schwab et al. (2010); Csontos et al. (2019)). Deconvolution of the C1s envelope can be challenging if used as an exploratory technique rather than confirmation. It would

also be difficult to decipher between mono-acid and di-acid groups. ETF 023, which was shown in ToF-SIMS and 3D Orbi-SIMS to have prominent of PDMS ions, had the highest amount of silicon concentration .

6.7 Conclusions

Presented in this chapter were four different techniques that were applied for the characterisation of deposits on diesel engine test filters. Engine tests allow specific fuel contaminants and additives to be tested to remove as many external factors as possible that could obscure the data. These tests are therefore extremely useful for deposit analysis.
Filters that were exposed to fuel with the highest sodium concentrations formed a film like layer on the surface of the filter which appeared to block the pores. The use of XPS and Orbi-SIMS analysis was used to confirm the saturation of carboxylate-sodium salt ions, which largely follows literature.
The Orbi-SIMS depth profiles show that the surface of these samples can vary drastically to the chemistry below. This may be a limitation to surface characterising techniques where the initial surface contamination on the samples is not removed prior to analysis.

Chapter 7

Field Samples

7.1 Introduction

In this chapter, three diesel fuel filters from different locations around the world have been analysed using the analytical techniques used in the previous chapters. Prior chapters have relied on contaminating fuel filters from one or two known sources which allows the minimisation of possible sources of contaminants. In contrast, fuel filters from the field see a variety of different fuel sources as well as external environmental conditions adding to the complexity of the deposits.

Whereas previous chapters have provided a statistical approach to analysing the deposits on filtration samples, here a more investigative approach is tried. The focus of this chapter was to compare the differences in deposits on diesel fuel filters from the field. The three fuel filters were from diesel engines in different environments and adhere to different fuel standards, although there were some common contaminations present specifically between FSF 001 and 003.

Table 7.1: *Summary of fuel used and geographical origin of field sample filters.*

Filter	Fuel used	Origin
CF 002	N/A	Reference filter
FSF 001	ASTM D975	USA
FSF 002	Unknown	Asia
FSF 003	EN590	EU

Three techniques have been employed for the analysis of these field sample filters (FSF) with the comparison to a reference, unused, filter CF 002 (Chapter 4). A summary of the fuel types and geographical location from Chapter 3.1.4 is shown in Table 7.1. SEM-EDX allows for the topographical analysis of the filters with EDX employed for basic elemental analysis. As SIMS data can be skewed by the ease of ionisation, XPS is used to quantify the elemental composition of the deposits and filtration media. SIMS has gained increasing popularity in the study of diesel deposits on FIE (Barker et al. (2014); Edney et al. (2020a); Feld and Oberender (2016); Lamb et al. (2021)). This chapter will employ similar techniques to analyse deposits on diesel fuel filter.

7.2 Scanning Electron Microscope

Secondary electron scans on the field sample filters (FSF) revealed the difference in morphology between samples. As discussed in Chapter 4.2 filter media can vary, although they usually consist of either a dual polyester-cellulose layered or a single layered media. From analysis of the size of the fibres of the filtration media (20µm) which matches the reference samples, FSF 001 – 003 are likely to be a dual polyester-cellulose.

Each of the deposit on these filters appears to be vastly different from each other, suggesting that the reason for blocking is unique. FSF 001, a filter from the US, had two types of deposit on it. From the elemental analysis A layer of organic species associated with sodium covered the filtration media. This layer did not to cover the filter to the extent of ETF 022 and ETF 027 in Chapter 6.2 as the filter fibres were still visible (Figure 7.1). Above the organic sodium layer there were areas of silicon and oxygen which appeared in a strand-like nature, examples are highlighted in Figure 7.1e. A second type of silicon distribution also appeared to be entrained throughout the filter deposit.

FSF 002, a filter of Asian origin, also had two distinct types of deposit present. A complex organic structure different to the layered like nature seen in FSF 001, which EDX showed to only contain carbon and oxygen, covered the filter (Figure 7.2). Trapped in the between the filter fibres and the complex organic layer there were iron oxide particles present highlighted in the EDX chemical maps in Figure 7.2. These particles are not common

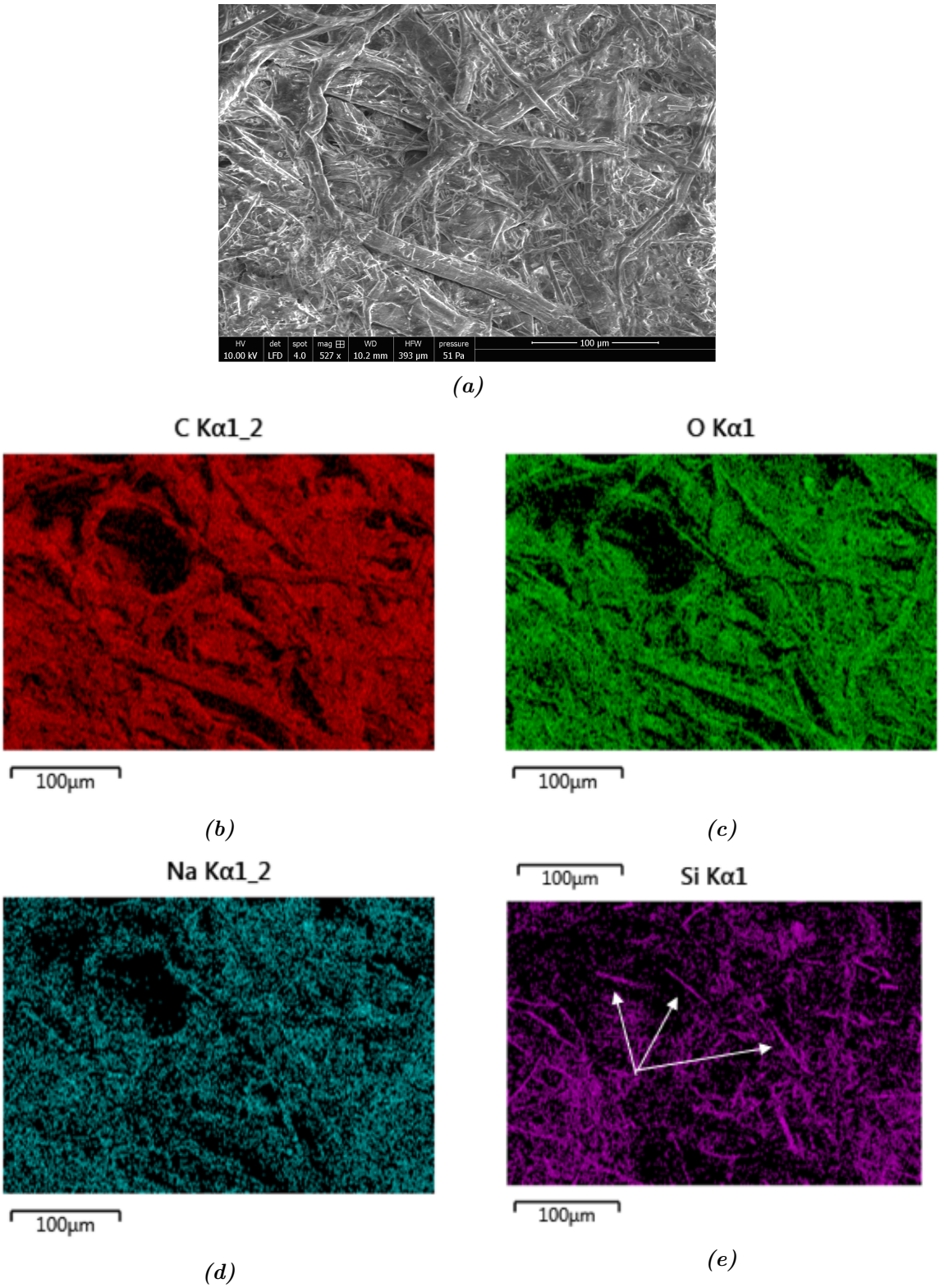
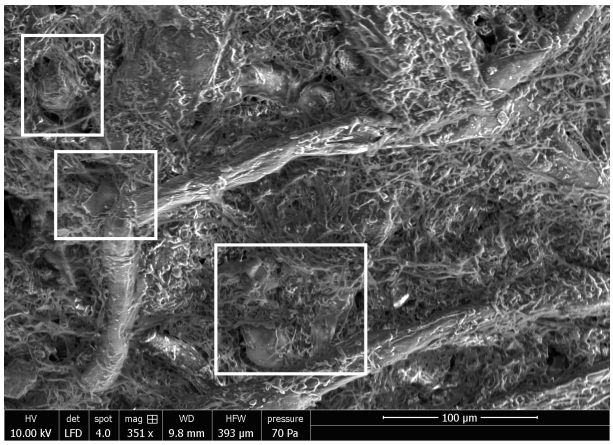


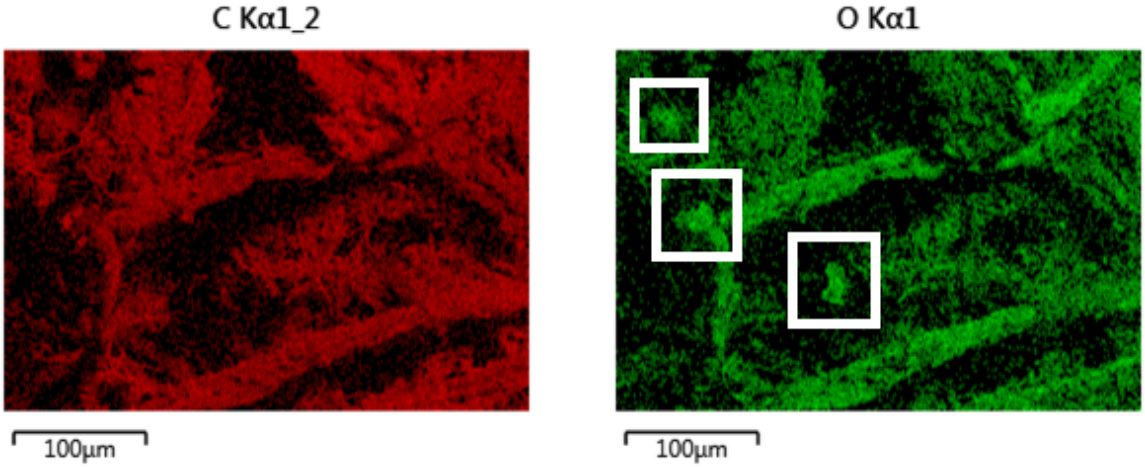
Figure 7.1: *From SEM analysis a a) secondary electron image of FSF 001. EDX analysis showed the b) carbon, c) oxygen, d) sodium, and e) silicon distribution on the filter. Highlighting strand like deposit present in the silicon EDX chemical map.*

fuel contaminants and are likely because of external contamination, for example, from the environment that the vehicle was used. Silicon also appeared to also be distributed throughout the deposit.

The last of the dual-phase filtration media, FSF 003, was from a vehicle in Europe. An EDX scan showed the presence of sulfur and calcium was distributed throughout the filter (Figure 7.3). Unlike the previous two filters there was no particle like deposit present. The EDX showed no presence of Silicon in this filter.

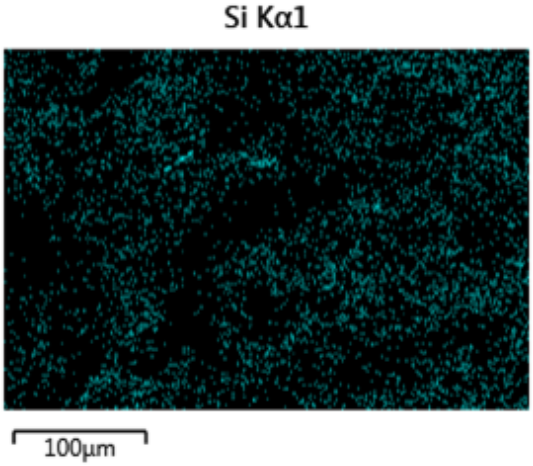


(a)

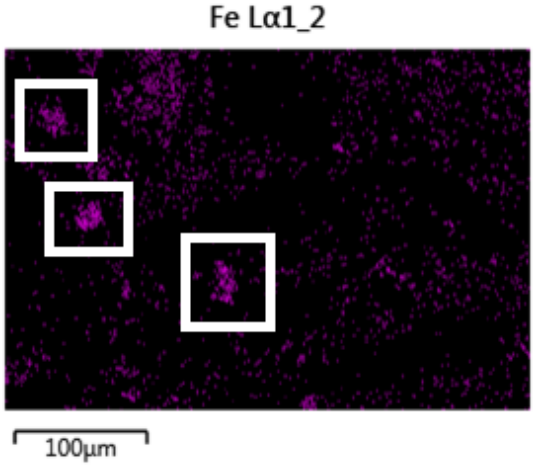


(b)

(c)

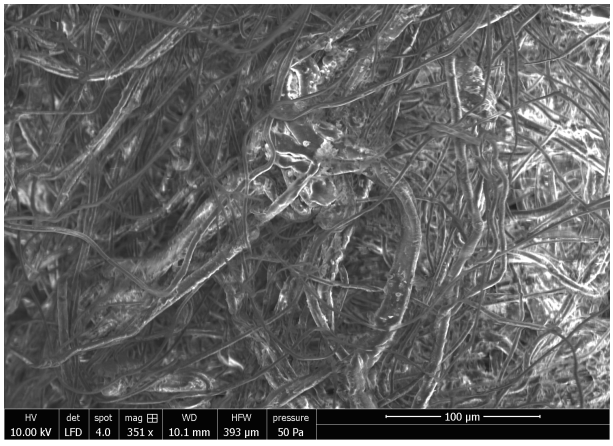


(d)

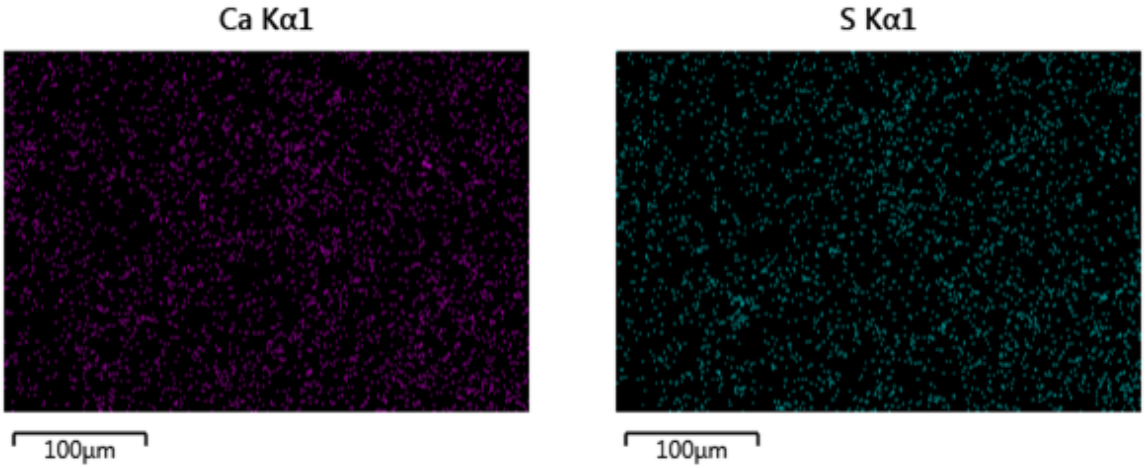


(e)

Figure 7.2: *From SEM analysis a a) secondary electron image of FSF 002. EDX analysis showed the b) carbon, c) oxygen, d) silicon, and e) iron distribution on the filter. Highlighting particle deposit present in the EDX chemical maps.*



(a)



(b) *(c)*

Figure 7.3: *From SEM analysis a a) secondary electron image of FSF 003. EDX analysis showed the b) calcium, and c) sulfur distribution on the filter.*

7.3 X-Ray Photoelectron Spectroscopy

A XPS survey scan was used to quantify the atomic concentrations from the surface of the filters. As with the previous survey scans, three points were analysed and then summed to increase signal-to-noise as well as averaging the compositions. The averaged compositions are shown in Figure 7.4, with CF 002, a dual-phase filtration media, as a reference for FSF 001 – 003.

In FSF 001 and 003 the atomic C:O ratio was greater (5.7 and 5.3) than the reference filter CF 002 (4.0), likely because of the increase in more carbonaceous deposit. The atomic C:O ratio of the Asian filter, however, remained similar (3.7). Nitrogen concentration increased across all filters compared to CF 002. The quantity of this increase is thought to be dependent on the source of diesel used rather than any additive or contaminant.

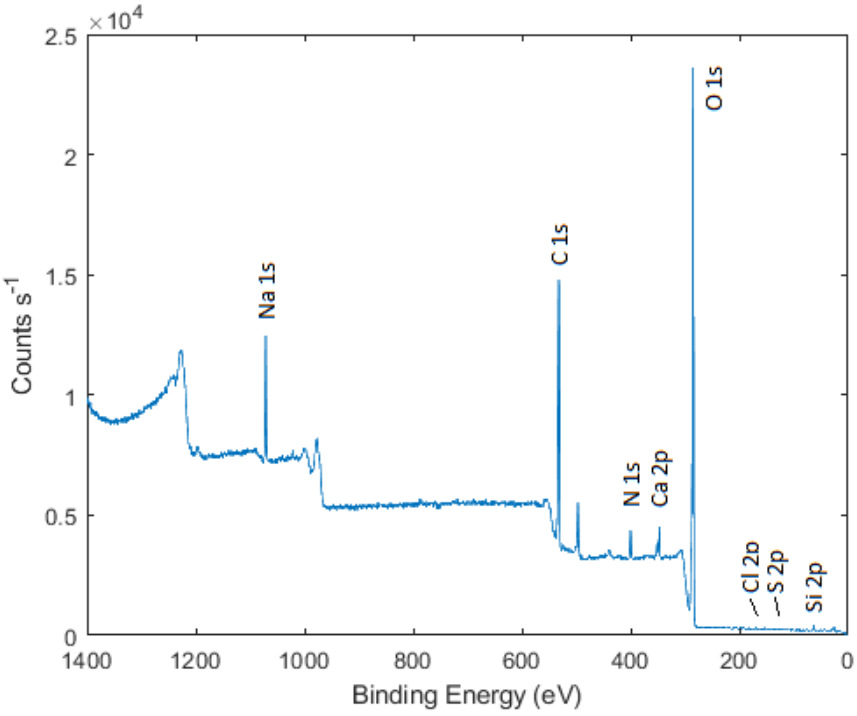
Silicon concentration was high in FSF 002 (4.6 %) and 003 (2.1 %). As XPS analysis is usually only representative of the first few nanometers of the surface. Comparison between XPS and EDX would suggest that the Silicon present in from the EDX analysis of FSF 001 is entrained below the surface of the deposit as the silicon concentration from the XPS survey spectra was lower (0.3 %) compared to the other FSF.

In FSF 001 there was a greater Sodium concentration compared to the other FSF. There also was a small concentration of Calcium and Sulphur on the surface, although this was greater in FSF 003.

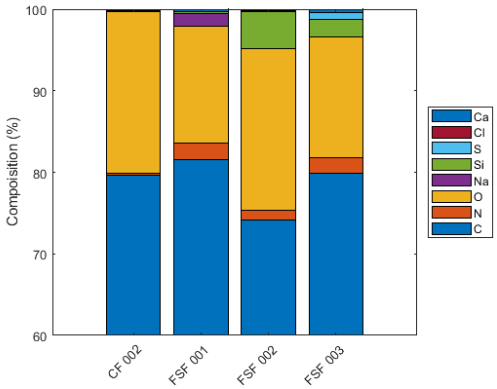
Analysis of the C1s envelope shows the bonding structures that are present in the samples. None of the FSF had any "shake-up" lines suggesting that the carbon present was predominantly aliphatic. A line representative of a carbonate with a peak at ∼289.45 eV was present in FSF 001 (Figure 7.5). This is assumed to be bonded to a sodium as there were no other metals present in the survey spectra.

Table 7.2: *Binding energy ranges for the C1s components of ETFs and reference filter CF 002 (Chapter 4.3).*

	C-C	C-O	C=O	O-C=O	$\pi - \pi*$	CO3
B.E range (eV)	285 - 285.1	286.1 - 286.6	287 - 288.4	288.5 - 289	290.5 - 291.3	289.4 - 289.5



(a)



(b)

Figure 7.4: *a) Survey spectra of FSF 001 (US) including elemental regions, and b) elemental compositions of reference filter CF 002 and field sample filters (FSF) from XPS survey spectra.*

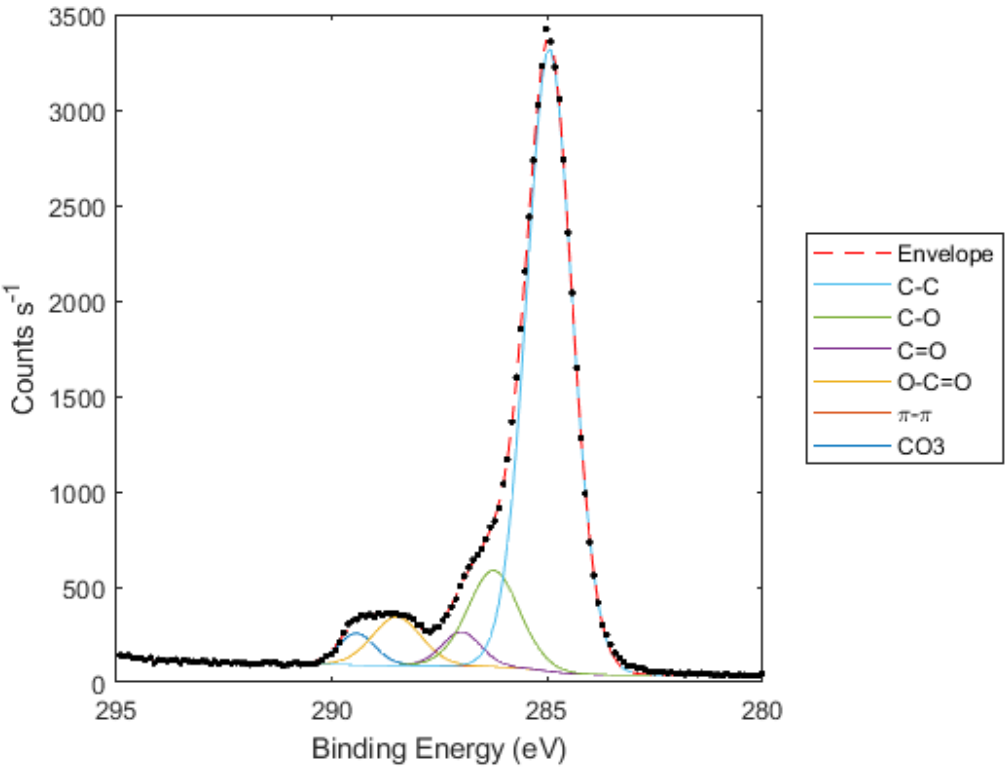


Figure 7.5: *High-resolution XPS spectra of the C1s region of FSF 001.*

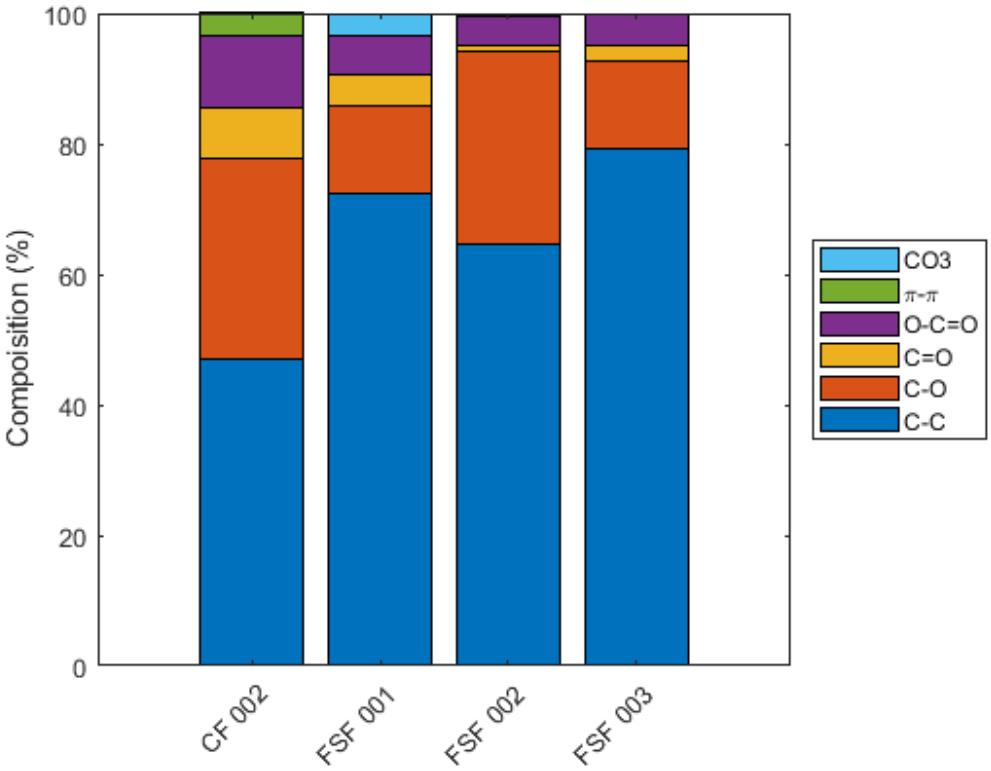


Figure 7.6: *Averaged compositions of the C1s envelopes for each of the FSF and reference filter CF 002 (Chapter 4.3).*

All of the FSF had an increased presence of sp3 bonded carbon compared to the CF 002 (Figure 7.6) suggesting that the deposits were predominantly aliphatic and carbonaceous as no shake up peaks were seen across any of the FSF. The carbonyl contribution was the smallest in FSF 002 (0.9 %) but the percentage of oxidized carbons was the largest (35 %), excluding the reference CF 002.

7.4 Dynamic Secondary Ion Mass Spectrometry

Using the Orbitrap^{TM} as the analyser in the 3D Orbi-SIMS allows for much greater mass resolution as compared to the ToF-SIMS. It is therefore possible to assign ions with much more certainty. Softer fragmentation using an Ar_{3000}^{+} gas cluster as the primary ion beam to sputter the sample results in the increased presence of high mass ions. This section will first describe the overall ion spectra, followed by a depth profile analysis for each filter.

7.4.1 North American Filter (FSF 001)

Calcium is a commonly used as a counter ion for detergents in lubricant oils. Calcium hydroxide ions of varied mass, which could have fragmented from these detergents, were present throughout the positive spectra (Figure 7.7). Analysis of the negative ion spectra showed there was a presence of alkylbenzene sulfonates (ABS) markers.

Alongside the Calcium hydroxide ions, the presence of Sodium derived organic and inorganic species similar to those seen in ETF 022 and ETF 027 (Chapter 6.4). These included di-Sodium DDS salts (Table 7.3: 2, 8, 13, 15, 16 and 18) as well as potential dimer acids with a sodium adduct (Table 7.3: 17 and 18). As with ETF 022 and 027, the $[M\text{-}H]^-$ ion of a single Sodium DDS salt ($C_{16}H_{26}O_4Na^-$) was also present, confirming the presence of the DDS salts in the deposit of FSF 001.

Non-negative matrix factorisation (NNMF) has been used in this thesis to distinguish between the different change in composition as a function of depth that occur in the samples. The benefit of using NNMF over principal component analysis for the analysis of depth profiles is the readability of the results, NNMF only produces non-negative results

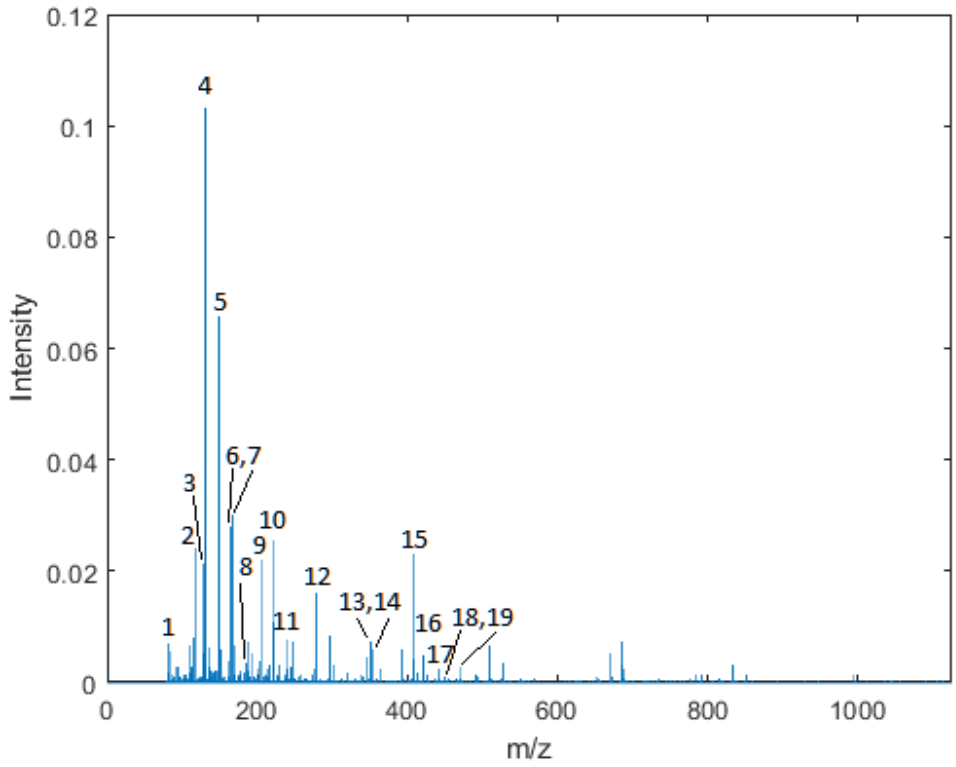


Figure 7.7: *FSF 001 (US) positive ion 3D Orbi-SIMS spectra. Proposed formula of identified peaks are shown in Table 7.3.*

Table 7.3: *Proposed formulas and their respective deviations of the peaks identified in Figure 7.7.*

ID	Proposed Formula	Deviation (ppm)	ID	Proposed Formula	Deviation (ppm)
1	Na_2Cl^+	1.9	11	$Ca_3O_7H_9^+$	0.4
● 2	$C_3H_3O_2Na_2^+$	0.4	12	$Ca_4O_7H_7^+$	0.2
3	$CO_3Na_3^+$	1.4	● 13	$C_{16}H_{26}O_4Na_3^+$	0.7
4	$Ca_2O_3H_3^+$	0.1	14	$Ca_5O_9H_9^+$	1.7
5	$Ca_2O_4H_5^+$	0.8	● 15	$C_{20}H_{34}O_4Na_3^+$	-0.2
6	$Na_3SO_4^+$	0.7	● 16	$C_{22}H_{38}O_4Na_3^+$	-0.2
7	$Ca_2O_5H_7^+$	0.5	● 17	$C_{26}H_{42}O_4Na^+$	0.9
● 8	$C_4H_4O_4Na_3^+$	1.4	● 18	$C_{23}H_{40}O_4Na_3^+$	1.9
9	$Ca_3O_5H_5^+$	0.4	● 19	$C_{28}H_{46}O_4Na^+$	0.9
10	$Ca_3O_6H_7^+$	1.1			

which are inherent of depth profiles.

In FSF 001, NNMF showed three distinct patterns of change in composition (Figure 7.8). The concentration of a nitrogen containing species $C_6H_{11}N_2^+$ shown in Figure 7.8 as well as, what is likely a fragment $C_4H_7N_2^+$ fell sharply in the initial stages of the depth profile, suggesting that this was a layer of contamination at the surface of the sample. The Sodium carbonate $CO_3Na_3^+$ ion also decreased in intensity sharply from the surface, however, the intensity remained steady after 100 seconds at a greater concentration than the nitrogen containing species. As discussed in previous chapters, this cannot be used to suggest the greater quantity of the latter ion as it is possible that the concentration of ions is affected by the matrix effect.

The second distinct pattern showed the increase in concentration of Calcium hydroxide ions as the proposed contamination species decreased in concentration. It reached a maximum about 200 seconds into the depth profile, after which it continued to slowly decreased out of the scope of this depth profile.

The third pattern was followed by a sodium sulfate ion and a carbonaceous ion, the latter likely representative of the filter media. They initially increased slowly and then plateaued around 100-300 seconds into the sputter. The origin of the sulfate has been suggested in literature to come from detergent additives in lubricant oil (Barker et al. (2020); Edney et al. (2020b)) although the consensus that it is the sole source has contested (Groeper, 2022). This sodium sulfate ion was seen in work from previous a chapter in ETF 022 and 027 filters which were dosed with a sodium contaminant but no detergent was added.

In the negative ion depth profile, the ABS marker, $C_8H_7SO_3^-$ (Figure 7.9), had a high relative intensity at the surface which reduced exponentially as the sputter time increased suggesting that this ion although somewhat present in the throughout the filter is predominantly present at the surface. There was a large contribution of an organosilicon ion at the in the initial few seconds of the depth profile but this fell rapidly and can therefore is likely to be surface contamination.

As discussed, Calcium is commonly used as a counter ion for ABS. The concentration of an ABS ion decreased at an inverse exponential rate with sputter time. The concentration

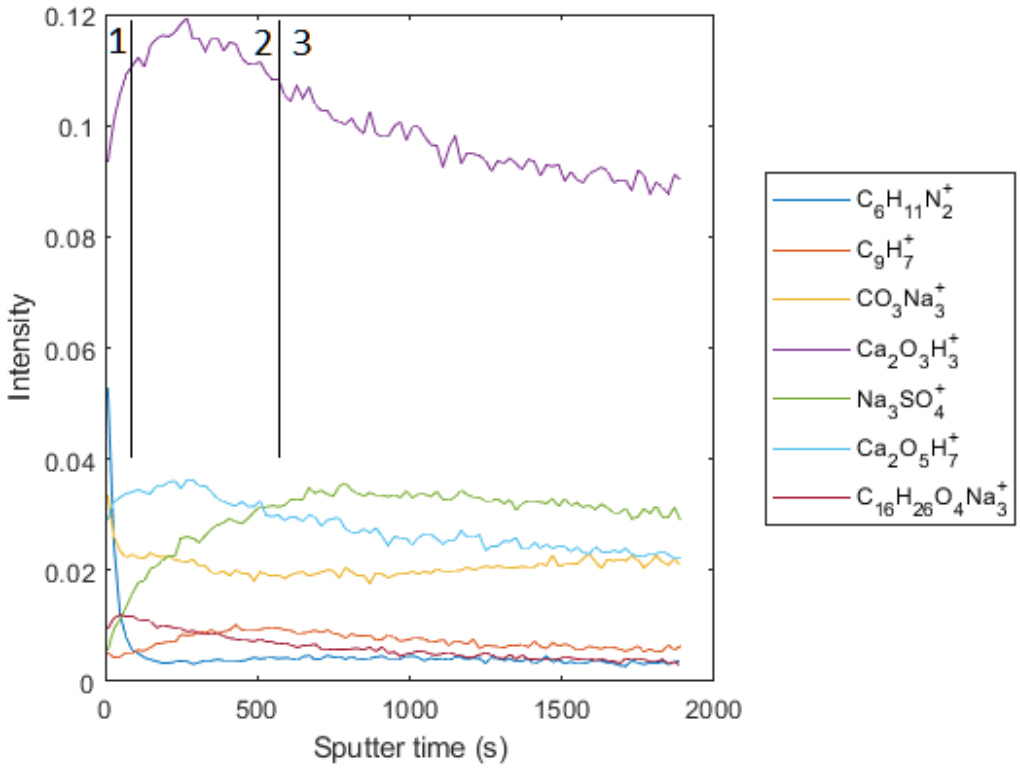


Figure 7.8: *Positive ion depth profile of selected peaks from FSF 001 (US).*

of a Calcium sulfonate ion did not follow the same change intensity, initially increasing and then decreasing later (∼250 s) into the depth profile. This would suggest that the calcium sulfonate may come from a different parent compound to the ABS ion fragment. The ion $C_7H_5O_2^-$, used as a marker for the filtration media gradually increased as with sputter time as expected. A carbonaceous ion, C8-, increased throughout the deposit but it is not possible to deduce the origin of this molecular ion. Other carbonaceous molecular ions (C_8H^-, C_9^-, and $C_{10}H^-$) also followed this trend but are not shown.

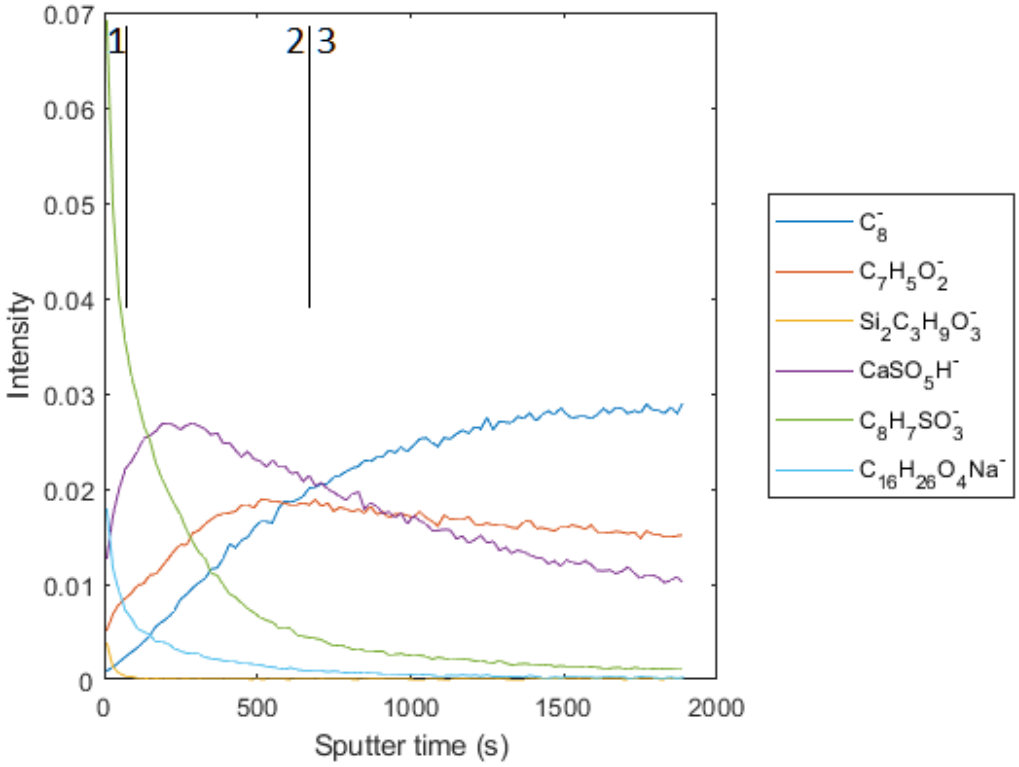


Figure 7.9: *Negative ion depth profile of selected peaks from FSF 001 (US).*

7.4.2 Asian Filter (FSF 002)

In the positive ion spectra of FSF 002 a series of high mass nitrogen-containing organic peaks (Table 7.4: 7-18) were present. The lowest mass of the series that has been identified (Table 7.4: 7) has a proposed formula of $C_{30}H_{57}N_2O_2^+$ $[M+H]^+$ with each successive identified peak in Figure 7.10 increasing by C4H8. The number of carbons in the highest mass of this molecular ion series was attributed to 74, although, this was the mass limit set to the orbitrap analyser. Perhaps the likely source of this series is polyisobutenyl succinicimide (PIBSI), which is commonly used as a deposit control additive. The double bond equivalent (4) of the proposed the formula suggests that the PIB part contained one unsaturated bond.

In Figure 7.11 the ions are indexed according to their possible parent ions. Through further analysis of the ion fragmentation pattern around the C42 $[M+H]^+$ ion it is proposed that the amine part of the succinimide is likely to be $C_3H_8N^+$.

Figure 7.12 shows the graphical representation of this possible fragmentation pattern

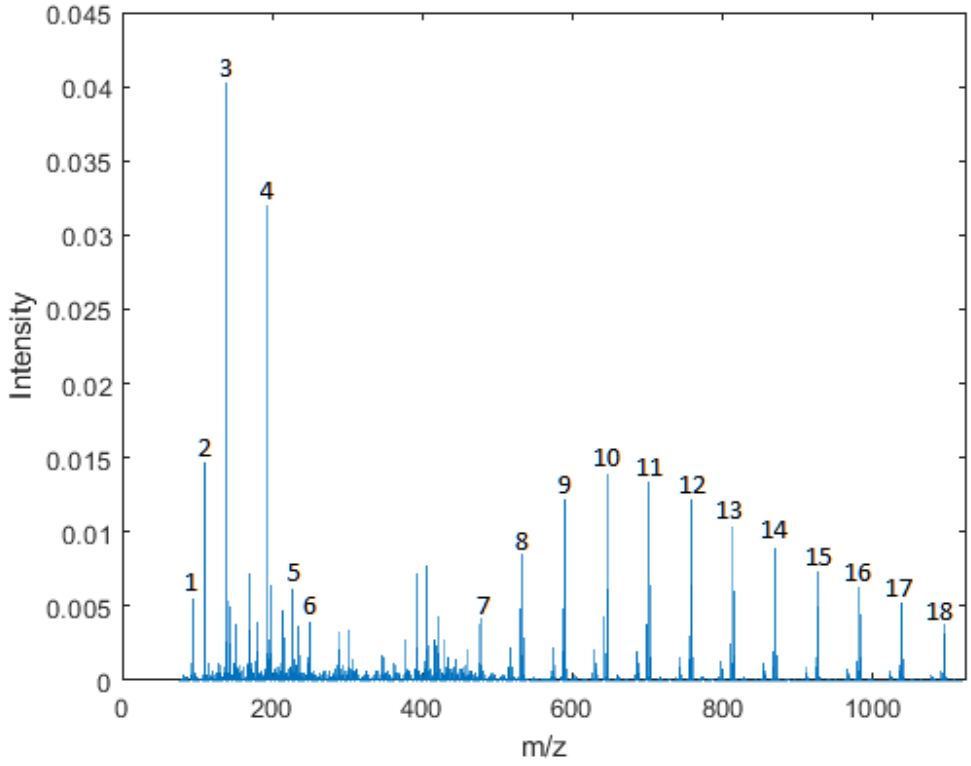


Figure 7.10: *FSF 002 (Asia) positive ion 3D Orbi-SIMS spectra. Proposed formula of identified peaks are shown in Table 7.4.*

Table 7.4: *Proposed formulas and their respective deviations of the peaks identified in Figure 7.10.*

ID	Proposed Formula	Deviation (ppm)	ID	Proposed Formula	Deviation (ppm)
1	$C_6H_7O^+$	1.8	10	$C_{42}H_{81}N_2O_2^+$	0.4
2	$C_5H_4NO_2^+$	0.4	11	$C_{46}H_{89}N_2O_2^+$	0.4
3	$C_7H_8NO_2^+$	-1.1	12	$C_{50}H_{97}N_2O_2^+$	0.3
4	$C_{11}H_{16}NO_2^+$	-0.3	13	$C_{54}H_{105}N_2O_2^+$	0.3
5	$Si_3C_4H_{15}O_5^+$	0.1	14	$C_{58}H_{113}N_{2O2}^+$	0.3
6	$C_{15}H_{24}NO_2^+$	-0.2	15	$C_{62}H_{121}N_2O_2^+$	0.3
7	$C_{30}H_{57}N_2O_2^+$	0.1	16	$C_{66}H_{129}N_2O_2^+$	0.1
8	$C_{34}H_{65}N_2O_2^+$	0.3	17	$C_{70}H_{137}N_2O_2^+$	0.5
9	$C_{38}H_{73}N_2O_2^+$	0.2	18	$C_{74}H_{145}N_2O_2^+$	0

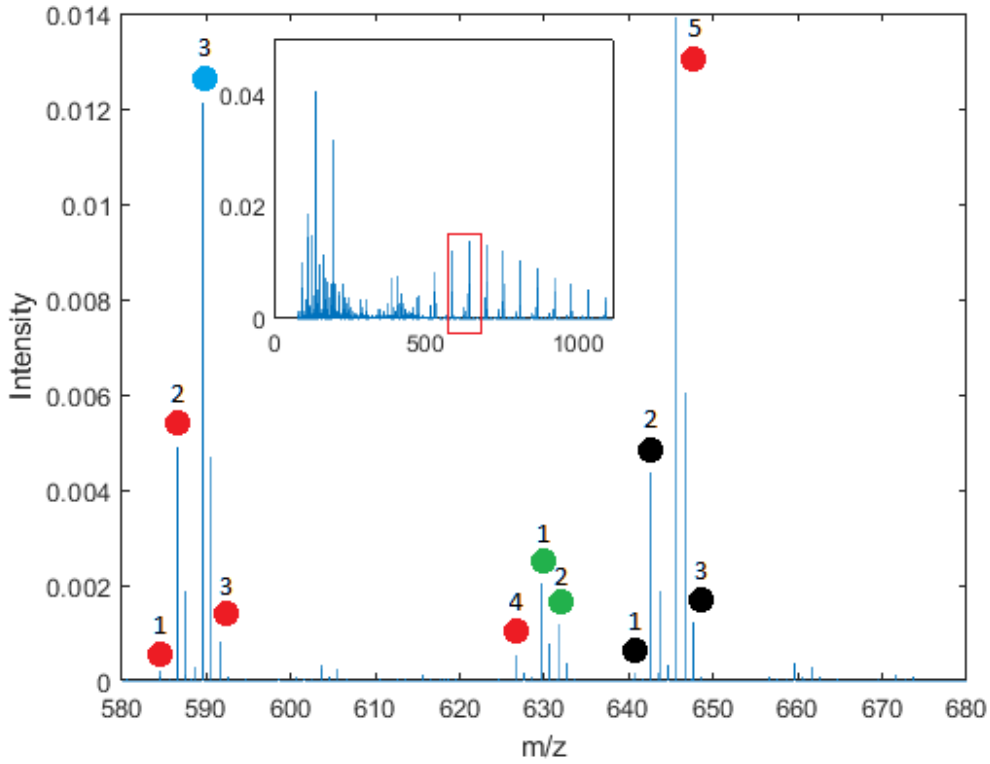


Figure 7.11: *Positive ion spectra (580 - 680 m/z) of FSF 002 (Asia) highlighting similar peaks. Proposed formula of the identified peaks are shown in Table 7.5.*

Table 7.5: *Proposed formulas and their respective deviations of the peaks identified in Figure 7.11.*

ID	Proposed Formula	Deviation (ppm)	ID	Proposed Formula	Deviation (ppm)
● 3	$C_{38}H_{73}N_2O_2^+$ $[X\text{-}C_4H_8]^+$	0.2	● 4	$C_{42}H_{76}NO_2^+$	0.4
● 1	$C_{41}H_{77}N_2O_2^+$	0.4	● 5	$C_{42}H_{81}N_2O_2^+$ $[X]^+$	0.4
● 2	$C_{41}H_{79}N_2O_2^+$ $[X\text{-}CH_2]^+$	0.3	● 1	$C_{43}H_{78}NO_2^+$	0.5
● 1	$C_{39}H_{70}N_2O_2^+$	0.3	● 2	$C_{43}H_{80}NO_2^+$	0.4
● 2	$C_{39}H_{72}N_2O_2^+$	0.2	● 3	$C_{46}H_{81}N^+$ $[Y+C_4H_8]^+$	-0.2
● 3	$C_{42}H_{73}N^+$ $[Y]^+$	-0.3			

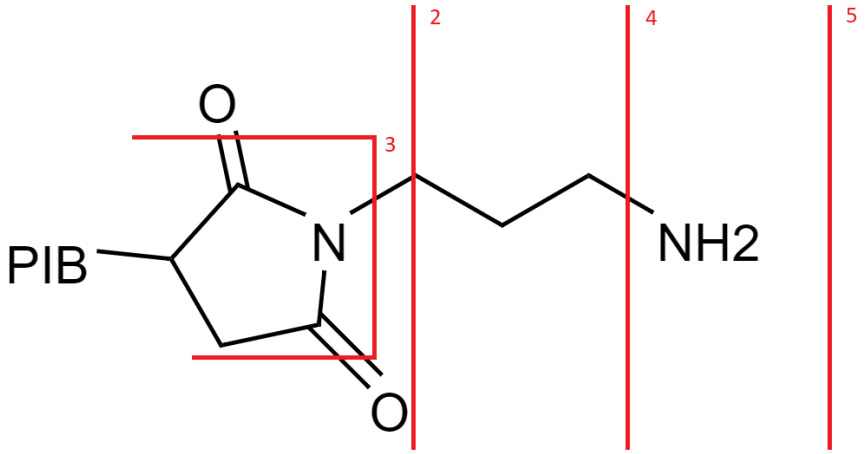


Figure 7.12: *Schematic of PIBSI and its possible fragmentation patterns labelled in red in Figure 7.11.*

where each number represents the number indexed in Table 7.5 with a red dot. The change between $C_{41}H_{79}N_2O_2^+$ and $C_{42}H_{81}N_2O_2^+$ is thought to be a result of the fragmentation in the PIB.

NNMF was used to distinguish three different patterns of change in composition of the deposit in the positive polarity of FSF 002. The first, likely surface contamination containing the organosilicon compound $Si_3C_4H_{15}O_5^+$ shown in Figure 7.13, although unlike other filters this organosilicon ion remained prevalent throughout the sample. The second pattern which followed an increase as the surface contamination was sputtered, reached a maximum at around 100 seconds, and then slowly decreased. This layer is thought to be the bulk of the deposit which contained the PIBSI series, and the other markers presented in Table 7.4. The finally a gradual increase intensity of the filter substrate shown by $C_9H_7^+$ in Figure 7.13 which dominated the composition once the PIBSI and other markers series had decreased in concentration.

Two Iron oxide ions (FeO_2^- and FeO_3^-, -1.7 and 0.3 ppm), increased in intensity logarithmically (Figure 7.13). The presence of iron oxides is consistent with the SEM-EDX analysis. Markers for the filtration media decreased steadily throughout the depth pro-

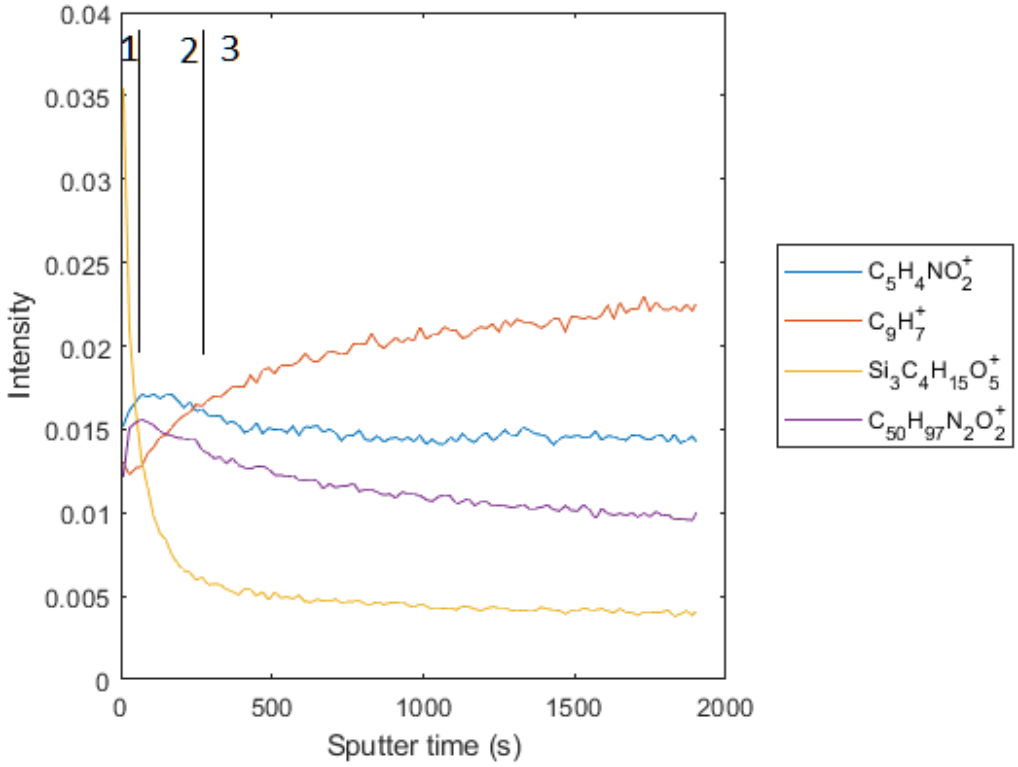


Figure 7.13: *Positive ion depth profile of selected peaks from FSF 002 (Asia).*

file. As with the positive polarity depth profile, a layer of organosilicon was seen at the beginning of the depth profile, but this rapidly decreased, although compared to FSF 001 at a lower rate, and levelled out around 500 s in. Three distinct patterns of composition change are shown which appear consistent with the change in composition seen in the positive ion depth profiles.

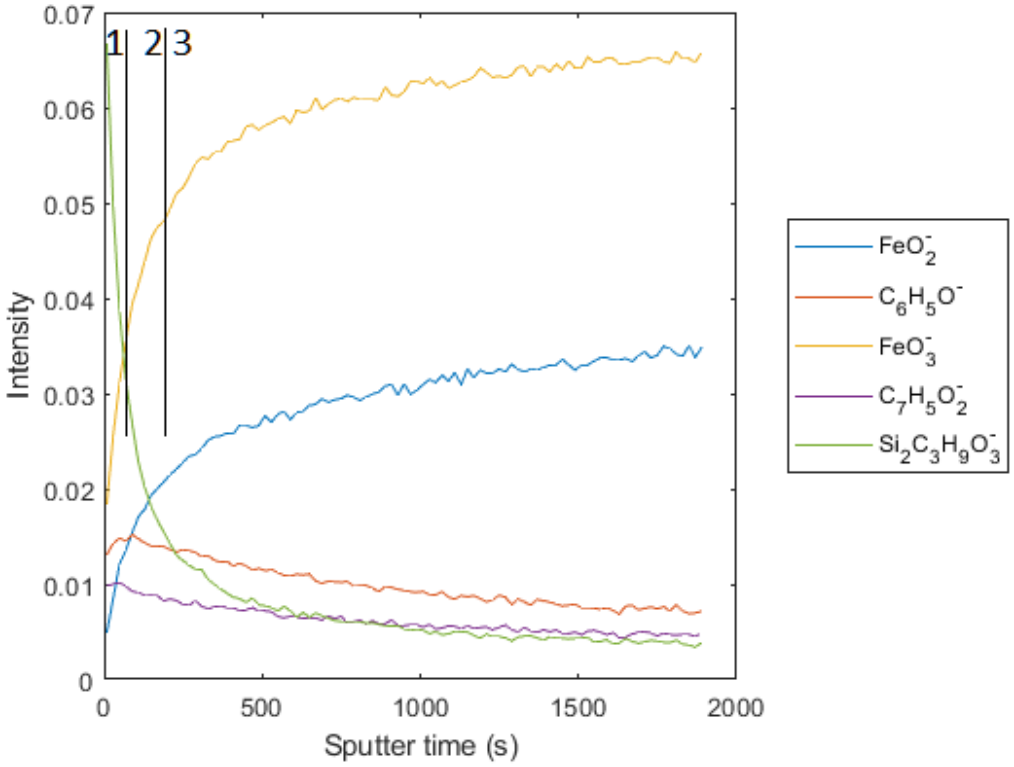


Figure 7.14: *Negative ion depth profile of selected peaks from FSF 002 (Asia).*

7.4.3 European Filter (FSF 003)

As with FSF 001, the total positive ion spectra of the European filter was dominated by calcium hydroxides (Figure 7.15). Unlike the US filter sample, there was no apparent sodium contamination. A series of PAH peaks consistent with that seen in the blank filters were also present which were identified with the in-house built algorithm and then removed from Figure 7.15 for clarity to show the underlying chemistry.

A positive ion depth profile of the European filter revealed that there was an initial layer

Table 7.6: *Proposed formulas and their respective deviations of the peaks identified in Figure 7.15.*

ID	Proposed Formula	Deviation (ppm)	ID	Proposed Formula	Deviation (ppm)
1	$C_6H_7O^+$	1.5	7	$Ca_3O_5H_5^+$	-0.6
2	$C_7H_5O_2^+$	-0.9	8	$Ca_3O_6H_7^+$	0
3	$Ca_2O_3H_3^+$	-0.4	9	$Ca_4O_7H_7^+$	-0.3
4	$Ca_2O_4H_5^+$	-0.8	10	$Ca_5O_6H^+$	-0.7
5	$Ca_2O_5H_7^+$	-1.1	11	$Ca_5O_9H_9^+$	-0.5
6	$C_{12}H_9O$	-1.7			

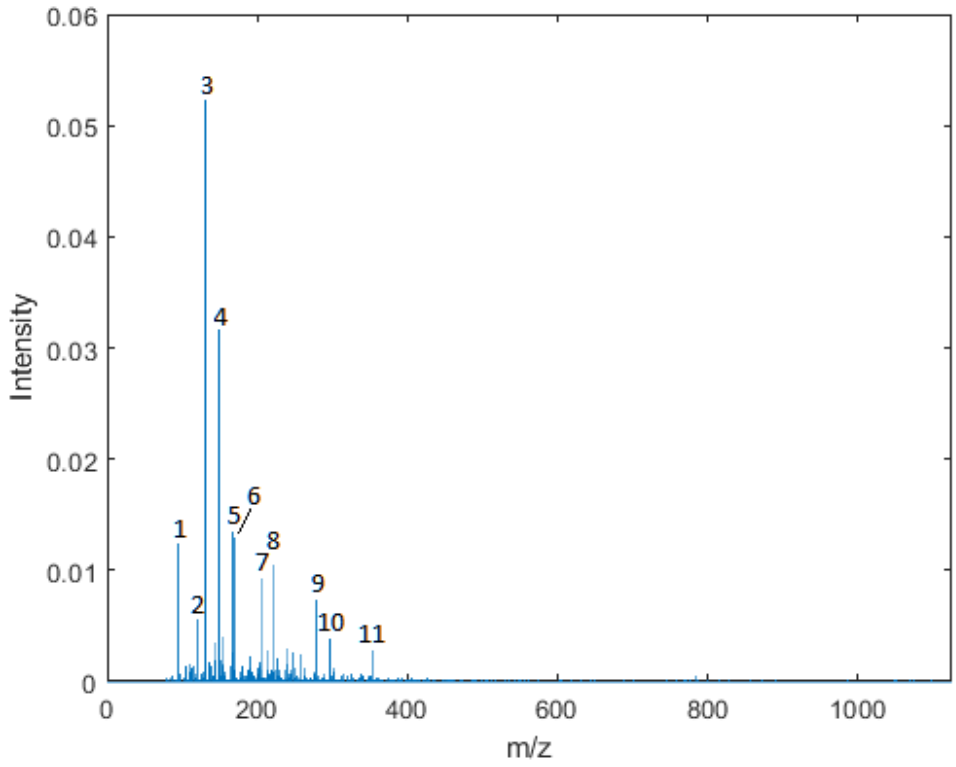


Figure 7.15: *FSF 003 (EU) positive ion 3D Orbi-SIMS spectra with CxHy ions removed. Proposed formula of identified peaks are shown in Table 7.6.*

of an organosilicon which quickly decreased in intensity while the bulk of deposit, Calcium hydroxide ions, increased sharply. Once a maximum intensity was reached, around 150 seconds, the calcium hydroxide ions fell in concentration. Markers of the filtration media increased gradually with sputter time represented by $C_{12}H_8^+$ in Figure 7.16.

Similar to the deposit on the US filter, in the negative ion depth profile, ABS markers which had a high intensity at the surface of the deposit decreased rapidly at the start of the sputter (Figure 7.17). As with the US filter, the calcium sulfate ion increased rapidly and then decreased in intensity from around 200 seconds. The trend of the negative calcium sulfate ions was similar to the calcium hydroxide in the positive ion depth profile (Figure 7.16).

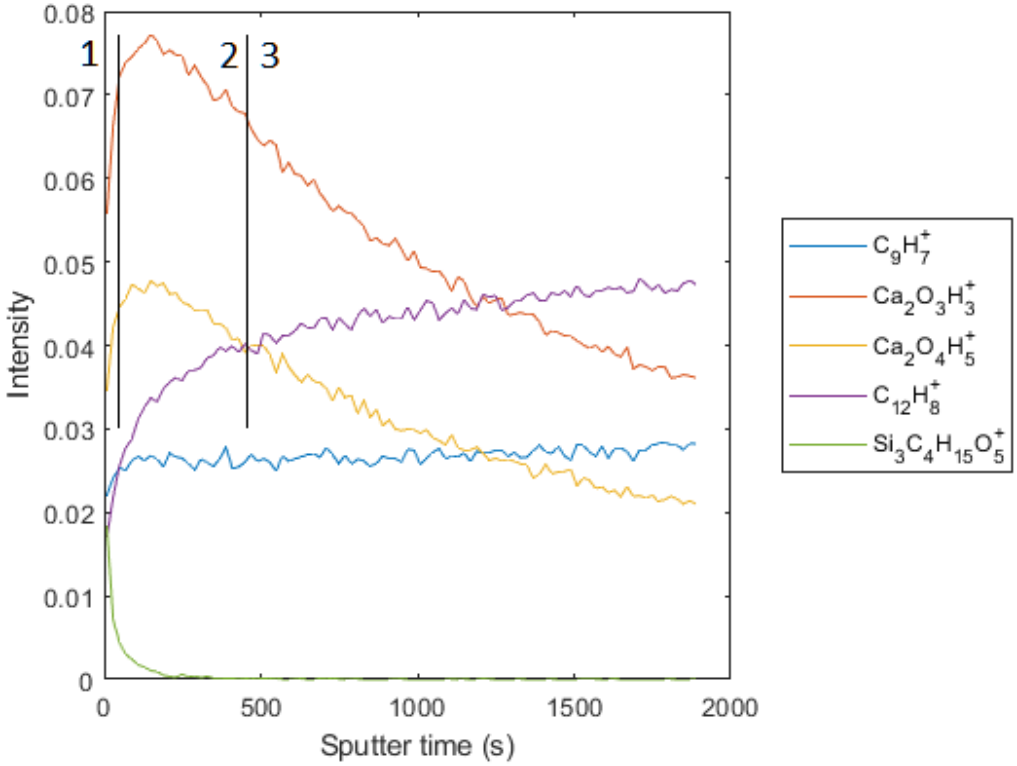


Figure 7.16: *Positive ion depth profile of selected peaks from FSF 003 (EU).*

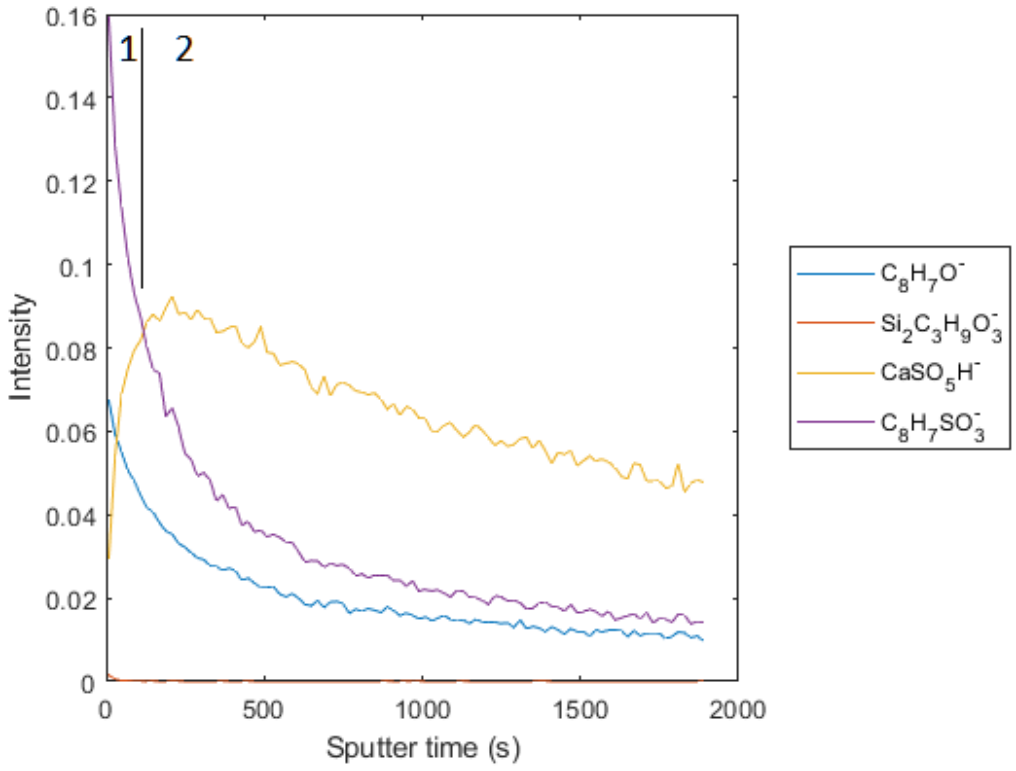


Figure 7.17: *Negative ion depth profile of selected peaks from FSF 003 (EU).*

7.5 Discussion

FSF 001, a fuel filter from the US, was the only sample that contained large amounts of Sodium. Analysis 3D Orbi-SIMS suggested that the origin of the sodium deposits was from carbonates and DDS salts. DDS acid is a commonly used as an additive in diesel fuel as a corrosion inhibitor. Similar ions were seen in engine test filters ETF 022 and 027, in which a corrosion inhibitor additive was added along with the doping of a sodium source.

The origin of the sodium carbonate is not clear, however, its presence in the engine test filters (Chapter 6.4) suggest that it is a degradation molecule from di-acid salts rather than mono-acid salts which has been suggested as a source of sodium contamination in other filters from the literature (Schwab et al., 2010). In FSF 001 there was no indication that sodium salts were formed with single acid organics. The morphology of the deposit on FSF 001 had a similar layer like structure to ETF 022 and 027, however, the inorganic sodium film appeared to be in the early stages as it was not covering the filter's fibres as seen in the ETFs.

Alongside the sodium deposit, FSF 001 also showed a presence of Calcium hydroxides in the positive ion data and calcium sulfonates in the negative ion data. Both polarities of SIMS data for FSF 003, a European filter, was also dominated by these ions, although no sodium was recorded. XPS suggested that at the surface of FSF 001, the quantity of calcium was small in comparison to sodium and EDX data also showed that the calcium presence throughout the bulk deposit was too small to be detected. In contrast, FSF 003 had a greater presence in both XPS and EDX data.

Calcium is commonly used as a counter ion to ABS, a deposit control additive used in lubricant oil. It is postulated that the lubricant oil additive presence in the filter is because of the re-circulation of fuel from the injectors, where lubrication oil is used to maintain the FIE. ABS ions were seen towards the surface of the deposit, however, the intensity of these ions decreased with depth in both the US and European filters. In contrast, the concentration of calcium hydroxides and sulfonates increased with depth which does not support this theory.

The deposit on FSF 002 was largely different from the other two field filters. SEM-EDX analysis indicated large ferrous oxide particles as well as entrained Iron throughout the filter. This was confirmed by the presence of FeO_2^- and FeO_3^- ions with the intensity growing throughout the filter. Ferrous metals are not a common contaminant in fuel, it is likely that the particles in FSF 002 are a result of environmental contamination of the fuel. PIBSI is deposit control additive (DCA), where the polar head group has an affinity for metal surfaces whilst the hydrocarbon tail promotes fuel solubility. In the positive polarity SIMS data, a series of high mass PIBSI ions as well as fragmentations were identified using an purpose built algorithm which processed the large data sets to identify this series.

This is the first time this class of contaminants have been identified due to the high mass resolution of the 3D Orbi-SIMS and the soft fragmentation of the gas cluster ion beam. Whilst DCA is intended to tackle small metal contamination, when large metal compounds, such as the ferrous particle seen in FSF 002, DCA could compound the amount of deposit and be detrimental. The continuous increase in intensity of the combined PIBSI and ferrous oxide markers throughout the filter suggest that the compound is not just a localised problem but entrained throughout the filter.

It has also been shown that deposits in filters do not necessarily pertain to one layer, rather multiple layers of distinct chemistries which can be identified through Orbi-SIMS depth profiles.

7.6 Conclusion

In this study it was found that the chemistry of filters varied with geographic location, likely because of the different fuel standards as well as external factors. Similarities in the deposits found on a filter from the US and engine test filters which were subjected to fuel saturated with sodium compounds.

Calcium containing ions were observed in filters from the EU and US which increased in concentration with depth. ABS, of which Calcium is commonly used as a counter ion in deposit control, however decreased in concentration with depth, suggesting the

dissociation of the ion pair within the filter.

A series of high-mass PIBSI ions were characterised for the first time in diesel fuel filters, which was made possible from the high mass resolution of the 3D Orbi-SIMS and assignment with an in-house designed algorithm.

Chapter 8

Final Conclusions

Characterisation of diesel fuel filters have been carried out with a wide range of analytical techniques including SEM-EDX, XPS and SIMS. As the analysis of the fuel filters were in-situ, to distinguish between the chemical information of the filter media and deposit, two reference dual phase melt blown filters were also characterised. The rest of the filter samples can be split into three categories; bench/laboratory rig test, engine test and filters from the field.

The presence of molecular ions from fragmentations of PET in both reference filters were identified using 3D Orbi-SIMS, which was used to assign molecular information to the deposits. The positive ion spectra of the reference filters were saturated with carbonaceous peaks assigned to PAH ions. The PAH ions ranged from $C_6H_6^+$ to $C_{66}H_{22}^+$ with a linear growth of DBE proportional to an increase in carbon number. Assignment of these ions was made using a custom in-house script, "compound_finder", which outputs possible ion assignment within a specified deviation limit.

The shake-up peaks, representative of aromatic species, in the analysis of the C1s envelopes of the reference filters contributed to a small proportion of the bonded carbon. As these ion peaks are present in reference filters, the presence of these ions is suggested to be because of the degradation of aromatic species in PET rather than the initial stipulation in literature that the presence in fuel filters is a result of recirculated species from the injectors. To be able to assess the underlying chemistries, such as the molecular ions representing PET, these carbonaceous peaks need to be removed from the spectra. This

is a recurring theme in most of the samples covered in this thesis, especially if there is not a significant layer of deposit on top of the filter fibres.

SEM-EDX was used to highlight the similarities and differences between the morphology and bulk surface elemental composition of filter deposits across all samples. Excluding a laboratory test fuel filter that blocked, LTF 003 blocked, the laboratory test filters did not appear to have any deposition on the filtration fibres. The deposit present in the blocked filter, which saw a reduction in flow rate after 28 hours of cycling with B100 fuel, appeared to be an organic film that also covered particle features on and between the filter fibres. The 3D Orbi-SIMS revealed a presence of sitogluside and fatty acids, to an unprecedented certainty (< 2.5 ppm), at the surface of this deposit which is concurrent with literature. The 3D Orbi-SIMS also allows for the analysis of the ions as a function of depth and showed that the intensity of the sitogluside and fatty acids reduced with depth which has not been shown before.

In the engine test filters SEM-EDX revealed a layer of organic species associated with sodium was formed if sodium and corrosion inhibitor were added to the fuel without the presence of a DCA. 3D Orbi-SIMS revealed that there was a presence of di-acid di-sodium salts present in the initial stages of the depth profiles which builds on the postulation in literature that di-acid corrosion inhibitors are instrumental in the formation of filter deposit build up. PCA was initially used to show the benefit of using statistical analysis when analysing multiple samples where individual deconvolution of the data would be difficult. Alongside the separation of filters based on the presence of inorganic sodium species which dominated the first PC and accounted for 83% of the variance, PC2 accounted for 8% of the variance and described the presence of organosilicon ions in another of the engine test filters.

Another statistical technique NNMF was used to show, the presence of patterns of change in compisition within fuel filter deposits. The deposit found in filters from the field were complex and, in some cases, originated from different sources. The morphology and elemental composition of the deposit varied between samples including iron oxide particulates, inorganic sodium layers as well as calcium containing inorganic species. Analysis

of the 3D Orbi-SIMS spectra showed that the although the US and EU filters showed a plethora of calcium associated ions the US filter also contained some sodium species. There is evidence to suggest the that calcium present in the deposits analysed was not a result of the use of acid additives in engine oils, as the possible counter ions followed a different change in composition as a function of depth. ABS, a common lubricant DCA, was seen at high intensity in the surface but also in smaller amounts in the bulk deposit of both EU and US filters.

In the Asian filter particles of iron oxide stuck in the filtration media were seen in the SEM-EDX analysis. An organic layer of complex structure partially covered the filter media and iron oxide particles. Through 3D Orbi-SIMS analysis and the use of the purpose built algorithm, it was shown that this was composed of a series of PIBSI like ions.

The advancement of analytical techniques has allowed for novel insight into identification of deposit on fuel filters which has been able to confirm the presence of species, such as sitogluside, and find new species such as ABS, calcium sulfates, DDS salts and dimer acids that have never been detected before. I hope that this thesis can be the building block to showcase and spur the further identification of species in filter deposit using advanced analytical techniques.

Chapter 9

Future Work

The ever advancement of analytical techniques, including innovations in statistical analysis mean that there are new and informative methods for the characterisation of deposits on diesel fuel filter deposits.

As discussed, quantitative interpretation of SIMS data can be skewed by the ease of ionisation. XPS has been used in this thesis in conjunction with SIMS data to give perspective to the elemental composition of the deposit surface. It is also possible to provide three dimensional XPS data, which has been used to show the compositional changes throughout injector deposits. Applying XPS depth profiling to filter deposits could possibly be used in a similar manner, unlocking the compositional data of the bulk deposit phase that has been shown to differ in chemistry from the surface with SIMS depth profiling.

Another possible route for the characterisation and quantification of diesel fuel filter deposits is the use of solvent extraction coupled with liquid chromatography mass spectrometry. Unlike SIMS and XPS, this technique may only be viable if a large amount of sample is present as the quantities of deposit are expected to be relatively small. As for the solvent, a mixture of a non-polar and polar solvent would be required, and it would need to be decided whether to remove diesel fractions from the filter prior to analysis.

An article by Cassiday (2008) discussed the use of matrix-assisted laser desorption/ionization (MALDI) mass spectrometry as a complementary technique to SIMS. Whilst MALDI exhibits a lower lateral resolution than SIMS, it has shown to be excellent at detecting

high mass molecules. MALDI works on the principle of desorbing molecules from a treated surface using a laser, preserving the molecule. MALDI may be used to characterise and confirm the high mass molecules of which the ions were postulated in SIMS.

In some samples presented in this thesis, it was shown that there was a thick layer of deposit on the filter fibres. Work by Barker et al. (2020) showed the use of combined focused ion beam (FIB) and SIMS to dig a trench and expose the layers of the deposit on a diesel injector. Although this technique was done with a ToF analyser which would provide good lateral resolution, it is possible that this work could also be used in conjunction with an Orbitra^{TM} to gain better mass resolution of the various chemistry present and deduce whether the deposits on filters are layered.

This thesis presented an initial study on the bench testing fuel filtration systems, however, some modifications to the rig could provide more information as well as more consistent results. The implementation of a heat exchanger would allow the fuel to be kept at a set temperature rather than fluctuating by 20°C. An inline flow reader would allow more measurements of flow rate without having to stop the run.

In agreement with literature, it has been shown that deposits on fuel filters from the field can vary depending on geographical location (fuel type and environment). This thesis has presented three types of filters from different locations, but it is always possible to analyse other samples. One thing of note is that no filter analysed had any ions representing sitogluside that were seen in the laboratory test filters and literature. This could be an indication that no fuel filter from the field was exposed to FAME fuel.

Bibliography

ACEA (2020), 'Acea pocket guide 2020-2021'.
URL: *https://www.acea.be/uploads/publications/ACEA_Pocket_Guide_2020-2021.pdf*

Alkhalili, B. E., Yahya, A., Ibrahim, N. and Ganapathy, B. (2017), 'Biodesulfurization of sour crude oil', *Modern Applied Science* **11**(9).

ASTM (2020*a*), *ASTM D7467 - 20a Standard Specification for Diesel Fuel Oil, Biodiesel Blend (B6 to B20)*, American Society for Testing and Materials.

ASTM (2020*b*), *ASTM D975 - 20c Standard Specification for Diesel Fuel*, American Society for Testing and Materials.

ATC (2013), 'Fuel additives: Use and benefits'.

Auto Express (2018), 'Petrol and diesel cars banned from areas in london', `https://www.autoexpress.co.uk/car-news/102510/petrol-and-diesel-cars-banned-from-areas-in-london`.

Autovista Group (2018), 'Court action on diesel bans in düsseldorf and stuttgart', `https://autovistagroup.com/news-and-insights/court-action-diesel-bans-dusseldorf-and-stuttgart`.

Barbour, R., Quigley, R. and Panesar, A. (2014), 'Investigations into fuel additive induced power gain in the cec f-98-08 dw10b injector fouling engine test', *SAE Technical Paper 2014-01-2721* .

Barker, J., Cook, S. and Richards, P. (2013), 'Sodium contaminatio of diesel fuel and

the resultant effects of filter plugging and injector fouling', *SAE Journal of Fuels and Lubricants* **6**, 826–838.

Barker, J. and Reid, J. (2014), Injector and fuel system deposits, *in* '10th International Colloquium Fuels Conventional and Future Energy for automobiles'.

Barker, J., Reid, J., Angel-Smith, S., Snape, C., Langely, G., Patel, K., Carter, A., Lapthorn, C. and Pullen, F. (2017), 'The application of new approaches to the analysis of deposits from the jet fuel thremal oxidation tester (jftot)', *SAE International Journal of Fuels and Lubricants* **10**.

Barker, J., Reid, J., Wilmot, E., Mulqueen, S., Angel-Smith, S., Scurr, D., Snape, S., Kersting, R., Gauld, R. and Mulvey, R. (2020), 'Investigations of diesel injector deposits characterization and testing', *SAE Technical Paper 2020-01-2094* .

Barker, J., Richard, P., Snape, C. and Meredith, W. (2011), 'Diesel injector deposits - an issue that has evolved with engine technology', *SAE Technical Paper 2011-01-1923* .

Barker, J., Richards, P., Goodwin, M. and Wooler, J. (2009), 'Influence of high injection pressure on diesel fuel stability: A study of resultant deposits', *SAE Journal of Fuels and Lubricants* **2**, 877–884.

Barker, J., Richards, P., Snape, C. and Meredith, W. (2009), 'A novel technique for investigating the nature and origins of deposits formed in high pressure fuel injection equipment', *SAE International Jourrnal of Fuels and Lubricants* **2**, 38–44.

Barker, J., Snape, C. and Scurr, D. (2012), 'A novel technique for investigating the characteristics and history of deposits formed within high pressure fuel injection equipment', *SAE International Journal on Fuels and Lubricants* **5**, 1155–1164.

Barker, J., Snape, C. and Scurr, D. (2014), 'Information on the aromatic structure of internal diesel injector deposits from time of flight secondary ion mass spectrometry (tof-sims)', *SAE Technical Paper 2014-01-1387* .

BBC (2001), 'Kyoto: Why did the us pull out?', http://news.bbc.co.uk/1/hi/world/americas/1248757.stm.

BBC (2017), 'New diesel and petrol vehicles to be banned from 2040 in uk', https://www.bbc.co.uk/news/uk-40723581.

Beamson, G. and Briggs, D. (1992), *High resolution XPS of organic polymers*, John Wiley & Sons.

Bennet, J. (2014), *Advanced fuel additives for modern internal combustion engines*, pp. 165–194.

Benninghoven, A. (1970), 'Die analyse monomolekularer festkörperoberflÄchenschichten mit hilfe der sekundÄrionenemission', *Physik* **230**, 403–417.

Benninghoven, A. (1994), 'Surface analysis by secondary ion mass spectrometry (SIMS)', *Surface Science* **299-300**, 246–260.

Berry, M. W., Browne, M., Langville, A. N., Pauca, V. P. and Plemmons, R. J. (2007), 'Algorithms and applications for approximate nonnegative matrix factorization.', *Computational Statistics and Data Analysis* **52**, 1155–173.

BloombergNEF (2020), Electric vehicle outlook 2020.

Briggs, D. (1986), 'Analysis of polymer surfaces by sims 6 – detection of cyclic oligomer on the surface of poly(ethylene terephthalate) film', *Surface and Interface Analysis* **8**, 133–136.

Buratti, R., Imarisio, R. and Peters, B. (2004), 'Experiences with common rail, a technology changing the image of diesels in europe', *SAE Technical Paper 2004-28-0072* .

Burrell, M. C. and Chera, J. J. (1999), 'Polybutylene terephthalate (PBT) spin cast films by XPS', *Surface Science Spectra* **6**.

Cames, M. and Helmers, E. (2013), 'Critical evaluation of the european diesel car boom - global comparison, environmental effects and various national strategies', *Environmental Sciences Europe* **25**.

CARB (2021), 'History'.

Cardenas Almena, M. D., Lucio Esperilla, O., Martin Manzanero, F., Murillo Duarte, Y., Quintero Toscano, L. C. and Wolf, G. (2012), 'Internal diesel injector deposits: Sodium carboxylates of c12 succinic acids and c16 and c18 fatty acids', *SAE Technical Paper 2012-01-1689* .

Carlsohn, E. and Nilsson, C. L. (2007), *Proteomic techniques for functional identification of bacterial adhesins*, Elsevier, pp. 299–325.

Cassiday, L. (2008), 'SIMS and MALDI: better together', *Analytical Chemistry* **80**, 8860.

CEC (1998), *CEC F-98-08, Direct Injection, Common Rail Diesel Engine Nozzle Coking Test*, European Commission.

CEN (2009), *EN 590 Automotive fuels - Diesel - Requirements and test methods*, European Committee for Standardisation.

Chavanne, G. (1937), 'Procedure for the transformation of vegetable oils for their uses as fuels', BE Patent 422,877.

Chen, X., Wang, X. and Fang, D. (2020), 'A review on C1s XPS-spectra for some kinds of carbon materials', *Fullerenes, Nanotubes and Carbon Nanostructures* **28**, 1048–1058.

Coursey, J. S., Schwab, D. J., Tsai, J. J. and Dragoset, R. A. (2015), Atomic weights and isotopic compositions (version 4.1), Database, National Institute of Standards and Technology, Gaithersburg, MD.

Csontos, B., Bernemyr, H., Erlandsson, A. C., Forsberg, O., Pach, M. and Hittig, H. (2019), 'Characterization of deposits collected from plugged fuel filters', *SAE International Journal of Advances and Current Practices in Mobility* **2**(2), 672–680.

Csontos, B., Bernemyr, H., Erlandsson, A., Hittig, H. and Pach, M. (2020), A measurement of fuel filters' ability to remove soft particles, with a custom-built fuel filter rig, *in* 'SAE Powertrains, Fuels & Lubricants Meeting', SAE International.

Daimler (2009), 'The birth of a legend: the 300 engine series introduced in 1949 is a big hit', `https://media.daimler.com/marsMediaSite/ko/de/9914319`.

Dallanegra, R. and Caprotti, R. (2014), 'Chemical composition of ashless polymeric internal diesel injector deposits', *SAE Technical Paper 2014-01-2728* .

Diesel Net (2007), 'Particle number limit added to euro 5/6 proposal', `https://dieselnet.com/news/2007/04eu.php`.

Diesel Net (2016), 'United states: Cars and light-duty trucks: Tier 3', `https://dieselnet.com/standards/us/ld_t3.php`.

Diesel, R. (1892), 'Working method and embodiment for internal combustion engines', DE Patent 67,207.

Diesel, R. (2001), 'Historical perspectives on vegetable oil-based diesel fuels', *Inform* **26**, 1103–1107.

Dimitriadis, A., Natsios, L., Dimaratos, A., Katsaounis, D., Samaras, Z., Bezergianni, S. and Lehto, K. (2018), 'Evaluation of a hydrotreated vegetable oil (hvo) and effects on emissions of a passenger car diesel engine', *Frontiers in Mechanical Engineering* .

DoT (2018), *Road Traffic Forecasts 2018*, Department of Transport.

Duffy, P. (1853), 'On the constitution of stearine', *Quarterly Journal of the Chemical Society of London* **5**, 303–316.

EC (1994), *Directive 94/12/EC of the European Parliament and the Council of 23 March 1994 relating to measures to be taken against air pollution by emissions from motor vehicles and amending Directive 70/220/EEC*, European Commission.

EC (1998*a*), *Directive 98/69/EC of the European Parliament and of the Council of 13 October 1998 relating to measures to be taken against air pollution by emissions from motor vehicles and amending Council Directive 70/220/EEC*, European Commission.

EC (1998*b*), *Directive 98/70/EC of the European Parliament and of the Council of 13 October 1998 relating to the quality of petrol and diesel fuels and amending Council Directive 93/12/EEC*, European Commission.

EC (2003), *Directive 2003/17/EC of the European Parliament and of the Council of 3 March 2003 amending Directive 98/70/EC relating to the quality of petrol and diesel fuels*, European Commission.

EC (2007), *Regulation (EC) No 715/2007 of the European Parliament and of the Council of 20 June 2007 on type approval of motor vehicles with respect to emissions from light passenger and commercial vehicles (Euro 5 and Euro 6) and on access to vehicle repair and maintenance information*, European Commission.

EC (2009), *Directive 2009/30/EC of the European Parliament and of the Council of 23 April 2009 amending Directive 98/70/EC as regards the specification of petrol, diesel and gas-oil and introducing a mechanism to monitor and reduce greenhouse gas emissions and amending Council Directive 1999/32/EC as regards the specification of fuel used by inland waterway vessels and repealing Directive 93/12/EEC*, European Commission.

EC (2016), *Commission Regulation (EU) 2016/646 of 20 April 2016 amending Regulation (EC) No 692/2008 as regards emissions from light passenger and commercial vehicles (Euro 6)*, European Commission.

Edney, M. K., Barker, J., Reid, J., Scurr, D. J. and Snape, C. E. (2020b), 'Recent advances in the analysis of GDI and diesel fuel injector deposits', *Fuel* **272**.

Edney, M. K., Lamb, J. S., Spanu, M., Smith, E. F., Steer, E., Wilmot, E., Reid, J., Barker, J., Alexander, M. R., Snape, C. E. and Scurr, D. J. (2020a), 'Spatially resolved

molecular compositions of insoluble multilayer deposits responsible for increased pollution from internal combustion engines', *ACS Applied Materials & Interfaces* **12**, 51026–51035.

EEA (2016), *Air quality in Europe - 2016 report*, European Environment Agency.

EEA (2018), 'GHG emissions by sector in the EU-28, 1990-2016', `https://www.eea.europa.eu/data-and-maps/daviz/ghg-emissions-by-sector-in#tab-chart_2`.

EEC (1993*a*), *Council Directive 70/220/EEC of 20 March 1970 on the approximation of the laws of the Member States relating to measures to be taken against air pollution by gases from positive-ignition engines of motor vehicles*, European Economic Community.

EEC (1993*b*), *Council Directive 93/12/EEC of 23 March 1993 relating to the sulphur content of certain liquid fuels*, European Economic Community.

EEC (1993*c*), Council directive 93/59/eec of 28 june 1993 amending directive 70/220/eec on the approximation of the laws of the member states relating to measures to be taken against air pollution by emissions from motor vehicles, Technical report.

EIA (2018), Biodiesels produced from certain feedstocks have distinct properties from petroleum diesel.

EPA (1990), *1990 Clean Air Act Amendment Summary*, Environmental Proctection Agency.

EPA (2007), The plain english guide to the clean air act, Technical report.

EPA (2016), *Light-Duty Vehicles and Light-Duty Trucks: Clean Fuel Fleet Exhaust Emission Standards*, United States Environmental Protection Agency.
URL: *https://www.epa.gov/emission-standards-reference-guide/epa-emission-standards-light-duty-vehicles-and-trucks-and*

EURACTIV (2008), Oil refiners ask for shelter from co2 trading perils.

Feld, N. and Oberender, N. (2016), 'Characterization of damaging biodiesel deposits and biodiesel samples by infrared spectroscopy (ATR-FTIR) and mass spectrometry (tof-sims)', *SAE International Journal of Fuels and Lubricants* **9**, 717–724.

Fletcher, J. S., Rabbani, S., Henderson, A., Blenkinsopp, P., Thompson, S. P., Lockyer, N. P. and Vickerman, J. C. (2008), 'A new dynamic in mass spectral imaging of single biological cells', *Analytical Chemistry* **80**(23), 9058–9064.

Gad, S. (2005), 'Diesel fuel', *Encyclopedia of Toxicology* pp. 19–22.

Galante-Fox, J. and Bennet, J. (2012), 'Diesel injector internal deposits in high pressure common rail diesel engines', *Fuel Systems for IC Engines* pp. 157–166.

Gallagher, N. B., O'Sullivan, D. and Palacios, M. (2020), 'The effect of data centering on pca models', `https://eigenvector.com/wp-content/uploads/2020/06/EffectofCenteringonPCA.pdf`.

Gardner, s. (2014), 'LA smog: the battle against air pollution', `https://www.marketplace.org/2014/07/14/la-smog-battle-against-air-pollution/`.

Gillis, N. and Glineur, F. (2012), 'Accelerated multiplicative updates and hierarchical als algorithms for nonnegative matrix factorization', *Neural Computation* **24**, 1085–1105.

Gopalan, K., Chuck, C. J., Roy-Smith, C. and Bannister, C. D. (2019), 'Assessing the impact of FAME and diesel fuel composition on stability and vehicle filter blocking.', *SAE International Journal of Advances and Current Practices in Mobility* **1**, 284–290.

GPO (1990), 40 CFR parts 80 and 86 regulation of fuels and fuel additives: Fuel quality regulations for highway diesel fuel sold in 1993 and later calendar years, Technical report.

GPO (2001), 40 CFR parts 69, 80, and 86 control of air pollution from new motor vehicles: Heavy-duty engine and vehicle standards and highway diesel fuel sulfur control requirements, Technical report.

Grigoratos, T., Martini, G. and Carriero, M. (2019), 'An experimental study to investigate typical temperature conditions in fuel tanks of european vehicles', *Environmental Science Pollution Research* **26**, 17608–17622.

Groeper, J. A. (2022), 'Formation of metal carboxylates in diesel fuel by cation metathesis', *Fuel* **318**.

Hafner, B. (2007), Scanning electron microscopy primer.

Hartman, J. (2007), *Turbocharging Performance Handbook*.

Hawthorne, M., Roos, J. W. and Openshaw, M. J. (2008), 'Use of fuel additives to maintain modern diesel engine performance with severe test conditions', *SAE Technical Paper 2008-01-1806* .

Herbstman, S. and Virk, K. (1991), 'Use of dispersants/detergents in diesel injector keep clean and clean up studies', *SAE Technical Paper 912330* .

ICCT (2015), 'Epa's notice of violation of the clean air act to volkswagen [press statement]', `https://theicct.org/news/epas-notice-violation-clean-air-act-volkswagen-press-statement`.

Ingram, W. (2015), Staff report: Calculating life cycle carbon, Technical report.

IOR Energy (2010), 'Fuel energy density', `https://web.archive.org/web/20100825042309/http://www.ior.com.au/ecflist.html`.

ISO (2003), *ISO 19438:2003 Diesel fuel and petrol filters for internal combustion engines — Filtration efficiency using particle counting and contaminant retention capacity*, International Organization for Standardization.

Jenčič, B., Vavpetič, P., Kelemen, M. and Pelicon, P. (2019), 'Secondary ion yield and fragmentation of biological molecules by employing 35cl primary ions within the MeV energy domain', *Journal of the American Society for Mass Spectrometry* **31**.

Johansson, B. (2006), 'Tof-sims imaging of lipids in cell membranes', *Surface and Interface Analysis* **38**(11), 1401–1412.

Jolliffe, I. T. and Cadima, J. (2016), 'Principal component analysis: A review and recent developments', *Philosophical Transactions of the Royal Society A* **374**.

Jolly, L., Kitano, K., Sakata, I., Strojek, W. and Bunting, W. (2010), 'A study of mixed-FAME and trace component effects on the filter blocking propensity of FAME and FAME blends', *SAE Technical Paper 2010-01-2116* .

Kala, S. V., Lykissa, E. D. and Lebovitz, R. M. (1997), 'Detection and characterization of poly(dimethylsiloxane)s in biological tissues by GC/AED and GC/MS', *Analytical Chemistry* **69**, 1267–1272.

Keenan, M. R. and Kotula, P. G. (2004), 'Accounting for poisson noise in the multivariate analysis of ToF-SIMS spectrum images', *Surface and Interface Analysis* **36**, 203–212.

Koopmans, T. (1934), 'Über die zuordnung von wellenfunktionen und eigenwerten zu den einzelnen elektronen eines atoms', *Physica* **1**, 104–113.

Krasinski, A. and Gradon, L. (2016), 'Comprehensive system for diesel fuel cleaning', *Filtration + Separation* **53**(1), 33–36.

Lacey, P., Gail, S., Kientz, J. M., Benoist, G., Downes, P. and Daveau, C. (2012), 'Fuel quality and diesel injector deposits', *SAE International Journal of Fuels and Lubricants* **5**, 1187–1198.

Lamb, J. S., Barker, J., Wilmot, E., Scurr, D. J., Snape, C. E. and Smith, E. F. (2021), 'Internal diesel injector deposit chemical speciation and quantification using 3D Orbisims and XPS depth profiling', *SAE International Journal of Advances and Current Practices in Mobility* **3**, 349–364.

Lambert, C. (2004), 'Solving the filtration challenges for diesel fuel', *SAE Technical Paper 2004-0148-7191* .

Lee, l., Pfalzgraz, L., Poppe, G., Powers, E. and Haines, T. (2007), 'The role of sterol glucosides on filter plugging', *Biodiesel Magazine* .

Lewis, S. A., Storey, J., Sluder, C. S., Cho, K., Connatser, R. and Barone, T. (2010), 'Carbonul formation during high efficiency clean combustion of face fuels', *SAE International Journal of Fuels and Lubricants* **3**, 849–856.

Loboda, A. V. and Chernushevich, I. V. (2009), 'A novel ion trap that enables high duty cycle and wide m/z range on an orthogonal injection tof mass spectrometer', *ASMS* **20**, 1342–1348.

Louette, P., Bodino, F. and Pireaux, J.-J. (2005*a*), 'Poly(acrylic acid) (PAA) XPS reference core level and energy loss spectra', *Surface Science Spectra* **12**.

Louette, P. L., Bodino, F. and Pireaux, J.-J. (2005*b*), 'Poly(ethylene terephthalate) (PET) XPS reference core level and energy loss spectra', *Surface Science Spectra* **12**.

Markov, A. (2000), 'Electrostatic axially harmonic orbital trapping: A high-performance technique of mass analysis', *Analytical Chemistry* **72**, 1156–1162.

Moulder, J. F., Stickle, W. F., Sobol, P. E. and Bomben, K. D. (1992), *Handbook of X-ray photolectron spectroscopy*, Physical Electronics Division.

Nazridoust, K. (2004), Session 14 - Thermodynamic cycles.

NESTE Oil (2012), Hvo, hydrotreated vegetable oil – a premium renewable biofuel for diesel engines, Technical report.

Niehuis, E., Möllers, R., Rading, D., Cramer, H.-G. and Kersting, R. (2013), 'Analysis of organic multilayers and 3d structures using ar cluster ions', *Surface and Interface Analysis* **45**(1), 158–162.

Ninomiya, S., Ichiki, K., Yamada, H., Nakata, Y., Seki, T., Aoki, T. and Matsuo, J. (2009), 'Molecular depth profiling of multilayer structures of organic semiconductor materials by secondary ion mass spectrometry with large argon cluster ion beams', *Rapid Communications in Mass Spectrometry* **23**(20), 3264–3268.

OCIA (2015), 'Passenger cars vehicles in use', https://www.oica.net/wp-content/uploads/PC_Vehicles-in-use.pdf.

Omori, T., Tanaka, A., Yamanda, K. and Bunne, S. (2011), 'Biodiesel deposit formation mechanism and improvement of fuel injection equipment (fie)', *SAE Technical Paper 2011-01-1935* .

Pacific Biodiesel (2019), 'History of biodiesel fuel', https://www.biodiesel.com/history-of-biodiesel-fuel/.

Park, B. H., Lee, M.-H., Kim, S. B. and Jo, Y. M. (2011), 'Evaluation of the surface properties of PTFE foam coating filter media using XPS and contact angle measurements', *Applied Surface Science* **257**, 3709–3716.

Passarelli, M. K., Pirkl, A., Moellers, R., Grinfeld, D., Kollmer, F., Havelund, R., Newman, C. F., Marshall, P. S., Arlinghaus, H., Alexander, M. R., West, A., Horning, S., Niehuis, E., Makarov, A., Dollery, C. T. and S, G. I. (2017), 'The 3D Orbisims - label-free metabolic imaging with subcellular lateral resolution and high mass-resolving power', *Nature Methods* **14**, 1175–1183.

Pfalzgraf, L., Lee, I., Foster, J. and Poppe, G. (2007), 'The effect of minor components on cloud point and filterability', *Biodiesel Magazine* .

Quingley, R., Barbour, R., Fahey, E., Arters, D. C., Wetzel, W. and Ray, J. (2010), A study of the internal diesel injector deposit phenomenom.

Rabbani, S. S. n., Razo, I. B., Kohn, T., Lockyer, N. P. and Vickerman, J. C. (2015), 'Enhancing ion yields in time-of-flight-secondary ion mass spectrometry: A comparative study of argon and water cluster primary beams', *Analytical Chemistry* **87**(4), 2367–2374.

Ratner, B. D. and Castner, D. G. (2009), *Electron spectroscopy for chemical analysis*, pp. 47–112.

Richards, P. (2014), *Automotive Fuels Reference Book*, 3 edn, SAE International.

Roosa, V. D. and Hodgkins, D. H. (1972), 'Development of a fuel filter and water separator for diesel engines', *SAE Transactions* **81**(4), 2323–2335.

Sano, H., Koshiro, K. and Inque, S. (2008), 'Electron microscopy for imaging interfaces in dental restorations', *Dental Biomaterials* pp. 58–80.

Savitzky, A. and Golay, M. J. E. (1964), 'Smoothing and differentiation of data by simplified least squares procedures', *Analytical Chemistry* **36**, 1627–1639.

Schwab, S. D., Bennett, J. J., Dell, S. J., Galante-Fox, J. M., Kulinowski, A. M. and Miller, K. T. (2010), 'Internal injector deposits in high-pressure common rail diesel engines', *SAE International Journal of Fuels and Lubricants* **3**, 865–878.

Shirley, D. A. (1972), 'High-resolution x-ray photoemission spectrum of the valence bands of gold', *PHYSICAL REVIEW B* **5**.

Smith, G. C., Hopwood, A. B. and Titchener, K. J. (2002), 'Microcharacterization of heavy-duty diesel engine poiston deposits', *Surface and Interface Analysis* **33**, 259–268.

Spanu, M., Reid, J., Barker, J., Scurr, D. and Snape, C. E. (2018), Detailed characterisation of diesel fuel filter deposits by ToFSIMS and other analytical methods, *in* '12th International Colloquium Fuels Conventional and Future Energy for Automobiles'.

Speight, J. G. (2018), *Introduction to Petroleum Biotechnology.*

Srivastava, V. C. (2012), 'An evaluation of desulfurization technologies for sulfur removal from liquid fuels', *RSC Advances* **2**, 759–783.

Sugiyama, G., Maeda, A. and Nagai, K. (2007), 'Oxidation degredation and acid generation in diesel fuel containing 5% FAME', *SAE Technical Paper 2007-01-2027* .

Tanakaa, A., Yamada, K., Omori, T., Bunne, S. and Hosokawa, K. (2013), 'Inner diesel injector deposit formation mechanism', *SAE International Journal of Fuels and Lubricants* **6**, 755–761.

Tang, H., De Guzman, R. C., Salley, S. O. and Simon Ng, K. Y. (2008), 'Formation of insolubles in palm oil-, yellow grease-, and soybean oil-based biodiesel blends after cold soaking at 4 °c', *Journal of the American Oil Chemists' Society* **85**, 1173–1182.

Tang, T.-W., Ku, Y.-Y. and L, C. C. (2016), 'Impacts of biodiesel blends on fuel filters of high pressure common rail (HPCR) system', *SAE Technical Paper 2016-01-1280* .

Touboul, D., Kollmer, F., Niehuis, E., Brunelle, A. and Laprévote, O. (2005), 'Improvement of biological time-of-flight-secondary ion mass spectrometry imaging with a bismuth cluster ion source', *Journal of the American Society for Mass Spectrometry* **16**(10), 1608–1618.

Transport and Environment (2017), 'Diesel: the true (dirty) story'.

Trindade, G. F. (2018), 'The development of multivariate analysis methadologies for complex ToF-SIMS datasets: Applications to materials science'.

Ullman, J., Geduldig, M., Stutzenberger, H., Caprotti, R. and Balfour, G. (2008), 'Investigation into the formation and prevention of internal diesel injector deposits', *SAE Technical Paper 2008-01-0926* .

UNFCCC (2008), Kyoto protocol reference manual, Technical report.

Vanbellingen, Q. P., Elie, N., Eller, M. J., Della-Negra, S., Touboul, D. and Brunelle, A. (2015), 'Time-of-flight secondary ion mass spectrometry imaging of biological samples with delayed extraction for high mass and high spatial resolutions', *Rapid Communications in Mass Spectrometry* **29**, 1187–1195.

Verdegan, B., True-Dahl, A., Haberkamp, W., Blizard, N., Genter, D. and Quillen, E. (2015), Filtration solutions for high pressure common rail fuel systems.

Vickerman, J. C. (2009), *Molecular spectrometry by SIMS*, pp. 113–205.

Wagner, C. D. (1978), 'X-ray photoelectron spectroscopy with x-ray photons of higher energy', *Journal of Vacuum Science and Technology* **15**(2), 518–523.

Wegh, R. S., Berendsen, B. J. A., Driessen-Van Lankveld, W. D. M., Pikkemaat, M. G., Zuidema, T. and Van Ginkel, L. A. (2017), 'Non-targeted workflow for identification of antimicrobial compounds in animal feed using bioassay-directed screening in combination with liquid chromatography-high resolution mass spectrometry', *Food Additives & Contaminants* **34**, 1935–1947.

Wucher, A. (2006), 'Molecular secondary ion formation under cluster bombardment: A fundemental review', *Applied Surface Science* **252**, 6482–6489.

Zanini, S., Massini, P., Mietta, M., Grimoldi, E. and Riccardi, C. (2008), 'Plasma treatments of PET meshes for fuel–water separation applications', *Journal of Colloid and Interface Science* **322**, 566–571.

Zubarev, R. A. and Markov, A. (2013), 'Orbitrap mass spectrometry', *Analytical Chemistry* **85**, 5288–5296.

Appendix A

SEM-EDX Work

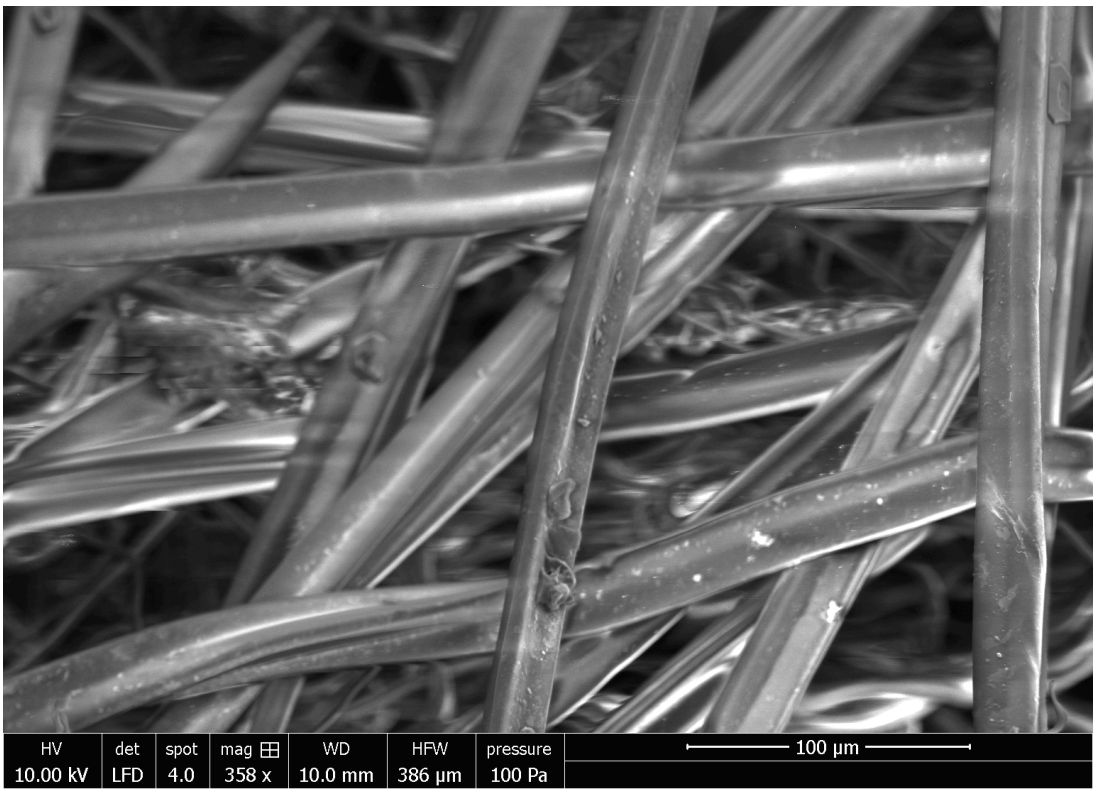


Figure A.1: *From SEM analysis a secondary electron image of LTF 002 (D100).*

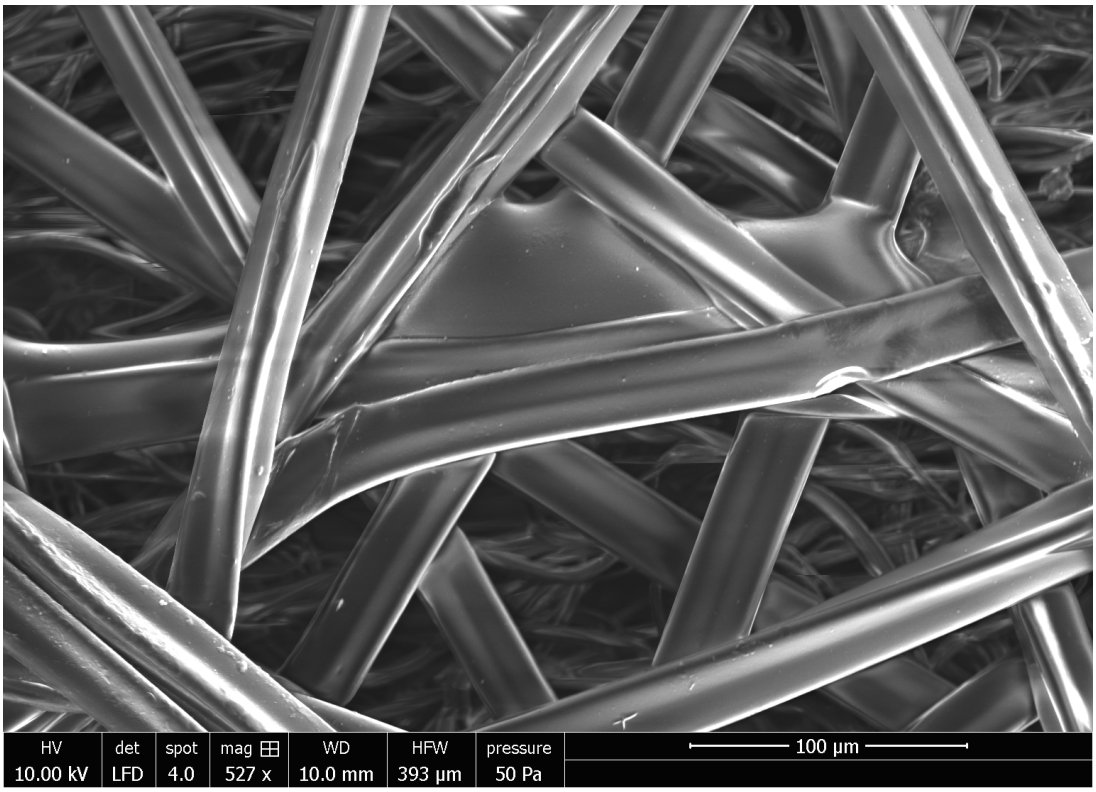


Figure A.2: *From SEM analysis a secondary electron image of LTF 004 (B20.*

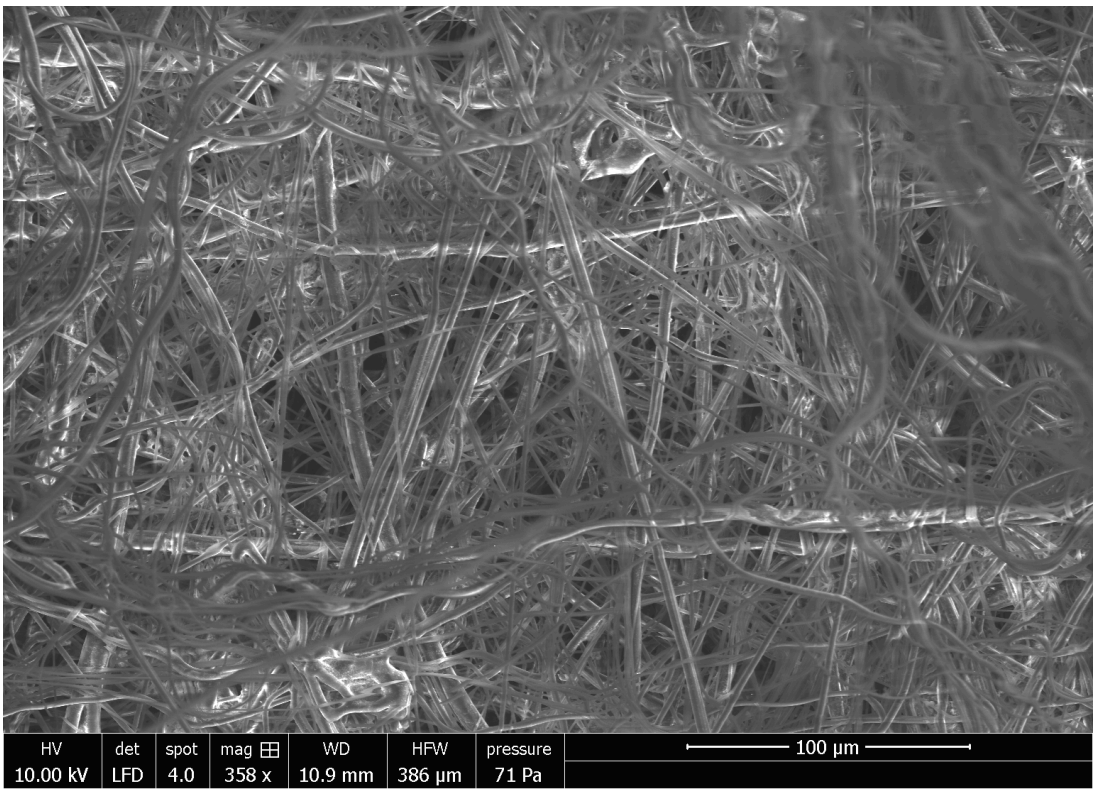


Figure A.3: *From SEM analysis a secondary electron image of LTF 005 (H100).*

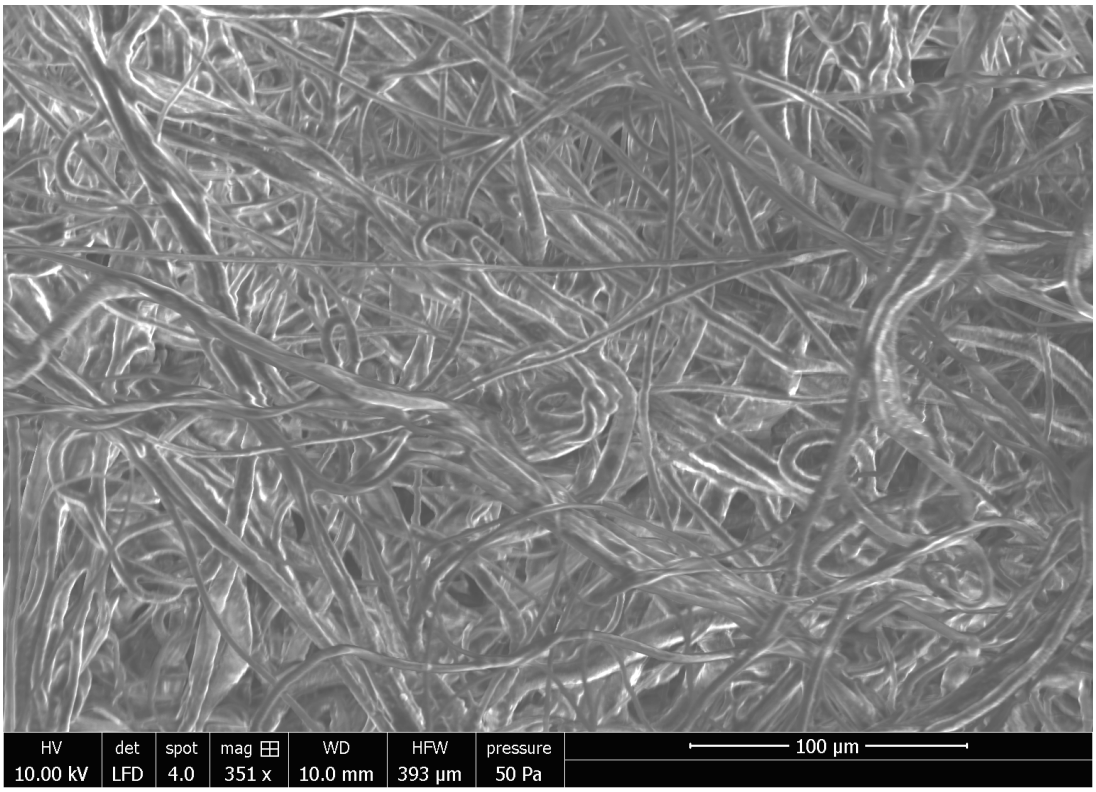


Figure A.4: *From SEM analysis a secondary electron image of LTF 006 (H20).*

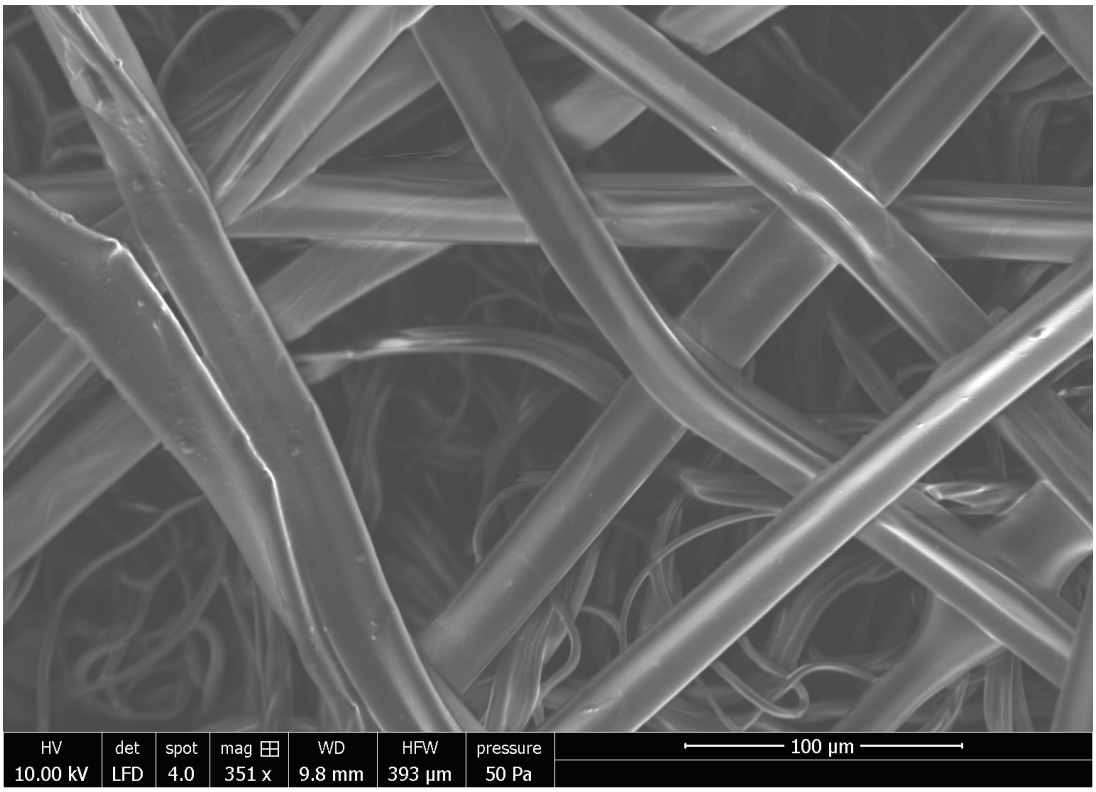


Figure A.5: *From SEM analysis a secondary electron image of LTF 007 (B50H50).*

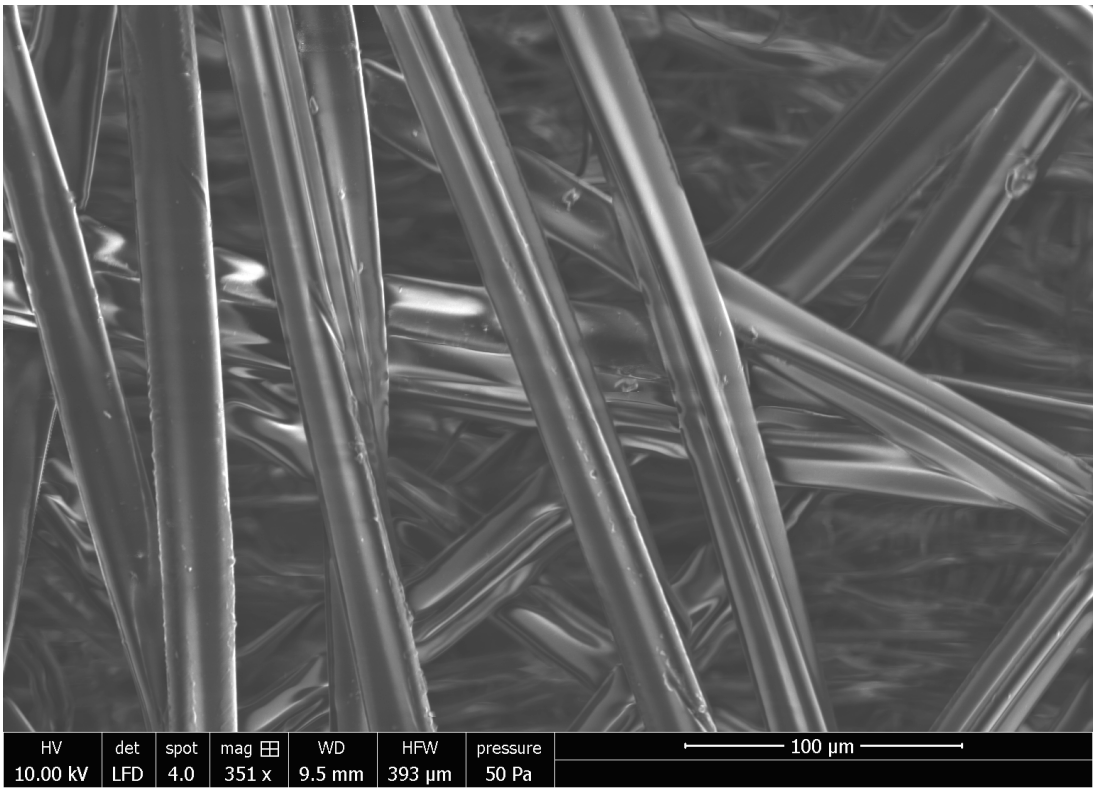


Figure A.6: *From SEM analysis a secondary electron image of LTF 008 (B10H10).*

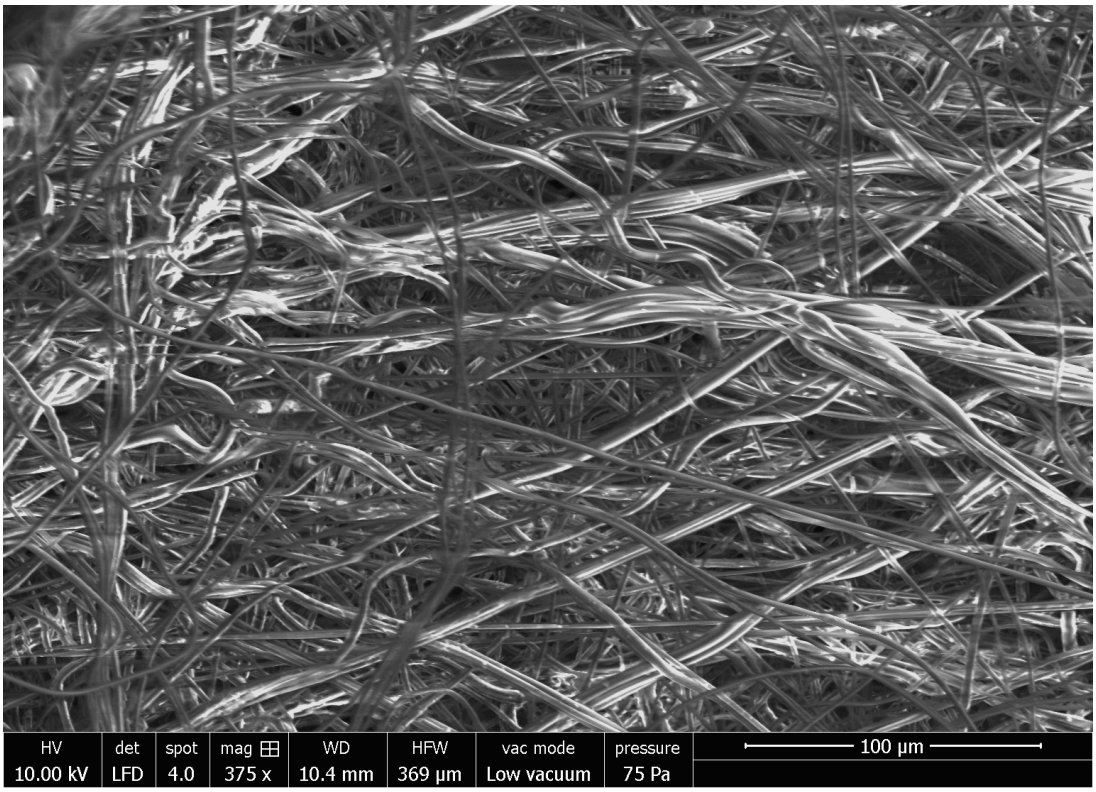


Figure A.7: *From SEM analysis a secondary electron image of ETF 020.*

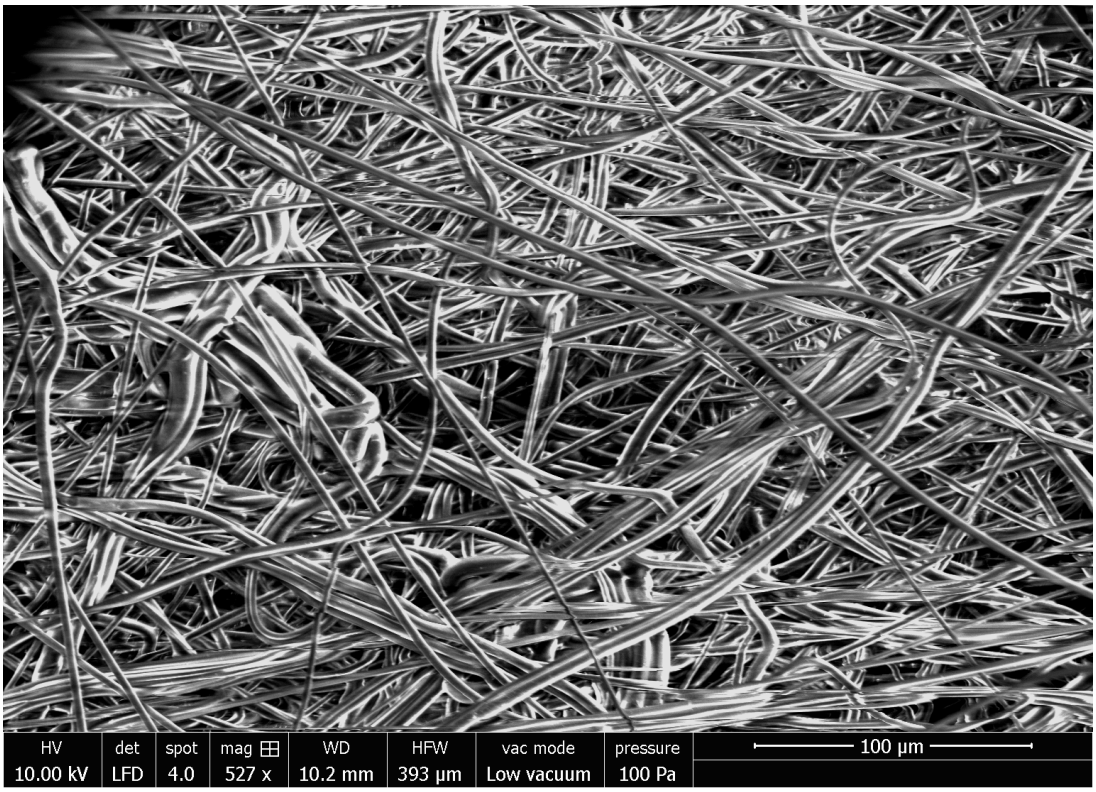


Figure A.8: *From SEM analysis a secondary electron image of ETF 021.*

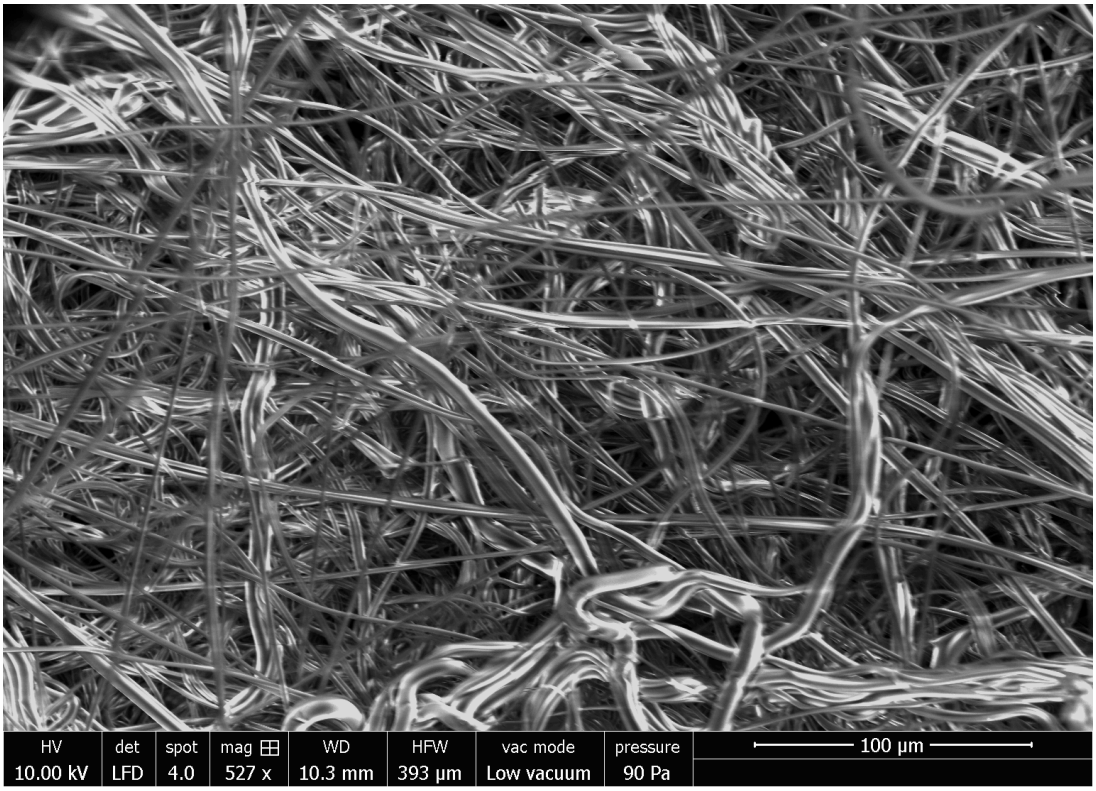


Figure A.9: *From SEM analysis a secondary electron image of ETF 024.*

Appendix B

Compound_finder

```
% In variable 'x', put your spectrum in here with the format format:
                  % column 1 column 2
                  % Mass     Intensity



%% SETTINGS

% Elements to search, H MUST be first
element_list = {'H' 'C' 'O' 'Na' 'N' 'Si' 'K' };
% min and max value for each element in element list
% set max_element to -1 if you want to cycle through all options
min_element = [ 0 0 0 0 0 0 0];
max_element = [-1 -1 0 0 0 0 0];

polarity = 1; % For -ve put -1
deviation_limits = [5,2.5]; % [Below 95 m/z, Above 95 m/z]

% min unsaturation limit and intensity limit
dbe_limit = 0;
```

```
intensity_limit = 0.0001;


%% SCRIPT
% Check to make sure element_list and start_element match
if size(element_list) == size(min_element) &...
        size(element_list) == size(max_element)



    formulas = ELEMENT_LOOP(x,element_list,min_element,max_element,...
        polarity,deviation_limits,ATOMIC_MASS(),dbe_limit,intensity_limit);


    % to print suitable combinations if only one mass checked
    if size(x,1) == 1
        for i = 1:size(formulas,1)
            for j = 1: size(formulas,2)
                if j > 4
                    fprintf('%i, ',formulas(i,j))
                    %fprintf(['%s_' '%i '],element_list{j-4},formulas(i,j))
                elseif j == 4
                    fprintf('%0.1f, ',formulas(i,j))
                else
                    fprintf('%.4f, ',formulas(i,j))
                end
            end
            fprintf('\b\b\n')
        end


    else
        DBE_ALL_CARBON_PLOT(formulas);
        SPECTRUM_PLOT(formulas);
        high_formula = DBE_FILTERED_CARBON_PLOT(formulas);
```

```
    end
else
    msgbox(['Make sure element_list and min_element and ',...
        'max_element are the same size'],...
        'Error','error')
end


clear deviation_limits element_list polarity i j
clear min_element max_element dbe_limit


function output = ELEMENT_LOOP(mass_inten_matrix,element_list,...
    min_element,max_element,polarity,deviation_limits,atomic_mass,...
    dbe_limit,intensity_limit)

    element_quant = size(element_list,2);


    % Generate element m/z list
    for i = 1:element_quant
        element_mass(i) = atomic_mass(element_list{i});
    end
    element_mass(end+1) = atomic_mass('e');

    % Find index of elements for DBE calc
    C_idx = find(strcmp(element_list, 'C'));
    C13_idx = find(strcmp(element_list, 'C13'));
    H_idx = find(strcmp(element_list, 'H'));
    N_idx = find(strcmp(element_list, 'N'));
    Cl_idx = find(strcmp(element_list, 'Cl'));
```

```
Cl37_idx = find(strcmp(element_list, 'Cl37'));
F_idx = find(strcmp(element_list, 'F'));
Si_idx = find(strcmp(element_list, 'Si'));



const_mass = 0;



output_i = 0;
tic
progress = 0;
fprintf('\b\t%3.0f%%',0)


for i = 1:size(mass_inten_matrix,1)
    % skip small intensities
    if mass_inten_matrix(i,2) < intensity_limit
        continue
    end

    progress = (100*(i/size(mass_inten_matrix,1)));

    mass = mass_inten_matrix(i,1);
    intensity = mass_inten_matrix(i,2);

    if mass < 95
        deviation_limit = deviation_limits(1);
    else
        deviation_limit = deviation_limits(2);
```

```
end



% Calculate max possible element for mass
for limit_idx = 1:element_quant
    if max_element(limit_idx) == -1
        element_limit(limit_idx) = ceil(mass/...
            atomic_mass(element_list{limit_idx}));
    else
        element_limit(limit_idx) = max_element(limit_idx);
    end
end

formula = min_element;

ready = false;

while ~ready

    % Calculate formula mass
    calc_mass = 0;
    for calc_idx = 1:element_quant
        calc_mass = calc_mass + ...
            formula(calc_idx) * element_mass(calc_idx);
    end

    calc_mass = calc_mass + (element_mass(end) * -polarity);

    % Calculate deviation in ppm
    deviation = (mass - calc_mass)* 10^6 / calc_mass;
```

```
% Prepare dbe formula
if ~isempty(C_idx)
    C = formula(C_idx);
else
    C = 0;
end
if ~isempty(C13_idx)
    C13 = formula(C13_idx);
else
    C13 = 0;
end
if ~isempty(N_idx)
    N = formula(N_idx);
else
    N = 0;
end
if ~isempty(H_idx)
    H = formula(H_idx);
else
    H = 0;
end
if ~isempty(Cl_idx)
    Cl = formula(Cl_idx);
else
    Cl = 0;
end
 if ~isempty(Cl37_idx)
    Cl37 = formula(Cl37_idx);
else
    Cl37 = 0;
end
```

```
if ~isempty(F_idx)
    F = formula(F_idx);
else
    F = 0;
end
if ~isempty(Si_idx)
    Si = formula(Si_idx);
else
    Si = 0;
end

dbe = (C + C13 + Si - H/2 + N/2 + (Cl+Cl37+F)/2 + 1);



% Conditions for output of formula
if abs(deviation) < deviation_limit && dbe >= dbe_limit
    output_i = output_i + 1;
    temp_output(output_i,:) = ...
        [mass deviation dbe intensity formula];

end

pass_check = false;
ready = true;

% Cycle through elements
for element_idx = 1:element_quant

    % Increase count of element each loop
    if element_idx == 1 && mass - calc_mass > 11
```

```
                formula(element_idx) = formula(element_idx) + 10;
            else
                formula(element_idx) = formula(element_idx) + 1;
            end

            if formula(element_idx) <= element_limit(element_idx)...
                    && (dbe > dbe_limit-1 || pass_check )
                ready = false;
                pass_check = false;
                break;
            end

            % If element count more than element limit, reset count
            % and move to next element
            formula(element_idx) = min_element(element_idx);

            % Allow formula to pass through previous condition once
            pass_check = true;
        end
    end
    fprintf('\b\b\b\b%3.0f%%',progress)
end
fprintf('\n')
toc
if exist('temp_output','var')
    output = temp_output;

    fprintf('%s\n','formulas variable format:');
    fprintf('%s','Measured m/z, Deviation, DBE, Intensity,');
    for print_idx = 1:element_quant
        fprintf('%s,',element_list{print_idx})
```

```
        end
        fprintf('\b\n')
    else
        output = [];
        fprintf('None found!\n')
    end



end

function atomic_mass = ATOMIC_MASS()
    %https://www.sisweb.com/referenc/source/exactmas.htm
    %https://physics.nist.gov/cgi-bin/Compositions/stand_alone.pl

    % Element list
    C_mass = 12;
    C13_mass = 13.003354;
    H_mass = 1.007825;
    N_mass = 14.003074;
    O_mass = 15.994915;
    S_mass = 31.972071;
    Ca_mass = 39.962591;
    Na_mass = 22.989769;
    F_mass = 18.998403;
    Cl_mass = 34.968852;
    Cl37_mass = 36.965902;
    Si_mass = 27.976927;
    Fe_mass = 55.934936;
    P_mass = 30.973761;
    K_mass = 38.963706;
```

```
    electron_mass = 0.0005489;

    % Add elements here making sure that keySet and valueSet are in the
    % correct order
    keySet = {'e','C','C13','H','N','O','S','Ca','Na',...
        'F','Cl','Cl37','Si','Fe','P','K'};
    valueSet = [electron_mass C_mass C13_mass H_mass N_mass O_mass ...
        S_mass Ca_mass Na_mass F_mass Cl_mass Cl37_mass Si_mass ...
        Fe_mass P_mass K_mass];

    atomic_mass = containers.Map(keySet,valueSet);
end
```

Appendix C

Identified Molecular Ions

Table C.1: *Proposed formulas of ions identified in this thesis, their respective deviations and information on their origin.*

m/z	Deviation (ppm)	Proposed formula	Sample type	Notes
77.0388	2.4	$C_6H_5^+$	Engine, Lab	Europe, US
80.948	0.7	Na_2Cl^+	Field	US
83.0605	3.9	$C_4H_7N_2^+$	Engine	
86.0153	1.7	$C_7H_2^+$	Engine, Lab	Europe, US
87.0231	1.6	$C_7H_3^+$	Engine, Lab	Europe, US
87.9257	4.3	FeO_2^-	Field	Asia
89.0387	1.5	$C_7H_5^+$	Engine, Lab	Europe, US
91.0543	1.2	$C_7H_7^+$	Engine, Lab	Europe, US
91.0544	1.7	$C_7H_7^+$	Engine	
93.0345	-1	$C_6H_5O^-$	Field	Asia
95.0493	1.5	$C_6H_7O^+$	Field	Europe
95.0495	1.8	$C_6H_7O^+$	Field	Asia
96.0005	-0.5	C_8^-	Field	US
97.0083	-0.7	C_8H^-	Field	US
98.0152	0.5	$C_8H_2^+$	Engine, Lab	Europe, US

99.0229	0.2	$C_8H_3^+$	Engine, Lab	Europe, US
102.0464	0	$C_8H_6^+$	Engine, Lab	Europe, US
102.9743	1.6	$Na_3H_2O_2^+$	Engine	
103.0542	-0.2	$C_8H_7^+$	Engine, Lab	Europe, US
103.9203	0.7	FeO_3^-	Field	Asia
108.0006	0.5	C_9^-	Field	US
109.0072	-0.5	$C_9H_1^+$	Engine, Lab	Europe, US
110.015	-0.6	$C_9H_2^+$	Engine, Lab	Europe, US
110.0237	0.4	$C_5H_4NO_2^+$	Field	Asia
111.0228	-0.8	$C_9H_3^+$	Engine, Lab	Europe, US
111.0916	-0.7	$C_6H_{11}N_2^+$	Engine	
113.0385	-1	$C_9H_5^+$	Engine, Lab	Europe, US
115.0541	-0.9	$C_9H_7^+$	Engine, Lab	Europe, US
115.0542	-0.2	$C_9H_7^+$	Engine	
116.9922	0.1	$C_3H_3O_2Na_2^+$	Engine	
116.9923	1.5	$C_3H_3O_2Na_2^+$	Field	US
117.0334	-1.4	$C_8H_5O^+$	Engine	
121.0084	0	$C_{10}H^-$	Field	US
121.0283	-0.9	$C_7H_5O_2^+$	Field	Europe
121.0296	0.8	$C_7H_5O_2^-$	Field	Asia
121.0296	0.8	$C_7H_5O_2^-$	Field	US
122.0149	-1.4	$C_{10}H_2^+$	Engine, Lab	Europe, US
123.0227	-1.6	$C_{10}H_3^+$	Engine, Lab	Europe, US
126.0462	-1.5	$C_{10}H_6^+$	Engine, Lab	Europe, US
127.054	-1.7	$C_{10}H_7^+$	Engine, Lab	Europe, US
128.0618	-1.7	$C_{10}H_8^+$	Engine, Lab	Europe, US
128.0619	-1.2	$C_{10}H_8^+$	Engine	
128.9534	-0.8	$CO_3Na_3^+$	Engine	

128.9534	1.3	$CO_3Na_3^+$	Field	US
130.9328	0.9	$Ca_2O_3H_3^+$	Field	US
130.9328	-0.4	$Ca_2O_3H_3^+$	Field	Europe
133.007	-2	$C_{11}H_1^+$	Engine, Lab	Europe, US
134.0148	-2	$C_{11}H_2^+$	Engine, Lab	Europe, US
137.0383	-2	$C_{11}H_5^+$	Engine, Lab	Europe, US
138.055	-1.1	$C_7H_8NO_2^+$	Field	Asia
139.0539	-2.1	$C_{11}H_7^+$	Engine, Lab	Europe, US
146.0148	-2.1	$C_{12}H_2^+$	Engine, Lab	Europe, US
148.9254	-0.5	$Na_3SO_3^+$	Engine	
148.9433	-0.8	$Ca_2O_4H_5^+$	Field	Europe
148.9435	0.2	$Ca_2O_4H_5^+$	Field	US
149.0096	0.2	$Si_2C_3H_9O_3^-$	Field	Asia, Europe US
150.0461	-2.1	$C_{12}H_6^+$	Engine, Lab	Europe, US
152.0617	-2.3	$C_{12}H_8^+$	Engine, Lab	Europe, US
152.0618	-1.6	$C_{12}H_8^+$	Engine	
152.9177	0.6	$CaSO_5H^-$	Field	Europe, US
158.0147	-2.3	$C_{13}H_2^+$	Engine, Lab	Europe, US
161.0382	-2.4	$C_{13}H_5^+$	Engine, Lab	Europe, US
163.0538	-2.4	$C_{13}H_7^+$	Engine, Lab	Europe, US
164.9202	1.3	$Na_3SO_4^+$	Field	US
164.9203	-0.5	$Na_3SO_4^+$	Engine	
165.0695	-2.1	$C_{13}H_9^+$	Engine, Lab	Europe, US
166.9538	-1.1	$Ca_2O_5H_7^+$	Field	Europe
166.9539	1.2	$Ca_2O_5H_7^+$	Field	US
169.0645	-1.7	$C_{12}H_9O^+$	Field	Europe
174.0461	-1.7	$C_{14}H_6^+$	Engine, Lab	Europe, US
176.0617	-1.7	$C_{14}H_8^+$	Engine, Lab	Europe, US

178.0773	-2.1	$C_{14}H_{10}^{+}$	Engine, Lab	Europe, US
183.0123	0.9	$C_8H_7SO_3^{-}$	Field	Europe, US
184.9796	-0.1	$C_4H_4O_4Na_3^{+}$	Engine	
184.9797	0.3	$C_4H_4O_4Na_3^{+}$	Field	US
185.0382	-1.8	$C_{15}H_5^{+}$	Engine, Lab	Europe, US
187.0539	-1.8	$C_{15}H_7^{+}$	Engine, Lab	Europe, US
189.0695	-1.9	$C_{15}H_9^{+}$	Engine, Lab	Europe, US
189.0696	-1.5	$C_{15}H_9^{+}$	Engine	
194.1175	-0.3	$C_{11}H_{16}NO_2^{+}$	Field	Asia
198.0461	-1.8	$C_{16}H_6^{+}$	Engine, Lab	Europe, US
200.0617	-1.7	$C_{16}H_8^{+}$	Engine, Lab	Europe, US
202.0773	-1.9	$C_{16}H_{10}^{+}$	Engine, Lab	Europe, US
204.9008	-0.6	$Ca_3O_5H_5^{+}$	Field	Europe
204.901	0.3	$Ca_3O_5H_5^{+}$	Field	US
209.0383	-1.5	$C_{17}H_5^{+}$	Engine, Lab	Europe, US
211.054	-1.2	$C_{17}H_7^{+}$	Engine, Lab	Europe, US
213.0696	-1.2	$C_{17}H_9^{+}$	Engine, Lab	Europe, US
215.0854	-0.8	$C_{17}H_{11}^{+}$	Engine, Lab	Europe, US
222.0462	-0.7	$C_{18}H_6^{+}$	Engine, Lab	Europe, US
222.9115	0	$Ca_3O_6H_7^{+}$	Field	Europe
222.9116	0.2	$Ca_3O_6H_7^{+}$	Field	US
224.0619	-0.7	$C_{18}H_8^{+}$	Engine, Lab	Europe, US
226.0775	-0.8	$C_{18}H_{10}^{+}$	Engine, Lab	Europe, US
226.0776	-0.4	$C_{18}H_{10}^{+}$	Engine	
227.081	0.5	$Si_3C_4H_{15}O_5^{+}$	Engine	
227.081	0.1	$Si_3C_4H_{15}O_5^{+}$	Field	Asia
227.0851	-1.8	$C_{18}H_{11}^{+}$	Engine, Lab	Europe, US
228.093	-1.7	$C_{18}H_{12}^{+}$	Engine, Lab	Europe, US

233.0383	-1.2	$C_{19}H_5^+$	Engine, Lab	Europe, US
235.0541	-0.7	$C_{19}H_7^+$	Engine, Lab	Europe, US
237.0697	-0.7	$C_{19}H_9^+$	Engine, Lab	Europe, US
239.0853	-0.9	$C_{19}H_{11}^+$	Engine, Lab	Europe, US
240.9222	1.9	$Ca_3O_7H_9^+$	Field	US
246.0462	-1	$C_{20}H_6^+$	Engine, Lab	Europe, US
248.0619	-0.7	$C_{20}H_8^+$	Engine, Lab	Europe, US
250.0775	-0.8	$C_{20}H_{10}^+$	Engine, Lab	Europe, US
250.1801	-0.2	$C_{15}H_{24}NO_2^+$	Field	Asia
252.0931	-1.1	$C_{20}H_{12}^+$	Engine, Lab	Europe, US
257.0382	-1.6	$C_{21}H_5^+$	Engine, Lab	Europe, US
259.054	-0.8	$C_{21}H_7^+$	Engine, Lab	Europe, US
261.0697	-0.7	$C_{21}H_9^+$	Engine, Lab	Europe, US
263.0853	-0.7	$C_{21}H_{11}^+$	Engine, Lab	Europe, US
265.1008	-1.5	$C_{21}H_{13}^+$	Engine, Lab	Europe, US
270.046	-1.4	$C_{22}H_6^+$	Engine, Lab	Europe, US
272.0618	-0.9	$C_{22}H_8^+$	Engine, Lab	Europe, US
274.0775	-0.8	$C_{22}H_{10}^+$	Engine, Lab	Europe, US
276.0932	-0.7	$C_{22}H_{12}^+$	Engine, Lab	Europe, US
278.8689	-0.3	$Ca_4O_7H_7^+$	Field	Europe
278.8692	0.9	$Ca_4O_7H_7^+$	Field	US
283.0539	-1	$C_{23}H_7^+$	Engine, Lab	Europe, US
285.0697	-0.7	$C_{23}H_9^+$	Engine, Lab	Europe, US
287.0853	-0.7	$C_{23}H_{11}^+$	Engine, Lab	Europe, US
289.1009	-1.1	$C_{23}H_{13}^+$	Engine, Lab	Europe, US
294.046	-1.5	$C_{24}H_6^+$	Engine, Lab	Europe, US
296.0618	-0.9	$C_{24}H_8^+$	Engine, Lab	Europe, US
296.7895	-0.7	$Ca_5O_6H^+$	Field	Europe

298.0775	-0.6	$C_{24}H_{10}^+$	Engine, Lab	Europe, US
300.0931	-0.7	$C_{24}H_{12}^+$	Engine, Lab	Europe, US
302.1086	-1.5	$C_{24}H_{14}^+$	Engine, Lab	Europe, US
305.1736	0.6	$C_{16}H_{26}O_4Na^-$	Field	US
307.0538	-1.3	$C_{25}H_7^+$	Engine, Lab	Europe, US
309.0696	-1	$C_{25}H_9^+$	Engine, Lab	Europe, US
311.0853	-0.9	$C_{25}H_{11}^+$	Engine, Lab	Europe, US
313.1008	-1.1	$C_{25}H_{13}^+$	Engine, Lab	Europe, US
320.0617	-1	$C_{26}H_8^+$	Engine, Lab	Europe, US
322.0774	-0.8	$C_{26}H_{10}^+$	Engine, Lab	Europe, US
324.0931	-0.8	$C_{26}H_{12}^+$	Engine, Lab	Europe, US
326.1086	-1.2	$C_{26}H_{14}^+$	Engine, Lab	Europe, US
331.0538	-1.3	$C_{27}H_7^+$	Engine, Lab	Europe, US
333.0695	-1.1	$C_{27}H_9^+$	Engine, Lab	Europe, US
335.0852	-0.9	$C_{27}H_{11}^+$	Engine, Lab	Europe, US
337.1009	-0.9	$C_{27}H_{13}^+$	Engine, Lab	Europe, US
339.1164	-1.3	$C_{27}H_{15}^+$	Engine, Lab	Europe, US
344.0617	-1.2	$C_{28}H_8^+$	Engine, Lab	Europe, US
346.0774	-1	$C_{28}H_{10}^+$	Engine, Lab	Europe, US
348.0931	-0.8	$C_{28}H_{12}^+$	Engine, Lab	Europe, US
350.1086	-1	$C_{28}H_{14}^+$	Engine, Lab	Europe, US
351.1519	0.1	$C_{16}H_{26}O_4Na_3^+$	Engine	
351.152	0.4	$C_{16}H_{26}O_4Na_3^+$	Field	US
352.8369	-0.5	$Ca_5O_9H_9^+$	Field	Europe
352.8372	0.8	$Ca_5O_9H_9^+$	Field	US
357.0695	-1.2	$C_{29}H_9^+$	Engine, Lab	Europe, US
359.0852	-1	$C_{29}H_{11}^+$	Engine, Lab	Europe, US
361.1008	-0.9	$C_{29}H_{13}^+$	Engine, Lab	Europe, US

363.1164	-1.3	$C_{29}H_{15}^+$	Engine, Lab	Europe, US
370.0773	-1.1	$C_{30}H_{10}^+$	Engine, Lab	Europe, US
372.093	-0.9	$C_{30}H_{12}^+$	Engine, Lab	Europe, US
374.1086	-1	$C_{30}H_{14}^+$	Engine, Lab	Europe, US
381.0694	-1.2	$C_{31}H_9^+$	Engine, Lab	Europe, US
383.0851	-1.1	$C_{31}H_{11}^+$	Engine, Lab	Europe, US
385.1008	-1.1	$C_{31}H_{13}^+$	Engine, Lab	Europe, US
387.1164	-1.2	$C_{31}H_{15}^+$	Engine, Lab	Europe, US
394.0772	-1.2	$C_{32}H_{10}^+$	Engine, Lab	Europe, US
396.0929	-1.1	$C_{32}H_{12}^+$	Engine, Lab	Europe, US
398.1086	-1.1	$C_{32}H_{14}^+$	Engine, Lab	Europe, US
400.1241	-1.3	$C_{32}H_{16}^+$	Engine, Lab	Europe, US
407.0851	-1.1	$C_{33}H_{11}^+$	Engine, Lab	Europe, US
407.2147	-0.2	$C_{20}H_{34}O_4Na_3^+$	Field	US
409.1007	-1.1	$C_{33}H_{13}^+$	Engine, Lab	Europe, US
411.1164	-1.1	$C_{33}H_{15}^+$	Engine, Lab	Europe, US
418.0772	-1.2	$C_{34}H_{10}^+$	Engine, Lab	Europe, US
420.0929	-1.1	$C_{34}H_{12}^+$	Engine, Lab	Europe, US
422.1086	-1.1	$C_{34}H_{14}^+$	Engine, Lab	Europe, US
424.1241	-1.2	$C_{34}H_{16}^+$	Engine, Lab	Europe, US
431.0851	-1.1	$C_{35}H_{11}^+$	Engine, Lab	Europe, US
433.1007	-1	$C_{35}H_{13}^+$	Engine, Lab	Europe, US
435.1164	-1	$C_{35}H_{15}^+$	Engine, Lab	Europe, US
435.246	-0.2	$C_{22}H_{38}O_4Na_3^+$	Field	US
441.2972	-0.8	$C_{26}H_{42}O_4Na^+$	Engine	
441.2979	1.5	$C_{26}H_{42}O_4Na^+$	Field	US
444.0928	-1.2	$C_{36}H_{12}^+$	Engine, Lab	Europe, US
446.1085	-1	$C_{36}H_{14}^+$	Engine, Lab	Europe, US

448.1242	-1	$C_{36}H_{16}^+$	Engine, Lab	Europe, US
449.2617	0.7	$C_{23}H_{40}O_4Na_3^+$	Field	US
455.318	-1.8	$C_{27}H_{44}O_4Na^+$	Engine	
457.1007	-1	$C_{37}H_{13}^+$	Engine, Lab	Europe, US
459.1164	-1	$C_{37}H_{15}^+$	Engine, Lab	Europe, US
461.132	-1	$C_{37}H_{17}^+$	Engine, Lab	Europe, US
469.3261	0.6	$C_{28}H_{46}O_4Na^+$	Engine	
469.3292	1.8	$C_{28}H_{46}O_4Na^+$	Field	US
470.1086	-0.9	$C_{38}H_{14}^+$	Engine, Lab	Europe, US
472.1242	-0.9	$C_{38}H_{16}^+$	Engine, Lab	Europe, US
477.4415	0.1	$C_{30}H_{57}N_2O_2^+$	Field	Asia
481.1008	-0.9	$C_{39}H_{13}^+$	Engine, Lab	Europe, US
483.1164	-0.9	$C_{39}H_{15}^+$	Engine, Lab	Europe, US
483.3444	0.5	$C_{29}H_{48}O_4Na^+$	Engine	
485.1321	-0.8	$C_{39}H_{17}^+$	Engine, Lab	Europe, US
494.1086	-0.8	$C_{40}H_{14}^+$	Engine, Lab	Europe, US
496.1242	-0.8	$C_{40}H_{16}^+$	Engine, Lab	Europe, US
507.1165	-0.7	$C_{41}H_{15}^+$	Engine, Lab	Europe, US
509.1321	-0.7	$C_{41}H_{17}^+$	Engine, Lab	Europe, US
520.1243	-0.6	$C_{42}H_{16}^+$	Engine, Lab	Europe, US
533.5042	0.3	$C_{34}H_{65}N_2O_2^+$	Field	Asia
589.5668	0.2	$C_{38}H_{73}N_2O_2^+$	Field	Asia
645.6295	0.4	$C_{42}H_{81}N_2O_2^+$	Field	Asia
701.6921	0.4	$C_{46}H_{89}N_2O_2^+$	Field	Asia
757.7547	0.3	$C_{50}H_{97}N_2O_2^+$	Field	Asia
813.8173	0.3	$C_{54}H_{105}N_2O_2^+$	Field	Asia
869.8799	0.3	$C_{58}H_{113}N_2O_2^+$	Field	Asia
925.9425	0.3	$C_{62}H_{121}N_2O_2^+$	Field	Asia

982.005	0.1	$C_{66}H_{129}N_2O_2^+$	Field	Asia
1038.0678	0.5	$C_{70}H_{137}N_2O_2^+$	Field	Asia
1094.1301	0	$C_{74}H_{145}N_2O_2^+$	Field	Asia